Local Symmetry and Domain Patterns: Ordering Phenomena in Transition-Metal Oxides

Inaugural - Dissertation
zur
Erlangung des Doktorgrades
der Mathematisch-Naturwissenschaftlichen Fakultät
der Universität zu Köln

vorgelegt von
Marcel Buchholz
aus Köln

Köln 2013

Berichterstatter:
Prof. Dr. Markus Braden
Prof. Dr. Liu Hao Tjeng

Betreuer:
Dr. Christian Schüßler-Langeheine

Vorsitzender der Prüfungskommission:
Prof. Dr. Ladislav Bohatý

Beisitzer:
Dr. Thomas Koethe

Tag der mündlichen Prüfung:
21. Januar 2013

Contents

Introduction

Transition-metal oxides (TMOs) are known for their variety of intriguing phenomena arising from the interplay of the metal ions with the surrounding oxygen ions. They are probably one of the most fascinating classes of materials studied in modern condensed-matter physics. Thereunder the most prominent phenomenon is high-temperature superconductivity (HTS) in copper oxides, in which the electrical resistivity vanishes below a critical temperature [1]. The fascination has led to a plenty of scientific publications, which delivered new insights into the puzzling complexity of these materials. While a complete understanding of the underlying physics is still lacking, the progress triggered the invention of various new theoretical and experimental methods.

Besides HTS, one finds different electronic and magnetic phases in TMOs, for example metallic and insulating phases, charge ordering, orbital ordering, ferroelectricity, ferro-, ferri-, and antiferromagnetism and many more [2]. The influence of external parameters like pressure, temperature, chemical doping, and magnetic or electric fields can lead to dramatic changes of these phases and results in complex phase diagrams. Examples are the colossal magnetoresistance (CMR) in manganate oxides, in which a dramatic change in the electrical resistivity is found [3], or different kinds of metal-to-insulator transitions (MIT) for example driven by doping or temperature [4].

In the last years inhomogeneous ground states as a mixture between competing phases were proposed [5]. Energetically close phases can coexist and small perturbations can lead to giant changes by a reorganization of different domains, which for example is believed to cause the CMR effect [6].

Furthermore, these properties can dramatically change, if the dimensionality in the material is reduced, for example by going from a bulk to a thin film sample [7, 8] or if different materials are combined [9–11]. The latter can lead to completely new phenomena at the interfaces due to the interplay of adjacent phases and the organization of the electronic wave functions. A simple example is the existence of a superconducting phase between two insulating TMOs [12], however, this complex interplay is far from being predictable and possible combinations are numerous, including also non-TMOs. For sure, this field of research offers an interesting playground for strongly correlated

physics in the 21st century.

Some of the advances and improvements in the understanding of TMOs have already led to technical applications and are omnipresent in our everyday life, like in data storage devices. Moreover, many properties will open up completely new possibilities, like spin polarized transport for spintronics [13] or electric switching of magnetic information in multiferroic materials [14–16].

All these interesting properties of TMOs originate in the various degrees of freedom of the partially filled electronic d states, namely its spin, charge and orbital degree of freedom [17]. In a crystal, in which neighboring wave functions overlap, strong electronic correlations change the energies and occupation probabilities of the electronic states. The atomic degeneracy is lifted, while the configuration can vary on different crystallographic sites. The influence of the local surrounding determines the occupation and shape of the respective lowest electronic states and may result in different charges, spins and orbitals on different sites. Magnetism, charge, and orbital occupation can thus be spatially modulated and cause magnetic, charge, and orbital ordering. Different kinds of ordering are known, for example ferro- and various antiferromagnetic ordering, charge stripe and checkerboard charge ordering or ferro- and antiferro-orbital ordering. These ordered phases are often in close relation to spectacular phenomena, like for instance superconductivity; however, the exact interplay is quite often a matter of debate and investigations on the formation of these modulations provide crucial input for the theoretical description of correlated electron systems.

The most important tools for structural investigations of ordered states are neutron and x-ray diffraction. As the interaction processes of neutrons and x-rays with matter are different this leads to an advantageous complementarity of both techniques. The neutron, as an uncharged particle that carries a spin, is mainly scattered by the nucleus due to strong interaction and by the spin and orbital moments of the electrons due to dipole-dipole interaction. Thus, nuclear scattering is the ideal tool for structural investigations and magnetic scattering reveals insight into the ordering of spin and orbital moments. Charge ordering cannot directly be detected by neutrons due to their uncharged character, but can be observed by concomitant changes in the crystallographic structure. The interaction of x-rays with matter is completely different. The strongest process that leads to structural diffraction is due to the interaction of the electrical field of the x-ray radiation with the whole electronic charge, namely Thomson scattering. In resonant x-ray diffraction (RXD) further contributions come from the interaction of the incident radition with the outer electrons. A virtual excitation of a core electron into the unoccupied states makes RXD sensitive to spin, charge and orbital ordering.

The theory behind RXD was developed in the late 1980s [18–20] and an experimental realization was only possible at tuneable synchrotron facilities. In the last decades the technique has shown its ability to directly detect different kinds of ordering for example in Holmium metal [21], copper oxides [22–25], manganese oxides [26, 27], nickel oxides [28], and magnetite (Fe_3O_4) [29–31]. Great power comes from the combination of spectroscopic sensitivity with structural resolution. The virtual excitation of the RXD process probes the unoccupied states and is extremely sensitive to the local anisotropy. Therefore, the scattering factor becomes a tensor and depends on the incoming and

outgoing polarization as well as the azimuthal orientation. Analysis of the polarization and azimuthal dependence can be used to reveal the electronic symmetry. Energy-selective probing makes it possible to address the ordering to a specific valence state or a specific orbital state.

The benefit of RXD has to be paid by a complex ultra-high vacuum (UHV) setup, as most of the interesting absorption edges of TMOs lie in the low energy soft x-ray regime, where strong absorption in air does not allow the use of standard x-ray scattering devices.

In the framework of this thesis a novel UHV diffractometer was build up and commissioned. The new instrument will be available as an user experiment at the new synchrotron facility PETRA III in the near future and provides excellent conditions to study samples by means of soft x-ray diffraction techniques. The installation of an in-vacuum CCD camera and the integration of a coherent x-ray diffraction (CXD) sample stage make this instrument well suited to study complex ordering phenomena in TMOs with resonant soft x-ray diffraction (RSXD) and CXD experiments. Partially using this new instrument, RSXD experiments were carried out for two prototypical TMO materials showing complex ordering phenomena.

The formation of stripe like ordering is found in several TMOs. In the copper oxide high-T_c superconductors charge and spin stripe phases are often found very close to the superconducting phase. Whether stripes promote or prevent superconductivity is, however, still a matter of debate. Interestingly, in the prototypical high-T_c superconductor $La_{1.88}Sr_{0.12}CuO_4$ (LSCO) only the magnetic stripe order had been found so far. In a RSXD experiment in LSCO we have found a peak at the position, at which charge stripe order is expected. The electronic origin of the (0.24 0 0) diffraction peak is similar to the one found in our reference sample $La_{1.48}Nd_{0.4}Sr_{0.12}CuO_4$ (LNSCO), in which the formation of charge stripes is well established. This is the first observation of charge stripe ordering in this compound. From comparison to high energy diffraction results, in which the peak was not found, we conclude that the formation of charge stripe order takes place in the near-surface area of the sample.

Charge and orbital ordering in magnetite (Fe_3O_4), the material for which charge ordering was suggested for the first time, is still not fully understood. We have studied the azimuthal dependence of the $(00\frac{1}{2})$ charge orbital ordering reflex, which is directly related to the symmetry of the electronic wave function. By analyzing the azimuthal dependence of the linear dichroism in the diffraction signal, we found that a pronounced monoclinic symmetry is reflected in the pattern. In a recent crystal-structure refinement, published this year, our findings were confirmed by the observation of a monoclinic crystal structure. From all orbital ordering models that were proposed so far only a complex-coefficient orbital ordering model could describe the results of our experiment. Further indications for the existence of complex-coefficient orbital ordering in magnetite is revealed by the azimuthal dependence of the circular dichroic diffraction signal.

The last project of this thesis deals with the dynamics of phase separation. Phase-separated materials are spatial inhomogeneous and show phase coexistences of different electronic phases. The idea was to explore the possibility of using coherent x-ray diffraction to follow the domain formation and domain-wall motion in real time. First results

could be obtained from $R_1Ca_{1-x}TiO_3$ (with R = Er, Y), in which the coexistence of metallic and charge ordered insulating regions was predicted. The insulating regions are characterized by superstructure reflections, which are absent in the metallic regions. The diffraction intensities of coherently illuminated charge ordered regions interfere and produce a speckle pattern on an area-resolved detector. Dynamics in real space should be visible in a fluctuating speckle pattern. In the first experiments it turned out that the lacking stability of the setup is a serious limitation for this kind of studies. To overcome this limitation a newly developed stable sample setup was used. In all quantitative and qualitative analyses of the temporally evolving speckle pattern domain-wall dynamics could not be found. By changing the temperature, the pattern changes from one static to a different static configuration on time scales that are not accessible in our experiments. New x-ray free electron lasers, like LCLS and the European XFEL, will extend the accessible time domain to much shorter time scales.

This thesis is organized as follows: The first chapter presents some basic information about the scattering formalism, providing the theoretical frame to analyze the data that is taken by x-ray diffraction experiments.

In the second chapter the new UHV diffractometer, which was build up and commissioned, is presented. First results of a characterization of x-ray reflectors as well as of an in-vacuum CCD camera are presented as well.

In the third chapter RSXD results of the prototypical high-T_c superconductor LSCO at the O-K and Cu-$L_{2,3}$ edge are presented, which clearly show that LSCO is close to the formation of charge stripe ordering and only a reduced dimensionality in the near-surface region enables its stabilization.

The fourth chapter presents RSXD studies of Fe_3O_4, in which the azimuthal dependence of the $(00\frac{1}{2})$ charge orbital ordering reflex is recorded. The experimental results are compared to symmetry considerations and theoretical predictions calculated by A. Tanaka on the basis of the complex-coefficient orbital ordering model.

In the last chapter a coherent scattering experiment on $Er_{0.6}Ca_{0.4}TiO_3$ (ErCaTiO) is presented. The chapter deals with the feasibility and challenges of this new scattering technique, which makes use of the interference of coherent x-ray photons from different regions of the sample.

CHAPTER 1

X-Ray Diffraction

1.1. Introduction

X-ray diffraction experiments can be used to gain information about the character and spatial arrangement of electronic modulations in TMOs. Basic questions about the electronic configuration range from the occupation and symmetry of the local electronic states on different atomic sites, to the spatial arrangement of these electronic states, and up to the domain pattern of different coexisting electronic phases.

The occupation of electronic states is probed with spectroscopic techniques, which reveal information about the density of states. In x-ray absorption spectroscopy (XAS) a transition of a core electron, which is excited by the absorption of a photon with a specific energy, into a final state above the Fermi level probes the unoccupied states. For example at the O-K edge an electron from an $1s$ state is excited into the $2p$ states. The symmetry of the electronic state can be probed either by the variation of the polarization of the incident x-ray light (polarization dependence) or by rotating the sample around a specific axis (azimuthal dependence). The occupation of the final state, the transition energy, and the local symmetry give information about the surrounding of the probed site and the correlations with neighboring states.

Different electronic wave functions can arrange in a periodic order and lead to novel electronic phases characterized by, for example, charge or orbital ordering. The spatial arrangement of these states can be determined by x-ray diffraction methods. The combination of x-ray diffraction with the spectroscopy sensitivity from XAS in the vicinity of x-ray absorption edges leads to resonant x-ray diffraction (RXD). RXD can be described within a two-step model. The first part of the scattering process is the absorption of the photon and the second one the re-decay under emission of a photon. The diffraction signal is sensitive to the transition energy and the spatial arrangement of the scattering sites.

A coexistence of different electronic phases can lead to a particular sensitivity of macroscopic properties to external perturbations. To study the mobility and dynamics of such an arrangement, for example across a phase transition that involves the coexistence and reorganization of at least one ordered phase, coherent x-ray diffraction (CXD) experiments can be performed, in which only the ordered phase contributes to the diffraction peak. The coherent illumination creates an interference pattern that is determined by the spatial arrangement of the contributing phases and reveals their dynamics.

The rest of this chapter is divided into three sections and organized as follows: it starts with a section on XAS (Sec. 1.2), in which the spectroscopic information available at soft x-ray resonances is illustrated by giving a few examples from literature. In the second section the two steps of the scattering process are described in detail. It is outlined how interference from all contributing scattering centers leads to the diffraction process. In the last section we discuss the CXD process. As a coherent photon beam is one important requirement for this technique the term coherence is introduced. Afterwards the interference of the scattered intensity and the resultant speckle pattern is discussed. In the end of this section it is described how to analyze the temporal evolution of the speckle pattern.

1.2. X-ray absorption spectroscopy

One of the most powerful spectroscopic techniques for the investigation of TMOs is x-ray absorption spectroscopy (XAS), in which the incident x-ray photon excites an electron from an occupied core state into an unoccupied state above the Fermi level [32]. This process reveals insight into the occupation of the probed states. Each transition from one into another state is connected with a change in the set of quantum numbers. Selection rules for the relation between changes in the set of quantum numbers and the incident photon polarization further constrain these transitions. A polarization, azimuthal and energy dependent experiment can therefore be used to uncover the electronic occupation and symmetry.

In a benchmark experiment C. T. Chen et al. have demonstrated the power of XAS to explore the electronic character of intrinsic and doped holes in $La_{2-x}Sr_xCuO_4$ (LSCO) for different doping levels [33]. They used linear polarized x-rays and varied the angle between the electric field vector of the light and the c-direction of the samples. The absorption spectra show an anisotropic behavior at both the O-K and Cu-$L_{2,3}$ edge and a shift of the resonance energy at the O-K edge. Furthermore, in the spectra a transfer of spectral weight was found with hole doping. From a careful analysis they determined the character of the intrinsic and doped holes in terms of occupation of O-2p and Cu-3d states.

XAS experiments in magnetite (Fe_3O_4) by Schlappa et al. were used to identify the three different Fe-sites (B-site Fe^{2+}, A-site Fe^{3+} and B-site Fe^{3+}) with distinct resonance energies. The knowledge of the resonance energies was utilized in a RXD experiment to determine the contributions from the different sites to the diffraction signal.

In x-ray magnetic circular dichroism (XMCD) experiments of a magnetized sample,

in which circular polarized light transfers a photon angular moment to the excited electron, a difference in the absorption of left and right circularly polarized x-ray light is found [34–37]. At the TM-L_3 edge the different photon moments for left and right circular polarization and the spin-orbit coupling of the initial state create electrons with opposite spins [38]. The absorption process in materials with a net magnetic moment is spin-dependent and makes it possible to determine the size and direction of the spin and orbital magnetic moments. XMCD measurements at the Fe-$L_{2,3}$ edge were used to investigate the magnetic structure of Fe_3O_4, in which the XMCD signal shows contributions from the three different Fe-sites [39]. In an antiferromagnetic material there is no circular dichroism but a linear dichroism, which can be used to determine the orientation of the antiferromagnetic axis [40–42].

1.3. Resonant soft x-ray diffraction

Resonant (elastic) x-ray diffraction (RXD), which is one of the techniques that was used in the frame of this thesis, evolved in the last decades on the basis of XAS and is well suited to study charge, orbital and spin order [43–48]. The scattering process of RXD involves a virtual electronic excitation from a core hole state to an unoccupied state, which is triggered by the absorption of the incident photon (Fig. 1.1). This

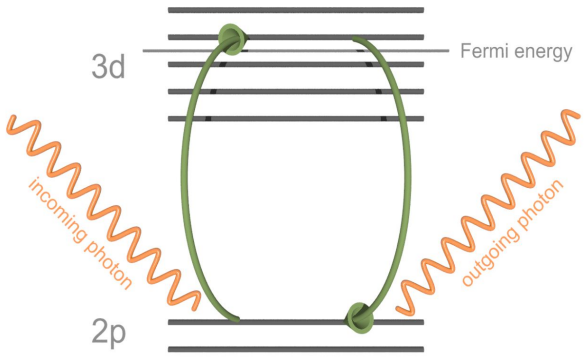

Fig. 1.1.: Virtual dipole excitations in a resonant scattering process at the L_2 edge: the incoming photon excites the $2p$ electron into an unoccupied $3d$ state above the fermi level, which then decays into a core hole by re-emitting the outgoing photon.

excited state relaxes back under emission of the scattered photon, which, in an elastic process, has the same energy as the incident one. A collective process on equivalent scattering sites leads to the interference of all these scattered photons and in case of constructive interference a diffraction peak can be observed. The energy dependence reveals spectroscopic information of the involved intermediate states similar as in XAS. In addition to the spectroscopic information, information on the arrangement of the scatterers is received.

In $3d$-TMO, the most interesting electronic transitions are those from the oxygen $1s \rightarrow 2p$ states (O-K edge) and those from the transition metal $2p \rightarrow 3d$ states

(TM-$L_{2,3}$ edge), as these outermost states mainly determine the electronic and magnetic properties.

To illustrate the contrast mechanism, we restrict to electric-dipole allowed transitions, in which the angular quantum number l changes by 1 ($\Delta l = 1$).

1.3.1. Atomic orbitals and transition integral

In the $1s$ states, the principle quantum number n is equal 1, the angular quantum number l is equal 0 and the magnetic quantum number m_l is equal to 0, whereas in the $2p$ states $n = 2$, $l = 1$, $m_l = -1, 0, 1$ and in the $3d$ states $n = 3$ and $l = 2$, $m_l = -2, -1, 0, 1, 2$. Therefore, there is one $1s$ orbital and there are three $2p$ orbitals, namely $2p_x$, $2p_y$ and $2p_z$, and five $3d$ orbitals, namely $3d_{xy}$, $3d_{xz}$, $3d_{yz}$, $3d_{x^2-y^2}$, and $3d_{z^2}$, all of which can be occupied with two electrons of opposite spin. A picture of these orbitals including their parity with respect to the coordinate axes can be found in Fig. 1.2. The possibility of a

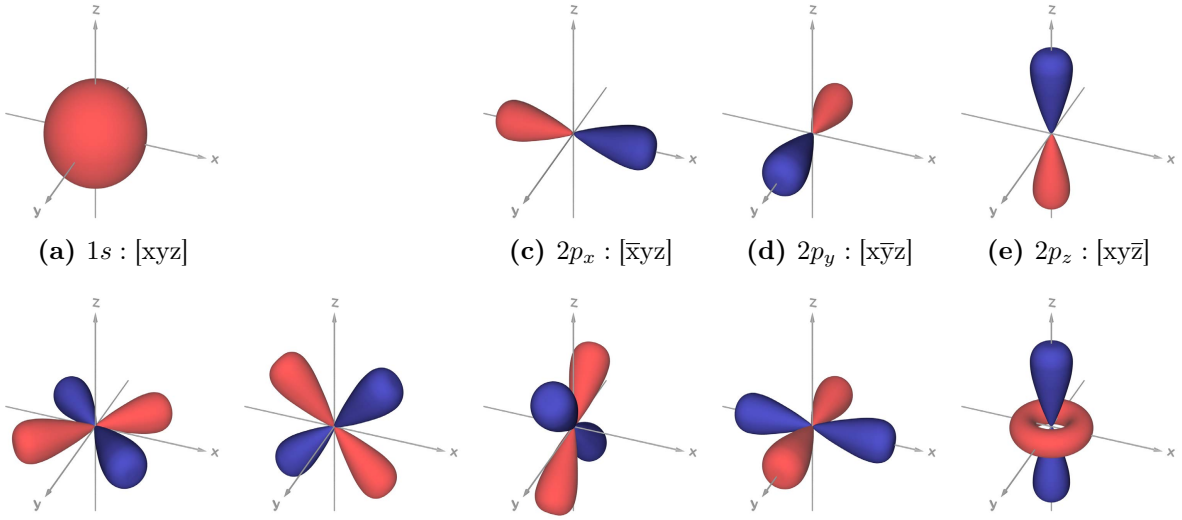

Fig. 1.2.: Schematically shape of the $1s$, $2p$ and $3d$ orbitals. The bracket notation gives the parity of the wave function with respect to the coordinate axes. Without (with) bar denotes an even (odd) parity.

transition can be calculated by evaluating the transition integrals $<i|d|f>$, where $\langle i|$ is the initial state, $|f>$ the final state and d the dipole operator [49]. The elastic resonant scattering process involves a second transition $<f|d'|i>$, from the final state back to the initial state, under emission of a scattered photon with the same energy as the incident one. The resonant scattering amplitude is given by [50, 51]:

$$\Delta F_j \sim \sum_f \frac{\langle i|d|f\rangle\langle f|d'|i\rangle}{\hbar\omega - (E_f - E_i) - i\frac{\Gamma}{2}}, \tag{1.1}$$

in which the resonant denominator contains the photon energy $\hbar\omega$, the energy of the initial (final) state E_i (E_f) and the inverse lifetime of the excited state Γ.

A first qualitative analysis comes from evaluating the integral in terms of the parity of the contributing functions. The following rules are adopted from Ref. [49].

For a possible transition the integral must be non-zero. Therefore, the integrand needs to be even. Assuming linear polarized light with its electrical field vector along the x axis. The dipole operator is then odd in x and even in y and z. Let's starts with a transition from a $1s$ state to completely unoccupied $2p$ states. As the $1s$ state is even in all three coordinates a transition can only take place into a state that is odd in x and even in y and z. Only the $2p_x$ state fulfills these criteria. Now, assuming a transition from a completely filled $2p$ orbital into an empty $3d$ orbital and keeping the polarization of the incident photon fixed to the x-direction. From an initial $2p_x$ orbital a transition to the final $3d_{x^2-y^2}$ or $3d_{z^2}$, from the $2p_y$ to the $3d_{xy}$, and from the $2p_z$ to the $3d_{xz}$ is possible. Similar rules can be derived for the other polarizations. An overview about all possible transitions and the polarization vector along the optical axes that connects the transition is given in Tab. 1.1.

$1s$		$3d_{xy}$	$3d_{xz}$	$3d_{yz}$	$3d_{x^2-y^2}$	$3d_{z^2}$
$\hat{\mathbf{x}}$	p_x	$\hat{\mathbf{y}}$	$\hat{\mathbf{z}}$		$\hat{\mathbf{x}}$	$\hat{\mathbf{x}}$
$\hat{\mathbf{y}}$	p_y	$\hat{\mathbf{x}}$		$\hat{\mathbf{z}}$	$\hat{\mathbf{y}}$	$\hat{\mathbf{y}}$
$\hat{\mathbf{z}}$	p_z		$\hat{\mathbf{x}}$	$\hat{\mathbf{y}}$	$\hat{\mathbf{z}}$	$\hat{\mathbf{z}}$

Tab. 1.1.: Possible dipole transitions of a $1s \leftrightarrow 2p$ and $2p \leftrightarrow 3d$ excitation or decay. The linear component of the polarization that is needed to stimulated the excitation or that is emitted during the decay is given in the table.

Assuming degenerate final states, the polarization of the incident photon is transferred to the outgoing photon. This changes if the degeneration of the final states is lifted [52]. As a simple example, we make a transition from $1s$ to a completely degenerated $2p$ orbital. If the energy is tuned to the $1s \rightarrow 2p_x$ transition and the polarization is along $\hat{\mathbf{x}}+\hat{\mathbf{y}}$ the transition integral $<1s|\hat{\mathbf{x}}+\hat{\mathbf{y}}|2p_x>$ can be split into the sum of $<1s|\hat{\mathbf{x}}|2p_x>$ and $<1s|\hat{\mathbf{y}}|2p_x>$ from which the first one is non-vanishing and the second one is zero. During the excitation the polarization component along $\hat{\mathbf{y}}$ is therefore simply neglected. The excitation takes place by the electrical field along $\hat{\mathbf{x}}$. The polarization of the outgoing photon that is emitted during the re-decay from the $2p_x$ orbital to the $1s$ orbital can only have a $\hat{\mathbf{x}}$-component. In this sense the polarization is rotated.

In general, the response of an atomic site j to the incident light can be expressed by a scattering tensor

$$\boldsymbol{F}^j = \begin{pmatrix} F^j_{xx} & F^j_{xy} & F^j_{xz} \\ F^j_{yx} & F^j_{yy} & F^j_{yz} \\ F^j_{zx} & F^j_{zy} & F^j_{zz} \end{pmatrix},$$

in which the complex and energy-dependent elements F^j_{mn} describe the scattering of incident light with polarization m to outgoing light with polarization n. The measured intensity is given by:

$$I = \left| \boldsymbol{\epsilon}' \cdot \boldsymbol{F}^j \cdot \boldsymbol{\epsilon} \right|^2,$$

where $\boldsymbol{\epsilon}$ and $\boldsymbol{\epsilon}'$ are the polarization vectors of the incident and scattered waves. By tuning the incident polarization and resolving the outgoing polarization different tensor elements can be measured. Diagonal elements of the scattering tensor do not rotate the polarization, whereas off-diagonal elements do rotate it.

1.3.2. Geometrical phase factor

In the presence of two scattering centers that are located at points O and P in space, a path length difference between the incident and outgoing radiation occurs, which depends on the directions of the incident and outgoing wave vectors $\mathbf{k}$ and $\mathbf{k}'$ and the exact spatial arrangement. This path length difference will cause a phase shift of both scattered waves. The phase shift leads to interference effects between the waves from

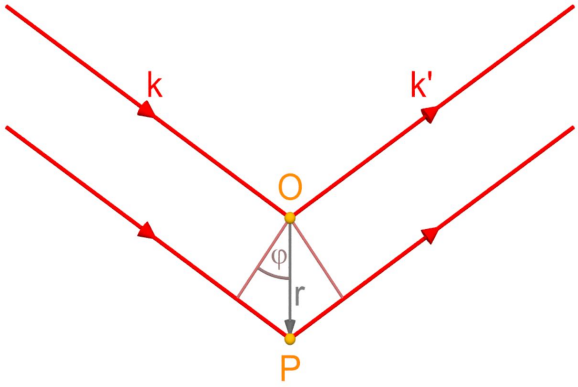

Fig. 1.3.: Path length difference due to scattering at two different positions in space. The incident wave with wave vector $\mathbf{k}$ is scattered at positions O and P. The outgoing waves with wave vector $\mathbf{k}'$ have a phase difference of $e^{i\mathbf{qr}}$.

both scattering center. The situation is schematically depicted in Fig. 1.3. The phase difference for the incident waves arriving at O and P is $-\mathbf{k}\cdot\mathbf{r}$. With similar considerations one gets a phase difference $\mathbf{k}'\cdot\mathbf{r}$ for the scattered waves. In total the path length difference is $(\mathbf{k}' - \mathbf{k}) \cdot \mathbf{r} = \mathbf{q} \cdot \mathbf{r}$, where $\mathbf{q}$ is the wave-vector transfer. The phase between the two scattered waves is given by $e^{i\mathbf{qr}}$.

1.3.3. Diffraction in a periodic arrangement of scatterers

In an assembly of many identical scatterers that are aligned in a periodic arrangement the diffraction process is governed by the interference of all scattered waves times their respective phases. The wave-vector transfer has to match a reciprocal lattice vector to fullfil the Laue condition. Depending on the exact arrangement of the scattering sites a diffraction peak can be observed. In Fig. 1.4 an one-dimensional chain of ten atoms is shown, which is probed by a wave that is either in phase or slightly out of phase. If all scatterers are in phase, the scattering tensor of the whole arrangement is the sum of all single scattering tensors. For a small variation $\mathbf{dq}$, neighboring atoms

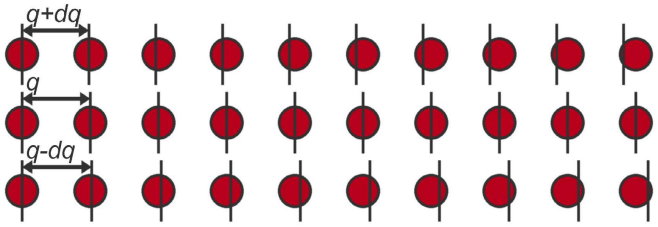

Fig. 1.4.: Phase relation of a scattering situation with different phase relations between neighboring sites. The vertical bars denote the probed periodicity. In the central row the wave is in-phase with all scattering sites, while slightly out-of-phase for a larger or smaller wave vector transfer.

are still moderately in phase, but the interference of all sites leads to a decrease of the diffraction-peak intensity. The interference conditions strongly depend on the length of the chain, or in a crystal on the dimension of the ordered region. For a shorter chain **dq** can be larger than for a longer chain. The exact arrangement of scatterers results in a three-dimensional object in reciprocal space which dimensions yield information on the correlation of the scattering sites.

In a real crystal, different atomic sites can exist that have different atomic scattering tensors. The interference conditions can lead to superstructure reflections that are due to a modulation of the electronic states. The resonant enhancement near an absorption edge results in a huge change of the resonant scattering tensor even if only a small fraction of the whole electron density is redistributed (for example charge or orbital ordering). This makes RSXD able to detect even small modulations. The whole scattering process is the interplay between all atomic scattering tensors, the exact spatial arrangement of the atoms, the incident energies, and the incident polarizations and can be best described by the sum of all scattering tensors times their respective phase factors:

$$\sum_j e^{i\mathbf{q}\mathbf{r}_\mathbf{j}} \boldsymbol{F}^j = \boldsymbol{F} = \begin{pmatrix} F_{xx} & F_{xy} & F_{xz} \\ F_{yx} & F_{yy} & F_{yz} \\ F_{zx} & F_{zy} & F_{zz} \end{pmatrix}.$$

Note that the energy dependence is contained in the tensor entries F_{kl}.

A diffraction peak that results from a spatial pattern of different scattering tensors can be analyzed in various ways. Its position reveals the periodicity and direction of the modulation, its dimensions in reciprocal space the correlation of the scatterers in the respective directions. Its energy and polarization dependence yields spectroscopic information on the scattering sites that are involved in the diffraction process. A rotation of the polarization with respect to the scattering sites can be used to determine the local symmetry of the electronic wave function.

1.4. Coherent x-ray diffraction

Coherent x-ray diffraction (CXD) is the ideal technique to reveal information about materials that show an inhomogeneous arrangement of different electronic phases (Fig. 1.5 (a)). To obtain a scattering contrast it is necessary that different electronic phases produce a different response on the incident coherent x-rays. If one of the phases has a modulation, which is characterized by a diffraction peak that is absent in the other

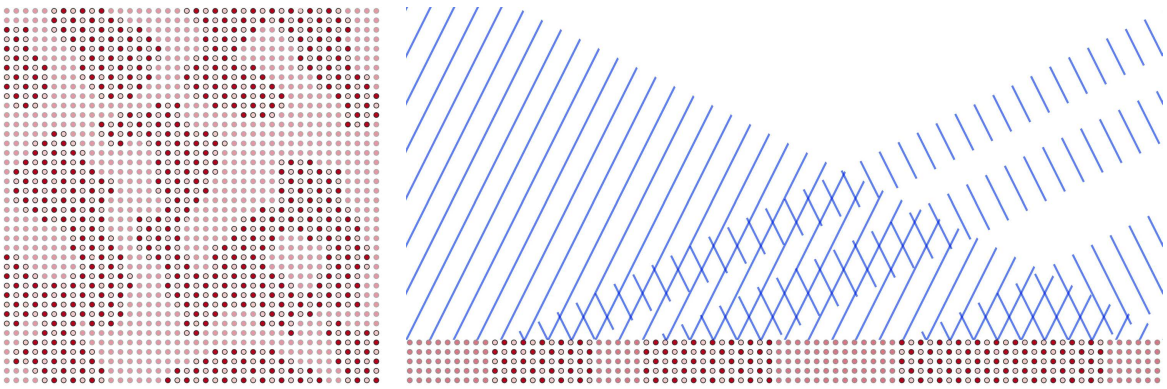

(a) **(b)**

Fig. 1.5.: Basic idea of CXD. (a) A sample with two coexisting electronic phases shows a specific arrangement of regions, in which one of the phases is dominant and regions in which the other one is dominant. The illustration shows a sketch of a sample, where circles denote atomic sites. In some regions a modulation of the electronic states takes place, which is characterized by a superstructure peak. (b) If the diffraction experiment is tuned to this superstructure peak, only those regions reflect the x-rays that are ordered. If coherent x-rays are used the contributions from all those regions will interfere and produce a speckle pattern.

phase, than only the modulated phase will contribute to the diffracted signal (Fig. 1.5 (b)). The diffraction peak is determined by the interference of all contributions and shows a modulation of the intensity, which strongly depends on the exact arrangement. A variation of this arrangement affects the interference (speckle) pattern and reveals insight into the dynamics that arise from domain-wall movements and domain reorganizations.

1.4.1. Coherence

Coherent illumination is crucial for the interference of all contributions from different regions. Coherence can be classified into longitudinal coherence L_L, which is determined by the wavelength λ and wavelength spread $\Delta\lambda$ of the source, and transversal coherence L_T, which is determined by the size D and distance R of the source [53]:

$$\begin{aligned} L_L &= \frac{\lambda^2}{2 \cdot \Delta\lambda}, \\ L_T &= \frac{\lambda \cdot R}{2 \cdot D}. \end{aligned} \tag{1.2}$$

The longitudinal coherence can be enhanced by reducing the wavelength spread (Fig. 1.6 (b)). At a 3rd generation synchrotron facility, at which the CXD experiments were performed, this is achieved by using a monochromator. The transversal coherence can be

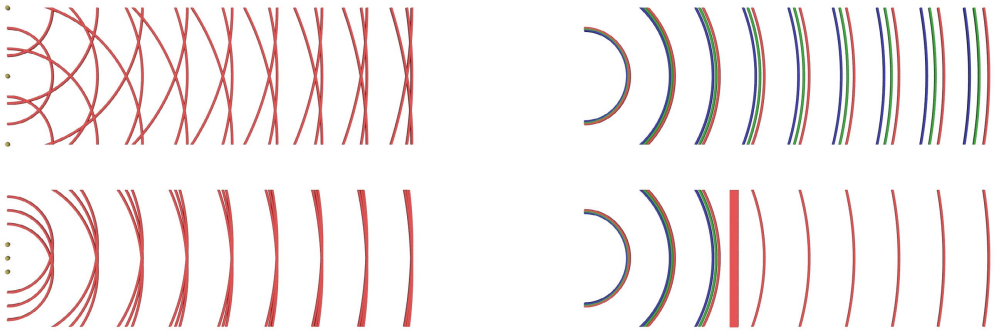

(a) **(b)**

Fig. 1.6.: (a) The transversal coherence is connected to the size and distance of the source. The phases of the wave fronts (red circles) from more distinct points (upper image) differ much stronger than for closer points (lower image). (b) The wavelength spread defines the longitudinal coherence. Using a wavelength filter (red bar) or monochromator that reduces the wavelength spread (lower image) enhances the longitudinal coherence.

increased by reducing the source size (Fig. 1.6 (a)). Therefore, we have used a coherence filter stage, which basically consists of two apertures. One of it is placed very close to the sample and the other one at a distance apart. Further details on the stage are given in Chap. 2.

1.4.2. Speckle pattern

If a spatially inhomogeneous sample, which shows a contrast in the diffraction signal between at least two regions, is illuminated coherently the diffraction peak shows a graininess in the intensity (speckle pattern) that is causes by the interference of light from different regions of the sample. The envelope of the coherent pattern is the same as for an incoherent illumination. As an example a speckle pattern of $Er_{0.6}Ca_{0.4}TiO_3$ (ErCaTIO) is shown in Fig. 1.7. Whereas in other coherent techniques, like for example in holography, a sophisticated algorithm has to be used to retrieve a real space image of the sample, the speckle dynamics are directly connected to the dynamics of the sample. The temporal evolution of the speckle pattern reveals direct insight into the domain-wall motion and reorganization. The intensity fluctuations can be interpreted by x-ray photon correlation spectroscopy (XPCS), in which a time series is autocorrelated. From the decay of this autcorrelation the characteristic time scales can be found.

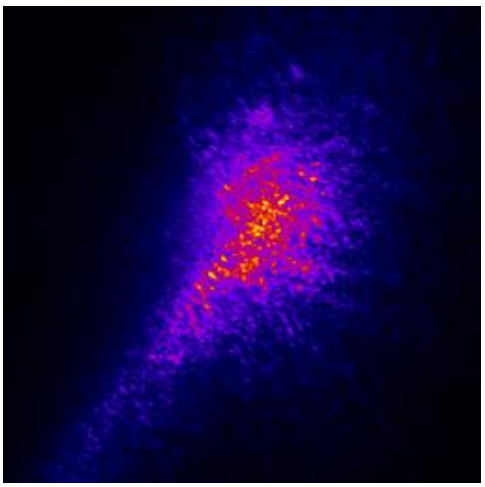

Fig. 1.7.: CCD image of a diffraction peak in ErCaTiO. Only charge ordered regions contribute to the signal and their spatial arrangement is connected to the speckle pattern. Brigther (darker) colors denote spots with higher (lower) intensity.

1.5. Discussion

RXD is a powerful tool to analyze ordering phenomena with spectroscopic sensitivity. The energy dependence of the resonant scattering tensor depends on the local environment of the scattering centers and the occupation of electronic states. This is used in Chap. 3 to identify charge order in LSCO. A polarization and azimuthal dependence yields the local electronic symmetry, as used in Chap. 4.

CXD experiments can be used to study the dynamics of phase-separated systems. A detailed analysis of ErCaTiO, in which coexisting charge ordered insulating and metallic region exist, is given in Chap. 5.

CHAPTER 2

Instrumentation

2.1. Introduction

The new and ultra-brilliant synchrotron radiation facility PETRA III provides unique possibilities for resonant soft x-ray diffraction experiments. It has seen its first light on 16th of April 2009. The reconstruction of the old PETRA II accelerator to the new light source started one and a half years earlier in September 2007. Presently, 14 undulator beamlines are built up and tested. Already since 2010 the first user experiments could be performed. PETRA III is operating at 6 GeV energy and delivers a positron current of 100 mA [54]. This high energy allows helical undulators to provide complete polarization in the first undulator harmonic with an ultra-high flux [55].The high flux as well as the high degree of photon polarization goes beyond the performance of lower energy machines like BESSY II or the Advanced Light Source (ALS) and makes PETRA III competitive and in some extent even outstanding compared to the European Synchrotron Radiation Facility (ESRF) and SPring-8.

One beamline that is very important in the frame of this thesis is the XUV beamline P04, which is presently under commissioning. This beamline is designed for soft x-rays. The APPLE-2 undulator delivers photons with variable polarization in the energy range from 250 to 3000 eV in the first undulator harmonic. This energy range is highly interesting as many important absorption edges of the elements in correlated electron systems lie within there (transition metal-$L_{2,3}$-edges, C-, N-, O-K edges and lanthanide-$M_{4,5}$ edges). The new beamline allows to extend resonant soft x-ray diffraction (RSXD), which is one of the key techniques used within this thesis, to a wider energy range than accessible so far at other sources. RSXD has been established as an essential technique in the study of correlated electron systems and combines spectroscopic sensitivity with its sensitivity to spatial order. The high degree of linear and circular polarization that can be achieved at P04 (close to 99.99 %) is helpful to explore the electronic character

of these strongly correlated systems, as the symmetry of the electronic wave function can be studied by analyzing the azimuthal dependence of the RSXD signal for different polarizations (Chap. 4). The high flux up to an x-ray energy of 3 keV makes it also possible to scatter from structural Bragg reflections. This is helpful for alignment of the sample, as intensity reference that can be traced during the experiment, and even as indicator of a structural phase transition, which can be used as an internal temperature calibration and to connect the lattice degree of freedom with the spin or charge degree.

The resolving power ($E/\Delta E$) of the XUV beamline is up to $4{\cdot}10^4$ and the photon flux is up to $4{\cdot}10^{12}$ photons per second at a resolving power of $1{\cdot}10^4$. The spot size is focused down to a $10 \times 10\,\mu m^2$ size and is therefore well suited to study small samples, nano devices or phase separated materials. Due to the low emittance of PETRA III, which is 1 nm rad in horizontal and 0.01 nm rad in vertical direction, the x-ray beam is nearly coherent. These technical information and further details can be found in Ref. [55]. A highly coherent beam is for example necessary to study domain wall dynamics in coherent x-ray diffraction (CXD) experiments. Furthermore, upcoming techniques like holographic or ptychographic imaging, which use the interference of a coherent beam with a defined aperture to retrieve a real space image of the sample surface, are well suited to the specifications of the XUV beamline.

As one of several end stations, which will be accessible for users of P04, we have designed and commissioned a new ultra high vacuum (UHV) x-ray diffractometer. The attenuation length of soft x-rays in air is typically several hundered micrometer. Therefore, the whole experiment has to be performed under UHV conditions. This makes the design of a soft x-ray diffraction experiment challenging, as an in-vacuum sample and the detector manipulation is required to tune the experiment to any desired scattering geometry.

The development of differentially pumped rotary feedthroughs as well as of in-vacuum motors have led to new possibilities in the design of such an instrument. Basically, two different approaches exist. Using differentially pumped rotary feedthroughs allows to put most of the moving parts outside vacuum [56–58]. In a different approach in-vacuum motors are used to move an in-vacuum goniometer as well as in-vacuum rotary stages [59–62]. Most of the moving parts of these designs are inside vacuum. In some designs a mixture of both approaches is used [63, 64]. The new UHV diffractometer for PETRA III uses two rotary feedthroughs for sample and detector translation and either a manipulator, which is motorized outside the chamber, or optionally a CXD sample stage, which is driven by in-vacuum motors.

The rest of this chapter is organized as follows: First, the design of the new UHV diffractometer, including all necessary components, is discussed. In the following the sample environment for conventional soft x-ray diffraction and the built-in detectors are discussed in more detail. For coherent diffraction experiments a new stable setup was used, which is presented afterwards. At the end of this chapter first experiments, taken with the new diffractometer, are presented. These are: a characterization measurement of multilayer reflectors, which will be installed in a polarization analyzer, and characterization of and first measurements with a new in-vacuum CCD camera. Finally, the

power of an area-resolved detector in comparison to a point detector will be explained.

2.2. UHV diffractometer for PETRA III

The new UHV diffractometer for PETRA III was designed to be a mobile instrument. Its spatial dimensions are a compromise between transportability and the need to accommodate detectors, the sample surrounding, beam and vacuum diagnostics, a magnet, a camera system and other useful equipment. A sketch of the whole design is displayed in Fig. 2.1. The instrument is based on a vertical cylinder with a diameter of 500 mm

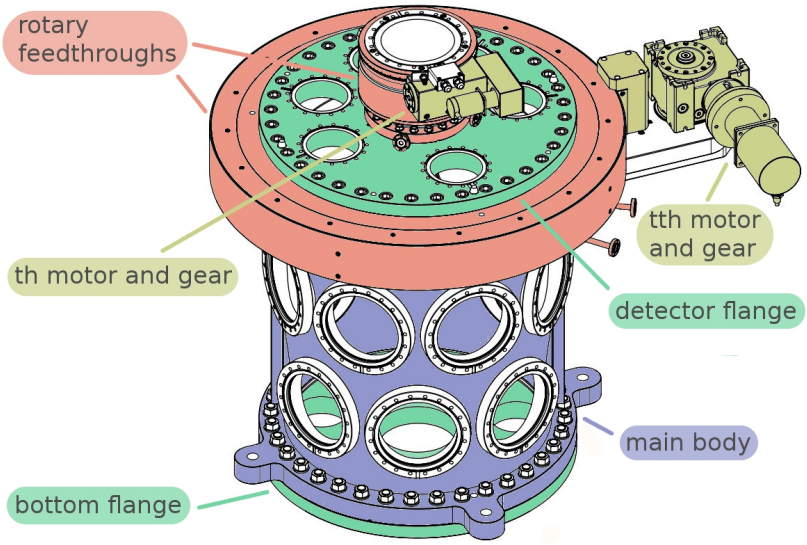

Fig. 2.1.: Sketch of the new UHV diffractometer.

and comprises two differentially pumped rotary feedthroughs for an independent sample and detector rotation in horizontal scattering geometry. The huge top flange, which covers the full diameter, is fully rotatable around the central axis and can carry complicated and massive detector setups (for example an in-vacuum CCD or a polarization analyzer). A planetary gear that is driven by a Phytron ZSH 87 motor and coupled to a cog wheel by a worm gear allows for low-backlash rotation. In the central CF 160 port of the detector flange the sample rotation, which is driven by a Phytron ZSS 42 motor with a planetary gear, is mounted. The sample rotation axis is called theta (th) rotation and the detector rotation twotheta (tth). The outer ports of the detector flange are used to carry infrastructure for the detectors. These are for example z-lifts, which are used to vertically adjust the detector height, or feedthroughs for water, which are needed for cooling of the CCD camera. In Fig. 2.2 the detector rotation, the sample rotation, including their respective rotary feedthroughs, and the z-lift for a silicon diode detector are shown. The central CF 160 port of the bottom flange is prepared to install a magnet.

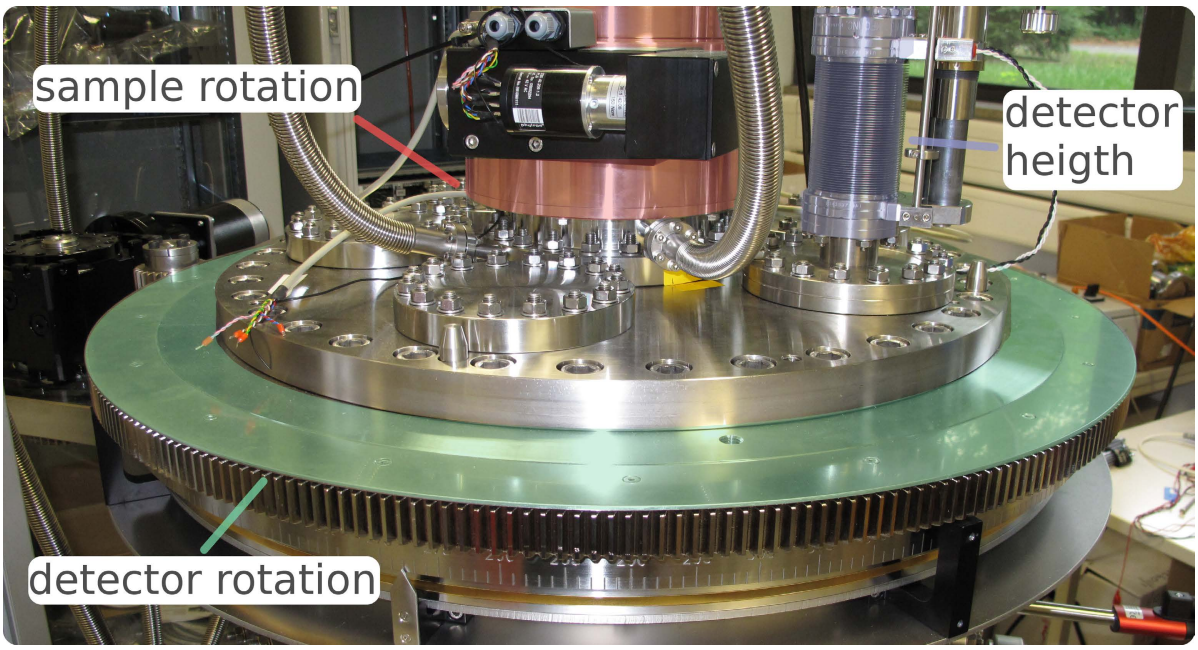

Fig. 2.2.: Rotational and vertically translational degree of freedom of the detectors and rotation of the sample of the new UHV

The main part of the diffractometer is the stainless steel chamber. It is surrounded by 2×8 CF 150 ports, half of it on the upper and the other half of it on the lower level. Every port is facing the central axis with an angle of 45° between neighboring ports. The alignment of the lower ports is rotated by 22.5° with respect to the upper ports around the central axis. All ports can be flexibly equipped with infrastructure for the experiment. The scattering plane lies within the upper level while the lower level is used for pumping, diagnostics, etc. Presently, the lower level (Fig. 2.3) comprises a Pfeiffer HiPace 700 turbo vacuum pump, a cold trap with titanium sublimation pump, a mass spectrometer and different vacuum sensors (Piezo, Pirani, cold cathode). The turbo pump is backed by a pumping stage that also pumps the differentially pumped rotary feedthroughs.

The instrument is coupled to the beamline via flexible bellows that allow the movement of the chamber for alignment (Fig. 2.4 top right). A combination of a full metal valve and a polyamide window valve can be used to differentially pump the beamline presection and the diffractometer and allows to operate the diffractometer at slightly higher pressures as the beamline requires. Opposite of the beamport a fluorescent screen can be attached, which helps for a rough alignment of the chamber (Fig. 2.4, lower left). Two ports are used for the sample transfer system (Fig. 2.4, upper left and right). This consists of a loadlock, which can be attached to almost any port, and a screwdriver that is based on a magnetic wobblestick. This screwdriver is used for sample transfer, azimuthal rotation, and to change the slit in front of the detector. Further details on the sample environment will be given in Sec. 2.2.2. The vacuum of the loadlock can be decoupled from the vacuum in the main chamber using a gate valve and pumped

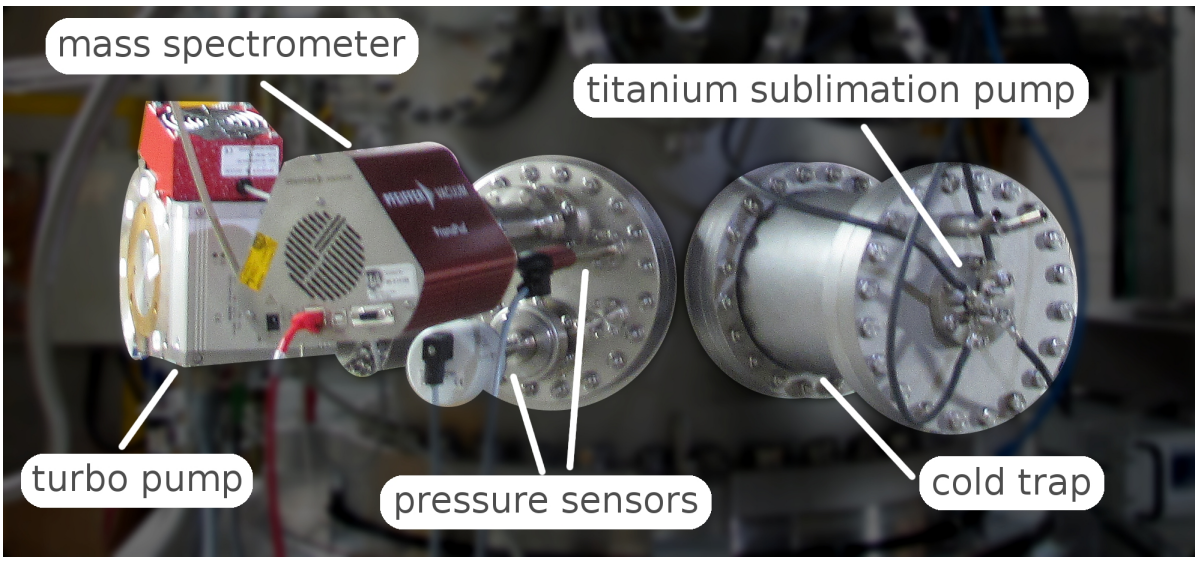

Fig. 2.3.: Lower port level of the instrument, equipped for pumping and diagnosis.

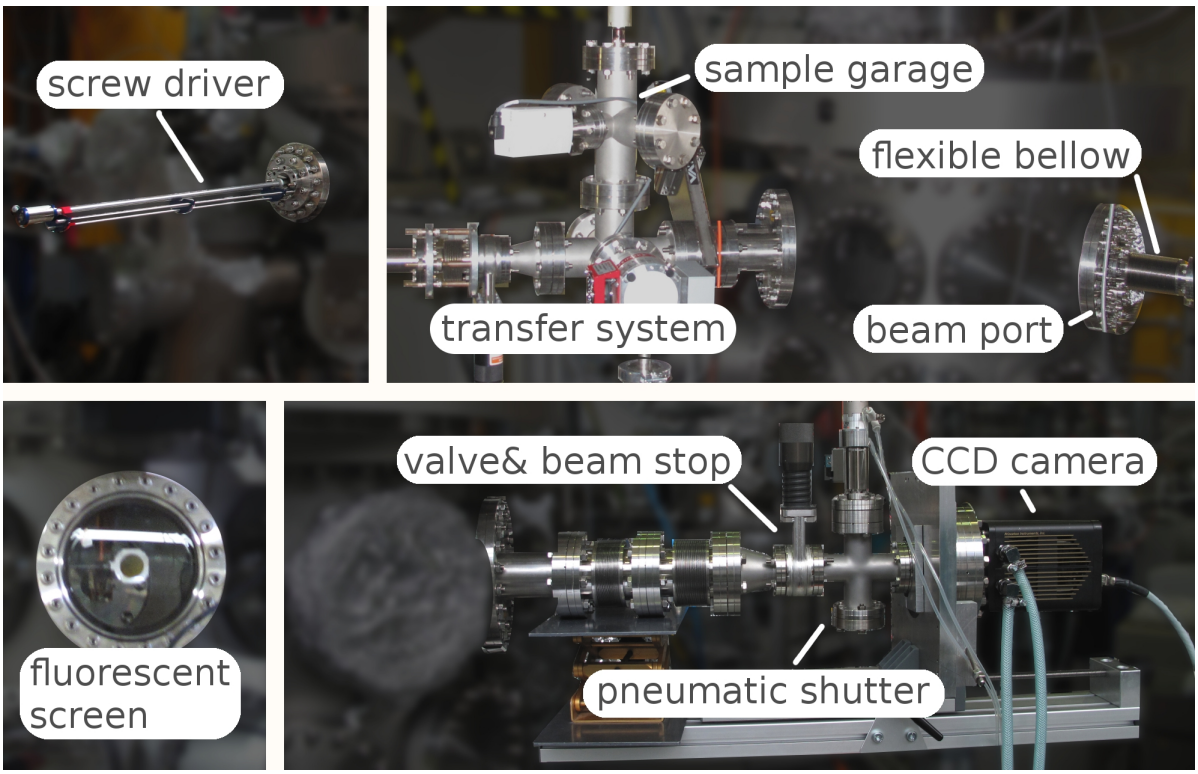

Fig. 2.4.: Different views of the upper port level of the new diffractometer, mainly used for equipment concerning the sample surrounding (transfer, azimuthal rotation) and x-ray beam detection (fluorescent screen, CCD camera).

or vented separately. Inside this loadlock a sample garage with different sample slots is mounted. The transfer of the samples between the two chambers is performed by

a magnetic transfer arm. A cleaver can be mounted inside the loadlock, if the study of a fresh sample surface is needed for the experiment. For pumping and pressure control of the loadlock a smaller turbo pump with pre-pump and pressure sensors is used. Instead of the loadlock it is possible to attach a molecular beam epitaxy (MBE) chamber, equipped with evaporators, thickness monitor, and LEED, to the chamber in order to study thin films grown in-situ. The remaining ports are usually equipped with view ports, which are used for direct inspection for example during the sample transfer, and can be equipped with a camera system. For speckle experiments a CCD camera, including a pneumatic shutter and a beamstop, was installed one meter apart from the chamber center at one of the ports (Fig. 2.4, lower right). To compensate the discrete arrangement of flanges and allow to place the CCD at a specific detector angle a rotation of the chamber and a tilted beamport adapter were used.

2.2.1. Alignment of the rotation axes

In order to align the rotation axes of the sample and detector circles the setup shown in Fig. 2.5 was used. It contains a circular adjustment gauge with a diameter of 100 mm

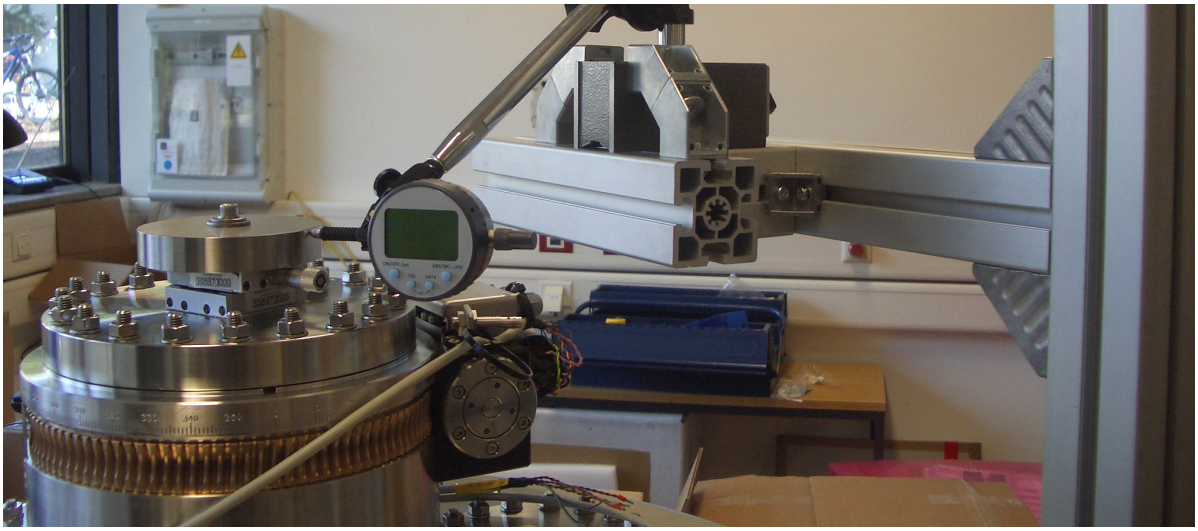

Fig. 2.5.: Setup for alignment of the two rotation axis in the home lab. Further details are given in the text.

and a precision of 1 µm, mounted on a manually driven xy-table with the same precision. A dial indicator was mounted on the frame of the diffractometer and used to read out the displacement of the adjustment gauge when rotated. In a first run, the detector circle was rotated and the xy-table was adjusted in such a way that the dial indicator did not change in the range of 1 µm for a full rotation. Therewith the center of the adjustment gauge falls within the rotation axis of the detector circle. In a second step only the sample circle was rotated. Now any displacement was corrected with a small displacement of the sample rotary feedthrough, by using a rubber mallet and trying to move the setup, which was not fully tightened at this point. In the condition as delivered

to us the accuracy was around 200 to 300 µm and could be improved by the procedure described above to around 25 µm.

2.2.2. Sample environment

There are two sample environments, one which is used for conventional x-ray diffraction and the other one which is used for coherent diffraction. The first one is discussed in the following and the second in combination with the whole speckle setup in Sec. 2.2.5. In

(a) **(b)**

Fig. 2.6.: (a) The four-axes manipulator placed on top of the sample rotation. Starting from the bottom it contains the tilting stage (not visible), the xy-stage and the z-stage. On top of the manipulator the liquid helium cryostat, including the transfer line is mounted. (b) View inside the diffractometer. The lower end of the cryostat is coupled to the copper sample holder. Cables for temperature control and sample current measurements are winded around the cryostat. The screwdriver, coming from the left, is used for sample transfer and azimuthal rotation of the sample.

the setup that is used in conventional soft x-ray experiments the sample rotation carries a manipulator to position the sample, a cryostat for cooling, and the sample holder. The manipulator has four axes: a vertical (zs), two in-plane translations (xs) and (ys), and a tilt that, depending on the orientation of the sample holder, can be used as χ (sample tilt) or ϕ (azimuthal rotation) motion. All of them are motorized by stepper motors. The resolution and repeatability of the three linear axes is in the µm range. The xs- and ys-stage can be moved by ± 12.5 mm, while the translation of the zs-stage is 100 mm. All three axes are equipped with limit switches. The tilt can be adjusted

within a range of $\pm 2°$ and is designed such that the center of the sample position stays at a fixed position. An image of the manipulator is shown in Fig. 2.6 (a).

To the manipulator, a Janis continuous-flow cryostat is placed. The transfer line, which connects the cryostat with the helium tank, can be inserted in the center of the cryostat. A pumping connection at the exhaust side is used to pump the liquid helium through the cryostat, while the temperature can be controlled and read out by an internal heater and an internal temperature sensor, respectively. At the cold face of the cryostat the sample holder, which can be exchanged for different experimental setups, is mounted (Fig. 2.6 (b)). In the standard configuration for resonant scattering experiments the sample holder is rigidly coupled to the cryostat and can be equipped with a sample, using the transfer system. The sample stage can be seen in Fig. 2.7, which shows a front view of the sample holder from Fig. 2.6 (b). The sample holder is

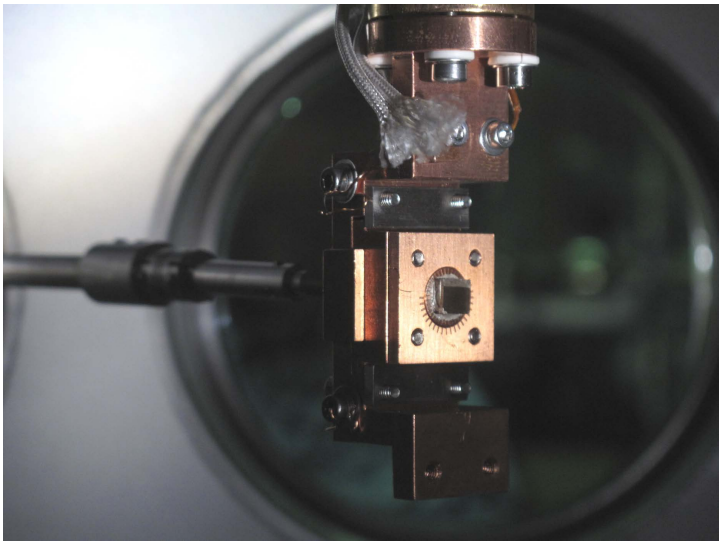

Fig. 2.7.: Close view of the current sample holder. The rectangular sample shuttle contains the sample plate, which can be azimuthally rotated using the screw driver, and is clamped to the sample holder. The whole shuttle can be transferred out of the chamber by using the same screwdriver to release the clamps and . To remove the shuttle the clamps below and above the shuttle are released. The sample holder is thermally coupled to the cryostat. To electrically isolate both components from each other ceramic bushes and a sapphire plate are used.

electrically decoupled from the cryostat by a monocrystalline, *c*-oriented sapphire plate and ceramic bushes below the screws. Therefore, it is possible to measure the sample drain current, which can be used to measure the absorption of x-rays inside the sample. Drain current is measured with a Keithley 6514 electrometer outside vacuum. Due to the moderately high thermal conductivity of the sapphire plate a good thermal coupling between the cryostat and the sample stage is given. To read out the temperature at the sample position silicon temperature diodes and platinum resistors are coupled to the sample holder by silver glue and additional copper clamps. Heating and temperature monitoring is controlled by a Lakeshore cryogenic temperature controller. The setup

shown in Fig. 2.7 can easily be cooled to 18 K. If needed, a gold-plated radiation shield can be mounted to the cryostat that increases the cooling efficiency. The sample itself is usually glued on a cylindrical copper plate and mounted into one of the shuttle slots. By using the screwdriver, as shown in Fig. 2.7, the sample can be azimuthally rotated by loosening screws on the back of the transfer holder and rotating the central screw that is connected to the sample plate. A vernier scale with a precision of 0.5° is used to read out the azimuthal angle ϕ. The same screwdriver is also used for transferring the sample. The upper and lower clamps that fix the transfer holder are released and the external thread of the screwdriver is used to fix the transfer holder and place it in a slot on the magnet arm of the loadlock. This way, shuttle and sample can be transferred out of the main chamber. A second sample slot on the transfer arm allows for a direct exchange of samples.

2.2.3. Detectors

Several detectors can be mounted on the detector flange. At present, two detectors (a diode and an in-vacuum CCD) are installed inside the chamber, while a third one is under development (polarization analyzer). The standard detector is an aluminum coated silicon photo diode from International Radiation Detectors, Inc., with a size of $10 \times 10\,\mu m^2$ (AXUV100 series). The aluminum coating reduces the transmission of visible light by a factor 10^{-4}, resulting in an overall dark current of around 0.1 pA. The large dynamic range of this detector makes it possible to detect the direct x-ray beam (a few µA) as well as low signals of a few hundred photons per second, which produce a signal in the pA range. The diode is mounted on a holder, which can be vertically moved by an external z-lift. The vertical acceptance of 3° is given by the vertical dimension of the diode and the sample to detector distance of 192 mm. A slit carousel, equipped with 0.5, 1, 2 and 4 mm wide vertical slits, is placed in front of the diode and can be rotated by the in-vacuum screwdriver to vary the horizontal angular acceptance between 0.15 and 1.2°.

The second detector is a Princeton Instruments PI-MTE in-vacuum charge-coupled device (CCD) camera, which can be completely placed inside the chamber. The back-illuminated CCD chip of $27.6 \times 27.6\,\mu m^2$ has 2048×2048 pixels, each of them a $13.5 \times 13.5\,\mu m^2$ large, and a dynamic range of 16-bit, which means that each pixel can have one out of 65536 possible values. Typically a few hundred soft x-ray photons saturate a pixel (65536 counts), but the exact number depends on the settings. The chip is able to detect soft x-rays between 1 and 10000 eV, with a quantum efficiency between 10 and 85 %. In the most relevant energy range, between 500 and 3000 eV, the quantum efficiency lies within 65 and 85 %. The CCD camera requires water cooling to transport the heat generated by the Peltier element, which cools the CCD chip. Therefore, a specialized camera port, including electrical and liquid feedthroughs, was designed. To avoid blocking of the x-ray beam when a different detector is used or to avoid a collision with the screwdriver or the transfer system, the whole CCD setup is mounted on a vertically movable z-lift with 75 mm travel length. In order to increase the distance between the sample and the CCD detector, which improves the angular resolution, the

camera was mounted under 45° with the active area pointing downwards. To avoid a damage of the CCD chip by the direct x-ray beam, a beam stop was installed on one of the bottom flanges. This beam stop is vertically movable. Therefore, the alignment of the direct beam can be performed with the photo diode. A drawing of the whole design is shown in Fig. 2.8.

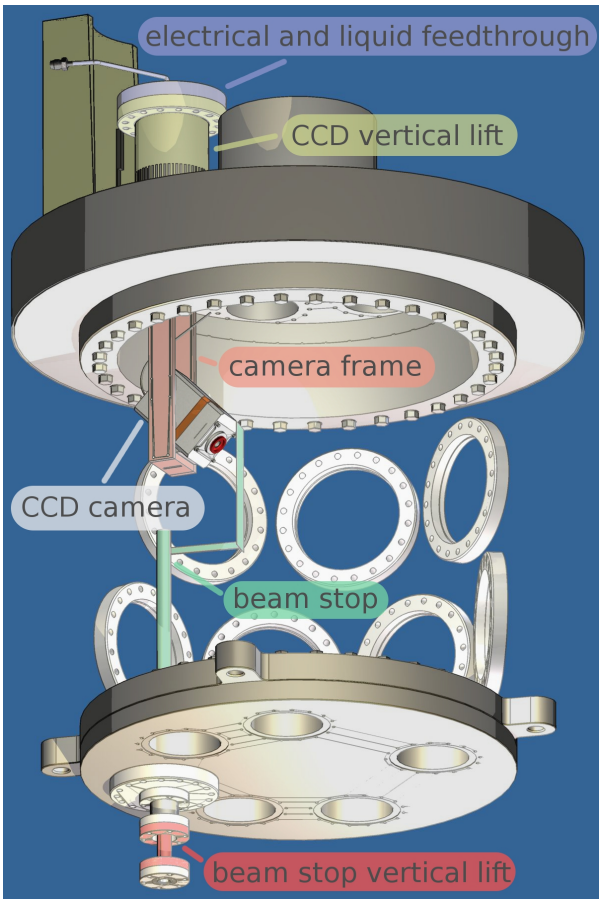

Fig. 2.8.: CCD setup inside the diffractometer. On top of the detector flange a vertical translation stage is mounted, which contains the electrical and liquid feedthroughs for readout and cooling of the camera. The CCD camera is tilted, to increase the detector-sample distance. A beam stop is mounted from the bottom flange of the diffractometer. Both the CCD camera and beam stop can be moved out of the scattering plane, to prevent blocking of the beam and collision with other components.

2.2.4. Diffractometer frame

In order to align the instrument a frame has been set up, which provides a stable and precisely movable support for the diffractometer and allows to use the instrument at different beamlines (Fig. 2.9). It is stable enough to carry the whole weight of the diffractometer, which is about 800 kg. The frame consists of a rotation stage, which

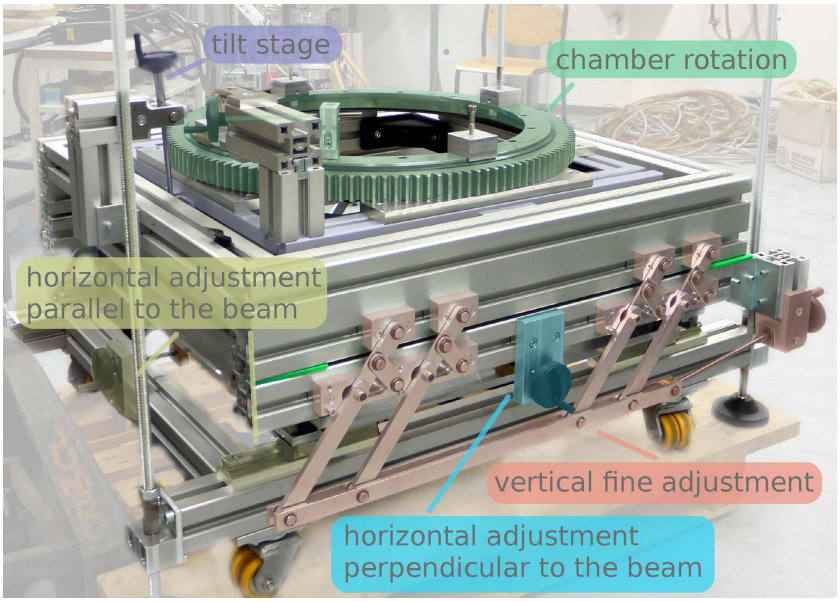

Fig. 2.9.: Support frame for the diffractometer. The various translational and rotational degrees of freedom allow to place the diffractometer in all required positions needed for a synchrotron experiment.

allows for a full rotation of the chamber, a tilt stage, which allows for a tilt of -5° to +10°, a translation stage, which allows for 200 mm translation perpendicular and parallel to the beam and a vertical fine adjustment of 25 mm. A motorization of the translational axes and limit switches will be installed.

2.2.5. Speckle setup

For the CXD experiments a different sample environment and a coherence filter stage were developed, in order to provide an ultra-stable sample setup and to enhance the coherence of the x-ray beam. X-ray photon correlation experiments require a coherent illumination of the sample to produce a speckle pattern that is otherwise averaged out in an incoherent scattering experiment. The coherent volume, given by the spatial and temporal coherence lengths, has to be of the order of the scattering volume. This can be achieved by a double-pinhole setup. While one of the apertures is placed a few cm away from the sample in the incoming beam the other one has to be close to the sample. The design of the pinhole stage was improved in several steps within the last years. In a first design [65], both pinholes were build on a pinhole stage that was placed between the chamber and the beamline. The first pinhole could be chosen from a set of pinholes with different sizes between 30 and 200 µm, all of them aligned in a vertical column. The vertical alignment was done by a linear drive. A horizontal movement perpendicular to the x-ray beam was used to center the respective pinhole in the beam. The second pinhole, with a 10 µm diameter, was mounted on a tube, which extended inside the chamber. With an xyz-manipulator this pinhole could be aligned in horizontal

and vertical direction as well as parallel to the beam. A picture of the setup is shown in Fig. 2.10 (a). During the first coherent scattering beamtimes it turned out that the

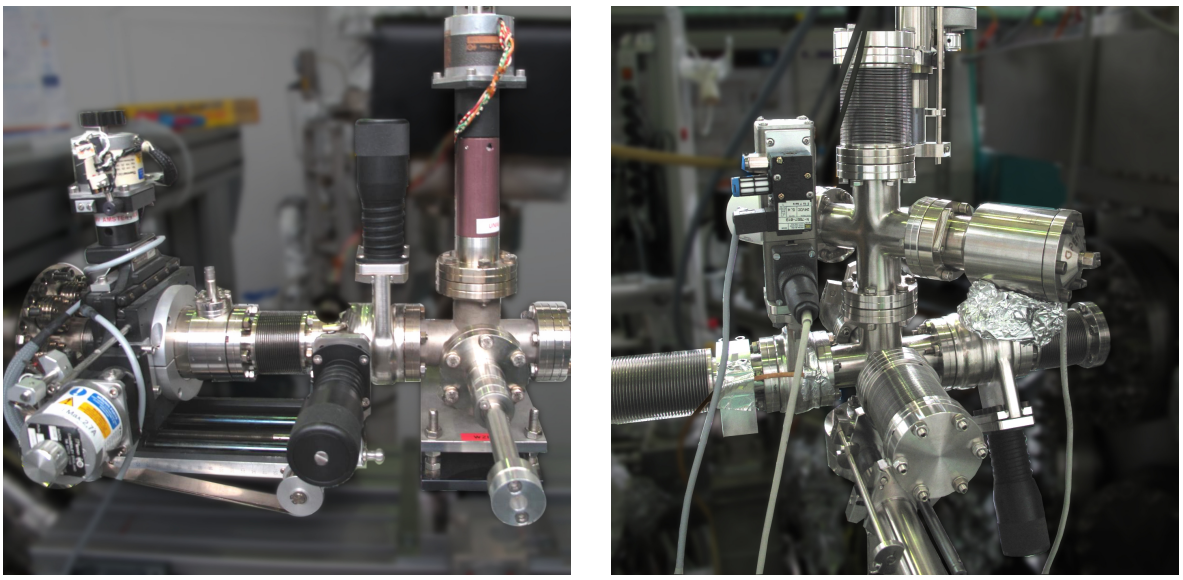

(a) **(b)**

Fig. 2.10.: (a) First design of the pinhole stage, containing both the first and second pinhole with respective translational stages. (b) Modified pinhole stage, which contains the first pinhole only.

temperature drift of the sample position was intolerably large, with respect to the second pinhole position. To avoid this, we coupled the second pinhole to the sample stage. In a first approach we tried to directly mount the pinhole to the sample shuttle. The drawbacks of such an assembly are: the probed position on the sample is fixed, the scattering angle cannot be varied without changing the effective pinhole size and sample position, and an alignment of the sample without pinhole is not possible. Therefore, in a second step an in-vacuum rotation stage, placed below the sample holder, was used to rotate a pinhole carousel around the sample (Fig. 2.11). This allowed for adjustment of any scattering angle, as well as probing the sample without pinhole. However, it turned out that the temperature drift of the whole sample holder, including the pinhole stage, made it impossible to record reliable data. Based on these experiences the present setup of an ultra-stable sample environment was developed. Larger parts were designed and constructed by Hans Ellermeijer from the University of Amsterdam. The basic idea is that the sample and the pinholes have a rigid mechanical coupling to the diffractometer and to the beamline, which is not affected by a temperature changes. In particular the support structure of the sample stage is kept at room temperature, while only the direct sample environment is cooled. The support structure is connected to the sample rotation by a stainless steel tube. Vertical translation of the whole tube is performed with a z-stage. Transversal movements within the scattering plane are performed by a piezo-driven in-vacuum xy-stage from Micos. The sample is cooled via flexible copper braids that are connected to a helium flow cryostat. Thermal decoupling of the cold

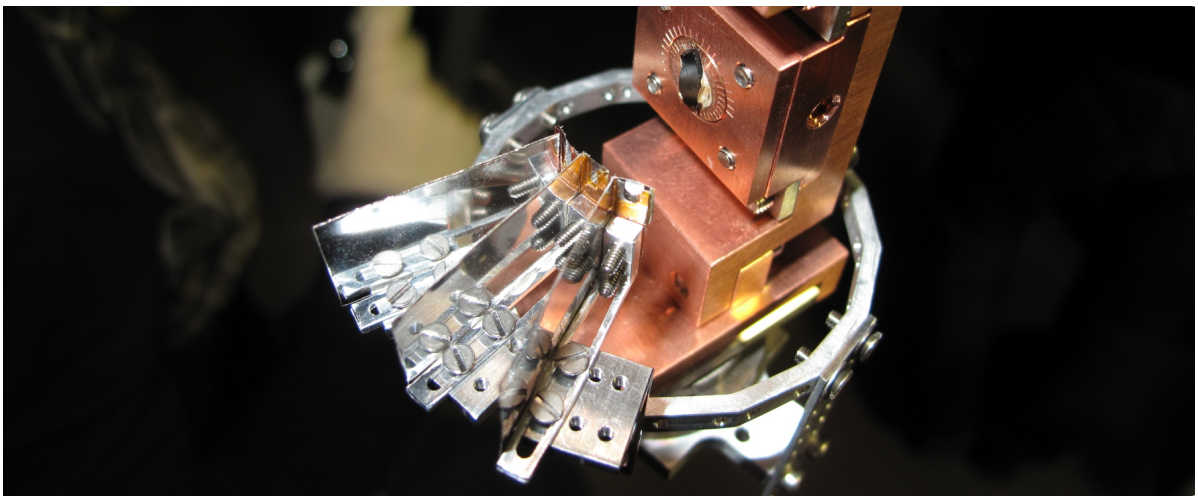

Fig. 2.11.: Intermediate design of the second pinhole stage: A carousel with different pinholes is fixed to the sample holder. The pinholes can be rotated around the sample to allow for any incident scattering angle.

sample stage and the support structure, which is at room temperature, is realized with a sophisticated structure, developed at PSI and the University of Amsterdam as the core piece of the CARVING manipulator. It minimizes the cross section for heat transport, but ensures a rigid mechanical support. The sample stage is furthermore stabilized by a counter bearing that is mounted to the bottom flange. The second pinhole is connected to the support structure and can be moved horizontally and vertically to the x-ray beam by a second set of in-vacuum translational stages. A drawing of the sample holder and an image of the setup, including the pinhole holder, can be seen in Fig. 2.12 (a) and (b), respectively. The first pinhole is replaced by a foil with horizontal slits of varying thickness, thus defining the vertical dimension. The horizontal openings can be adjusted by two baffles, which can be positioned in horizontal direction. The first pinhole stage is shown in Fig. 2.10 (b).

2.2.6. Drift of the detector circle

The first test of the diffractometer was done in the lab, by checking the rotational detector accuracy. Therefore, the built-in Renishaw position encoder with optical readout was used. In this test it turned out that the detector circle keeps on moving after the motor has stopped. In the diagram, shown in Fig. 2.13, the exponential drift of the motor position was about 0.02° within 25 minutes after stopping the motor, which corresponds to roughly 70 µm in horizontal direction at the detector position. The drift is slow and in the typical time window of 1-2 s after stopping the motor, the position changed by 0.002 to 0.004°, which is only a few microns at the detector distance and thus less then one per cent of a typical slit size of the point detector and only a fraction of a single pixel of the area detector. In 10 s after stopping the motor the drift is only twice that large.

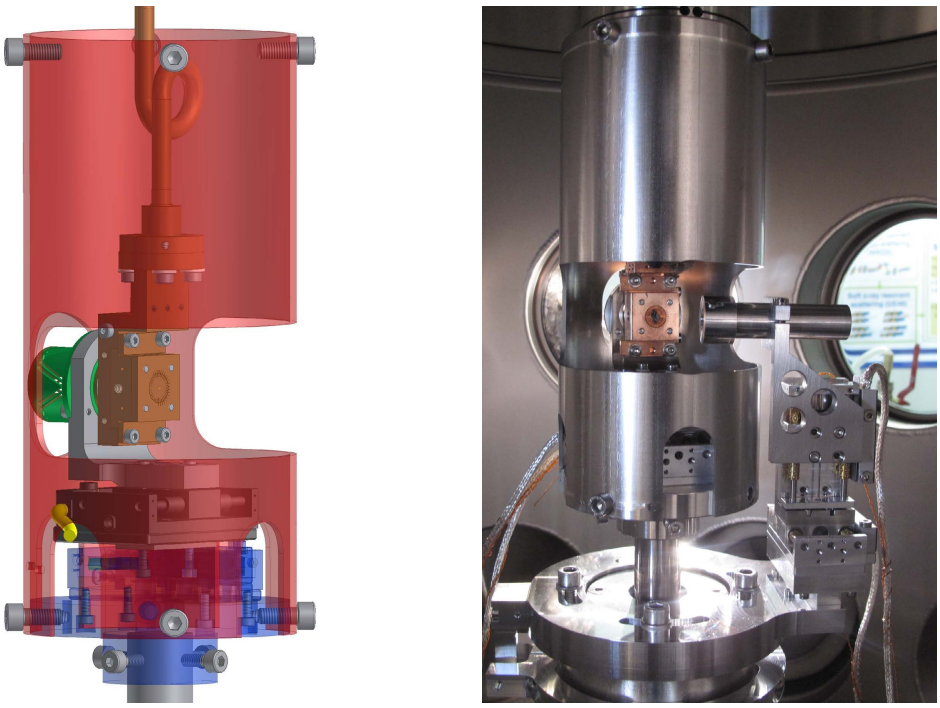

(a) (b)

Fig. 2.12.: (a) 3D-drawing of the sample setup, designed and constructed at the University of Amsterdam. The sample holder is connected to the z-stage on top of the sample rotation by a stainless-steel tube (red). A piezo-driven xy-stage is used to manipulate the sample. The green component thermally decouples the sample at low temperatures from the support structure, while being mechanical stable. The cooling is realized by flexible copper braids. (b) Image of the setup inside the chamber. In addition to the sample setup, the first pinhole which points to the sample is visible. The manipulation is performed by a second piezo-driven xy-stage.

2.2.7. First commissioning of the new diffractometer

A first commissioning of the whole instrument was done in October 2009 at BW3 beamline of HASYLAB at the DESY site in Hamburg. The interplay of all components could be successfully tested. Additionally, we were able to record first data on nickelate and holmium samples with the new diffractometer. An image of the diffractometer at BW3 beamline is shown in Fig. 2.14. Further commissioning was carried out at BESSY II, where the instrument was used in several beamtimes, for example at UE56/2-PGM-1 beamline in a resonant scattering experiment on the orbital ordering reflex in Fe_3O_4 (Chap. 4) and at UE52 beamline, where multilayer reflectors for the polarization analyzer were tested (Sec. 2.3).

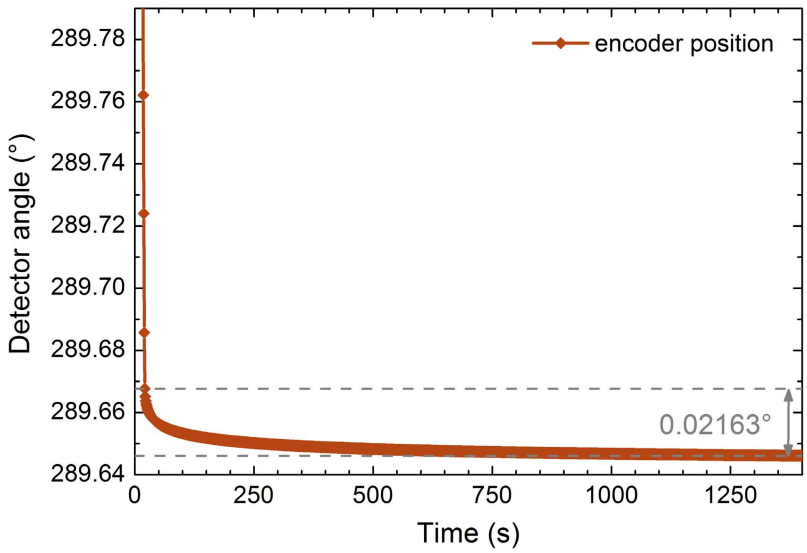

Fig. 2.13.: Drift of the detector circle, measured by the integrated optical encoder of the diffractometer. The motor stopped at the intersection of the data points and the dashed line.

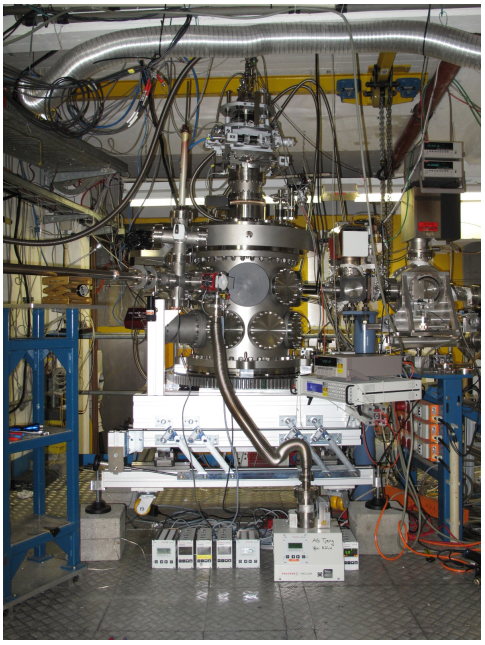

Fig. 2.14.: The new UHV Diffractometer during the first operation at BW3 beamline of HASYLAB at DESY.

2.3. Test of multilayer reflectors for a polarization analyser

In a next step the instrument shall be equipped with a polarization analyzer based on soft x-ray multilayer reflectors. The basic needs are a high reflectivity at reflection angles of 45° and a clear intensity difference in the reflectivity of horizontally and vertically polarized x-rays, achieved by reflection under the Brewster angle. In a first step, we commissioned two different types of multilayers. One type of multilayer, manufactured by Axo, is designed with a gradient of the periodicity across the reflector, in such a way that the energy maximum of the reflectivity shifts with the position on the multilayer. A second type, manufactured by Rigaku, reflects the incoming x-rays in a broad energy range for all positions on the reflector. A comparison of two O-multilayers, one from Rigaku and one from Axo, which are designed for x-rays of photon energys around the O-K edge, is shown in Fig. 2.15.

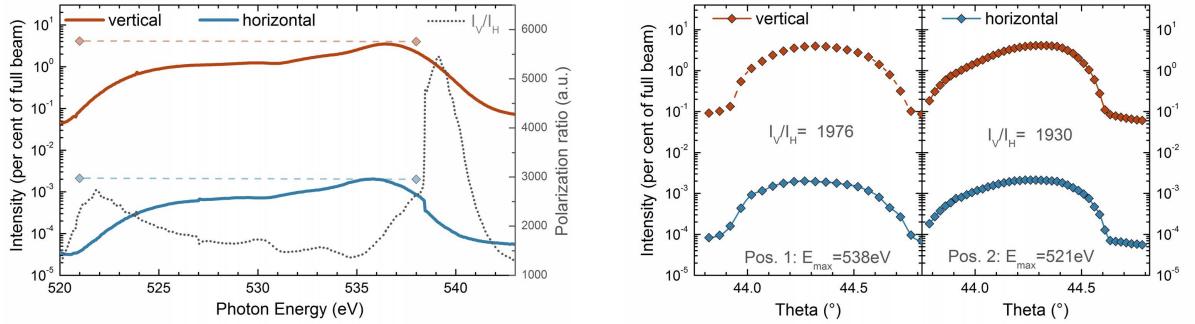

(a) **(b)**

Fig. 2.15.: Reflectivity of the O-multilayer from (a) Rigaku and (b) Axo in a logarithmic plot. (a) The red and blue curves show the energy dependence of the reflectivity of vertically (I_V) and horizontally (I_H) polarized x-rays, respectively. The vertical reflectivity is of the order of one to four per-cent in the energy interval of 525 eV to 540 eV. The dotted grey line denotes the ratio I_V/I_H, which is between 1000 and 5000. For comparison the results from the Axo multilayer are plotted as slightly transparent data points connected with a dashed line. (b) Reflectivity, obtained by a rocking scan of the AXO reflector at two different positions on the multilayer reflector. For both positions, the energy maximum of the reflected intensity is different, while the ratio I_V/I_H of the intensity of both polarizations and the order of magnitude of the reflectivity is very close to each other at both positions.

Both tested multilayer reflect a few per cent of the incident x-ray beam intensity for vertically polarized light. While the reflectivity is a little bit higher and more or less constant with respect to energy variations for the Axo reflectors, it slightly changes in dependence of the energy of the reflected radiation for the Rigaku reflectors. The same is true for the ratio between the intensities of the two incident polarizations. This changes by a factor between 1000 and 5000 with a sharp maximum around 540 eV. The advantage of the Rigaku multilayer, however, is the position independent reflectivity,

which reduces the degree of freedom that need to be moved in parallel during an energy scan.

A second multilayer from Axo designed for energies around the Fe-$L_{2,3}$ absorption edge was tested. The results can be seen in Fig. 2.16. The dependence of these Fe-multilayers

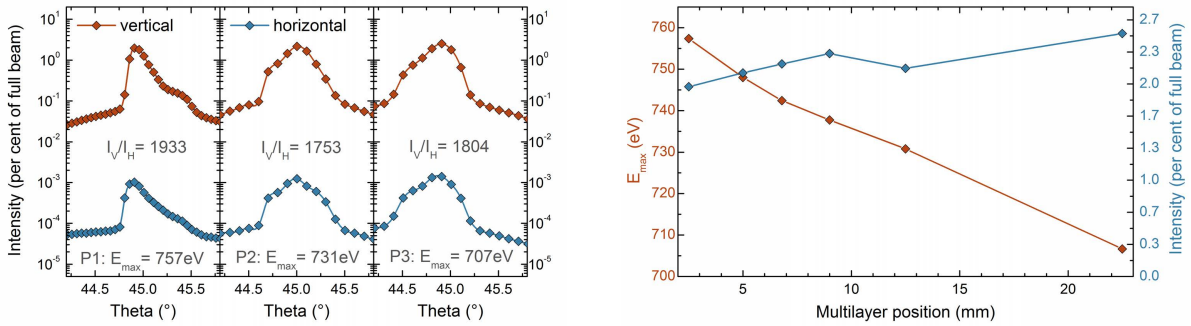

(a) **(b)**

Fig. 2.16.: Fe-multilayer from Axo. (a) Reflectivity at three different positions of the multilayer, similar to Fig. 2.15 (b). (b) The intensity of the reflection maxima and the respective energy maxima plotted versus the position on the multilayer. Both change more or less linear with position.

is similar to the oxygen reflectors. In addition, the position dependence of the intensity and energy maximum of the reflectivity was mapped in greater detail, showing the essentially linear relationship. Both Axo multilayer reflectors show a constant reflected intensity perpendicular to the gradient direction, while the intensity of the reflected x-ray beam is constant on any position tested on the whole Rigaku reflector (not shown here).

2.4. Test and calibration of a CCD detector

The new in-vacuum CCD camera, operating in our new UHV diffractometer, was commissioned in January 2012 during a RSXD beamtime at UE56/2-PGM-1. The specular reflectivity from a magnetite sample was recorded on different spots on the CCD. Details on the beamtime and the sample can be found in Chap. 4. For that purpose, the CCD camera was rotated around the sample (*tth*) and vertically translated (*zs*). At each position an image was taken with an unchanged exposure time. The resultant grid, which is shown in Fig. 2.17, is the sum over all these images. Horizontally aligned reflexes arise from the *tth* rotation of the CCD camera, while the vertically aligned reflex chain arises from the *zs* translation of the camera. This pattern was analyzed with respect to two different aspects. First, the position of the reflexes was extracted, and, secondly, the intensity was used to map the sensitivity of different regions within the CCD sensor. The positions of the reflexes are shown in Fig. 2.18. From both diagrams it is visible that the vertical (horizontal) position on the detector changes linearly with the detector height (rotation), whereas the horizontal (vertical) position stays more or less fixed.

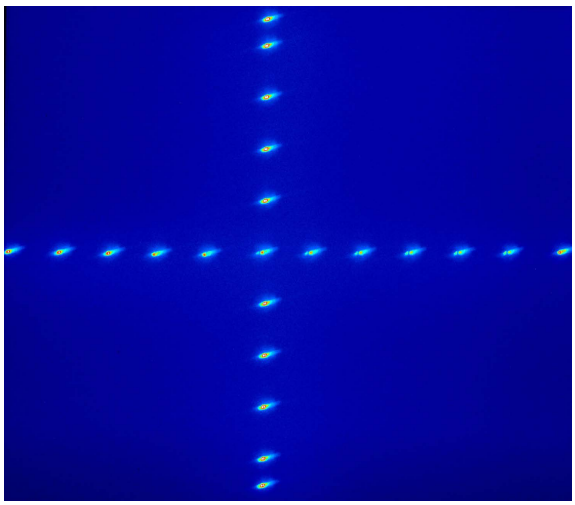

Fig. 2.17.: Sum of multiple images of the specular reflectivity from a magnetite sample at different camera positions.

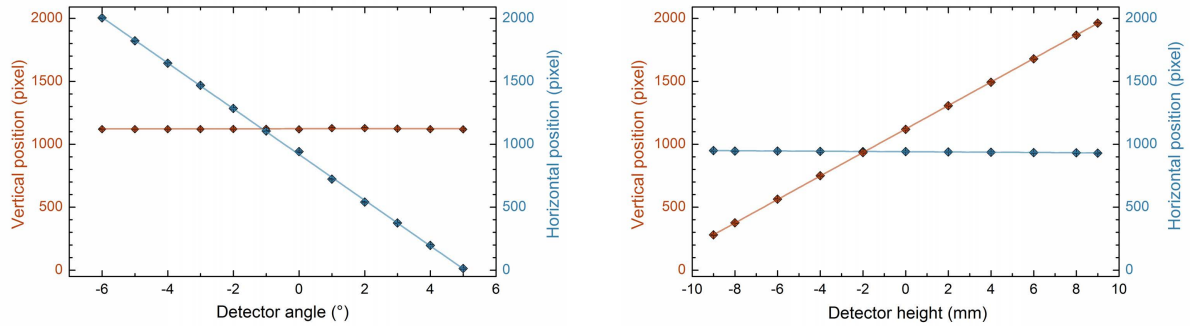

Fig. 2.18.: Horizontal and vertical positions of the reflexes shown in Fig. 2.17 for the (a) horizontally aligned reflexes, which arise from a detector rotation around the sample, and (b) vertically aligned reflexes, which arise from a vertical translation of the detector.

From the linear change, the angular to pixel and height to pixel relation and the angular acceptances can be calculated. The horizontal detector acceptance was determined to be 11° and the conversion factor is roughly 180 pixel per degree, giving a minimal resolution of roughly 0.005°. From the angular acceptance, the sample to detector center distance was calculated to be 134 mm. The vertical acceptance is 18 mm, which is in good agreement with the 45° tilted sensor, giving an angular acceptance of 7.5° and an average resolution of roughly 0.004° per pixel. Due to the tilted mounting of the CCD, this varies in the range of 10 percent.

The analysis of the peak intensity of the reflection grid, shown in Fig. 2.17, is given in Fig. 2.19. It is clearly visible that the intensity of the reflexes varies in horizontal direction, while being almost stable in vertical direction. The reason for the deviation is not clear yet, but as the reflex in the center was additionally recorded between the horizontal

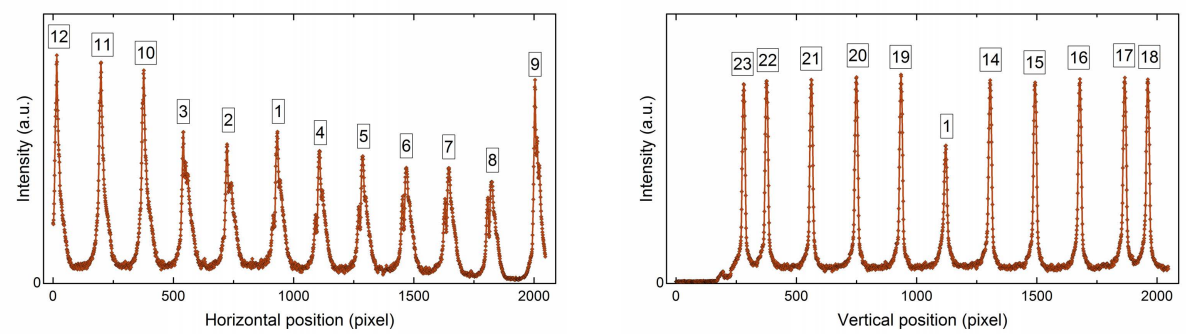

Fig. 2.19.: Horizontal (a) and vertical (b) line cut through the reflexes shown in Fig. 2.17. The small numbers above the peak indicate the order of being measured.

and vertical set (not shown here), giving again a different intensity, the variation seems to be no property of the camera sensor. More likely, something else influenced the signal strength, for example movements of the sample or changes of the beam position. A more detailed commissioning of the CCD sensor will follow in one of the future beamtimes.

2.4.1. Data recording with the new CCD camera

The power of an area detector is that one can extract much more information from a single scan in comparison to a scan performed with a point detector. Strictly speaking, a point detector is an area detector of a finite size that returns a single intensity, which is given by the integration of the whole detector signal. Usually, a silicon photo diode is used, but it can as well be an avalanche photo diode, a channel electron multiplier or another kind of point detector. In x-ray diffraction experiments one typically studies the dimensions and evolution of a reflex in reciprocal space under fixed or varying conditions (temperature, photon energy, photon polarization, etc.). This reflex is a three-dimensional object in reciprocal space. In principle, one would like to get the whole information about the scattered intensity for every volume element within this three-dimensional object. This can be mapped out, by tuning the experimental parameters. The wavelength λ of the x-ray photons and the orientation of the incident and outgoing wavevector, $\mathbf{k}$ and $\mathbf{k}'$, determine the direction and length of the wavevector transfer $\mathbf{q} = \mathbf{k}' - \mathbf{k}$. The crystallographic lattice of the sample and its orientation determines the orientation of the reciprocal space with respect to the wavevector transfer. By rotating $\mathbf{q}$ through reciprocal space all these positions are probed. This can be done by a combined sample and detector rotation. Tuning of the photon energy is used to change the length of $\mathbf{q}$, although, in many cases one is restricted to a certain resonance energy. The accessible reciprocal space is limited by the used photon energy, the sample orientation, the minimal and maximal detector positions, and by the vertical angular acceptance and translation of the detector. Whereas a point detector integrates across the probed cut or volume of the reciprocal space, an area detector resolves the $\mathbf{q}$ dependence of the reflex.

To gain all the information of a probed reflex, a set of basic scans are used in x-ray diffraction experiments. In our case, these are (a) a rocking or *th*-scan (transverse direction), where only the sample is rotated, (b) a detector scan, where only the detector is rotated and (c) a coupled *th2th*-scan (radial direction), where both the detector and the sample are rotated. Using an ideal point detector, which is infinitesimal small and records a single **q** information only, within a *th*-scan the wavevector transfer **q** does not change in size but in its direction. While in a *th2th*-scan **q** would change in size but not in direction, size and direction of **q** are changed in the detector scan. More complex scans allow, depending on the orientation of the sample and by a combined rotation of the detector and the sample to map a specific direction in the reciprocal space, for example reciprocal h, k or l direction (h-scan, k-scan, l-scan) or a combined direction (hkl-scan).

The cut through reciprocal space that is recorded by a finite size area detector is a segment of a spherical shell, which is projected onto the plane of the CCD chip. The radii are determined by the photon energies and the wavelength spread. Depending on the scan type this spherical surface segment is moved on a different path through the reflex. App. B gives an overview about different scan types in real and reciprocal space. The advantage of resolving this segment by the pixels of the area detector compared to the point detector is obvious. The drawback of using a CCD camera, besides the small dynamic range, is that all these information are stored in image files, which use much more space than the data produced by a point detector.

In most cases, it is not necessary to move the CCD detector, if the cut through reciprocal space recorded by the detector comprises the whole reflex during the scan. This implies that one can extract a *th*- as well as *th2th*-scan as recorded by a point detector from the images taken during a single *th*-scan. The procedure is described in the following for a CCD movie obtained from the magnetic (001) reflex in $La_{2-2x}Sr_{1+2x}Mn_2O_7$ (LSMO) using 641 eV photons at the Mn-L_3 edge.

A rocking scan of the magnetic (001) reflection was recorded within a series of CCD images. Every frame was taken at a different *th* angle. The CCD camera was fixed in position during the data acquisition. By rotating the sample, the reflex moved horizontally across the CCD sensor. The peak appears at different positions with its intensity maximum near the horizontal center. This data set contains the information of a *th*- and *th2th*-scan as recorded by a point detector. To illustrate this, Fig. 2.20 shows a series of a restricted CCD area for different *th* values. In a conventional *th*-scan, in which the point detector is placed in the intensity maximum and does not move during data acquisition, one would record the intensity in the highlighted red area. The size of this virtual aperture in front of the point detector is roughly chosen to be of the order of 1 mm in horizontal direction and 2 mm vertically. In a conventional *th2th*-scan the detector moves together with the sample. The region detected by this detector in a *th2th*-scan is illustrated by the transparent yellow areas.

The highlighted areas of Fig. 2.20 are horizontally aligned in Fig. 2.21. By integrating the intensity of each of these sub-frames one gets back the respective scans, as recorded by a point detector. This is shown for different slit sizes in Fig. 2.22. During the *th*-scan, the reflex moves through a fixed detector slit and a point detector would record a very

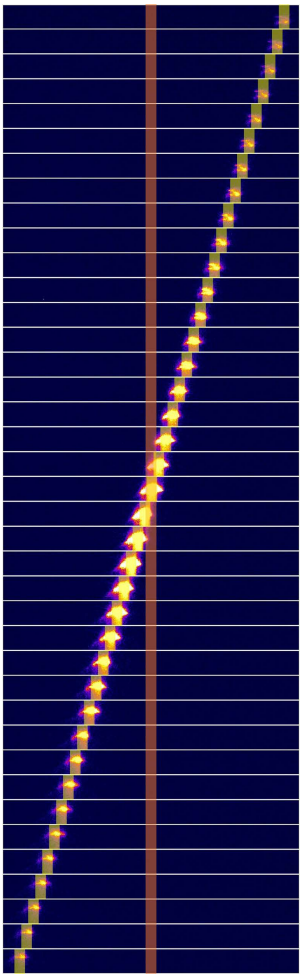

Fig. 2.20.: A restricted area of the CCD sensor is extracted frame by frame and attached in a cloumn. Lighter (darker) colors denote higher (lower) count rates. Every frame was taken for a different *th* angle. In a *th*-scan of a point detector with a $1{\times}3\,\mu m^2$ (horizontal by vertical) slit (indicated by the red highlighted area) the detector would not move, while in a *th2th*-scan with the same kind of detector, the detector position shifts with the maximum of the reflex (indicated by the yellow highlighted area).

sharp peak (Fig. 2.22 (a)). The peak widths depends on the horizontal slit size but not on the choice of the vertical slit size. Interestingly, the slit sizes have no huge impact on the width of the *th2th*-scans (2.22 (b)). Even the integration of the area that was crossed by the moving reflex (restricted CCD area, which is shown in Fig. 2.20 (a)) results in the same peak width (yellow data marker) if a constant background was subtracted, which arises from the remaining intensity in the area around the reflex and is simply a constant offset to the data. In both cases the peak position shifts for specific choices of the slit settings.

Integration of the intensity as described above allows to reconstruct the result of a conventional *th*- and a *th2th*-scan from a single data set, but still throws away much of

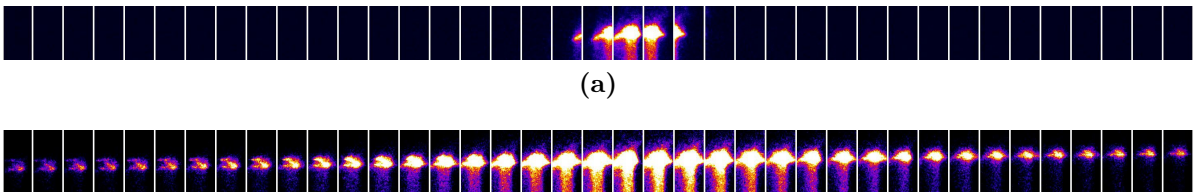

(a)

(b)

Fig. 2.21.: (a) *th*- and (b) *th2th*-scans, extracted from the CCD movie, as seen by a $1 \times 2\,\mu m^2$ slit. Lighter (darker) colors denote higher (lower) count rates. The additional intensity below the peak is attributed to the read out of the CCD camera.

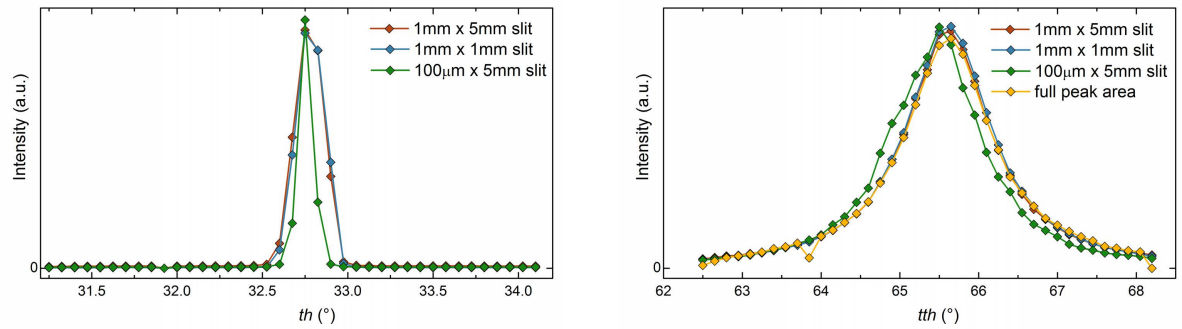

(a) (b)

Fig. 2.22.: The CCD images were used to extract a *th*-scan (a) and *th2th*-scan (b) for different virtual slit settings. The first value refers to the horizontal slit size and the second to the vertical slit size. The width of the *th*-scan strongly depends on the choice of the horizontal slit size, but not on the vertical slit size. Also the peak position is affected by the slit choice. The width of the *th2th*-scan is not that much affected, but the choice of the slit settings may shift the peak position.

the information recorded by an area detector. In fact, the camera data can be projected back to the reciprocal space to rebuild the whole three-dimensional reflex. In a first approximation this can be done by arranging the images one behind each other. This is not completely correct, as the cut through reciprocal space is of spherical shape, resulting in distortions of the image, but it is a good approximation to start with, as the curvature is expected to be small. From the combined three-dimensional image of the reflex in reciprocal space it is possible to directly view its shape and extract its extensions in any desired direction. A cut through the horizontal plane is shown in Fig. 2.23. In the direction along the frames it was interpolated and smoothed in all direction. The very elongated peak profile shows the two-dimensional character of the magnetic order in LSMO.

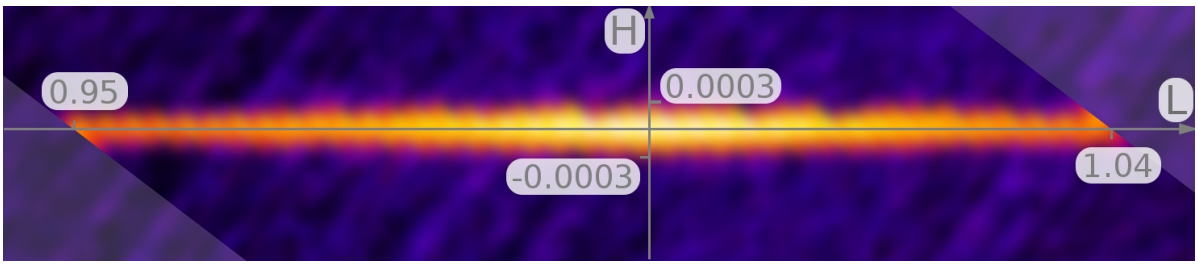

Fig. 2.23.: Cut through the three-dimensional data set of the (001) magnetic reflex at k =0 of LSMO that was recorded by a CCD camera during a single *th*-scan. The images were attached behind each other. The lighter area on the upper right and lower left edge is simply attached to fill the space of the image. The curvature of the **q** space segment that is probed by each frame would lead to a distortion of each frame before attached together and was neglected in this first approximation. Furthermore the frames should be shifted against each other in horizontal direction depending on the exact orientation of the probed volume to the axis of the reflex. This was neglected as well, but would lead to a shearing of the whole set of image along the horizontal direction, which runs diagonal from upper right to lower left in this image. A logarithmic scaling of the intensity was used for better visibility, where lighter colors denote higher and darker colors lower intensity.

2.5. Discussion

We successfully built up and commissioned a new UHV diffractometer for low energy x-ray diffraction. The instrument is well suited for resonant and coherent x-ray diffraction experiments and will be available as an user instrument at the new synchrotron radiation facility PETRA III. Especially our experiences with coherent diffraction during the last years has helped to develop and provide a stable sample environment, well suited for CXD measurements. The new instrument was already used in a couple of beamtimes at DESY, BESSY II and FLASH. First results from characterization measurements of multilayer reflectors and the new in-vacuum CCD, for which the benefit of an area resolving detector is explained, were presented. RSXD experiments in Fe_3O_4 at the O-K and Fe-$L_{2,3}$ edge that were performed with the new diffractometer are presented in Chap. 4.

CHAPTER 3

Charge Stripe Order Near the Surface of $La_{1.88}Sr_{0.12}CuO_4$

The results presented in this chapter have been published partly in:

H.-H. Wu, M. Buchholz, C. Trabant, C. F. Chang, A. C. Komarek, F. Heigl, M. v. Zimmermann, M. Cwik, F. Nakamura, M. Braden & C. Schüßler-Langeheine: Charge stripe order near the surface of 12-percent doped $La_{2-x}Sr_xCuO_4$, Nature Communications **3**, 1023 (2011).

3.1. Introduction

3.1.1. High-temperature superconductivity

Copper oxide systems are known for the unusual temperature dependence of their electrical resistivity. In 1986 Bednorz and Müller discovered the first member of this new class of high-temperature superconducting materials [1]. Fig. 3.1 shows a sketch of the K_2NiF_4-type crystal structure for the prototypical superconductor $La_{2-x}Sr_xCuO_4$ (LSCO), which we will focus on in the following. The high-temperature tetragonal (HTT) crystal system with $I4/mmm$ symmetry has lattice parameters of about $3.8\,\text{Å} \times 3.8\,\text{Å} \times 13.2\,\text{Å}$. The key structural building units are the CuO_2 planes with weak interplanar coupling, which are sandwiched between layers containing La and Sr. It is well established that these two-dimensional structures are crucial for superconductivity (SC) in the cuprates, while the remaining part between these planes acts as a charge reservoir and stabilizes the structure.

Below a doping-dependent transition temperature LSCO undergoes a structural transition from the HTT to a low-temperature orthorhombic (LTO) crystal structure, which is characterized by a tilt pattern of the oxygen octahedra (Fig. 3.6). The LTO unit cell is rotated by 45° around the c-axis with respect to the HTT unit cell and is twice as large [66].

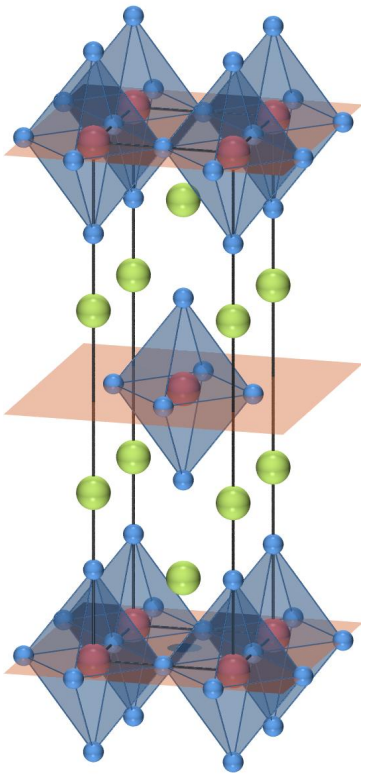

Fig. 3.1.: High temperature tetragonal (HTT) crystal structure of LSCO and related compounds. Copper ions in red are octahedrally surrounded by oxygen ions, displayed in blue. Oxygen octahedra arrange in a corner-shared manner, resulting in 180° Cu-O-Cu coupling. The CuO_2 planes (light red) are separated by lanthanum or strontium oxide planes.

The parent compound of LSCO, La_2CuO_4 (LCO), is insulating with an energy gap of approximately 2 eV. In the undoped compound the copper ions have a d^9 configuration with one hole in the $3d_{x^2-y^2}$ orbital, forming a half filled band with a total spin of $1/2$ per copper site. LCO is a Mott insulator because the Coulomb repulsion between different sites exceeds the hopping integral. This localizes the charges on the copper sites, leaving only the spin degree of freedom to orient. The spins of neighboring $3d$ copper electrons order antiferromagnetically in each copper oxide layer due to superexchange interaction through the oxygen ions [67]. Fig. 3.2 shows a schematic sketch of the copper oxide layer and the antiferromagnetic alignment of the copper spins. These antiferromagnetic correlations survive even in the doped (metallic) compounds [68]. By doping Ba or Sr into the system, thus replacing part of the trivalent lanthanum by divalent ions, the cuprates are rendered conductive and later on even superconductive. A schematic phase diagram for LSCO is shown in Fig. 3.3 for the hole doping range around the superconducting phase. The phase diagram comprises different regions with varying prevalent electronic character. For low Sr doping (up to x=0.02) LSCO is an antiferromagnetic insulator with a Néel temperature that decreases with doping from 320 K for the undoped LCO [70].

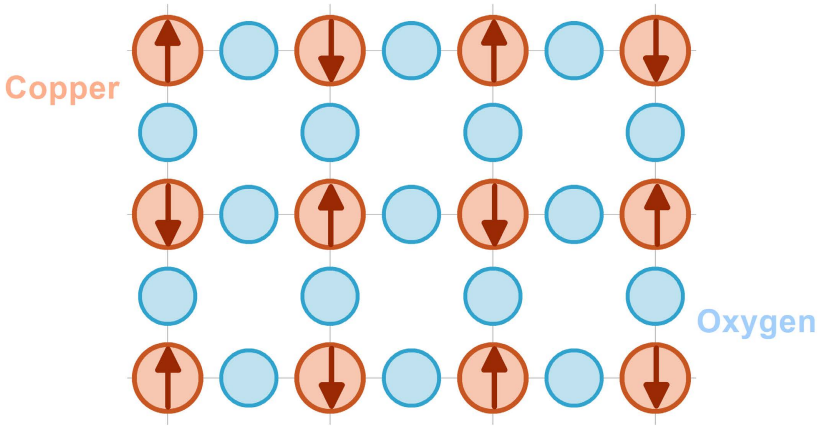

Fig. 3.2.: The CuO_2 plane is the key structural element for cuprate high-temperature superconductors. The schematic plane above shows the antiferromagnetic Mott insulating ground state for the case of the undoped LCO, where the copper ions have a valence of 2+ and the oxygens 2-. Every copper atom is octahedrally surrounded by oxygen. Four of the six oxygen ions are within the CuO_2 planes. Antiferromagnetic ordering of the copper spins, indicated by the red arrows, is mediated via superexchange interaction through the 180° Cu-O-Cu bond.

For higher Sr doping one enters the pseudogap regime. This regime is characterized by a suppression of the density of states at the Fermi level, similar to what is found in the superconducting regime, while SC itself is absent. Going further in doping the superconducting dome arises with a maximum of T_c at optimal doping around x_{opt}=0.16. Compounds with $x < x_{\text{opt}}$ are named underdoped, while overdoped for $x > x_{\text{opt}}$. For a hole density of 1/8 per copper site a local minimum in T_c is observed, which is much more pronounced for $La_{2-x}Ba_xCuO_4$ (LBCO) [71]. Above T_c a phase called strange metal (non-Fermi liquid) is found, which exists up to roughly 1000 K [72]. There, the temperature dependence of the resistivity follows a linear relation ($\propto T$) instead of a quadratic one ($\propto T^2$), like proposed for an ordinary metal (Fermi liquid) in the Landau-Fermi liquid theory. On the higher doping end of the phase diagram the system enters a Fermi liquid phase. The extrapolation to $T = 0$ between the phase boundary of the pseudogap and the strange metal as well as the boundary of the Fermi liquid and the strange metal phase is believed to end in a quantum critical point [73, 74].

The pairing mechanism in conventional superconductors, which leads to the formation of Cooper pairs, is phonon-based and can be well described within the BCS theory. The associated order parameter, containing the energy gap and the symmetry of the pairing, describes the deviation from the normal state. In the BCS theory the symmetry of the pairing is of s-wave (spherical symmetry) type. Soon after the discovery of HTS it was realized that the charge carriers are electron pairs as well [75]. Later on, d-wave pairing

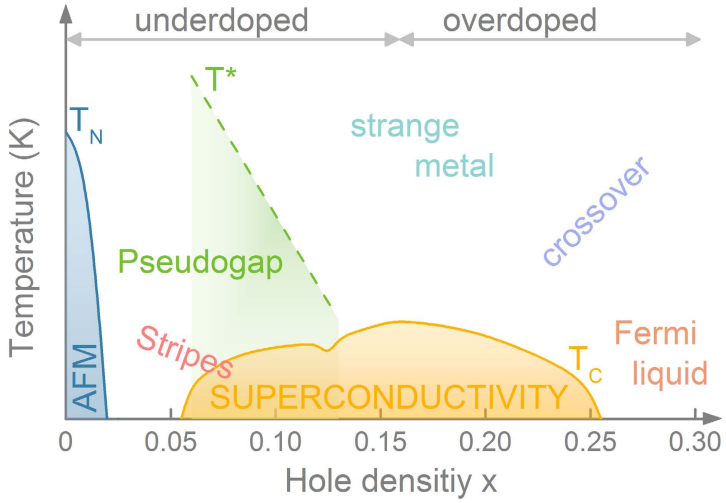

Fig. 3.3.: Phase diagram of hole-doped LSCO, after [69], showing regions of different electronic character like antiferromagnetism, SC, a pseudogap, a strange metal and a Fermi-liquid phase. A more detailed description of the different phases is given in the text. The critical temperature of SC is slightly suppressed for a hole doping of 1/8, which is stronger visible in LBCO, and has a maximum at around $x = 0.16$, defining the optimally doped, the underdoped and the overdoped regions.

symmetry ($d_{x^2-z^2}$) was determined [76, 77]. Thus, cuprate superconductors cannot be described within BCS theory.

A much smaller isotope effect evidences a different electron-phonon interaction than in conventional superconductors. As a consequence a different Cooper pairing mechanism has to be found for HTS. A number of different interactions and mechanisms promoting SC were proposed (for example in Ref. [74, 78–82]). All of them are strongly debated. A theory that describes the superconducting state adequately has to imply all observed phases, like the pseudogap or the strange metal phase. This is the reason why extensive studies were done in the whole phase diagram, shown in Fig. 3.3, and of course far beyond that. A couple of comprehensive reviews can be found in Ref. [69, 83, 84]. One of the most prominent examples is a charge carrier modulation, building a stripe-like formation of the carrier density.

3.1.2. Stripe order in copper oxides

In La_2CuO_4 (LCO) antiferromagnetism is the dominating correlation. Replacement of La with Sr dopes holes into the system. To account for the frustrated mobility of these holes in the antiferrmagnetic surrounding, charge agglomeration into stripes was theoretically predicted [85, 86]. Doping holes into LSCO removes one of the electrons from one of the copper ions and makes it possible for the surrounding electrons to hop into the now empty $3d_{x^2-y^2}$ state. Note that hopping of nearest-neighbor electrons,

which have opposite spin compared to the spin of the removed electron, destroy the local antiferromagnetic order, if they occupy the empty site. In this sense the hole motion is frustrated.

For a higher hole concentration, these holes can arrange in a regular pattern to allow movements at lower energy cost. In this stripe formation holes align in one-dimensional chains inside the two-dimensional CuO_2 layer. Movement of the whole stripe is not frustrated and keeps the local antiferromagnetic ordering. In Fig. 3.4 a scheme of the spin and charge stripe pattern in LSCO is shown for a hole concentration of 1/8. One-

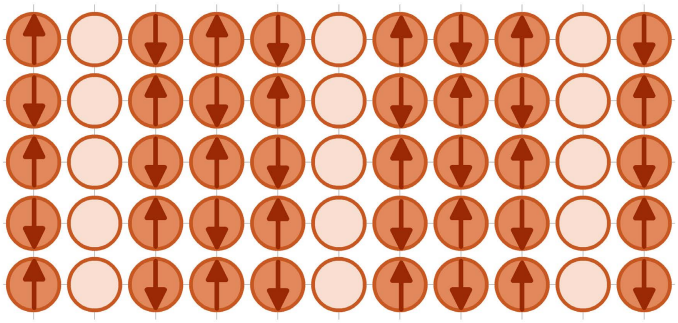

Fig. 3.4.: Stripe order of LSCO in the CuO_2 plane, according to [87]. Only the copper sites are shown, where light filling of the circles denotes hole-rich and darker filling hole-poor regions. The arrows indicate the spin directions.

dimensional walls of hole-rich regions separate two-dimensional hole-poor regions, in which nearest neighbors order antiferromagnetically. Note that two copper sites in the hole rich regions share one hole. In this configuration the stripes act as antiphase domain walls. By crossing the domain wall the antiferromagnetic order is shifted by π. This new superstructure has a different periodicity with eight Cu-Cu distances parallel to the charge modulation for the magnetic unit cell and four Cu-Cu distances for the charge unit cell. In reciprocal space (Fig. 3.5) this arrangement produces magnetic superstructure reflexes that are displaced by ϵ from the commensurate antiferromagnetic Bragg peaks (red and blue triangles) and charge superstructure peaks that are displaced by 2ϵ from the fundamental Bragg reflections (red and blue squares). The displacement ϵ depends on the amount of Sr doping and is equal to 1/8 for x =1/8 [88].

Experimentally, spin stripe order was first observed in LSCO [89], while charge stripe order was first observed in iso-structural nickelate compounds [90, 91], followed by the observation of charge stripes in $La_{1.6-x}Nd_{0.4}Sr_xCuO_4$ by means of neutron scattering experiments [87]. By partially substitution of La with Nd, LNSCO undergoes a second structural phase transition from the LTO to a low-temperature tetragonal (LTT) crystal structure. Tilting of the oxygen octahedra around the $[1\,0\,0]_{\mathrm{HTT}}$ and $[0\,1\,0]_{\mathrm{HTT}}$ directions

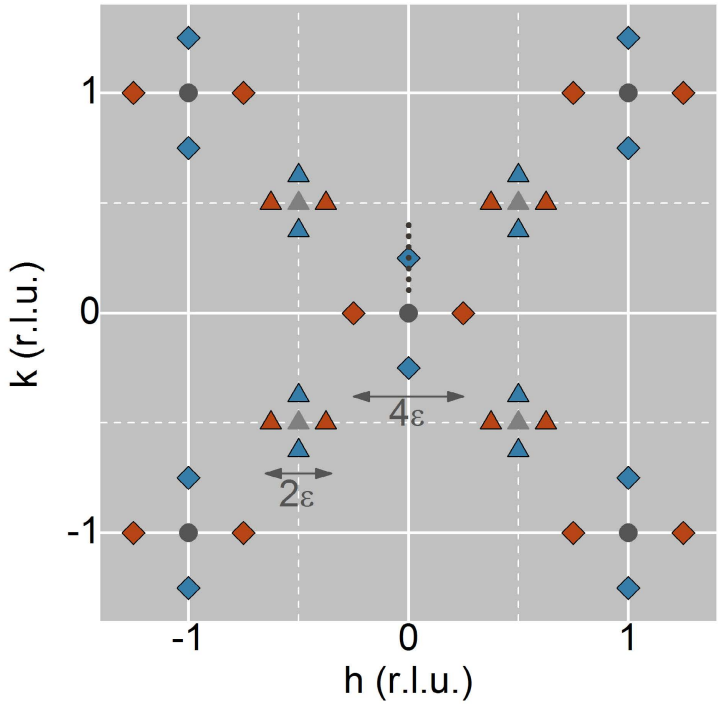

Fig. 3.5.: Theoretical reciprocal space map of 1/8 doped LSCO: Fundamental Bragg peaks (dark grey circles) fulfill $h + k = 2n$; charge order peaks (red and blue squares) are split by 2ϵ from the fundamental Bragg peaks; and spin order peaks (red and blue triangles) are split by ϵ from the commensurate spin order reflex of the undoped compound (light grey triangle). Red and blue colored symbols represent reflexes for stripes running parallel to b_{HTT} and a_{HTT}, respectively. Scattering from a single stripe orientation would lead to either of them. The dotted line through (h k)=(0.25 0) indicates a typical scan done in the experiment.

in adjacent layers (Fig. 3.6) generates a buckling pattern of the CuO_2 plane that stabilizes the formation of static stripes along the O-Cu-O bonds [92, 93].

Blue and red symbols arise from charge and spin stripes propagating in $[1\,0\,0]_{\mathrm{HTT}}$ and $[0\,1\,0]_{\mathrm{HTT}}$ direction, respectively. The LTT tilt pattern alternates from CuO_2 layer to CuO_2 layer and gives rise to an alternate stacking of stripes running in either a or b direction [94].

After the first observation of charge stripes in $La_{1.48}Nd_{0.4}Sr_{0.12}CuO_4$ (LNSCO) by means of neutron diffraction it took only a few years until complementary hard x-ray experiments confirmed their existence [95]. In recent resonant soft x-ray experiments charge stripes in the LTT phase of LBCO and $La_{2-x-y}Eu_ySr_xCuO_4$ (LESCO) were found [24, 96]. The existence of stripes in the LTT phases of high-T_c cuprates is therefore well established, whereas the interplay between stripes and SC is still an ongoing matter of debate. Indications that stripes compete with SC come from the observation that SC is suppressed in 1/8 doped LBCO (Fig. 3.7), while pronounced charge stripe order is found for this composition [98]. On the other hand, SC does not strictly exclude stripe

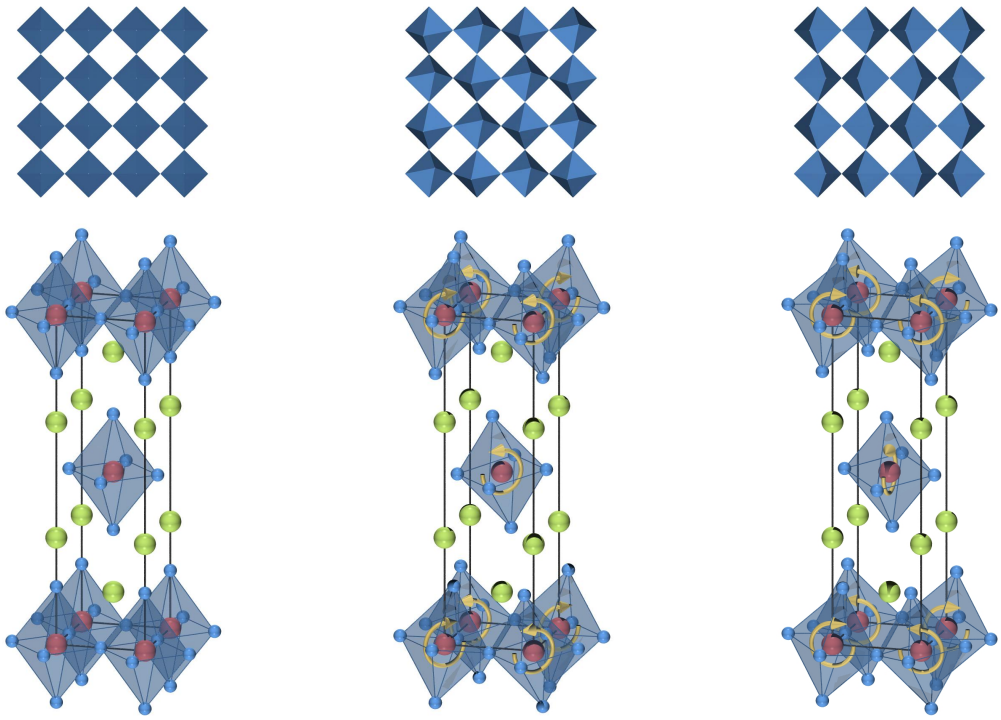

Fig. 3.6.: HTT (a), LTO (b) and LTT (c) symmetry. CuO_2 buckling pattern with the respective tilting pattern of the oxygen octahedra (shown below). Yellow arrows indicate the tilting direction of the octahedron in the respective directions. Note that for better visibility the tilt angle is magnified and the crystal cell is restricted to the HTT unit cell.

order: Coexistence of charge stripe order and bulk SC is found in LBCO and LNSCO for Ba doping concentrations beyond 1/8 [99,100] as well as coexistence of charge stripes and two-dimensional SC in 1/8 doped LBCO [101,102]. In any case SC and stripes have an intriguing relation.

While the LTT phase clearly stabilizes the formation of charge stripe [103–105], it is less clear whether the LTO phase prevents it. So far charge stripe order was only found in systems showing the LTT phase [106]. Fujita et al. propose a close relation between stripe order and the structural transition from the LTO to LTT phase [106]. In LNSCO the temperature for the LTO to LTT transition (T_{str}) and the charge stripe oder temperature (T_{CO}) are coincident and only the spin stripe order temperature (T_{SO}) is lower. In $La_{1.875}Ba_{0.125-1}Sr_xCuO_4$ (LBSCO), where T_{str} is lower than in LNSCO, the structural transition pushes charge and spin stripe oder to a collective temperature. If oppositely T_{str} increases, like found in LESCO, all transitions will be decoupled, with $T_{SO} < T_{CO} < T_{str}$ [96,107]. Recent studies from Wilkens et al. and also our findings show that charge stripe order sets in below T_{str}, while in LBCO $T_{SO} < T_{CO} = T_{str}$ [62]. Hücker et al. have even found charge stripe order in the HTT phase by applying pressure on LBCO [108].

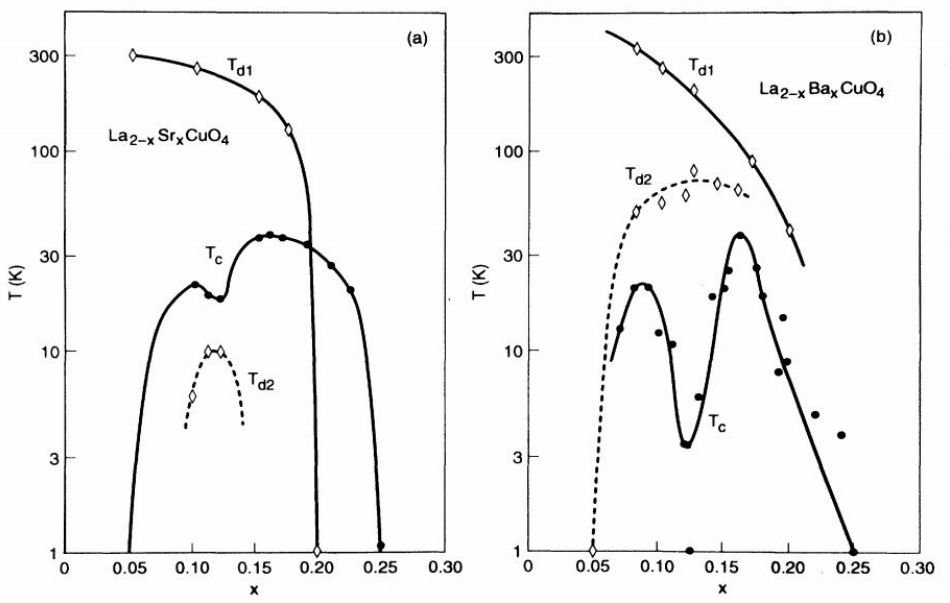

Fig. 3.7.: Doping dependence of the critical temperature for SC in LSCO (left) and LBCO (right). The anomaly at 1/8 doping is visible due to the supression of the superconducting state. Reprinted Fig. (a) and (b) with permission from J.C. Philips et al., Phys. Rev. B **44**, 2863-2866 (1991) [97]. Copyright (1991) by the American Physical Society: `http://link.aps.org/abstract/PRB/v44/p2863`.

In LSCO no indications for charge stripe order had been found so far, but certain experimental results indicated a proximity to charge stripe formation. Among these, the existence of magnetic satellite reflexes that are split from the antiferromagnetic reflex of the parent compound [109] by ϵ, as expected for spin stripe order (Fig. 3.5), is the most puzzling one. The position of the reflexes as well as the temperature dependence of the peak intensity, found by neutron scattering, are presented in Fig. 3.8. A scenario of long-range modulated antiferromagnetic order, as it is necessary to describe the splitting of the antiferromagnetic reflection into satellites without involving the charge degree of freedom is hard to imagine. Within Ref. [109] the authors determined the fraction of any LTT phase, if present at all, to be less than one percent, concluding that the tetragonality is not crucial for spin stripe formation. Another indication for the proximity to charge stripe formation is the reduction of the critical superconducting temperature for 1/8 doping (Fig. 3.7). Although less pronounced as in LBCO, the reduction indicates a mechanism competing with superconductivity. Furthermore the softening and broadening of the phonon mode in 15-percent doped $La_{2-x}Sr_xCuO_4$ is a strong indication for charge ordering, as presented in [110].

Since novel x-ray methods like resonant soft x-ray diffraction as well as high energy x-ray diffraction provide an extremely high sensitivity for charge stripe ordering [24, 28, 95, 96, 99, 108, 111], we set out for a new search for charge stripe order reflexes in 12-percent doped LSCO using both these methods complementarily.

The rest of the chapter is organized as follows: First methodical and experimental

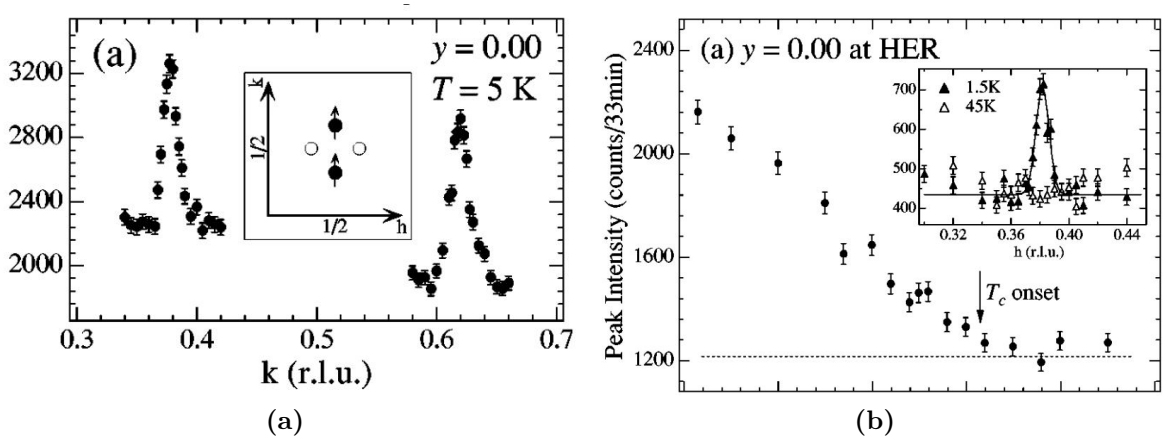

Fig. 3.8.: Magnetic reflex in 1/8 doped LSCO. In (a) a scan through the reciprocal k direction clearly shows both satellites split by ϵ from the antiferromagnetic peak position of the undoped compound. In (b) the temperature dependence of the peak intensity is shown. Note that the magnetic ordering sets in at about the same temperature as superconductivity. Reprinted Fig. (a) and (b) with permission from H. Kimura et al., Phys. Rev. B **59**, 6517-6523 (1999) [109]. Copyright (1999) by the American Physical Society: `http://link.aps.org/abstract/PRB/v59/p6517`.

details are given. Afterwards we turn to the results from the resonant low energy x-ray experiment of LSCO at the O-K and Cu-$L_{2,3}$ edges, in which we found a reflex at the same position where a charge stripe reflex has been found in LNSCO. A comparison of the diffraction spectra of the reflex in LSCO with spectra taken from a LNSCO reference sample and spectra of LESCO and LBCO from literature reveals that the electronic origin of the reflex is the same for all four compounds. While in LNSCO, LESCO and LBCO the existence of charge stripe order is well established, this is the first time that charge stripe order has been found in LSCO. Thereafter, we present results from a hard x-ray diffraction experiment in LSCO where no reflex was found. From the different probing depths of high energy and low energy x-rays we conclude that the surface is fundamentally different from the bulk. To exclude that charge stripes have been introduced by the sample surface preparation method, we show a comparison of results from a polished and a cleaved sample. Charge stripe order could be verified independently on the preparation method. At the end of the chapter we discuss a radiation-induced feature that appeared during some of the measurements.

3.2. Method

We have studied 12-percent doped $La_{2-x}Sr_xCuO_4$ (LSCO), the prototypical superconductor, where charge stripe order had not been found so far, by means of resonant soft x-ray diffraction (RSXD). This technique has proven its ability and high sensitivity to directly detect stripe order. Due to its close relation to x-ray absorption spectroscopy,

RSXD is sensitive to spatial modulations of different electronic states.

Diffraction experiments of soft (low energy) x-rays are moderately surface sensitive with a typical probing depth of several nm. In the high energy x-ray regime the probing depth is of the order of mm. The interpretation of low and high energy x-ray data has to take the different probing depths into account. While RSXD is able to directly detect charge stripes, high energy x-ray diffraction probes the distortion of the lattice caused by the charge stripe modulation.

The accessible reciprocal space is determined by the size of the wave vector $|\mathbf{k}| = k = 2\pi/\lambda$ and the surface orientation of the sample. Since k is smaller for low energy x-rays, a smaller fraction of reciprocal space can be studied. In a resonant diffraction experiment at the O-K and Cu-$L_{2,3}$ edges the accessible charge stripe positions are restricted to the four reflexes around the central Bragg reflex (Fig. 3.5).

To minimize any difficulties in finding the reflex we have used an equally 12-percent doped $La_{1.6-x}Nd_{0.4}Sr_xCuO_4$ (LNSCO) sample. The LNSCO sample was prepared in the same manner as the LSCO sample and a similar experimental procedure has been performed with both samples. The LNSCO sample acts like a direct reference sample and helps to identify the electronic character of the charge stripe reflex in LSCO.

3.3. Experimental details

High energy x-ray experiments were performed by Alexander Komarek and Martin von Zimmermann at the BW5 beamline of DORIS in Hamburg [112]. An x-ray energy of 100 keV was used to study the samples. The RSXD experiments were carried out at the UE46-PGM1 beamline at BESSY II in Berlin. The x-ray energies used during the soft x-ray experiment were chosen to be in resonance with the oxygen $1s$ to $2p$ (O-K) and the copper $2p$ to $3d$ (Cu-$L_{2,3}$) absorption transitions. The energy resolution was given by the exit slit of the beamline and varied between 60 to 590 meV for a 20 to 100 µm slit.

A two-circle UHV diffractometer, designed by Eugen Weschke and Enrico Schierle, was used in horizontal scattering geometry. For low temperature experiments a helium flow cryostat was used, allowing to perform temperature-dependent measurements down to 18 K. A silicon diode detector was mounted 160 mm from the center and a rectangular slit in front of the diode defined the angular acceptance to 0.35° in plane and 3.5° out of plane.

The samples were cut from a large piece, which was grown by F. Nakamura from the Hiroshima University using the traveling solvent floating zone method. By using the Laue method samples with a surface orientation of $[1\,0\,0]_{\mathrm{HTT}}$ and $[0\,0\,1]_{\mathrm{HTT}}$ were prepared.

For the a-oriented sample only the $(0.24\,0\,0)_{\mathrm{HTT}}$ charge stripe reflex was accessible out of the four charge stripe reflections around $(0\,0\,0)$. The sample surface was lapped with boron carbide and polished with 0.5 µm alumina suspension until a shiny surface was visible. The sample was glued on a copper sample disk using conducting and UHV compatible silver paste. In vacuum it was aligned with the **c** axis lying in the scattering

plane. By using vertical ($\boldsymbol{\sigma}$) x-ray polarization the electrical field vector of the incoming x-rays lies always inside the CuO_2 planes, more precisely always parallel to **b**.

The *c*-orientation is the cleavage plane of LSCO, attributed to the layered crystal structure. Samples of LSCO from the same pieces as the *a*-oriented one were cut into an elongated rectangular shape and fixed with silver glue to the copper sample holder. Epoxy adhesive was used to mechanically stabilize the sample. The samples were cleaved in the load lock at a base pressure of 10^{-5} to 10^{-6} mbar.

A comparison of both samples is used to exclude the stabilization of charge stripe order due to the treatment of the sample surface. The *c*-oriented sample was also used to search for the four charge stripe reflexes at $(\pm 0.24\,0\,0)_{\mathrm{HTT}}$ and $(0\,\pm 0.24\;\;0)_{\mathrm{HTT}}$.

Throughout the following the high-temperature tetragonal (HTT) unit cell with $a = 3.8$ Å, $b = 3.8$ Å and $c = 13.2$ Å is used, if not specified differently.

3.4. Results

3.4.1. Resonant soft x-ray diffraction experiment

In the soft x-ray experiment we clearly found reflexes in the 12-percent doped LSCO samples at the positions in reciprocal space where charge stripe order reflexes have been found in the Nd-stabilized LNSCO compound. The existence is independent of the sample surface orientation and preparation method. Scans in the reciprocal *h* direction (*h*-scans) across the reflex from the *a*-oriented LSCO and LNSCO reference samples are shown in Fig. 3.9. A weak peak on an albeit huge background is clearly visible in our

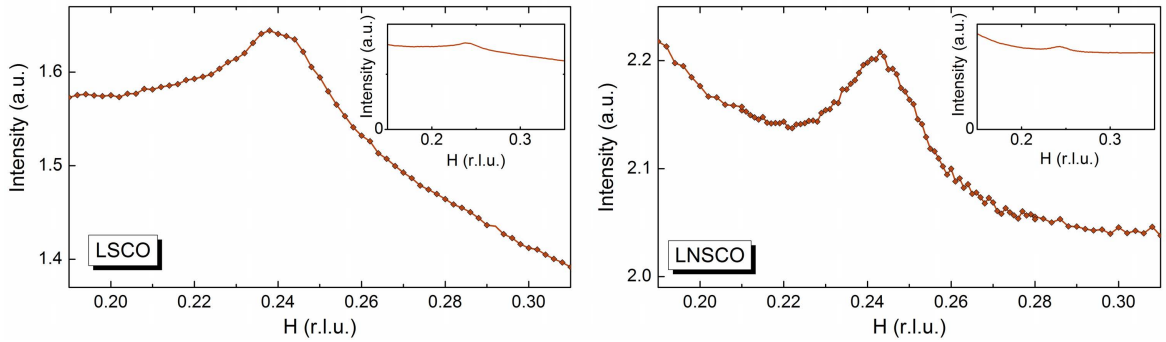

Fig. 3.9.: RSXD scan in the LSCO sample (a) and LNSCO reference sample (b) across the (0.24 0 0.05) reflex taken at the Cu-L_3 energy resonance maximum. In the inset the y axis starts at zero, while in the main graph it is scaled for better visualization of the peak.

RSXD experiment for both samples. Although we clearly found the peak in all studied samples the peak to background intensity ratio varied strongly across the sample surface and between different samples, making this experiment very challenging. Background

subtraction and data treatment was therefore done with particular care as is explained in the following.

Data analysis and background subtraction

The data acquisition and analysis procedure is illustrated for a few h-scans taken from the Cu-L_3 energy-dependent data set of LSCO. The raw data are plotted in Fig. 3.10 (a), the h-values are given in reciprocal lattice units (r.l.u.) and the intensity is always

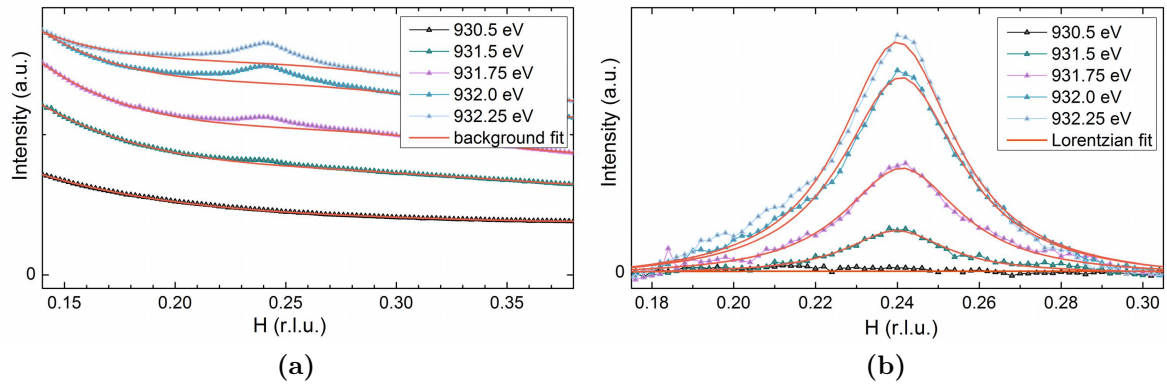

Fig. 3.10.: (a) Exemplarily selected experimental data sets and associated polynomial background fits of the charge stripe reflex in LSCO. (b) Lorentzian fit to a few selected background corrected h-scans.

normalized to the monitor signal. The background, mainly arising from fluorescence coming from the sample, changes the peak shape and peak intensity with varying photon energy. To correctly distinguish the background from the charge stripe reflex, the data have been recorded in a wide range of h around h=0.24. To account for the shape of the background, a polynomial of fifth order was fitted to the data, excluding the data around the peak position. Exemplarily selected h-scans, including the background fit, are shown in Fig. 3.10 (a). A Lorentzian or Gaussian peak function was fitted to the background corrected data. A few examples of the Lorentzian fits to the energy-dependent h-scans at the Cu-L_3 edge are shown in Fig. 3.10 (b). This kind of procedure was performed for all data sets.

Peak profile in reciprocal space

The (0.24 0 0) peak profile of LSCO in the h-l zone has been mapped by performing h-scans at different l values. For better visibility all background corrected data points have been plotted together in an h-l zone map in Fig. 3.11 (a) and (b). Lighter colors denote data points with higher intensity and darker colors those with lower intensity. The expected weak coupling between neighboring CuO_2 planes leading to a small correlation length along the **c** direction is reflected in the anisotropic profile. The h-integrated

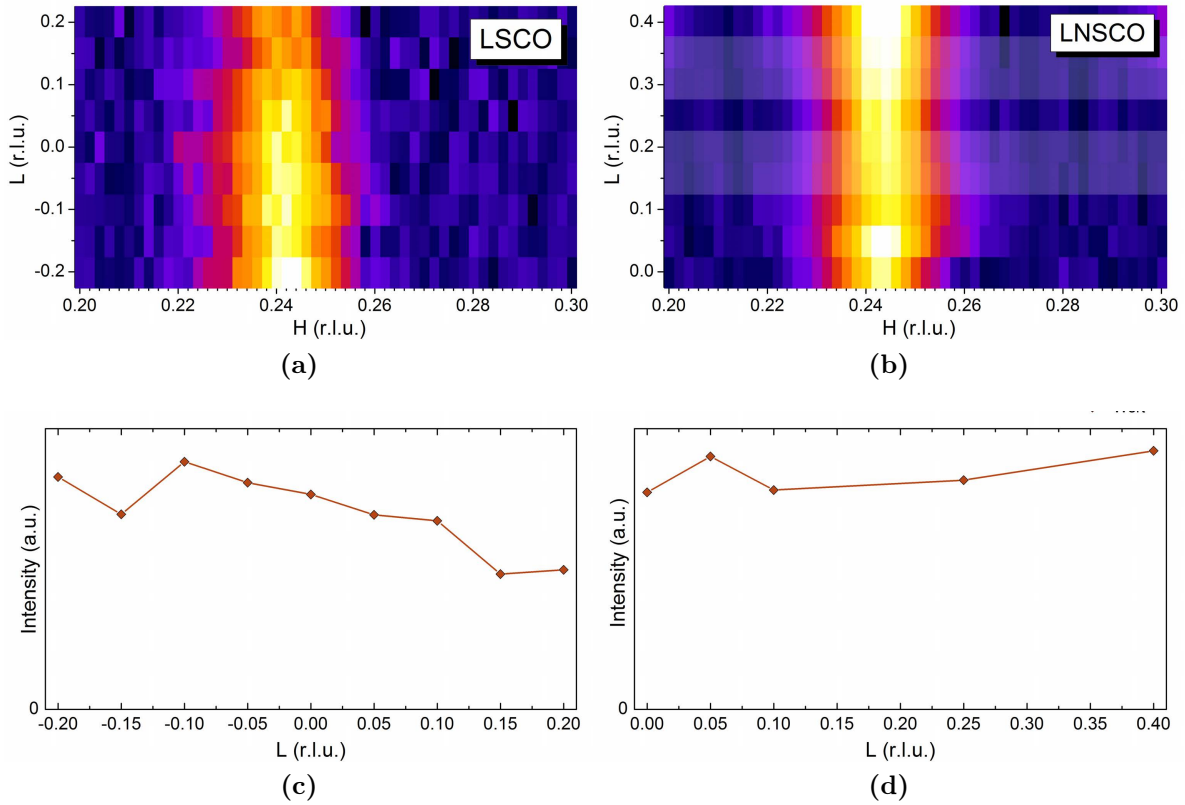

Fig. 3.11.: l-dependence of the integrated intensity of the (0.24 0 0) charge stripe order scattering reflex of LSCO at the O-K edge (a) and LNSCO at the Cu-L_3 edge (b). A hl-map of the charge stripe order reflex in LSCO (c) and LNSCO (d). Higher intensities are displayed by brighter colors, lower intensities by darker colors. The long correlation length along **a** and the short correlation length along **c** can be calculated by the inverse widths in both directions. Note that the slightly transparent values in (b) for l=0.15, 0.2, 0.3 and 0.35 are interpolated and that the l range for LSCO and LNSCO is different.

intensity is plotted in Fig. 3.11 (c) and (d) and shows a more or less constant l dependence. No indications are found for a minimum in the intensity lor l=0 or an increase towards l=0.5 as found in high-energy x-ray diffraction for LNSCO [95]. This result suggest that the correlation length is smaller than the c lattice constant and therefore the stripe ordering in adjacent CuO_2 planes is really decoupled.

For LTT cuprates the charge stripe peak is found at four different positions in the h-l zone of reciprocal space around (0 0 0). Twice in reciprocal h and $-h$ direction as well as twice in reciprocal k and $-k$ direction, split by 2ϵ from the center (Fig. 3.5). The explanation is that the stripes are alternating parallel to the **a** or **b** direction, varying from layer to layer. To check whether LSCO shows a similar four-fold pattern, we used the c-oriented sample, for which all four possible positions are accessible. The short correlation along the **c** direction, which produces extended reflexes in reciprocal l

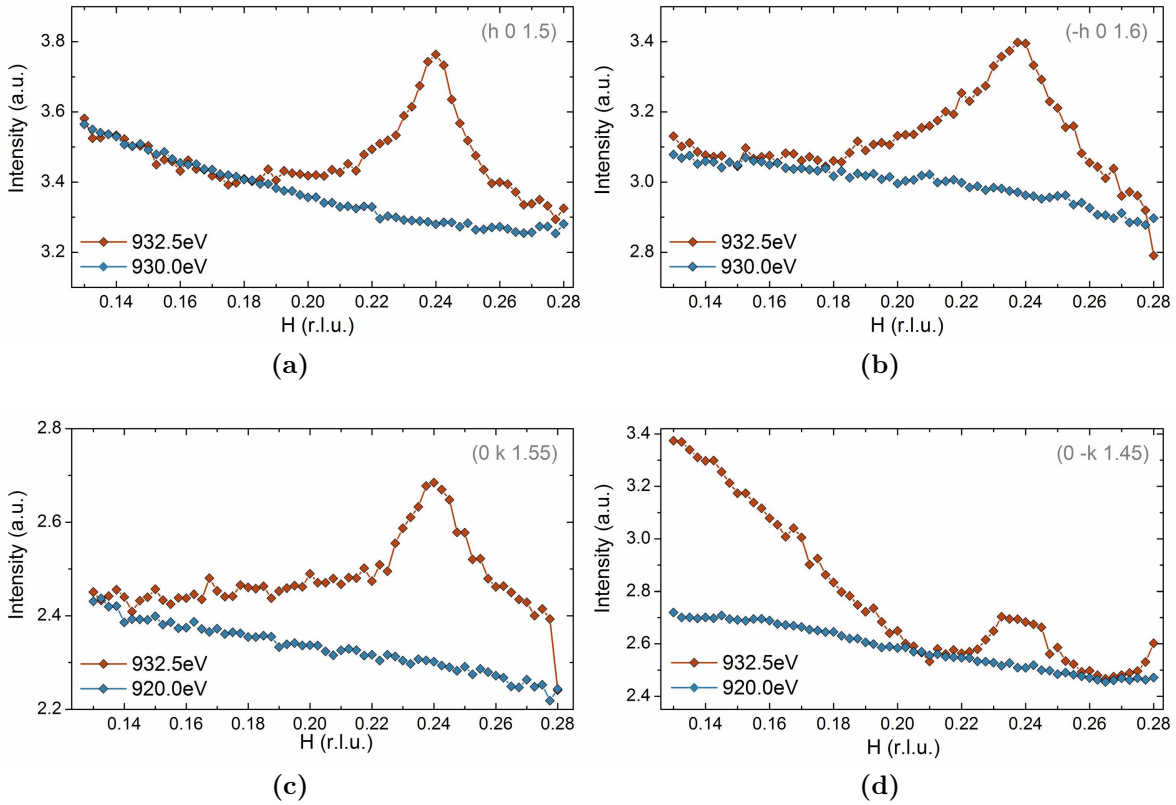

Fig. 3.12.: All four accessible charge stripe order reflexes of a cleaved *c*-oriented sample, recorded for different sample azimuthal angles. Red curves are taken at the Cu-L_3 resonance maximum and blue curves are recorded off-resonance. The blue curves are shifted by a constant offset to match the red curves. The comparable low profile in (d) might be caused by misalignment or sample geometry, although all possible adjustments were made to optimize the peak intensity.

direction, is crucial for the accessibility of the peak positions. To scan all four reflexes the sample was azimuthally rotated around the **c** direction, alternatively rotating **a** or **b** in the scattering plane. Scans in the reciprocal h and k direction around $h, k{=}\pm 0.24$ have been performed at the Cu-L_3 resonance energy for different l values. All four reflexes could be found being best visible for l values around 1.5 (Fig. 3.12). To verify that the observed reflexes are no artifacts, the same scans were repeated off the Cu-L_3 resonance maximum, clearly showing that the peak vanishes. Our finding demonstrates that the stripes are running into **a** as well as into **b** direction, while we cannot differentiate between a scenario with crossed stripes in adjacent layers and one with regions of different stripe orientations. A detailed analysis of the results obtained from the *c*-oriented sample will follow in the section dealing with the influence of the sample surface preparation.

Energy dependence

To explore the origin of the reflex which was found in LSCO, its energy and temperature dependence was investigated and compared to the LNSCO reference sample. Energy-dependent h-scans of the (0.24 0 0) reflection in a-oriented LSCO and LNSCO were performed at the Cu-$L_{2,3}$ and O-K edge at a temperature of 18 K (Fig. 3.5). This is the lowest temperature that could be reached with the used setup. LNSCO data were taken with an exit slit of 40 µm, which gave an energy resolution of 90 meV at the O-K and 210/220 meV at the Cu-$L_{2,3}$ edge, whereas a 100 µm slit was used for the LSCO data resulting in a resolution of 240 meV at the O-K and 570/590 meV at the Cu-$L_{2,3}$ edge. The reason for the larger slit is the overall lower intensity of the reflex in LSCO compared to LNSCO.

Fig. 3.13 shows a comparison of the resonance spectra. The peak intensity was deter-

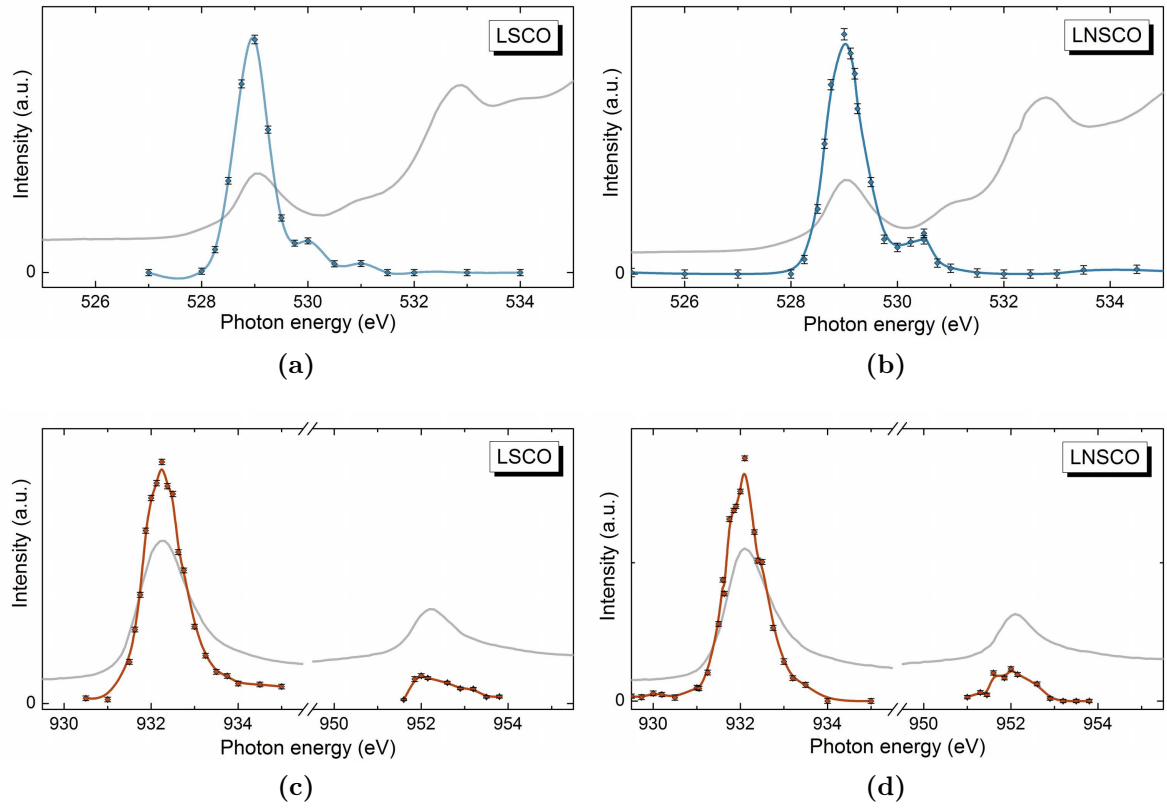

Fig. 3.13.: Energy dependence of the integrated charge stripe reflex intensity in LSCO (a+c) and LNSCO (b+d). At both the O-K (a-b) and Cu-$L_{2,3}$ (c-d) x-ray absorption edges a similar behavior of the integrated RSXD diffraction signal is observed. As an energy reference XAS data are diplayed (light grey). Solid lines represent guides to the eye. All data are taken at a temperature of 18K.

mined by fitting a Lorentzian peak profile. In light grey the corresponding fluorescence yield absorption signals are plotted as an energy reference. We find a remarkable sim-

ilarity between the data in LSCO and those from LNSCO, for which the existence of static charge stripe order is well established.

At the O-K edge both reflexes have a strong resonance around 529 eV, which can be assigned to the transition into the doped hole levels in the O $2p$ conduction band. Besides

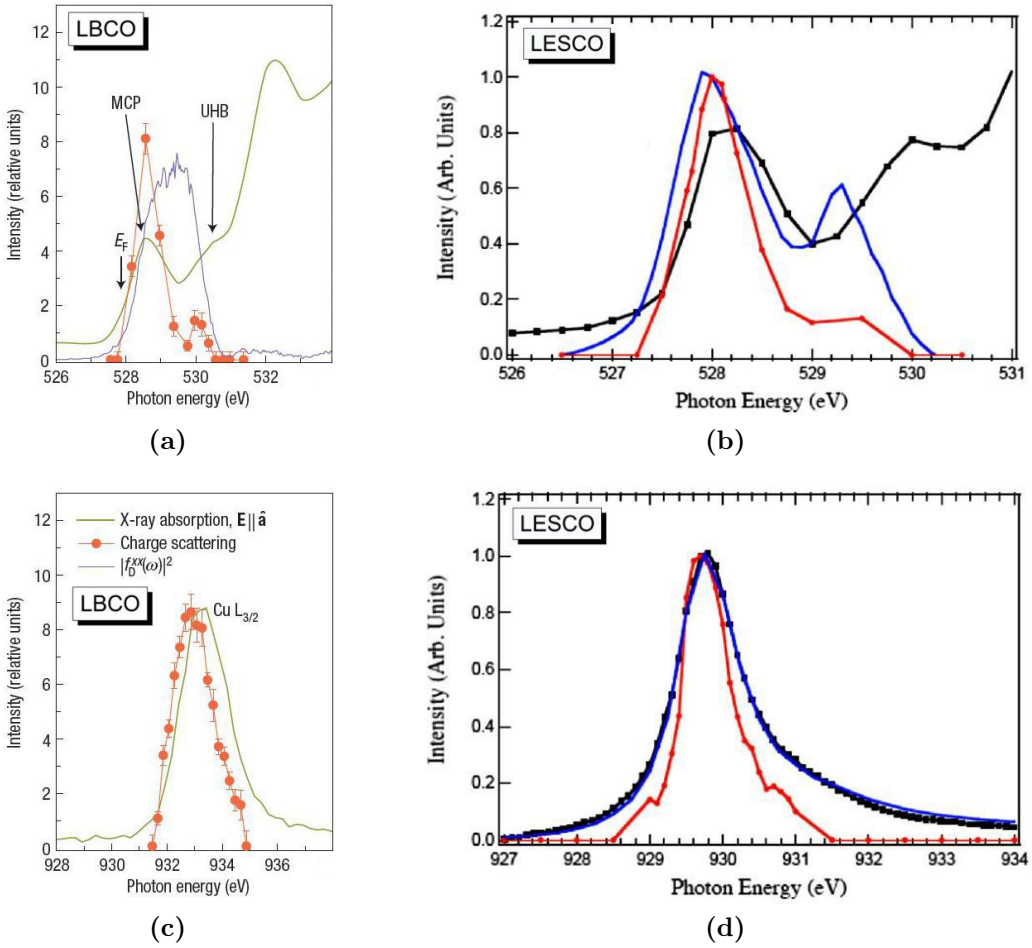

Fig. 3.14.: Energy dependence of the charge stripe reflex intensity in LBCO (a,c) and LESCO (b,d) at the O-K and Cu-L_2 edge. The energy dependence at both edges is very similar to our findings in LSCO and LNSCO. For comparison to the data obtained in LSCO and LNSCO during the experiment see Fig. 3.13. The integrated charge stripe peak intensity is displayed in orange (red) for LBCO (LESCO) and the absorption signal in green (black).
Reprinted Fig. (a) and (c) with permission from Macmillan Publishers Ltd: P. Abbamonte et al., Nature Physics **1**(3), 155-158 (2005) [24], copyright 2009: `http://www.nature.com/nphys/journal/v1/n3/abs/nphys178.html`.
Reprinted Fig. (b) and (d) with permission from J. Fink et al., Phys. Rev. B **79**, 100502 (2009) [96]. Copyright (2009) by the American Physical Society: `http://link.aps.org/abstract/PRB/v79/p100502`.

the strong resonance at 529 eV there is also a smaller contribution at the high energy side, which coincides with the so-called upper Hubbard band peak of the absorption

signal at around 531 eV. Here a transition into the neighboring Cu $3d$ level hybridized with the O $2p$ states takes place. There is no contribution coming from transitions lying above 531 eV.

At the copper edge there is a contribution at both the L_2 and the L_3 edge, while the resonances of the scattered signal match the resonances of the absorption signal. The high energy asymmetry of both the RSXD signal and the XAS signal is usually ascribed to transitions into Cu $3d^9$ ligand-hole states.

Our finding is very similar to the results obtained in literature. In Fig. 3.14 the energy-dependent scattering intensity of the charge stripe reflex in LBCO and LESCO is shown. The LBCO data is taken from reference [24], the LESCO data from [96]. From the comparison of the spectra from LSCO to those from our reference sample LNSCO and to the results from literature we can conclude that all studied reflections have a common electronic origin.

The widths of the reflexes in LSCO and LNSCO at the O-K and Cu-$L_{2,3}$ edges provide information about the in-plane correlation length l_a in the a direction. The correlation length l_a is equal to the inverse half width at half maximum (HWHM). An overview about all the extracted correlation lengths can be found in Tab. 3.1. From the results it

		HWHM (r.l.u)	l_a (Å)
LSCO	Cu-L_3	0.0173 ± 0.0001	35.0 ± 0.3
LNSCO	Cu-L_3	0.0086 ± 0.0001	70.7 ± 0.4
LSCO	Cu-L_2	0.0139 ± 0.0005	43.5 ± 1.7
LNSCO	Cu-L_2	0.0097 ± 0.0005	62.7 ± 2.9
LSCO	O-K	0.0114 ± 0.0002	53.3 ± 0.9
LNSCO	O-K	0.0072 ± 0.0001	84.0 ± 1.2

Tab. 3.1.: Overview of the different experimentally obtained correlation lengths, calculated from the half widths at half maximum of the Lorentzian peak fits at the three different absorption edges and in the two different samples LSCO and LNSCO.

is clearly visible that the correlation length in LSCO is much smaller than in LNSCO. The correlation length that we have found in LNSCO is of the same order as found by other groups [62]. Herein the correlation length of the charge order in LBCO is reported to be approximately twice as large as in LNSCO.

Temperature dependence

We have further analyzed the temperature dependence of the (0.24 0 0) reflection. At different temperatures, h-scans were taken for both LSCO and LNSCO at the Cu-L_3 edge. The integrated intensity was determined by Lorentzian peak fitting. The resultant temperature dependence of the Cu-L_3 integrated intensity of the (0.24 0 0) reflex can be seen in Fig. 3.15. As guides to the eye a Boltzmann function was fitted to the intensities. The integrated intensity shows a gradual decay with temperature for both samples. In LSCO it vanishes between 80 and 120 K, which is much higher than the

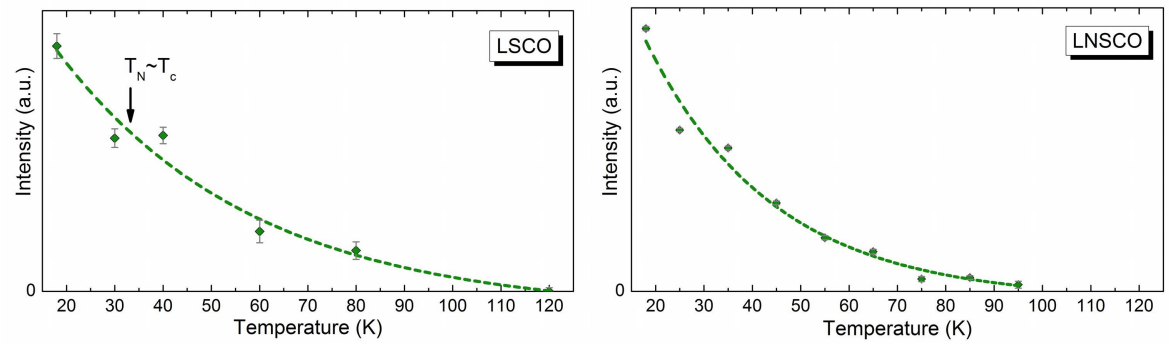

(a) **(b)**

Fig. 3.15.: Temperature dependence of the area of the Lorentzian fits to the background subtracted charge stripe peak for both LSCO (a) and LNSCO (b) at the Cu-L_3. Dashed lines are Boltzmann fits to the data and act as guides to the eye.

magnetic ordering temperature. From literature it is known that the magnetic ordering temperature coincides with T_c (Fig. 3.8). To determine T_c for our sample, susceptibility measurements were carried out by Susanne Heijligen using a small piece of the same crystal from which our samples have been cut from. A field of 50 Oe was used after zero-field cooling. The susceptibility curve is shown in Fig. 3.16 and is compared to the results from Ref. [109] taken in an equally doped LSCO sample. The results for

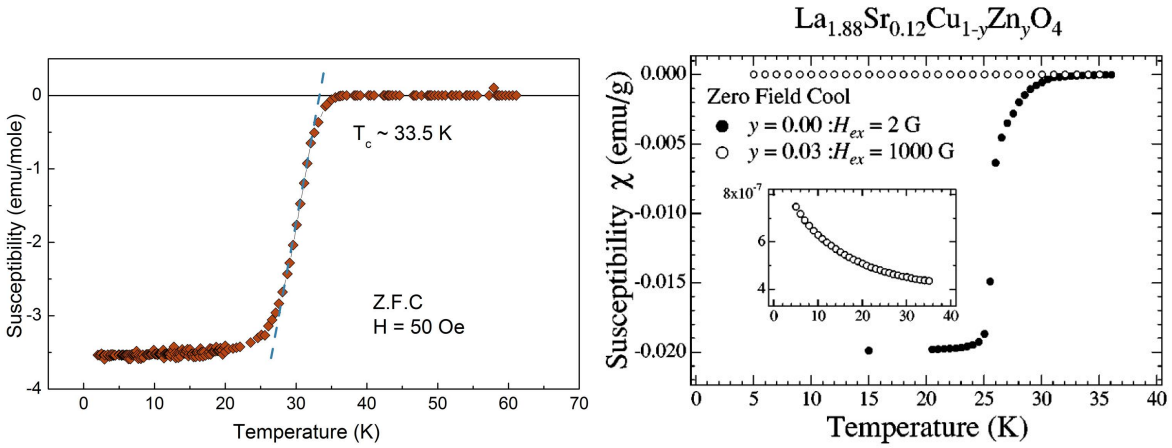

(a) **(b)**

Fig. 3.16.: Susceptibility in LSCO. Fig. (a) was experimentally recorded from the same crystal that was used for the x-ray diffraction experiments. In (b) results from literature are compared to our findings.
Reprinted Fig. (b) with permission from H. Kimura et al., Phys. Rev. B **59**, 6517-6523 (1999) [109]. Copyright (1999) by the American Physical Society: `http://link.aps.org/abstract/PRB/v59/p6517`.

T_c are very close to each other, thus, we can safely assume that the magnetic reflex in our sample, which was not accessible in the experiment, vanishes at a temperature at which the (0.24 0 0) reflex is still visible. This is exactly what is expected for stripe order in layered cuprates [113] and clearly allows us to assign the (0.24 0 0) reflection in 12-percent doped $La_{2-x}Sr_xCuO_4$ to charge stripe order.

3.4.2. Bulk versus surface

An extensive search for charge stripe reflections in LSCO was performed by Alexander Komarek and Martin von Zimmermann within hard x-ray diffraction experiments. The used sample was cut from the same piece as the samples studied with soft x-rays. Several nominal positions where charge stripe order was found in similar compounds were scanned without any positive result. One examplary scan across the expected peak position at (1.75 0 0) is shown in Fig. 3.17. From the red dotted line the detection limit

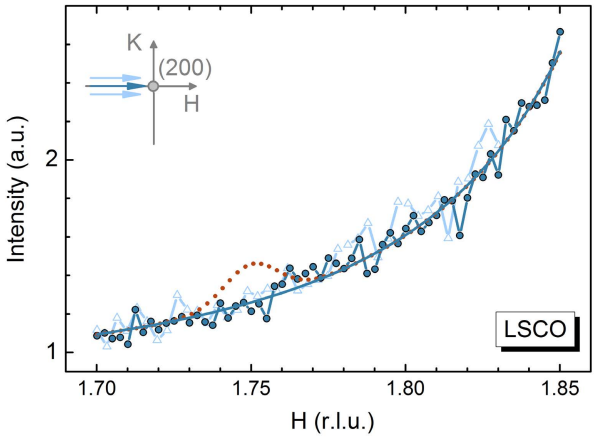

Fig. 3.17.: Scan through a nominal charge stripe order peak position in LSCO within the high-energy x-ray experiment at DORIS. The dark blue data points were recorded for k=0, while the light blue data points are obtained for a scan slightly off in k. The dark blue solid line is a Lorentzian fit to the experimental data. The red dotted line represents an estimate of the smallest reflection that would have been detected within the experiment (detection limit). The graphic is taken from [112] with permission of the author and has been slightly modified.

was estimated to be at least 10^{-8} of a strong Bragg peak. For this estimation the (1 0 3) Bragg peak was chosen. Details can be found in [112]. From the combined data taken by soft and hard x-rays and the different probing depths within the respective experiments, we conclude that charge stripe order can be found in the near-surface area only. As mentioned in the beginning, the sample probing depths is of the order of mm for hard x-rays and thus really bulk sensitive, while soft x-rays probe a surface layer of around 10 nm thickness only. As the correlation lengths perpendicular to the surface, listed in Tab. 3.1, are smaller than the probing depths, the lower limit for the thickness of the charge stripe-ordered layer is determined by the former. We conclude that in LSCO

either the topmost four to six nanometers or a thicker layer with regions of the same size are charge ordered.

3.4.3. Influence of the surface preparation

To study whether the charge stripes near the surface have been induced by the surface preparation method, we have compared the ex-situ polished surface with that from an in-situ cleaved sample of LSCO. A similar experimental procedure as for the polished samples was performed, in which the existence of charge stripe order also in a freshly cleaved sample was successfully confirmed.

To get an idea of the signal quality, scans through the reciprocal h direction at a resonance energy of 932.0 eV and off resonance at 934.0 eV are compared with each other in Fig. 3.18 (a) for l=1.6. Although the peak to background ratio is small, the

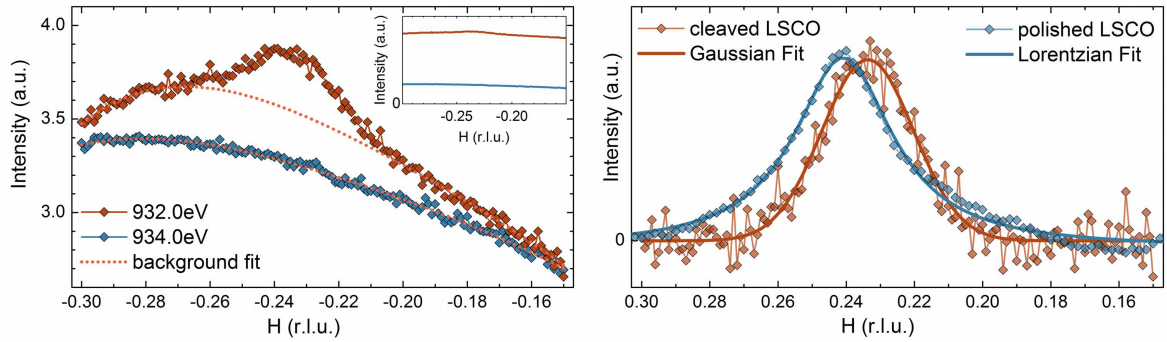

Fig. 3.18.: (a) h-scans of a cleaved LSCO sample taken at (red symbols) and off (blue symbols) the Cu-L_3 resonance maximum. The datasets are shifted towards each other for a better representation. The fit to the background is shown by the dotted red lines. The inset shows the experimentally obtained data without shift on the entire background. (b) Gaussian fit to the background corrected data from the cleaved (red) and Lorentzian fit from the polished (blue) sample. Both curves are scaled to their maxima.

charge order reflex is clearly visible. The background of the data was treated as discussed before. The result of the background subtraction, including the Gaussian peak fit to the data, is displayed in Fig. 3.18 (b). The full width at half maximum of the Gaussian fit function is very similar to the results obtained from the polished sample, although the probing geometry was very different: 0.032 r.l.u. for the cleaved sample in comparison to 0.035 r.l.u. for the polished one. The in-plane correlation length along a is therefore 38 Å. In Fig. 3.18 (b) a comparison of the peak fit results for the polished and cleaved sample at the Cu-L_3 edge is shown. The peak positions are shifted against each other, which might be due to a misorientation of the azimuthal sample angle or due to a slightly different amount of strontium doping. Note that the charge order reflex of the cleaved sample can be nicely described by a Gaussian profile, whereas for the polished sample the

Lorentzian profile was more suitable. We attribute the different profiles to the different probing geometries. While in the polished sample radial h-scans were performed, h-scans with a large transversal component were performed in the case of the cleaved samples. In the former the scattered intensity is much stronger affected by extinction effects due to absorption than in the latter.

The overall lower signal of the cleaved sample could be attributed to the different l values or the local orientation of the surface, which showed different facets after the cleave, building up valleys and bumps.

The energy dependencies of the charge stripe order intensity for the cleaved and for the polished sample around the Cu-L_3 resonance are plotted in Fig. 3.19 (a). Besides a

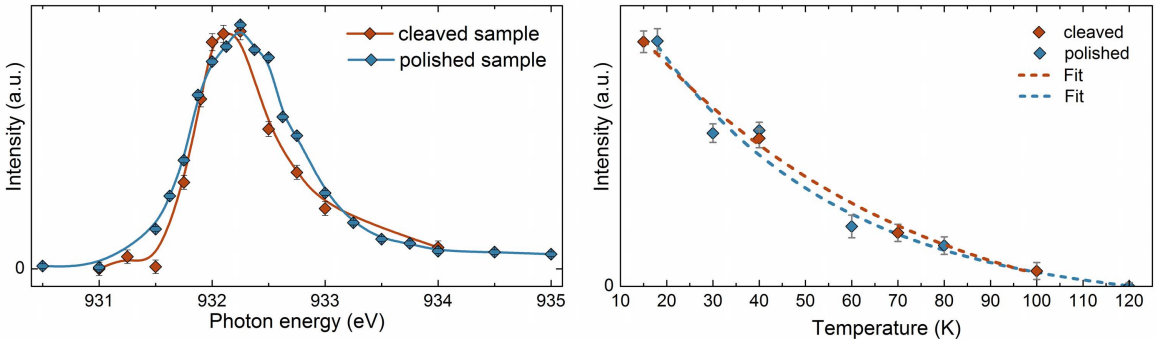

Fig. 3.19.: (a) Comparison of the energy dependence of the integrated charge stripe reflex intensity in a cleaved LSCO (red) and a polished LSCO sample (blue). The red and blue lines are guides to the eye. Data are taken at 18 and 15 K for the polished and cleaved sample, respectively. (b) Comparison of the temperature dependence of the integrated charge stripe reflex intensity in a cleaved LSCO (red) and a polished LSCO sample (blue). The dotted red and blue line are fits of a Boltzmann function to the data.

small energy shift, which might be due to beamline settings, the energy dependence is very similar and confirms the identical electronic origin of both signals.

The temperature-dependent data, displayed in Fig. 3.19 (b) shows a decay of the integrated intensity for the cleaved sample that nicely matches the temperature-dependent decay in the polished sample.

From the comparison of the results obtained for the cleaved and polished samples we conclude that the surface preparation method does not affect the stabilization of the stripe phase near the surface in LSCO. We take the data as a proof for the proximity of LSCO to charge stripes, which stabilize in the near-surface region and are independent on the surface treatment.

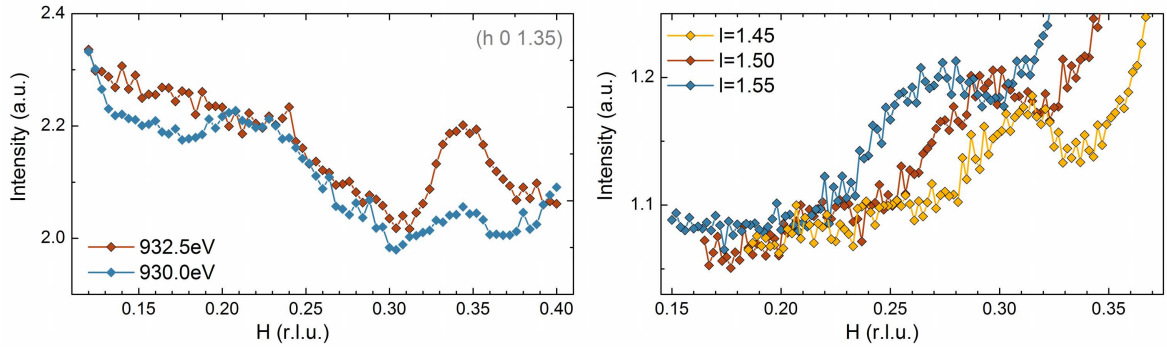

Fig. 3.20.: (a) Data taken on (red) and off (blue) the Cu-L_3 resonance maximum in 15-percent doped LSCO. The blue curve is scaled to match the red one. (b) h dependence of the reflex for different l values. The reflex shifts in reciprocal space and shows the bahavior expected from a powder ring.

3.4.4. Different doping levels

In order to check if similar stripe order peaks occur for higher doping levels, investigations were done on 22-percent and 15-percent doped samples. In the 22-percent doped sample we clearly did not find any indications for a charge stripe reflex, however, we found a peak in the 15-percent doped and c-oriented sample, which was cleaved in-situ. As it is visible from Fig. 3.20 (a) the peak resonates at the Cu-L_3 edge, similar to the charge stripe reflex in the 12-percent doped sample, but the h position of the reflex shifts with varying l (Fig. 3.20 (b)). This resembles what is found for a powder ring. While the origin of the signal in the 15-percent doped sample remains unclear, it certainly has a different origin as the charge stripe peak found in 12-percent doped LSCO.

3.4.5. Radiation induced low-q peak

In some of the h-scans, from both the polished and the cleaved LSCO samples, we observed additional intensity on the low-q side of the main peak. This intensity grew with time and seems related to the exposure to x-ray radiation. Fig. 3.21 shows the temporal evolution of the low-q peak at h=0.22 as recorded during an energy-dependent data set at the Cu-L_3 edge. The blue curve of Fig. 3.21 was recorded at a time ($t = 0$) within the data set. The same scan was repeated 3 hours (red curve) and 4.5 hours (yellow curve) later. The three curves can be described by fitting of two Lorentzian peak functions, from which one is placed at h=0.24 and one between h=0.21 and 0.22. It is clearly visible that the intensity of the low-q peak increases and shifts to lower h values with time. During the scans that are shown here and even hours before the blue scan was taken, the sample was constantly exposed to x-rays with an energy around the Cu-L_3 resonance.

As visible from the red curve, in some even rare cases an additional high-q peak became

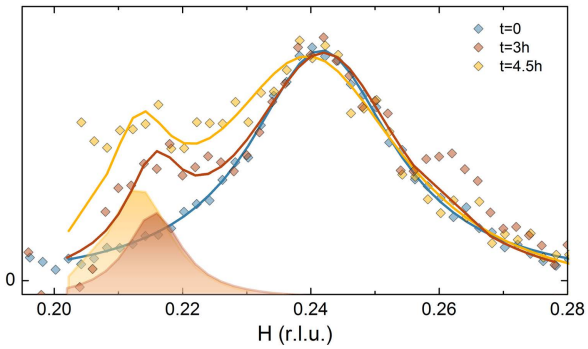

Fig. 3.21.: Temporal evolution of the low-q component observed during an energy series at the Cu-L_3 edge. Data taken from an a-oriented LSCO sample are background substracted. The point in time when the blue data was taken is defined as 0. The red and yellow data sets are recorded 3 and 4.5 hours later, respectively. Tee colored symbols denote experimentally obtained data point and solid lines are fits of two Lorentzian peak functions, one around h=0.24 and one between h=0.21 and 0.22.

visible as well. Both additional features may arise from changing the local stoichiometry of the sample, for example the amount of oxygen excess or deficiency. This would change the hole-doping level and cause a shift of the charge stripe peak to higher or lower h values.

In a temperature-dependent data set of an a-oriented LSCO sample at the O-K resonance maximum we found that the low-q peak survives up to higher temperatures, excluding a similar origin as the one of the main peak. The temperature-dependent

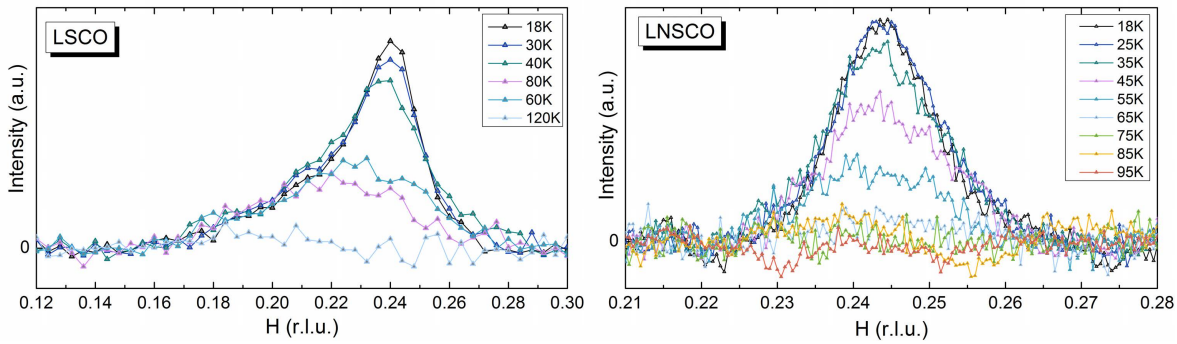

Fig. 3.22.: Temperature-dependent h-scans through the (0.24 0 0) charge stripe peak of LSCO on the left and LNSCO on the right taken at the O-K edge. Note that the x-axis range in (a) and (b) is different.

data sets of the a-oriented LSCO and LNSCO samples taken at the O-K edge are shown in Fig. 3.22. As clearly visible, the reflex in LSCO is asymmetric in h, whereas the peak in LNSCO is almost symmetric. A more detailed analysis of the data obtained

from LSCO showed that the whole temperature-dependent data set can be accurately described by the sum of two Gaussian peak functions at h=0.24 and h=0.22. In the case of LNSCO a single Gaussian was sufficient. A fit to the LSCO data and the evolution of the two components with temperature can be seen in Fig. 3.23. The component at

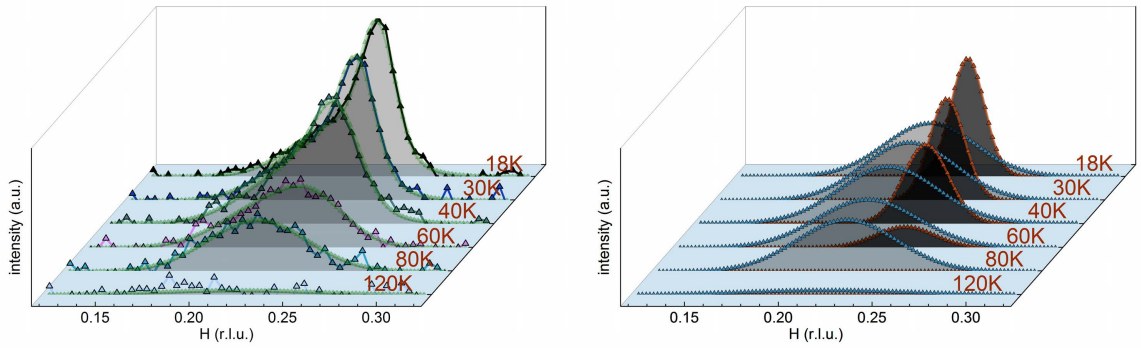

Fig. 3.23.: Double peak analysis of the O-K edge temperature dependence of the charge stripe order reflex in LSCO. (a) The raw data are shown as symbols and the cumulation of the two Gaussian peak functions as grey area below the experimental data. (b) Temperature dependence of the two different components at h=0.24 and h=0.22, obtained by fitting a double Gaussian to the raw data.

higher h values, which is the main charge stripe reflex, vanishes between 60 and 80 K, while the h=0.22 component stays more or less unchanged upon this temperature and is almost suppressed completely at 120 K. The temperature dependencies of both peaks in LSCO are compared to the temperature dependence obtained at the Cu-L_3 edge in Fig. 3.24 (a) and to the decay of the charge stripe intensity in LNSCO at both energy resonances in Fig. 3.24 (b). The data from the Cu-L_3 edge are the same as displayed in Fig. 3.15.

At the O-K edge the decay of the charge stripe intensity at h=0.24 in LSCO is similar to the decay of the charge stripe intensity in LNSCO at the O-K edge (red symbols). The low-q intensity in LSCO (blue symbols) remains at least more or less unchanged upon 100 K and vanishes around 120 K. For comparison the temperature dependencies of the charge stripe reflex intensities in LSCO and LNSCO, obtained at the Cu-L_3 edge (green symbols) are plotted as well inside each of the respective figures. A Boltzmann function was fitted to the integrated intensities. Interestingly, the decay at the O-K edge does not set in before 40 K, while at the Cu-L_3 edge the intensity decreases already below 40 K. Comparing the results from the two energy resonances yields that the charge ordering seems to melt for lower temperatures at the O-K edge than at the Cu-L_3 edge. Whether the decay is really different at both edges is hard to state because the number of data points is not really sufficient for such a conclusion. This can be shown by different scaling of the decay at the O-K with respect to the decay at the Cu-L_3 resonance. If scaled in such a way that they more or less match each other for low temperatures (dark red curves), the two curves from both resonances cross at temperatures between

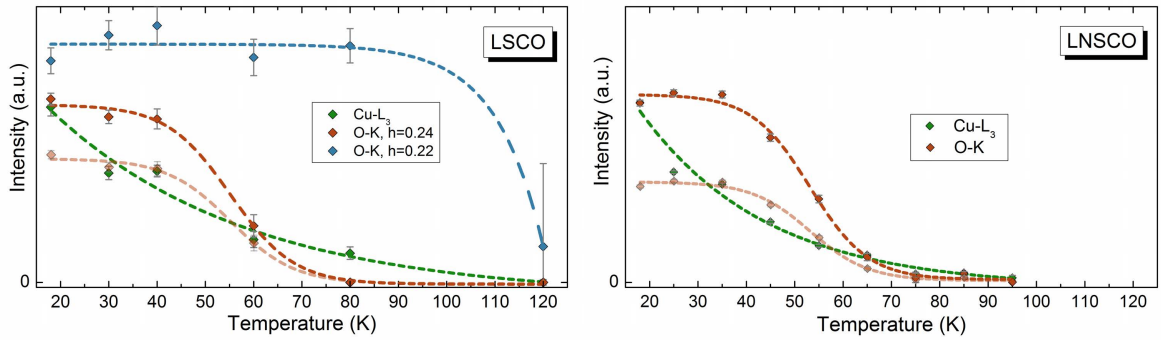

(a) (b)

Fig. 3.24.: Temperature dependence of the charge stripe peak intensity at the O-K edge (red symbols) and Cu-L_3 edge (green symbols) for LSCO (a) and LNSCO (b). The temperature dependence of the low-q peak intensity in LSCO is displayed as blue symbols and related to the exposure to x-ray radiation. Dashed lines are fitting results of a Boltzmann function to the data and used as guides to the eye. The temperature-dependent charge stripe intensities at the O-K edge are scaled such that they match each other at the lowest temperature (dark red symbols and curves) and such that they match the Cu-L_3 data points at intermediate temperatures (light red symbols and curves).

60 and 70 K. On the other hand, the curves can be scaled such that they perfectly match for intermediate temperatures between 30 and 60 K (light red curves). In any case the intensity of the charge stripe reflex seems to decay faster at the O-K than at the Cu-L_3 edge, especially in LSCO.

3.5. Discussion

The most important result is that we clearly found a charge stripe order reflex in 12-percent doped LSCO within the RSXD experiment. Indications for charge stripe ordering are given by the strong similarity to data obtained from an equally doped LNSCO sample. The charge stripe reflexes are located at the same positions in reciprocal space in LSCO as in LNSCO, which are the expected positions for charge stripe ordering.

The electronic origin of the charge stripe modulation in LSCO has been studied by analyzing its energy and temperature dependence, which is very similar to the results from LNSCO and to the results in LBCO and LESCO, as reported in literature [24, 96].

We exclude an influence of the surface preparation method by comparing polished and cleaved samples, all of which showed charge stripe modulation reflexes. However, in all cases the intensity of the reflex was very low and inhomogeneous across the sample surface.

The peak profile was either of Gaussian or Lorentzian shape. In the a-oriented sample, where radial h-scans were performed, the profile was of Lorentzian shape at the Cu-L_3 and of Gaussian shape at the O-K edge. This indicates that at the Cu-L_3 edge, where the

x-ray penetration depths is much smaller than at the O-K edge, the exponential decay of the x-ray intensity due to absorption effects is visible in the scattered signal. Thus the probed volume at the Cu resonance is smaller than at the O resonance. This may also explain the smaller out-of-plane correlation length and the smoother temperature decay obtained at the Cu-L_3 edge if compared to the results at the O-K edge. In the c-oriented sample the peak profile can always be described by a Gaussian profile, indicating that within the performed h-scans no limitation due to the penetration depths takes place. Interestingly, the in-plane correlation length at the Cu-L_3 edge obtained in the a-oriented and c-oriented samples is similar.

Due to the different results from the low and high energy x-ray diffraction experiments, where the former is rather surface and the latter bulk sensitive, we conclude that the formation of stripes takes place in the topmost 4 to 5 nm. The reduced dimensionality at the surface may have a huge impact on the local tilting of the oxygen octahedra. It might be possible that this leads to a LTT-like structure in the near-surface region.

In both LSCO and LNSCO the charge stripe ordering temperature is much higher than the spin stripe ordering temperature, decoupling the charge and spin degree from each other. In comparison to the results found in literature for LBCO and LESCO [24, 96], where in LBCO T_{str}=T_{CO}>T_{SO} and in LESCO T_{str}>T_{CO}>T_{SO}, there seems to be no obvious relation between charge, spin and lattice degrees of freedom and superconductivity.

As reported in reference [109], tetragonality is not crucial for the formation of spin stripe order. Whether this is also the case for charge stripe order cannot be stated from our results, since a structural analysis of the surface layers is missing.

Furthermore we found some additional intensity, which we could ascribe to radiation damages. The temperature dependence looks different from the results of the charge stripe reflex. Exclusion of this additional components yields the same results in LSCO as in LNSCO. Although most of the data did not show this kind of radiation damage, special care was taken that this additional peak was excluded in the analysis.

CHAPTER 4

Complex Coefficient Orbital Order in Fe_3O_4

The results presented in this chapter have been published partly in:

A. Tanaka, C. F. Chang, M. Buchholz, C. Trabant, E. Schierle, J. Schlappa, D. Schmitz, H. Ott, P. Metcalf, L. H. Tjeng & C. Schüßler-Langeheine: Symmetry of Orbital Order in Fe_3O_4 Studied by Fe $L_{2,3}$ Resonant X-Ray Diffraction, Phys. Rev. Lett **108**, 227203 (2012).

4.1. Introduction

Magnetite has attracted much attention of mankind since almost three millennia. It appears for example in Chinese, Greek, and Mayan historic literature or has been found in archaeological excavations. While in China it was previously used as a fortune teller, the fascinating property of this so called lodestone to align in the magnetic earth field was made use of in the spoon-shaped lodestones around 400–200 B.C.

Beginning with Thales, magnetite and magnetism have often been topic in many of the great Greek philosophers' works, for example by Aristoteles or Pliny the Elder. Reading through the chapters of Natural History (published 77–79 A.D. by Pliny) gives a feeling of the genius work done at this time, which has been a fundament for modern scientific achievements [114].

From that time on, magnetite was used as a tool for geographical orientation. Although it was not the first material that was used for navigation (another example is the sun stone, a silicate mineral, used by the Vikings, which changes color with respect to the direction of the sun or more correctly the direction of the photon polarization), it was the first one, which permitted to navigate in the absence of day- or starlight.

A deeper understanding of magnetite followed in the 19th century by the extensive work of many scientists, for example by Oerstedt, who discovered the influence of electric currents on a compass needle, as well as by Faraday, Gauss, and Ampère, who further

contributed to the understanding of the relationship between magnetism and electricity, which some years later was put into a more mathematical formalism by Maxwell.

Since the 20th century, magnetite plays an important role in modern electronics, as it is contained in transistors, inductors, radio antenna, or magnetic data storages. Due to its ferrimagnetic and half metallic properties Fe_3O_4 has become a hot topic for spin-polarized applications and still remains to be a multifunctional material.

Magnetite's importance in modern condensed-matter physics comes from the Verwey transition, named after the Dutch physicist E. J. W. Verwey; however, the first detection of this transition was reported in 1925 by Parks and Kelley, who found an anomaly in the specific heat between 113 and 117 K [115]. Further attention was attracted after Verwey's discovery of a large decrease of the electrical conductivity by two orders of magnitude during cooling through the so-called Verwey temperature T_V around 120 K [116, 117].

At high-temperatures, Fe_3O_4 crystallizes in the inverse spinel-type crystal structure AB_2O_4 with the cubic $Fd\bar{3}m$ space structure ($a, b, c = 8.3967$ Å) [118]. The term spinel originates in the mineral spinel ($MgAl_2O_4$). Oxygen ions are arranged in a face-centered cubic (*fcc*) lattice with a lattice period of 4.2 Å (half of the lattice constant). There are two kinds of interstices between the oxygens, so-called *A*-sites and *B*-sites. The first one is coordinated by 4 nearest neighboring oxygen ions, building a tetrahedron, while in the latter case 6 neighboring oxygen ions form an octahedron. *A*-sites and *B*-sites are thus also called tetrahedral and octahedral sites, respectively [119]. In an arrangement of 32 oxygen ions there are in total 64 possible tetrahedral and 32 possible octahedral sites, covering the complete space (Fig. 4.1 (a)).

In the high-temperature unit cell of Fe_3O_4 comprised of 8 formula units (24 iron and 32 oxygen atoms) 8 tetrahedral *A*-sites are occupied by trivalent iron ions, while there is an 1:1 intermixing of di- and trivalent iron ions at the 16 octahedral *B*-sites, resulting in the notation $Fe^{3+}[Fe^{2+},Fe^{3+}]O_4$ (Fig. 4.1 (b)). This site preference of the Fe^{3+} ions can be explained by the smaller ionic radius of 0.67 Å (in comparison to 0.83 Å for Fe^{2+}), favoring the smaller tetrahedral lattice sites [119].

The strongest exchange coupling is between the *A*-sites and *B*-sites, resulting in an antiferromagnetic ordering of *A*-site and *B*-site moments below T_N=860 K and an parallel coupling of the two different *B*-site moments [118]. The moments of Fe^{3+} ($[\mathbf{Ar}]3d^5$, S=5/2) on the different sites completely compensate, while the Fe^{2+} ($[\mathbf{Ar}]3d^6$, S=2) provide a theoretical magnetic moment of $4\,\mu_B$ per formula unit, which was experimentally confirmed ($4.07\,\mu_B$) [120].

During cooling through the Verwey transition, magnetite undergoes a first-order structural phase transition from a cubic into a monoclinic distorted structure [121, 122]. The monoclinic low-temperature (LT) phase is characterized by $(001)_c$ and $(00\frac{1}{2})_c$ superstructure reflections, where the subscript c refers to the high-temperature cubic unit cell. From neutron diffraction experiments a supercell with monoclinic *Cc* symmetry containing 32 formula units was determined by Izumi et al. [123]; however, due to twinning of different *Cc* domains a first refinement of the atomic positions was only possible using a pseudo-orthorhombic *Pmca* symmetry [123]. The authors report that no reliable indications for charge ordering were found. In recent refinements by Wright et al. using a $P2/c$ symmetry with orthorhombic *Pmca* constraints different displacements than in

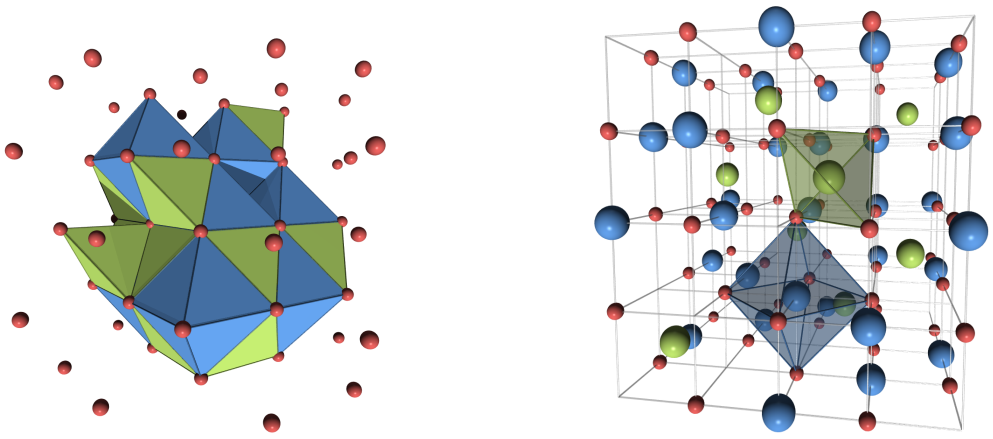

(a) **(b)**

Fig. 4.1.: (a) Tetrahedral (green) and ocatahedral (blue) interstices are filling the space between the oxygen *fcc* lattice (red) of the Fe_3O_4 unit cell. For better visualization only specific polyhedra are shown. (b) *A*-site iron (green) and *B*-site iron (blue) are surrounded by tetrahedral and octahedral oxygen (red) coordination, respectively, which are depicted for one specific site by the transparent green and blue polyhedron. In total there are 8 tetrahedral *A*-sites and 16 octahedral *B*-sites per unit cell.

Ref. [123] were found [124, 125]. Bond valence sum (BVS) analysis gives evidence for charge order of two different *B*-site ion groups with approximately 2.4+ and 2.6+ valence. I will refer to this refinement as the Wright2001-structure. Only in this year, a refinement using the monoclinic *Cc* symmetry was published suggesting a complex electronic structure, where the minority t_{2g} electrons of each Fe^{2+} ion are delocalized over two neighboring Fe^{3+} *B*-sites building a so-called trimeron [126, 127]. *B*-site Fe^{3+} ions participate in up to three of these trimerons, where the exact number corresponds to the number of occupied t_{2g} orbitals. I will refer to this structure as Senn2012-structure.

Orbital ordering models were proposed already before the latest refinement by means of density functional theory (DFT) using the refined Wright2001-structure as input [128–131]; however, the proposed real-coefficient orbital order is not the only possible model. Instead, an orbital order using complex-coefficient linear combinations of orbitals was proposed in Ref. [132]. The idea of complex-coefficient orbital order had already been discussed for the case of manganites [133]. In their complex-coefficient orbital order model in magnetite Uzu and Tanaka found a spontaneously formed orbital moment of $0.6\,\mu_B$ per *B*-site. Because of non-collinear order of these moments a net orbital moment of $0.2\,\mu_B$ per *B*-site results.

The experimentally obtained orbital moments per *B*-site are contradictory. Huang et al. found a large moment of $0.33\,\mu_B$ [134], Göring et al. found a vanishing orbital moment [135], recently attributed to be hidden by antiparallel alignment of large moments at the *A*-sites and *B* sites [120]. More recent x-ray magnetic circular dichroism (XMCD) and

resonant inelastic x-ray scattering (RIXS) measurements by Cezar et al. found an orbital moment of $0.22\mu_B$, which is in good agreement with the theoretical predictions from the complex-coefficient orbital order model [136], but which could also be explained by a mixing of real space orbitals driven by spin-orbit coupling.

4.1.1. RSXD pre-work

In resonant x-ray diffraction (RXD) studies of magnetite performed at the Fe-K edge [137] the absence of half integer superstructure reflections was interpreted as lack of ionic charge order. The authors determine the upper limit for any charge disproportion to a tenth of an electron's charge, challenging the Wright2001 analysis. RSXD experiments at the O-K edge were interpreted in terms of charge orbital ordering at the oxygen sites [138]. Further confirmation that the Verwey transition is caused by electronic ordering was given by a RSXD experiment at the Fe-$L_{2,3}$ edge [139]. Direct evidence for

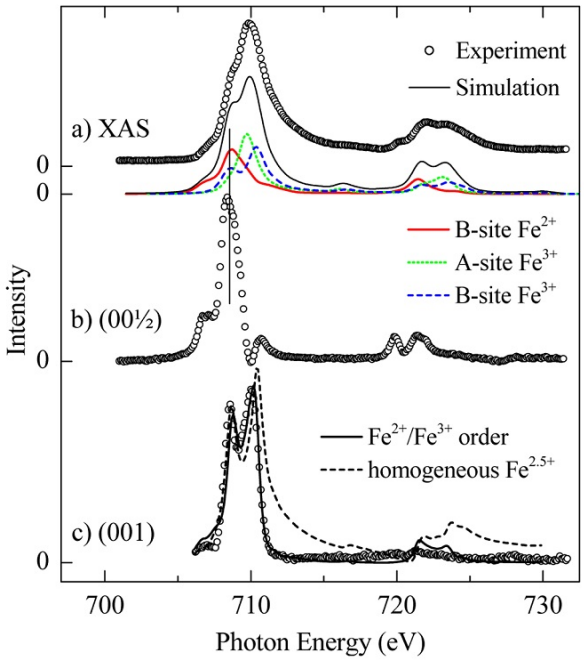

Fig. 4.2.: Energy dependence of the $(001)_c$ and $(00\frac{1}{2})_c$ diffraction peaks compared to the x-ray absorption signal. (a) Experimental XAS spectrum of Fe_3O_4 at the Fe-$L_{2,3}$ absorption edge (black circles). The simulation of the absorption spectrum is the sum of contributions (green, blue and red lines) arising from the Fe^{3+} A-sites, Fe^{3+} B-sites and Fe^{2+} B-sites, respectively. (b) Energy dependence of the $(00\frac{1}{2})_c$ reflection. The energy of the maximal intensity coincides with the main resonance energy of the Fe^{2+} B-site contribution to the XAS simulation. (c) Energy dependence of the $(001)_c$ reflection. The peak shows a characteristic intensity splitting that was attributed to Fe^{2+}/Fe^{3+} charge ordering. Reprinted Fig. with permission from J. Schlappa et al., Phys. Rev. Lett. **100**, 026406 (2008) [139]. Copyright (2008) by the American Physical Society: `http://link.aps.org/abstract/PRL/v100/p026406`.

orbital order was found by comparing the energy dependence of the $(00\frac{1}{2})_c$ scattering peak with the site-resolved x-ray absorption spectroscopy (XAS) signal, thus addressing the order to be caused by Fe^{2+} (Fig. 4.2 (b)), which can only be understood in terms of an orbital ordering model. Note that the resonance spectrum of the $(001)_c$ reflection shows a characteristic intensity splitting (Fig. 4.2 (c)) which was characterized as indicator for charge ordering.

Shortly after the publication of these data it was claimed that the $(00\frac{1}{2})_c$ reflection could be explained by the structural phase transition only, without any need of orbital or charge ordering [140, 141]. Interestingly, as we could show, the experimental data used for this interpretation could be understood by implying a dead layer on top of the sample, which did not contribute to the signal, while deforming the shape of the spectra and shifting the peak position [30].

Detwinning magnetite using epitaxial strain

During cooling through T_V the monoclinic c_m axis can align in any of the cubic (100) directions, slightly tilted away from the cubic axis. The tilt direction determines the monoclinic a_m and b_m directions and gives rise to 24 possible orientations (twinning) [142]. The occurrence of crystallographic twins in the LT phase of magnetite makes all investigations challenging and makes it difficult to obtain information on a single domain. Twinning can for example be reduced by cooling in a magnetic field that is aligned with one of the cubic axes [143], by strain [144], or study of micro samples [126].

In his dissertation C. F. Chang could show that, using a stepped substrate, detwinning takes place in 40nm thick epitaxially grown Fe_3O_4 films [145].

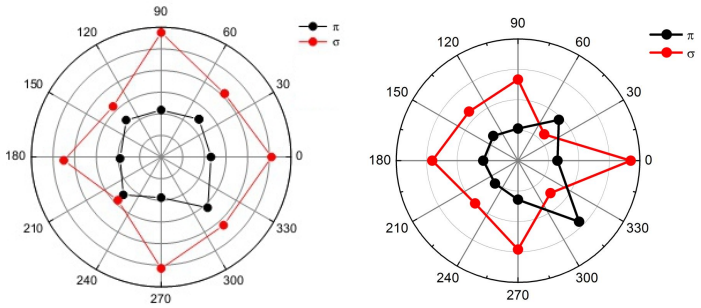

Fig. 4.3.: Azimuthal angle dependence of the scattered intensity for horizontal (black) and vertical (red) polarization. A fully twinned magnetite thin film shows a fourfold symmetry pattern (a), while a magnetite thin film on top of a stepped substrate, has only one axial symmetry (b). Due to epitaxial strain, only two of the possible twins are present. Pictures are taken from [145] with permission of the author.

His argumentation is explained in the following: in a resonant x-ray diffraction experiment at the Fe-L edge the azimuthal polarization dependence of the $(00\frac{1}{2})_c$ reflection of a magnetite film on a flat and on a stepped MgO substrate was analyzed. The experiment

is only sensitive to the four domains with c_m parallel to the thin film normal. While the pattern has a fourfold rotational symmetry in the case of the flat substrate, the symmetry of the azimuthal pattern was reduced to an axial symmetry for the stepped substrate. The axis of symmetry is aligned with the step direction of the substrate, indicating that only two of the four possible twins contribute to the signal (Fig. 4.3).

The implications of this result, however, were not understood at that time and are the topic of this chapter.

The rest of this chapter is organized in the following way: First a brief description of the experiment is given. Then, the azimuthal dependence of the linear dichroic $(00\frac{1}{2})_c$ diffraction intensity is presented, which is analyzed in terms of symmetry considerations of the scattering tensor. It turned out that the azimuthal plot reflects a $3d$ wavefunction symmetry, which is lower than the symmetry of the Wright2001-structure. The Senn2012-structure was not published at the time of this outcome. Afterwards a complex-coefficient charge order model is presented, which is the ground state predicted by band structure calculations. The calculations were performed by A. Tanaka using the Wright2001-structure as input. The complex-coefficient charge order model has a true monoclinic symmetry and predicts the correct linear dicroic azimuthal dependence of the diffraction intensity. Furthermore the model predicts a circular dichroism in the $(00\frac{1}{2})_c$ azimuthal dependence. The respective experimental results presented at the end of the chapter are in good agreement with these predictions.

4.2. Experimental details

Resonant soft x-ray experiments at the Fe-$L_{2,3}$ edge ($2p \rightarrow 3d$) were carried out at the UE56/2-PGM-1 beamline of the Helmholtz-Zentrum Berlin at BESSY II. The new UHV diffractometer, presented in Chap. 2, was used in horizontal scattering geometry. Temperature was set to around 80 K, which is far below the Verwey transition. The c-oriented magnetite samples on a stepped MgO substrate were grown by C. F. Chang and M. Döhler using the molecular beam epitaxy (MBE) technique. The stepped surface reduces the number of possible orientations of the a_m axis in the low-temperature phase. Samples were mounted on a $5 \times 4.5\,\mathrm{mm}^2$ SmCo permanent magnet plate. The field of approximately 100 to 300 mT defines a preferential axis for the orientation of the monoclinic low-temperature c_m axis and is used to align most of the domains' magnetic easy axis.

The azimuthal dependence of the $(00\frac{1}{2})_c$ reflection, which is sensitive to the symmetry of the $3d$ wave function, was studied with different x-ray polarizations and recorded in angular steps of 20°. Fig. 4.4 shows a sketch of the diffraction process. Different samples were characterized and the one with the most intense and most homogeneously distributed signal was used.

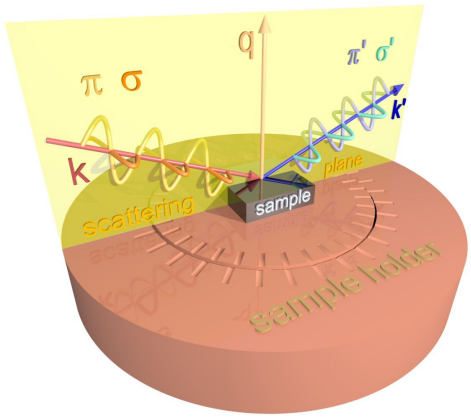

Fig. 4.4.: Schematic representation of the diffraction process of linear polarized light in specular geometry. The sample is mounted on a copper plate and can be azimuthally rotated. The incident **k** and outgoing **k**' wave vectors with electrical polarization vectors parallel (π, π') and perpendicular (σ, σ') to the scattering plane (yellow) define the wave-vector transfer **q**.

4.3. Method

The goal of the experiment was to determine and analyze the shape and symmetry of the azimuthal pattern. Special care has therefore been taken to always probe the same spot on the sample for all azimuthal angles. This was done by probing the sample position that is located in the center of the azimuthal rotation. To locate the center of rotation the intensity of the fluorescence signal was mapped in horizontal and vertical direction across the sample. This procedure was repeated in 90° azimuthal steps, thus oversampling the center position. With this method the center of rotation was determined within at least 50 µm accuracy. The intensity does not change much within this range ($\pm 2.5\%$). As the azimuthal rotation is performed manually, it is possible that the probed position differs from the center even more than the accuracy. Fig. 4.5 shows the variation in intensity for a position change within ± 0.5 mm. In this region the intensity curve is moderately flat giving additional confidence that the azimuthal pattern is not seriously affected by position shifts.

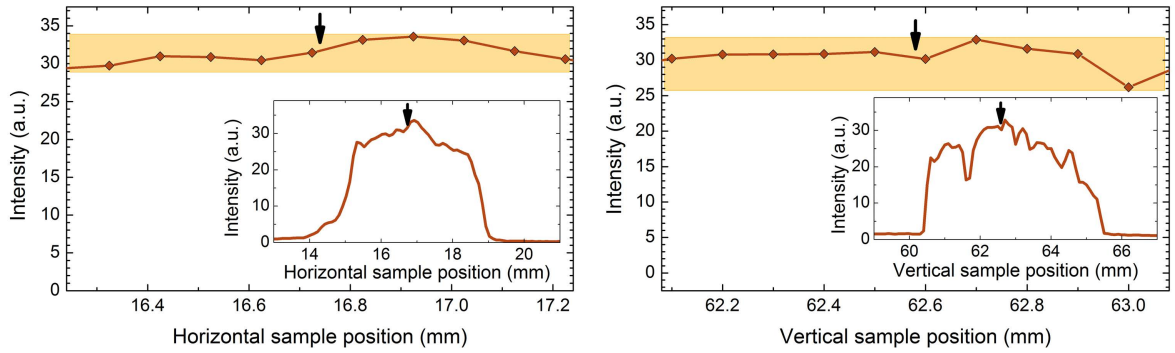

Fig. 4.5.: Spatial plots of the $(00\frac{1}{2})_c$ peak intensity across the sample in (a) horizontal and (b) vertical direction. The main plots are restristed to the vicinity (± 0.5mm) of the center of rotation and the insets show the plots across the complete sample. The intensity is stable within approximately $\pm 10\%$ in the vicinity of the rotation center.

4.4. Results

4.4.1. Angular anisotropy of the linear dichroism

The experiment was carried out on a detwinned magnetite thin film. During this and previous beamtimes, we could not find any difference in the linear dichroism (LD) of thin films that were placed on a permanent magnet and those without a magnet. The azimuthal dependence of the LD, which is presented in the following, was recorded during 2 shifts within 30 hours. Special care has therefore been taken on any long term variation of the intensity. As a monitor signal of the incident x-ray intensity, the current from the last beamline mirror was used. The detector signal is always normalized on this monitor signal to account for any intensity variations coming from the beamline section.

At every azimuthal angle φ, the detector and sample positions were optimized to account for the misalignment between the c-axis of the sample and the azimuthal axis. Radial scans along reciprocal l direction (l-scan) were performed with horizontally ($\boldsymbol{\pi}$) and vertically ($\boldsymbol{\sigma}$) polarized incoming x-rays. The photon energy was tuned to the Fe-L_3 resonance maximum. A typical data set, taken at one specific azimuthal angle, is shown in Fig. 4.6 (a). Blue data points were taken with vertically and red with horizontally polarized incoming light. The reflectivity background varied strongly with x-ray polarization and azimuthal angle, due to the polarization dependence of the reflectivity and the effective change of the geometry caused by the rotation of the sample holder. To account for that, a polynomial of fourth order was fitted to the data excluding the peak. The background subtracted data were fitted by a Voigt profile, which gave the best agreement between fit and data, compared to Gauss and Lorentz fits (Fig. 4.6 (b)). The azimuthal dependence of the integrated intensity for both polarizations is plotted in Fig. 4.7.

For better visualization of the symmetry, the data are depicted in polar plots with

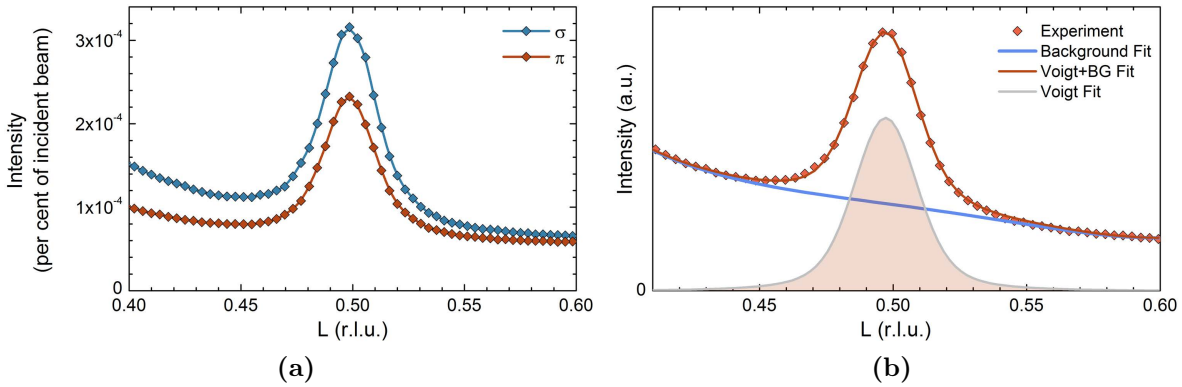

Fig. 4.6.: (a) Resonant diffraction scans of the $(00\frac{1}{2})_c$ reflex at the Cu-L_3 resonance. Scans in the reciprocal l direction for $\boldsymbol{\sigma}$ (blue marker) and $\boldsymbol{\pi}$ (red marker) polarization are taken below the Verwey transition. Solid lines are guides to the eye. (b) Fit of the experimental l-scan by a polynomial background and Voigt profile. Red data marker denote the intensity as recorded during the experiment. The background fit is displayed as solid blue line and the combined fit of background and Voigt profile as solid red line. The Voigt profile is displayed as solid grey line.

the azimuthal angle defining the angular coordinate and the intensity of the polarization channel plotted on the radial axis. Data markers are L_3-integrated intensities as obtained by the peak fit. Note that the error obtained by the fit is of the order of 1% and thus smaller than the symbol size. Solid lines are spline interpolations as guides to the eye.

The azimuthal plot is similar to the one in Fig. 4.3, but contains more details, due to the higher angular resolution. We found a low-symmetric angular anisotropy of the LD. At 0° the sample was aligned with the descending step direction in the scattering plane pointing towards the x-ray beam. The LD of the diffracted signal changes its sign four times, being strongest for $\boldsymbol{\sigma}$ polarization at 0° and between 40° and 60° for $\boldsymbol{\pi}$ polarization.

A closer look to the experimentally obtained polar plot in Fig. 4.7 reveals a scattering of the data taken at 0° and 80°, which were taken repeatedly over the whole series. The variation shows a long term drift of the scattered intensity.

Long term drift of the intensity

Within this and previous experiments on magnetite, we generally found some long term drift of the $(00\frac{1}{2})_c$ diffraction intensity. This intensity drift appears to be connected to the incident x-ray radiation and the peak height decreases during constant x-ray exposure of the sample. While visible in different magnetite samples, this radiation induced effect did only affect the intensity and did neither change the shape of the peak profile nor the energy dependence of the peak. We do therefore attribute the drift to a chemical change of the material. To account for the change in intensity we repeated the scans at 0° and 180° azimuthal angles intermittently after data was taken from three

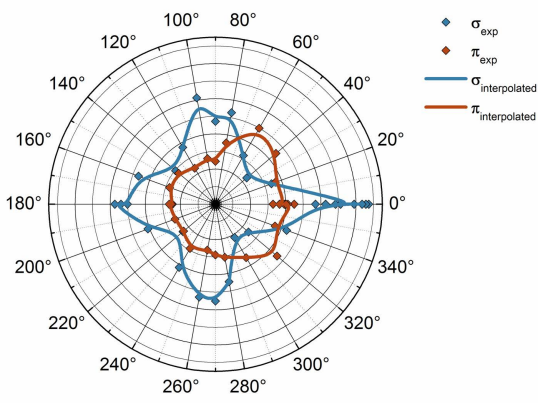

Fig. 4.7.: Azimuthal dependence of the $(00\frac{1}{2})_c$ diffraction peak as obtained from the RSXD experiment. Blue (red) data marker show the results for vertically (horizontally) polarized x-rays. A spline was plotted to the experimental data (solid line). The y-axis starts from zero. Errors of the integrated intensity as retieved from the Voigt fit are smaller than the data marker.

to four subsequently following azimuthal angles. The temporal evolution of the data taken at 0° for the vertical polarization channel is plotted in Fig. 4.8 and is used as reference to correct the intensity of the data taken in between. The vertical polarization

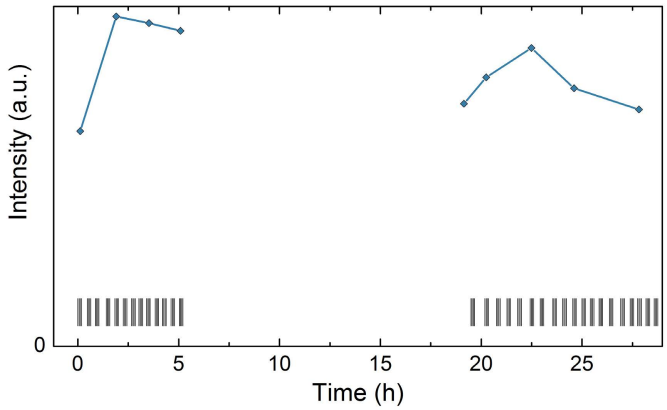

Fig. 4.8.: The intensity of the vertical polarization at $\varphi = 0°$ (blue marker) was used for normalization of the long term drifts. Every l-scan was taken at a specific point in time marked by a vertical black line marker. The reference signal was interpolated and used to correct the data set. As the azimuthal series was recorded within two beamtime shifts there is a gap of roughly 12 hours, in which no data was taken.

channel at $\varphi = 0°$ was chosen because of its higher intensity. Intensity variations of the signal are thus better visible. Blue data marker denote the integrated intensity of the background subtracted $(00\frac{1}{2})_c$ diffraction signal. The vertical black data marker illustrate the time when data was taken. As the whole azimuthal angle series was taken within two beamtime shifts, a gap of 12 hours can be seen. During the two shifts the

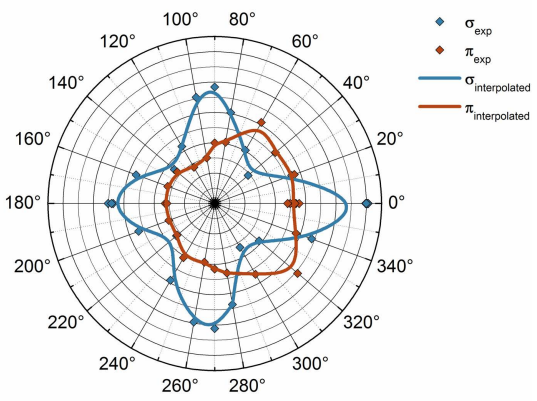

Fig. 4.9.: Corrected azimuthal dependence of the $(00\frac{1}{2})_c$ reflex as obtained from the RSXD experiment. Blue (red) data marker show the results for vertical (horizontal) linear polarized x-rays. A spline was plotted to the experimental data (solid line). The y-axis starts from zero. The correction is further explained in the text.

sample was kept cold to minimize any changes in the setup. Every l-scan was scaled by the interpolated reference signal at the respective time. The corrected azimuthal dependent polar plot of the $(00\frac{1}{2})_c$ RSXD signal is shown in Fig. 4.9. The repeatedly taken $\varphi = 0°$ data of the $\boldsymbol{\sigma}$-channel were scaled to each other by the correction method: the reduced data scattering at 180° for $\boldsymbol{\sigma}$-polarization and at $0°, 180°$ for $\boldsymbol{\pi}$-polarization show the effectivity of the correction.

Symmetry considerations

We found a low symmetry pattern with a strong linear dichroism of the diffraction signal, which is characterized by a symmetry axis that is spanned by the 0° and 180° azimuthal angles, thus perpendicular to the step edges of the substrate.

This azimuthal pattern can be discussed in terms of the symmetry properties of the scattering tensor. For this discussion the intermediate states of the resonant scattering process were approximated by a single level, which is justified by the large spectral weight that is concentrated on the most intense feature of the spectra (Fig. 4.2). The resonant scattering amplitude can be written as:

$$A(\boldsymbol{\varepsilon}, \boldsymbol{\varepsilon}') \sim \sum_j e^{i\mathbf{q}\mathbf{r_j}} \sum_{k,l} \varepsilon_k \varepsilon'_l F^j_{kl}, \tag{4.1}$$

where the last sum with indices $k, l = x, y, z$ is equal to $\boldsymbol{\varepsilon}' \cdot \boldsymbol{F}^j \cdot \boldsymbol{\varepsilon}$. Here $\boldsymbol{F}^j$ is the atomic scattering tensor (Eq. 1.3.3) of site j at $\mathbf{r_j}$, $\mathbf{q}$ is the wave-vector transfer, and $\boldsymbol{\varepsilon}$ ($\boldsymbol{\varepsilon}'$) are the polarization vectors of the incident and outgoing light. A most general scattering tensor consists of 9 entries, all of them being complex. Off diagonal elements, which change the orientation of the incident polarization, can arise from an anisotropic arrangement of the electron wave function as well as from magnetism, while diagonal elements, which do not alter the polarization, come from isotropic charge configurations.

In detail the scattering tensor looks like:

$$\boldsymbol{F} = \begin{vmatrix} \mathrm{Re}[F_{xx}] + \mathrm{i}\cdot\mathrm{Im}[F_{xx}] & \mathrm{Re}[F_{xy}] + \mathrm{i}\cdot\mathrm{Im}[F_{xy}] & \mathrm{Re}[F_{xz}] + \mathrm{i}\cdot\mathrm{Im}[F_{xz}] \\ \mathrm{Re}[F_{yx}] + \mathrm{i}\cdot\mathrm{Im}[F_{yy}] & \mathrm{Re}[F_{yy}] + \mathrm{i}\cdot\mathrm{Im}[F_{yy}] & \mathrm{Re}[F_{yz}] + \mathrm{i}\cdot\mathrm{Im}[F_{yz}] \\ \mathrm{Re}[F_{zx}] + \mathrm{i}\cdot\mathrm{Im}[F_{zx}] & \mathrm{Re}[F_{zy}] + \mathrm{i}\cdot\mathrm{Im}[F_{zy}] & \mathrm{Re}[F_{zz}] + \mathrm{i}\cdot\mathrm{Im}[F_{zz}] \end{vmatrix}.$$

Assuming the *Pmca* orthorhombic symmetry of the lattice structure and alignment of the magnetic moments along the *c*-direction, the symmetry can be described by $P\underline{mc}a$, where the underscore denotes the time reversal symmetry operator. Fig. 4.10 shows how a magnetic moment aligned along *c*-direction is affected by mirror and time reversal symmetry operations. The direction of the magnetic moment flips if the normal vector

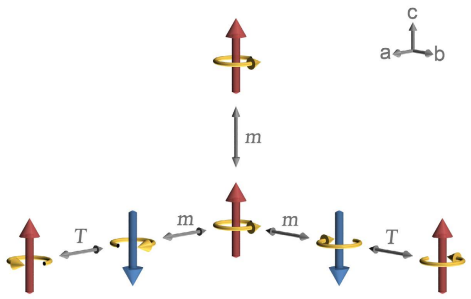

Fig. 4.10.: $\underline{mmm}$ symmetry of a magnetic moment aligned along *c*-direction. The direction of the magnetic moment keeps sign if mirrored along the *c*-direction, while it changes sign if mirrored along *a* and *b*-direction. Additional time reversal is needed to keep the moment invariant under the combined symmetry operation. The mirror symmetry operation is labeled as *m* and the time reversal as *T*.

of the mirror plane is perpendicular to *c*. To conserve the orientation of the magnetic moment an additional time reversal operation needs to be applied. This introduces a combined $\underline{m}$ element that is the combination of time reversal and a mirror plane.

The $P\underline{mc}a$ symmetry reduces the number of entries in the scattering amplitude:

$$A_{P\underline{mc}a}(\boldsymbol{\varepsilon}, \boldsymbol{\varepsilon}') \propto (\varepsilon_y\varepsilon'_z + \varepsilon_z\varepsilon'_y)\mathrm{Re}[F_{yz}] + \mathrm{i}(\varepsilon_z\varepsilon'_x - \varepsilon_x\varepsilon'_z)\mathrm{Im}[F_{zx}], \tag{4.2}$$

where only the real part of F_{yz} and the imaginary part of F_{zx} contribute. If the symmetry operations of the monoclinic $P\underline{2}/\underline{c}$ space groups are applied to the scattering amplitude, a third component, the real part of F_{xy} contributes:

$$A_{P\underline{2}/\underline{c}}(\boldsymbol{\varepsilon}, \boldsymbol{\varepsilon}') \propto (\varepsilon_y\varepsilon'_z + \varepsilon_z\varepsilon'_y)\mathrm{Re}[F_{yz}] + \mathrm{i}(\varepsilon_z\varepsilon'_x - \varepsilon_x\varepsilon'_z)\mathrm{Im}[F_{zx}] + (\varepsilon_x\varepsilon'_y + \varepsilon_y\varepsilon'_x)\mathrm{Re}[F_{xy}].$$

The associated $\boldsymbol{F}$-tensor then, is:

$$\boldsymbol{F}_{P2/c} = \begin{vmatrix} 0 & \mathrm{Re}[F_{xy}] & \mathrm{i}\cdot\mathrm{Im}[F_{zx}] \\ \mathrm{Re}[F_{xy}] & 0 & \mathrm{Re}[F_{yz}] \\ -\mathrm{i}\cdot\mathrm{Im}[F_{zx}] & \mathrm{Re}[F_{yz}] & 0 \end{vmatrix}.$$

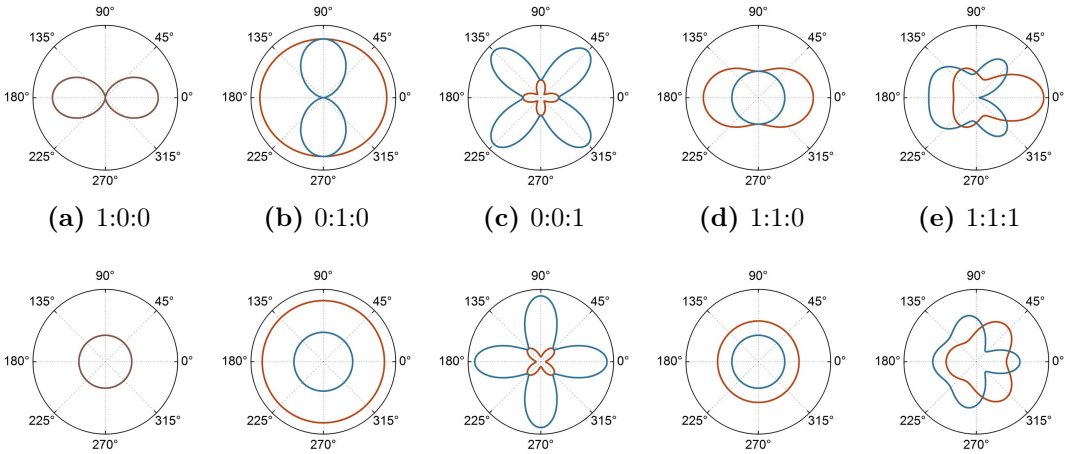

(a) 1:0:0 **(b)** 0:1:0 **(c)** 0:0:1 **(d)** 1:1:0 **(e)** 1:1:1

(f) 1:0:0 **(g)** 0:1:0 **(h)** 0:0:1 **(i)** 1:1:0 **(j)** 1:1:1

Fig. 4.11.: Azimuthal and polarization dependence of the $(00\frac{1}{2})_c$ scattering reflex. Red and blue lines represent horizontally and vertically polarized incoming x-rays, respectively. The upper row is for a single domain, the lower one for two domains with an orientation of $\Delta\varphi = \pm 45°$ with respect to the single domain, as found in a Fe_3O_4 thin film grown on a stepped MgO substrate. Different columns represent different ratios of the contributing entries of the $\boldsymbol{F}$-tensor elements $\mathrm{Re[F}_{yz}\mathrm{]} : \mathrm{Im[F}_{zx}\mathrm{]} : \mathrm{Re[F}_{xy}\mathrm{]}$ as denoted below each plot. (a,f) display the symmetry of *Pmca*, (d,i) of *Pmca* and (e,j) of $P2/c$ space group.

The azimuthal intensities of the $(00\frac{1}{2})_c$ reflection for incident linear polarized light, can be best calculated in the coordinate system of the sample. Consequently, the polarization instead of the sample is rotated by the angle φ. Thus, the incident and outgoing polarizations, denoted by $\boldsymbol{\varepsilon_\mu}$ and $\boldsymbol{\varepsilon'_\mu}$, where the index μ is either equal to $\boldsymbol{\pi}$ or $\boldsymbol{\sigma}$, can be expressed as:

$$\begin{aligned} \boldsymbol{\varepsilon}_\sigma &= \boldsymbol{\varepsilon}'_\sigma = (-\sin\varphi, \cos\varphi, 0), \\ \boldsymbol{\varepsilon}_\pi &= (\cos\varphi\sin\theta, \sin\varphi\sin\theta, \cos\theta), \\ \boldsymbol{\varepsilon}'_\pi &= (-\cos\varphi\sin\theta, -\sin\varphi\sin\theta, \cos\theta). \end{aligned} \tag{4.3}$$

Due to the fact that we did not use a polarization analyser, the diffracted intensity for incoming horizontally and vertically polarized x-rays contains both outgoing polarizations. The total intensity of each channel is given by:

$$I_\mu(\varphi) = |A_\mathrm{m}(\boldsymbol{\varepsilon}_\mu, \boldsymbol{\varepsilon}'_\sigma)|^2 + |A_\mathrm{m}(\boldsymbol{\varepsilon}_\mu, \boldsymbol{\varepsilon}'_\pi)|^2 . \tag{4.4}$$

The azimuthal and polarization dependence of the $(00\frac{1}{2})_c$ reflection directly reflects the weight of these three scattering-tensor elements. The azimuthal dependence is shown in Fig. 4.11 for $\mathrm{Re}[F_{yz}]$, $\mathrm{Im}[F_{zx}]$, $\mathrm{Re}[F_{xy}]$ and their superpositions. The upper row is calculated using only a single domain, while the lower row displays the azimuthal dependence of Eq. 4.4 for two domains, which are rotated around the c-direction by $\pm 45°$ with respect to the single domain. The incoming vertical (horizontal) polarization channel is displayed by blue (red) lines. In (a-c) and (f-h) the azimuthal and polarization dependence of the three contributing scattering tensor elements are plotted. If the

$3d$ wave function symmetry would reflect the pseudo-orthorhombic *Pmca* symmetry we would observe a centrosymmetric polar plot like displayed in (f), which contains

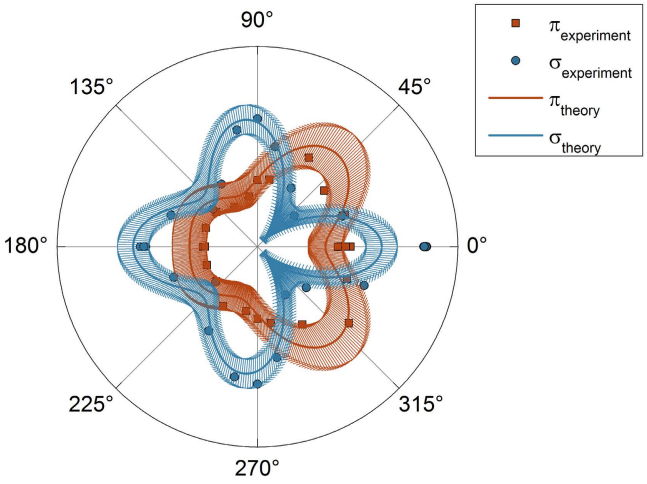

Fig. 4.12.: Comparison of experiment and theory for $\mathrm{Re[F}_{yz}\mathrm{]:Im[F}_{zx}\mathrm{]:Re[F}_{xy}\mathrm{]} = 1:1.4:2$. Red and blue data point denote experimental data for incident horizontal and vertical polarization, respectively. Solid curves represent theoretical calculations. The y-axis starts from 0. Within an error of $\pm 20\%$ of the theoretical values the experimental data can be nicely described.

no polarization dependence. In the *Pmca* symmetry (i) the pattern shows only an intensity difference between both polarizations, but no sign change. Obviously the low-symmetry pattern found in the experiment is caused by the superposition of all three tensor elements (j) and reflects the monoclinic $P\underline{2}/\underline{c}$ symmetry.

In order to fit the experimental data the ratio was tuned, providing the best result for $\mathrm{Re}[F_{yz}]:\mathrm{Im}[F_{zx}]:\mathrm{Re}[F_{xy}] = 1:1.4:2$ (Fig. 4.12). The experimental data can be nicely described with the symmetry considerations within an error of $\pm 20\%$. Only a few data points lie not within this range.

The distortion from orthorhombic to monoclinic is strongly reflected in the azimuthal plot, due to the high value of $\mathrm{Re}[F_{xy}]$, which would be zero for the pure orthorhombic lattice. Our findings that $\mathrm{Re}[F_{xy}] = 2$ describes the data best, strongly deviates from a contribution of $\mathrm{Re}[F_{xy}]$ equal to $|\cos\beta| = 0.004$ as assumed in Ref. [140], which would be the case for a $3d$ wave function symmetry which does reflect the pseudo-orthorhombic *Pmca* symmetry of the structure found in Ref. [124, 125]. Only very recently (after our findings had been submitted to Phys. Rev. Lett.) a lattice refinement using monoclinic *Cc* symmetry (Senn2012-structure) was published [126]. With these findings the lattice symmetry is fully reflected in the symmetry of the $3d$ wave function.

With the simulation of the symmetry model, the orientation of the two contributing magnetic domains to the diffraction signal can be determined. The a_m axes are rotated $\pm 45°$ from the mirror axis and point towards the descending step direction of the substrate.

Full model

The symmetry considerations agree very well with the experimentally observed azimuthal pattern which reflects the symmetry of the electronic wavefunction; however, they do not yield any insight in the origin of the electronic ordering mechanism.

In a spinless three band Hubbard model, H. Uzu and A. Tanka found a stabilization of a complex number orbital ordering with monoclinic symmetry and t_{2g} orbital ordering

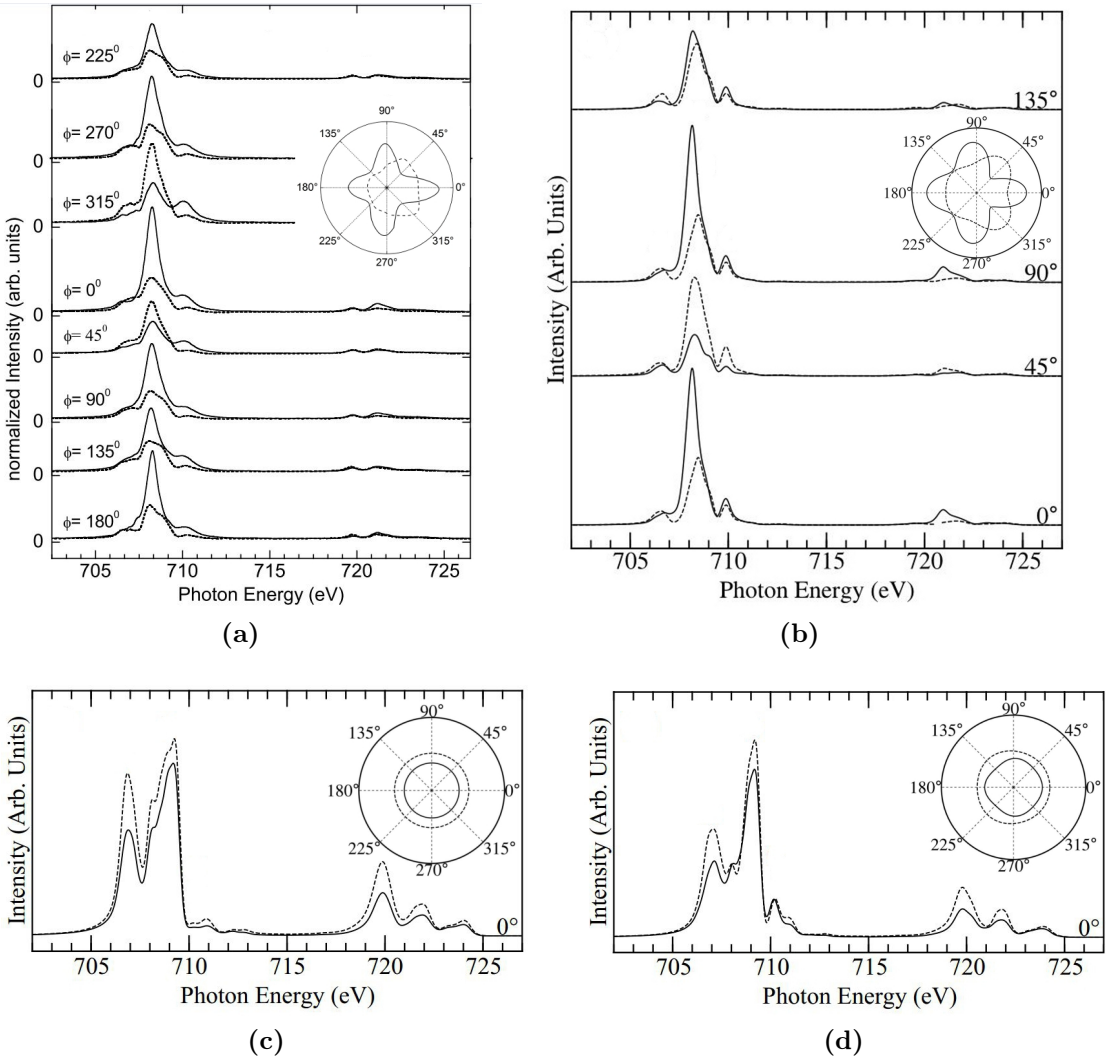

Fig. 4.13.: Experimental (a) and theoretical (b-d) energy dependence of the $(00\frac{1}{2})_c$ reflection intensity. Solid and dashed lines denote the intensities for incident $\boldsymbol{\sigma}$ and $\boldsymbol{\pi}$ polarized x-rays, respectively. (b) shows spectra for the complex-coefficient charge order model, (c) for the real-coefficient orbital order model with *Pmca* symmetry and (d) for the real-coefficient orbital order model with *Cc* symmetry. The inset shows the azimuthal and polarization dependence of the peak intensity. Pictures are modified from [146].

[132]. The orbital degree of freedom spontaneously breaks time inversion symmetry and

generates large non-collinear orbital moments, while spin-orbit coupling is rather small. A real space image of the orbital moments in the low-temperature unit cell can be seen in Fig. 4.14 (a). Contrarily, in LDA+U and GGA+U calculations different kinds of real-coefficient orbital ordering were found [128–130].

In a configuration interaction FeO_6 cluster calculation, performed by A. Tanaka, the azimuthal angle dependences of the $(00\frac{1}{2})_c$ scattering intensity were calculated for the

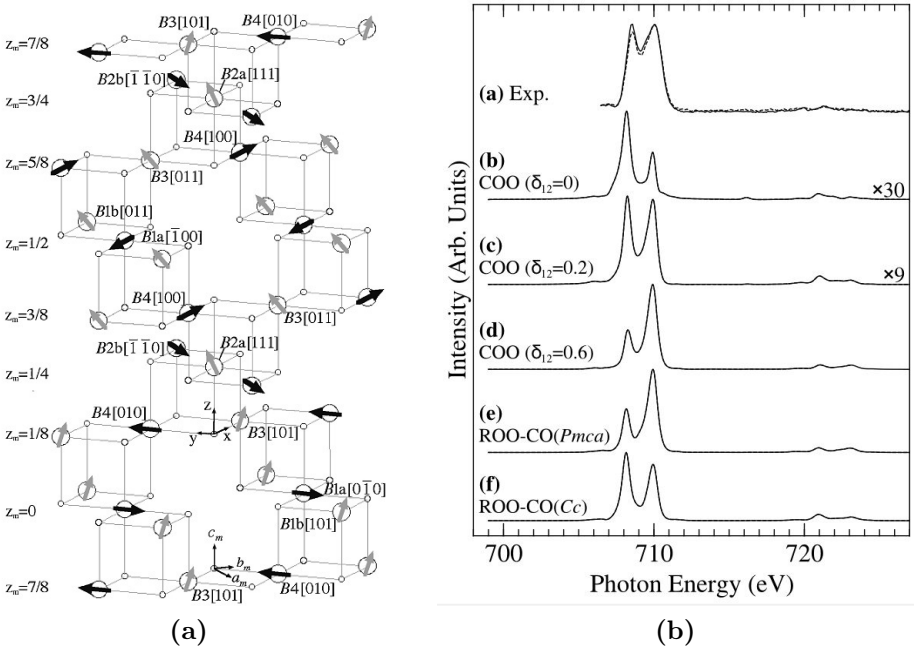

Fig. 4.14.: (a) Collinear arrangement of orbital moments in the complex-coefficient charge order model. Sites are labeled in the *Pcma* symmetry notation. Large circles denote Fe B-site ions and small circles oxygen ions. Black arrows indicate a larger and grey a smaller orbital moment. (b) Experimental and theoretical energy dependence of the $(001)_c$ scattering reflex. The peak splitting obtained in the experiment can be explained within the complex-coefficient orbital order even without a charge disproportion δ. Pictures are taken rom [146].

complex-coefficient charge order as well as for the real-coefficient orbital order models of Leonov et al. and Jeng et al. A comparison of the resultant resonance spectra to experimental data can be found in Fig. 4.13. It reveals that only the complex-coefficient charge order model describes the experimental results adequately.

Interestingly, the complex-coefficient charge order model does not necessarily involve charge ordering as can be seen by analyzing the energy dependence of the $(001)_c$ scattering reflex (Fig. 4.14 (b)). While $3d$ charge disproportions are needed to explain the peak splitting by a real-coefficient orbital order model, the complex-coefficient charge order model reproduces the spectral shape without any charge disproportion; however, a small t_{2g} charge disproportion of 0.2 describes the experimental findings much better.

4.4.2. Angular anisotropy of the circular dichroism

The complex-coefficient charge order model is therefore the only one out of the so far proposed models for orbital ordering that predicts the correct spectra. Another remarkable prediction related to this model is that the RSXD intensity should show a pronounced circular dichroism (CD) [146]. The CD should show as well a pronounced angular anisotropy. CD in RSXD is rather rare and only observed in materials showing a magnetic chirality [147–150].

In order to see the CD, the amount of structural and magnetic twinning should be minimized. Therefore, circular dichroic RSXD experiments of a magnetized magnetite thin film on a stepped MgO substrate were performed. The small permanent magnet that was mounted between the substrate and the sample plate, has its field direction parallel to the film normal. The field aligns the magnetic moments along the [001] easy axis to create a single magnetic domain. To check the amount of magnetization, x-ray absorption magnetic circular dichroism (XMCD) spectra were recorded in normal incidence geometry with the photon spin parallel and antiparallel to the field direction. These spectra were compared to the results from a fully magnetized bulk sample [136]. From the comparison of the XMCD signal ratios we find a magnetic circular dichroism

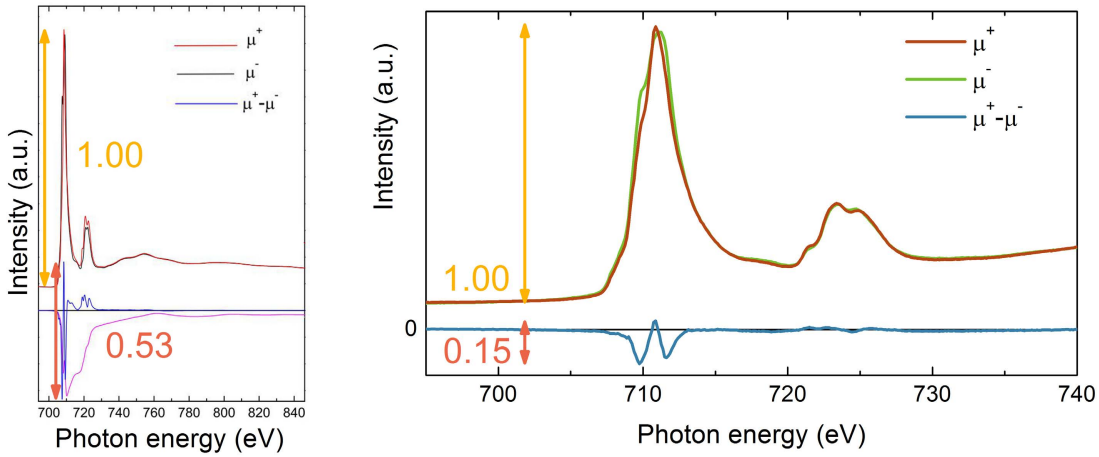

Fig. 4.15.: XMCD effect obtained in (a) bulk Fe_3O_4 using a high magnetic field of 5 T and (b) of a Fe_3O_4 thin film in the field of a small permanent magnet. Red (green and black) curves denote the XAS signal with different right (left) circular polarized x-rays. The XMCD signal, defined as the difference of the XAS signals with different helicities is displayed in blue. The magenta line in (a) displays the integrated XMCD signal. From the ratio of the signal height to XMCD effect the ratio of domains with a magnetic alignment parallel and antiparallel to the field direction can be determined. Fig. (a) is taken from [136].

of 29% as compared to the bulk sample (Fig. 4.15). This corresponds to 64.5 % of the magnetic moments that have an out-of-plane component parallel to the field direction and 35.5 % with an anti-parallel out-of-plane component. The exact alignment will be determined by the shape and magnetocrystalline anisotropy.

A theoretical azimuthal plot for a domain ratio of 1:0.4 was extracted from the cluster calculations of A. Tanaka and is compared to the experiment in Fig. 4.16. It is clearly

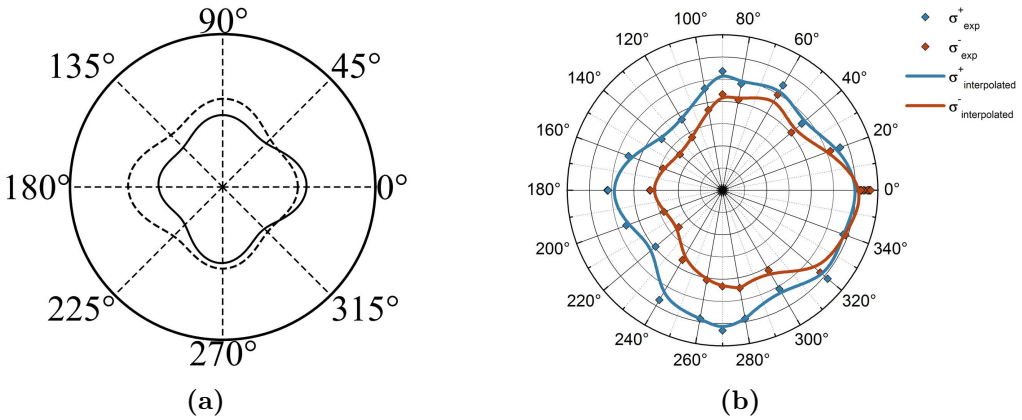

(a) (b)

Fig. 4.16.: Theoretically (a) and experimentally (b) obtained circular dichroism of the $(00\frac{1}{2})_c$ diffraction azimuthal dependence. In (a) the ratio of magnetic domains that are aligned in and opposite to the magnetic field direction is assumed to be 1:0.4. Fig. (a) was provided by A. Tanaka.

visible that the low symmetry shape of the circular dicroic $(00\frac{1}{2})_c$ diffraction intensity predicted by the complex-coefficient charge order model is in amazing similarity to the experimentally observed data. The experimentally obtained polar plot was recorded by a similar azimuth series as the linear dichroic azimuthal angle dependence. Data handling was performed in the same manner as described above.

4.5. Discussion

We have studied the azimuthal and polarization dependence of the $(00\frac{1}{2})_c$ charge orbital order peak in Fe_3O_4 by means of resonant soft x-ray diffraction (RSXD) at the Fe-L_3 edge. RSXD is sensitive to the symmetry of the electronic wave function. The linear dichroism of the integrated intensity shows a low-symmetric angular anisotropy. By symmetry considerations of the scattering tensor we found that the azimuthal dependence reflects to a large amount a monoclinic symmetry of the d-wave function. This is further confirmed in a cluster calculation performed by A. Tanaka, in which he found that our experimental results can only be accurately described using a complex-number orbital ordering model. Only shortly after we submitted our findings to PRL the Senn2012-structure was published. Within this new refinement of the crystal structure the global crystallographic symmetry is fully reflected in the local electronic symmetry. The calculations of A. Tanaka that are based on the complex-coefficient charge order model further predict an angular anisotropy of the circular dichroism, which we clearly found in our experiment. All real-coefficient orbital order models that were proposed so far could not reproduce our findings.

CHAPTER 5

Complex Behavior in Correlated Oxides: Doped $RTiO_3$

5.1. Introduction

Transition-metal oxides with correlated electrons are known for their wide range of intriguing phenomena, caused by the competing interplay of charge, orbital, spin, and lattice degrees of freedom. Already small external perturbations can lead to giant changes in electrical and magnetic properties [5]. One of the most prominent examples is the colossal magnetoresistance (CMR) in manganese oxides, in which the application of a comparably small magnetic field accounts for a tremendous change in the electrical resistivity of the material. One possible explanation is that ferromagnetic metallic (FM) and antiferromagnetic insulating (AFI) regions coexist and, instead of a complete phase transition of the whole sample, a percolation of metallic domains can lead to macroscopic metallicity [151, 152]. Besides in the 113-manganites [153–155], electronic phase separation is for example also discussed in 214-manganites [156, 157] and doped rare earth titanates [112, 158, 159].

Study of the spatial distribution and dynamics of such almost degenerated, coexisting electronic and magnetic phases will provide crucial insights for the understanding how the local electronic structure of correlated electron systems connects to their macroscopic properties. Therefore, a spectroscopically and/or structurally selective technique is needed that is sensitive to the spatial arrangement and fast enough to probe the temporal evolution due to domain wall dynamics. Scanning tunneling microscopy experiments have demonstrated their ability to detect domains with different electronic structure [160, 161], but are limited to the surface area only. Time-resolved optical reflectivity measurements, which are fast enough to detect changes in the domain structure, are blind to the exact spatial arrangement as they average over the whole illuminated area [162].

Coherent x-ray diffraction (CXD), in which the interference pattern of coherently

illuminated domains is recorded, is sensitive to the exact spatial arrangement of the domains and is able to probe bulk properties or the near-surface region in dependence of the x-ray energy [163]. The temporal resolution in a CXD experiment at a third generation synchrotron facility is typically of the order of a few Hz and will be dramatically enhanced by using new x-ray free electron laser facilities. If tuned to an element specific absorption edge, the technique is combined with spectroscopic sensitivity. Here CXD is used to study the domain dynamics of hole-doped titanates.

The parent compounds of $R_{1-x}Ca_xTiO_3$ (R= Y, Er), $YTiO_3$ and $ErTiO_3$ are Mott insulators. Doping with divalent Ca renders part of the Ti valence from 3+ to 4+, and therefore the $3d$ configuration from d^1 to d^0 [4]. In the undoped compounds the movement of the single d^1 electron (per Ti site) is blocked by on-site Coulomb repulsion. Doping holes into the $3d$ shell should render the system metallic. Interestingly, $R_{1-x}Ca_xTiO_3$ stays insulating up to a high doping concentration around x=0.4 [164,165]. This is different from the observations in $La_{1-x}Sr_xTiO$, in which already for small doping concentrations of $x = 0.05$ a metallic behavior is found [166, 167]. Recent x-ray and neutron diffraction studies of doped titanates have shown that the stability of the insulating phase can be attributed to a charge and orbital ordering [112, 158].

At around 40 % doping a temperature driven metal-insulator (MI) transition occurs, which is accompanied by a thermal hysteresis in the electrical resistivity and mag-

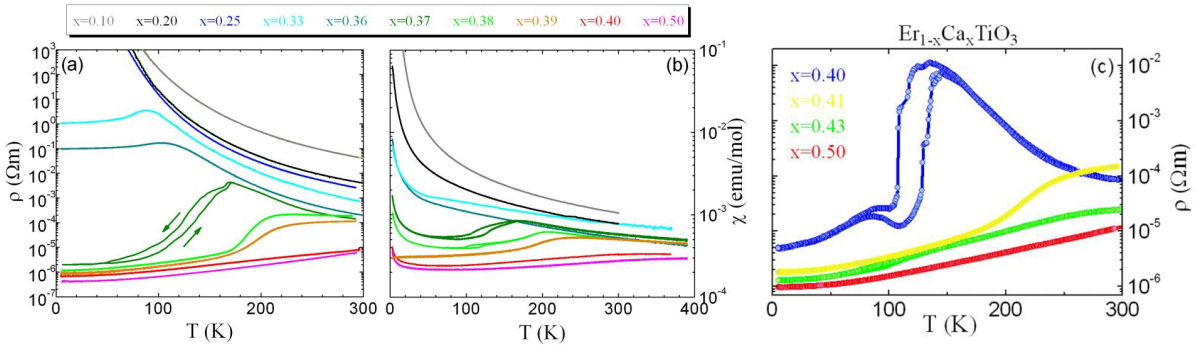

Fig. 5.1.: Temperature dependence of the resisistivity (a) and the susceptibility (b) in $Y_{1-x}Ca_xTiO_3$ and of the resistivity (c) in $Er_{1-x}Ca_xTiO_3$. All pictures are taken from Ref. [112] with permission of the author.

netic susceptibility [112, 158, 168]. In Fig. 5.1 the temperature-dependent resistivity and susceptibility is shown for the most interesting dopind levels in $Y_{1-x}Ca_xTiO_3$ and $Er_{1-x}Ca_xTiO_3$. Studies of the structural phase transitions in this doping range indicate that the MI transition is decoupled from the high-temperature orthorhombic (HTO) to low-temperature monoclinic (LTM) phase transition. Below the unusual MI transition, in which the metallic phase evolves at low temperatures, a phase coexistence of the LTM and a low-temperature orthorhombic (LTO) phase, which is different from the HTO phase, exists [169]. While the LTO phase is assigned to the metallic behavior, the LTM phase hosts the charge and orbital ordered insulating properties. Therefore, phase separation seems to be connected to the MI transition.

The LTM phase is characterized by $(0\,1\,1)_{\mathrm{LTM}}$ and $(0\,1\,3)_{\mathrm{LTM}}$ superstructure reflections that correspond to a three-dimensional checkerboard charge order in the pseudo-cubic Perovskite structure [158]. Their positions in reciprocal space are found to be independent of the exact doping concentration [112]. This further strengthens the model that only part of the sample is charge ordered. In more recent studies it is claimed that, instead of phase separation, the MI transition is caused by the structural transition only [170], but this appears incompatible with the detailed results of Ref. [112, 158].

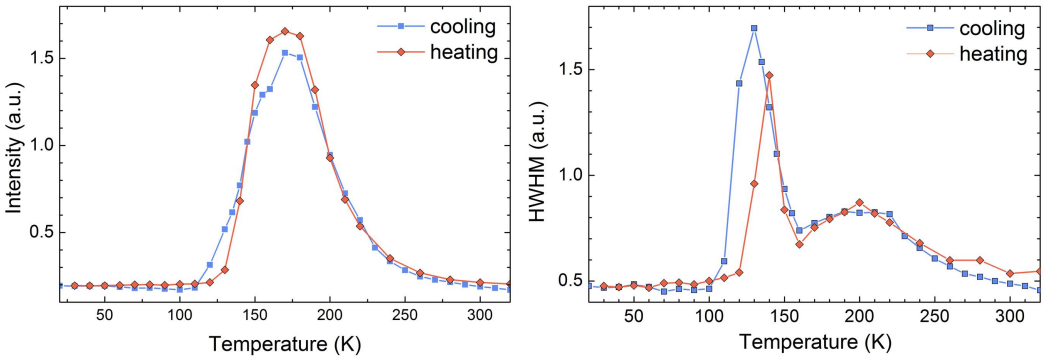

Fig. 5.2.: Temperature dependence of the (0 1 1) superstructure peak intensity (a) and width (b) of $Er_{0.6}Ca_{0.4}TiO_3$ recorded at the MagS beamline, BESSY II at the Ti-K edge [158].

The superstructure reflections of the LTM phase, which are glide-plane forbidden in the LTO phase, were characterized by x-ray and by neutron diffraction techniques [112, 158]. These reflections can be used as indicator for the charge ordered and insulating regions and reveal the volume fraction of this LTM phase, which changes strongly between a value of 0% and 90% for different doping levels around $x = 0.4$ and with temperature around the MI transition [112, 169].

Further indications for the occurrence of phase separation come from x-ray diffraction measurements of the (0 1 1) charge order peak intensity and width. In Fig. 5.2 the temperature dependent peak intensity and peak width of the (0 1 1) reflex in $Er_{0.6}Ca_{0.4}TiO_3$, which were recorded at the MagS beamline at BESSY II, are shown [158]. During cooling the peak intensity increases due to the formation of the charge ordered LTM phase. Below about 170 K the intensity decreases simultaneously with the electrical resistivity [112, 158], indicating that a transition from insulating LTM to the metallic LTO phase takes place. Simultaneously, the peak width changes dramatically and is maximal on the low-temperature slope of the peak intensity signal. Here the correlation length of the LTM domains has its minimum. Following the temperature to even lower values, the (0 1 1) peak width and intensity decrease to a non-vanishing and nearly constant value. In this region a remanent LTM volume fraction survives showing phase coexistence. During heating a hysteresis of both the intensity and the width is observed. The most interesting region to study domain dynamics in this systems is the temperature

region in which the peak width changes most dramatically. In this region an extensive domain reorganization is expected to happen.

The rest of this chapter is organized as follows: First methodical and experimental details are given. Afterwards we turn to the results, in which we start with coherent x-ray diffraction results obtained from $Er_{0.6}Ca_{0.4}TiO_3$ at the ESRF. These first experiments were seriously limited by the lacking stability of the setup. The results, obtained within these limitations, indicate that the dynamical domain reorganization takes place on much shorter time scales than it was possible to probe. In the time regime of hours after a temperature change only static speckle pattern were observed in the whole temperature region of interest. The analysis of a speckle movie that was taken at 130 K is discussed in detail.

Coherent x-ray diffraction results from $Y_{0.64}Ca_{0.36}TiO_3$ taken at PETRA III are presented afterwards. In this experiment a new sample stage has been used. Within the analysis of the data, the focus is on a satellite reflection that splits off from the main (0 1 1) reflex below the MI transition. Speckle pattern recorded from this satellite and from the main reflex during a second PETRA III beamtime revealed that the dynamics take place on even faster time scales than accessible with the new setup.

Results from our coherent soft x-ray experiments at BESSY II are presented in the end of the chapter. A new sample setup was developed during this time. The PETRA III setup, which was mentioned before, is based on this new design. In this section we want to discuss the difference between a coherent experiment with soft and hard x-rays. Besides a smaller probing depth, a different cut through reciprocal space is performed during a soft x-ray experiment. Furthermore, larger speckles allow to decrease the distance between the detector and the sample.

5.2. Method

For the CXD experiment we used the different diffraction responses of the LTO and LTM phase. If tuned to one of the superstructure reflections, only the charge ordered LTM domains contribute to the diffraction signal. Furthermore, if coherent photons are used, the contributions from all illuminated LTM domains interfere and create a speckle pattern. The dynamics of this speckle pattern are directly connected to the dynamics of the real space distribution of insulating and metallic domains.

A change of the speckle pattern with time that exceeds the statistical photon noise is expected for a domain reorganization. This should be visible in different intensity distributions for successive recorded patterns. The aim of the analysis of such data is to obtain a characteristic time scale, which may also vary for different length scales.

Fluctuations in the speckle pattern due to dynamics in the sample can, however, be superimposed by further fluctuations due to experimental and statistical reasons. These are (a) statistical variations in the photon events, (b) changes in the sample due to an uncontrolled change of the sample temperature, (c) changes in the x-ray beam position on the sample, and (d) changes of the intensity and intensity profile of the x-ray beam. A considerable effort had to be spent during development of this project to avoid these

effects. Intensity modulations of the speckle pattern due to (a) cannot be accounted for, but have to be estimated in size. We have realized that the fluctuations in many data sets are of the same size as expected from the statistical variations, indicating that the sample is in a static configuration. Fluctuations of the speckle intensities that are due to (b) have to be minimized experimentally. To control the sample temperature as good as possible a few arrangements were made: (1) In all experiments a helium return line is used, in which the pressure fluctuates. To compensate for, liquid helium is pumped through the cryostat instead of using overpressure. (2) A precise temperature controller, which allows for a stable control of the heating power, was used, and (3) the temperature is controlled by a button heater that is placed in the vicinity of the sample. However, although these arrangements have improved the setup significantly, one cannot change the temperature and immediately assume stable conditions. We typically have to wait a few minutes up to half an hour until stable conditions are reached. To avoid changes of the interference conditions due to (c), the speckle setup which is described in Sec. 2.2.5 was partly used within the experiments. Intensity modulations due to (d) are experimentally difficult to handle and may also have an influence on (b). So far, we could not find any indications for huge changes of the x-ray intensities and modulations within the beam profile. This may strongly change at a free electron laser facility, where the intensity of different pulses can vary by orders of magnitude. Assuming stable experimental conditions, a movie of the speckle pattern can be recorded for different temperatures. The time scale on which the pattern changes is expected to change for different temperatures.

We expect the dynamics to happen in a specific time window T and involve a characteristic time scale t. If T is shorter than the time we have to wait until the sample temperature has stabilized, we will find a static configuration. Assuming that T is of the order of minutes to hours and dynamics take place on a time scale t that is similar to the frame repetition rate fluctuating speckles should be visible. A qualitative analysis can be performed by comparing the spatial intensity variations of different frames (for example line profiles) and a quantitative analysis by the autocorrelation of different speckles with time (x-ray photon correlation spectroscopy).

For slower fluctuations one will observe a change in the speckle contrast for different exposure times. A static configuration should only change on the scale of the statistical photon noise. Dynamics can also vary spatially across the Bragg peak, originating from different time scales that are associated with respective length scales.

5.3. Experimental details

We have studied $Er_{0.6}Ca_{0.4}TiO_3$ (ErCaTiO) and $Y_{0.64}Ca_{0.36}TiO_3$ (YCaTiO) by means of CXD. In the Er doped samples an enhancement of the insulating properties is found [112]. All the samples were grown by Alexander Komarek using the traveling solvent floating-zone growth technique and further characterized by different experimental methods like electrical resistivity, magnetic susceptibility, powder x-ray diffraction, x-ray single crystal diffraction and neutron diffraction within his dissertation. The lattice constants of the

Y-doped samples were determined to be $a = 5.34$ Å, $b = 5.58$ Å and $c = 7.65$ Å and those of the Er-doped one to be $a = 5.36$ Å, $b = 5.54$ Å and $c = 7.67$ Å [112].

The samples were oriented in (0 1 1) direction using the Laue method, lapped with boron carbide and polished with 0.5 µm alumina suspension until a shiny surface was visible. All samples were glued on a copper sample disk using conducting and UHV compatible silver glue. The sample disks can easily be mounted to the respective sample setups. Experiments were performed in horizontal scattering geometry with the sample oriented such that the *c*-direction was pointing out of the scattering plane. For alignment the structurally allowed (0 2 2) and (0 2 1) reflexes were used.

Pre-characterization of the Er-doped sample at the MagS beamline of BESSY II revealed that there is no significant enhancement of the superstructure reflection by using resonant x-ray photons with an energy around the Ti-*K* edge instead of off-resonant photons with energies around 8 keV. Therefore, energies of 8 keV are chosen for the high x-ray experiments at the ESRF and PETRA III, as the used beamlines are optimized for this energy and since the larger attenuation length in air simplifies the experimental setup. Complementary non-resonant soft x-ray experiments, performed at BESSY II, were used to probe the near-surface region of the sample. Further experimental details concerning the respective beamtimes will be given in each section.

5.4. Results

5.4.1. Hard x-ray diffraction experiment at the ESRF

Data were recorded at ID10A Troika beamline of the European Synchrotron Radiation Facility (ESRF) using an ANDOR IkonM CCD camera, which was mounted at a distance of 1.69 m away from the sample. The camera has 1024 × 1024 pixels, each of them $13 \times 13\,\mu m^2$ large. The photon energy was tuned to 8.08 keV and the CCD detector was placed at an angle of roughly 19.5° to fulfill the Bragg condition for the (0 1 1) reflex. The x-ray beam is monochromatic of the order of $1.4 \cdot 10^{-4}$ (δE/E) and roughly 10×10 μm^2 in size, which was achieved by beryllium compound refractive lenses and horizontal and vertical baffles. This allows for a coherent illumination of the sample, which is a crucial requirement for x-ray photon correlation spectroscopy (XPCS). The sample was mounted on a helium flow cryostat, covered by a beryllium cap that is transparent to x-rays, and placed on a Huber six-circle diffractometer that allows for translation and rotation of the sample.

Different CCD movies were taken from the (0 1 1) charge order superstructure reflex of $Er_{0.6}Ca_{0.4}TiO_3$ (ErCaTiO) around the MI transition at 150 K. In the beginning these data were taken in rough temperature steps at 150, 130, 120, 110 and 80 K. At each temperature a few thousand images, including dark images, were taken. The sample position and the exposure time was always adjusted. The exposure time changed from 0.3 s at higher temperatures to 3 s at lower temperatures, at which the intensity is much weaker (Fig. 5.2). In a second run, the sample was warmed up in 5 to 10 K steps to 250 K and further data were recorded at each temperature step. Afterwards data were

taken during a temperature sweep from 190 K down to 80 K and back. It turned out that the lacking stability of the sample setup was a serious limitation to obtain reliable data for fixed temperatures. The drift of the sample position caused by the thermal expansion of the sample holder led to a drift of the diffraction signal across the detector. Only a few data sets appeared usable, from which all of them show a static behavior of the speckle pattern. To further explain these findings an analysis of the stability of the pattern is presented in the following. It is necessary to go through this analysis for every movie before a correlation of the intensities can be performed.

Stability of the CCD pattern

To show how to determine the stability, a more detailed analysis of a movie captured at 130 K (130 K-movie), which did not show large intensity modulations due to temperature changes, is presented. The movie was recorded a few hours after the sample was cooled down from 150 K. Movies that were taken at the time before the setup had stabilized showed a drift of the pattern across the CCD. The 130 K-movie consists of 1000 frames, each of which was taken with the whole CCD sensor that was exposed to the diffracted x-rays for 0.5 s per frame. Afterwards 50 dark images were recorded with the same

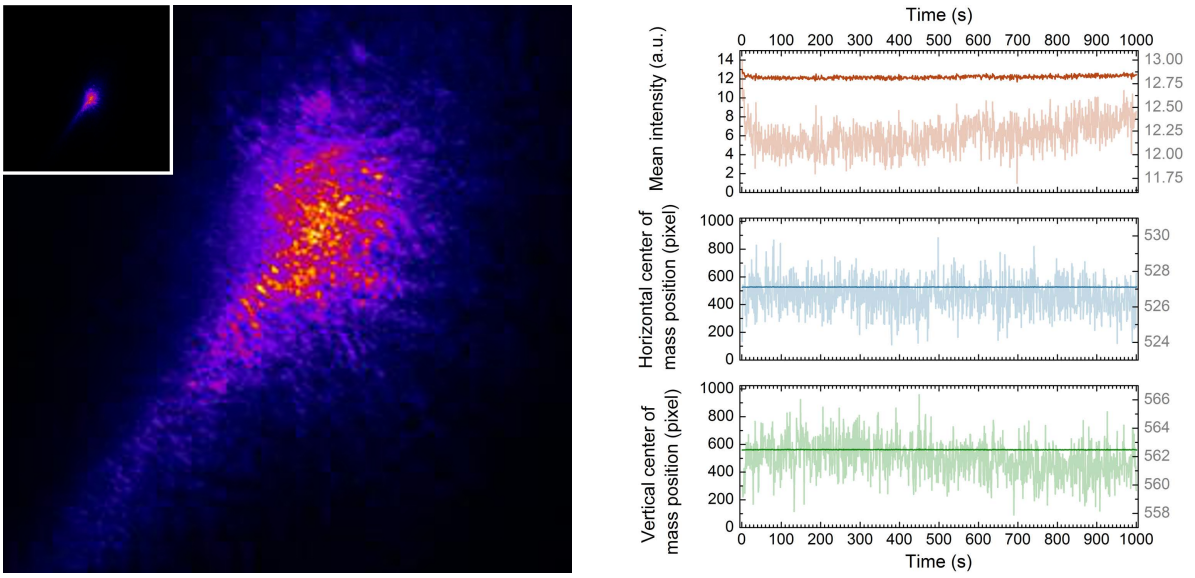

(a) **(b)**

Fig. 5.3.: CCD image of the (0 1 1) charge order reflex in ErCaTiO at 130 K and basic analysis. (a) Average of the 130 K-movie, from which an averaged dark image was subtracted. Black regions contain no or low intensity, while lighter color denote higher intensities. The inset shows the full CCD image and the main image a cut-out containing the peak. (b) Evolution of the mean intensity and center of mass position extracted from the movie. The slightly transparent curves are a zoom of each curve. The respective y-axis scale is plotted on the right of each diagram.

settings. To account for dark and readout noise, an average of the dark images was

subtracted from each of the 1000 frames. An average of all 1000 resultant frames is shown in Fig. 5.3 (a). Negative values were set to zero, which is displayed as black. Lighter color denote higher intensity.

A fundamental criterion for the stability is that the peak does not move across the CCD detector with time. Such drifts may come from temperature changes, vibrations, for example from a pump or other mechanical instruments of the setup, and can even be due to instabilities in the x-ray beam. Large movements might be visible to the bare eye. Smaller movements were determined by calculating the center of mass (COM) of the image. The COM can only be accurately determined if the background from dark and readout noise is subtracted.

A second stability criterion is the evolution of the mean intensity of each frame. Both the mean intensity and the horizontal and vertical COM positions of the 130 K-movie are plotted in Fig. 5.3 (b). The evolution of the mean intensity shows a slight drop within the first twenty to thirty frames. Such a drop was always observed and seems to be an intrinsic problem due to the readout of the CCD camera, which needs a few acquisitions until it has stabilized. In the analysis these starting frames were excluded. The motion of the center of mass on the detector is around 2 pixels in horizontal and vertical direction, which does not necessarily has to come from vibrations or temperature drifts. Instead, fluctuations in the peak intensities may change the COM position slightly. The stability is sufficiently high, as can be confirmed by the observation with the bare eye. In contrast, many other movies, especially those which were recorded right after a temperature change, showed a reflex that visibly moved across the detector and a much larger change in the center of mass position. In addition, the mean intensity varied much stronger than the one of the 130 K-movie. Such movies cannot be analyzed in terms of their intensity fluctuations. In the following we will concentrate on the 130 K-movie, if not specified differently.

Spatial analysis of the CCD pattern

With the experience gained throughout the analysis of CXD data obtained during the last years, it is highly advisable to go through a basic analysis of the CCD pattern before directly analyzing the data in terms of an intensity autocorrelation. Otherwise the extracted time scales cannot be addressed to be characteristic for the dynamics of domain wall motions and domain reorganizations.

In the previous section we have confirmed that the conditions are stable for the 130 K-movie. In this section we will have a closer look to the intensity distribution recorded with the CCD. This is closely related to the CCD detection mechanism.

We start with a vertical line profile through the peak obtained from a single frame (Fig. 5.4). One can clearly identify characteristic count heights at specific discrete values. An accumulation of count heights around 2000 can be seen by eyes. The width of each plateau is 2 to 4 pixels and corresponds to the speckle size. To further understand the distribution of the count heights it is necessary to translate the counts into photons. Every x-ray photon creates one electron-hole pair per 3.65 eV photon energy [171], resulting in 2214 electron-hole pairs for 8.08 keV photons. The accurate conversion fac-

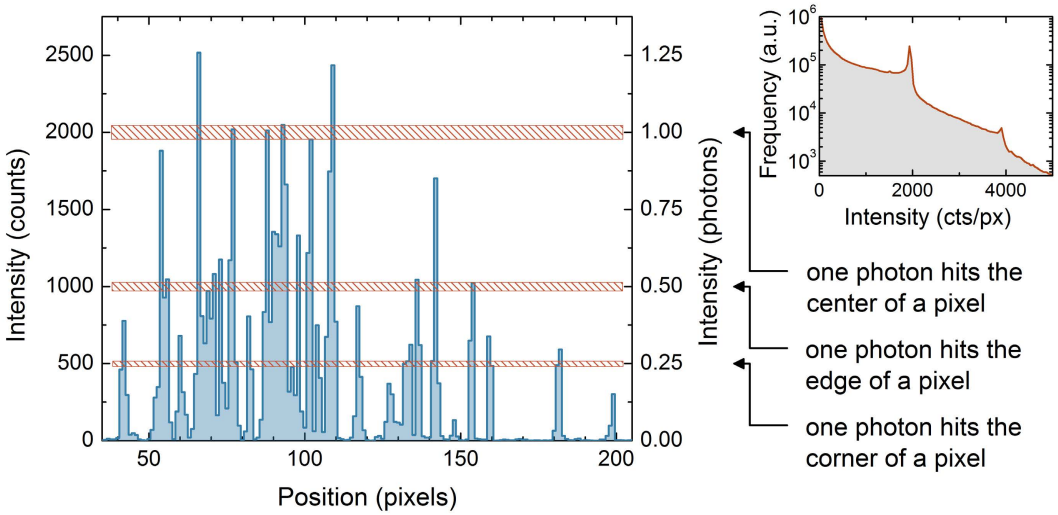

Fig. 5.4.: The main figure (left) shows a vertical line profile of the first CCD frame taken from the movie of the charge order reflex of ErCaTiO at 130K. An accumulation of intensities around 2000 counts that indicate one single photon impact can be found in this line profile. In the histogram of the whole movie (upper right) this value can clearly be seen. Furthermore a peak around 4000 counts indicates a two photon impact. Depending on the exact photon impact within the CCD depletion area, these 2000 counts distribute on a number of pixels, thus producing any possible intensity value.

tor further depends on the settings of the CCD camera and is communicated by the beamline scientist of ID10A to be roughly 2000. With this value the count rates can be converted into photons and the discrete values that are present in the line profile can be assigned to different processes that are described on the right of the diagram.

A single photon that hits the depletion area of the CCD will produce charge carriers that can be detected in the adjacent pixels. Every photon can therefore be detected in different ways. First it can hit a pixel in the central region and all counts are attributed to this pixel. Furthermore it can hit the edge of adjacent pixels and produce shared counts in both pixels. At last it can hit near the corner of a pixel and produce counts in 3 to 4 adjacent pixels. Depending on the exact photon impact location and depth within the depletion layer any value between these discrete processes is possible. This pixel sharing is clearly visible in the histogram of the whole movie (Fig. 5.4 upper right), where a clear peak is visible around 2000 and 4000 counts, which indicates one and two photon impacts, respectively. Any value between zero and the maximal intensity can be found back in the histogram. Note that a logarithmic scale was used in the histogram. The peak around 2000 counts further confirms the counts-to-photons conversion factor. With the conversion factor the number of photons that are detected per second in the CCD during the 130 K-movie can be calculated to be around 7000.

The CCD image in Fig. 5.3 shows the graininess of the intensity in the peak profile as expected for a speckle pattern. The characteristic spatial dimensions of the pattern

is the speckle size and can be calculated by [172, 173]:

$$S = \lambda \cdot \frac{D}{L}, \tag{5.1}$$

where L is the aperture size, which determines the illuminated area of the sample and D is the sample to detector distance. Here $\lambda = 1.5 \cdot 10^{-10}$ m, $L = 10\,\mu$m, and $D = 1.69$ m give a speckle size of 26 µm at the detector distance, which is equal to 2 pixels.

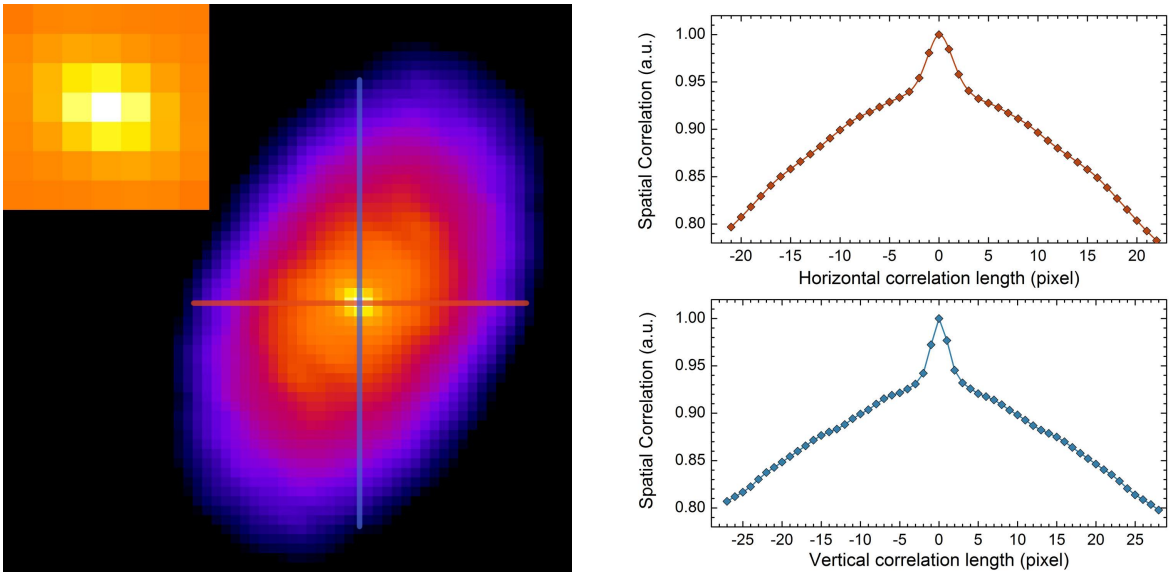

(a) **(b)**

Fig. 5.5.: (a) Spatial intensity autocorrelation of a 128×128 pixels clipping of the image shown in Fig. 5.3 (a) with a blow-up of the center region in the inset. The red and blue lines indicate the line profile that is plotted in the respective diagrams at the right. (b) Line profile through the center of the autocorrelated image, shown in (a), in horizontal (red) and vertical (blue) direction.

To check whether the speckle size agrees with the graininess of the pattern, the CCD image is spatially correlated. In this case the mean intensity pattern of the whole movie was used (Fig. 5.3 (a)). To improve the result, the autocorrelation was restricted to a region that contained most of the intensity. This way a contribution from the background, where no speckles should be visible, is minimized. The output image contains a correlated intensity at each pixel. The central pixel comprises the intensity of the autocorrelation of the image, while all the other pixels contain the intensity of the correlation of the image with a shifted copy of the image. The horizontal and vertical shift of the image is equal to the respective pixel distance from the center. The correlated image, including a blow-up of the central region in the inset, is shown in Fig. 5.5 (a). In (b) two line profiles, one passing the center of the autocorrelated image in horizontal and the other one in vertical direction, are shown. From these it is clearly visible that the recorded image contains a characteristic length scale of the order of 2 to 4 pixels, which is in good agreement with the calculated speckle size.

To check whether the pixel sharing, as discussed above, has any impact on the characteristic length scale of the images, the spatial correlation was repeated for an incoherently illuminated CCD image recorded during a temperature drift. Both the incoherent illu-

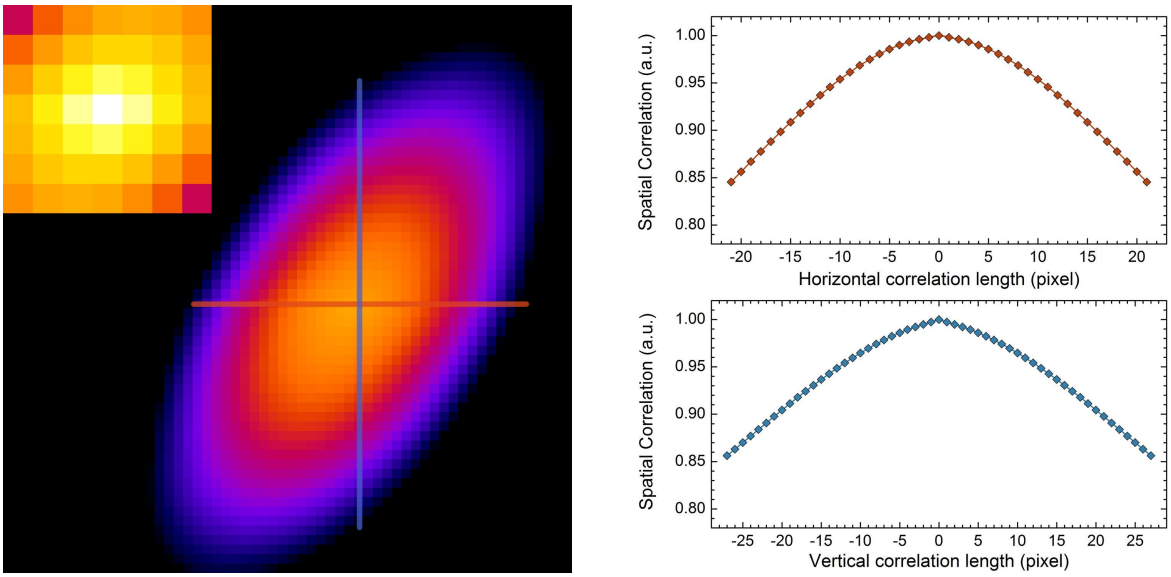

(a) **(b)**

Fig. 5.6.: (a) Spatial intensity autocorrelation of a 128×128 pixels clipping of an incoherently illuminated image (not shown) with a blow-up of the center region in the inset (different color scaling). The red and blue lines indicate the line profile that is plotted in the respective diagrams at the right. (b) Line profiles across the center of the autocorrelated image of (a) in horizontal (red) and vertical (blue) direction.

mination and the movement of the reflex across the CCD sensor during the temperature drift should lead to a pattern that does not show any speckle or fine structure. The autocorrelation of the pattern can therefore be used to determine the effect of pixel sharing. The results can be seen in Fig. 5.6. Although the inset of (a) shows a similar cross pattern as the inset of Fig. 5.5 (a), the autocorrelation is much smoother and does not show any sharp peak in the line profiles. Obviously, the pixel sharing does not visibly contribute to the peak in the autocorrelation of the coherent image. With this result it is confirmed that the coherent pattern of the charge order superstructure consists of speckles and a temporal analysis of the intensity fluctuations can be performed.

Temporal analysis of the CCD pattern

One of the main aspects in x-ray photon correlation spectroscopy (XPCS) is to study the temporal intensity variation of the speckles mentioned above. This kind of study is fairly new for single crystal studies and most frequently used in other materials, like colloids. To get an idea about the intensity variation, the temporal evolution of a vertical and horizontal line profile across the reflex is plotted in Fig. 5.7. The evolution shows the whole 1000 frames and therefore a time window of approximately 10 minutes. A

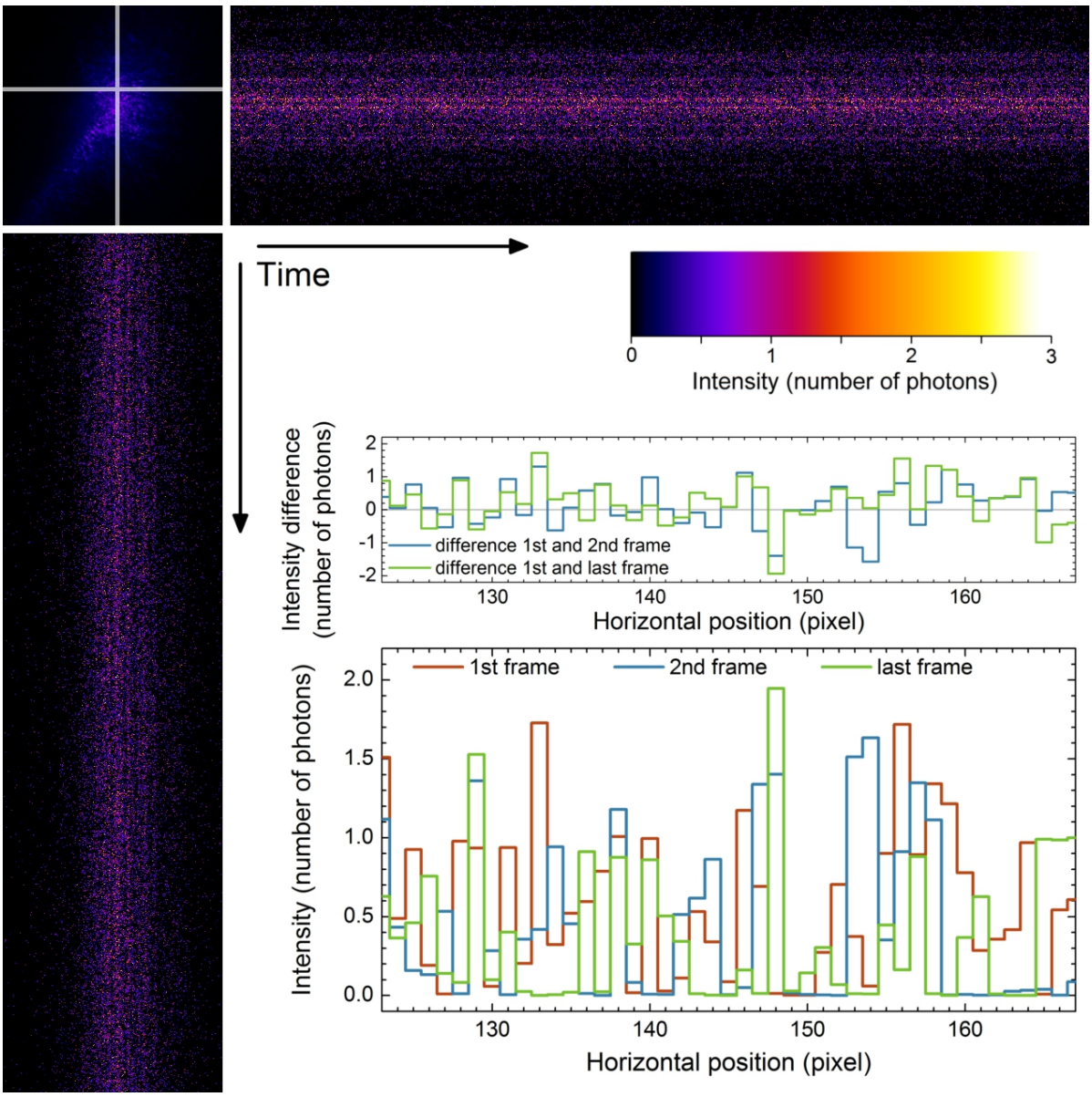

Fig. 5.7.: Temporal evolution of a vertical and horizontal line profile (marked by the light bar in the averaged image on the upper left) across the reflex. The evolution of the vertical (horizontal) line profile is shown in the upper right (lower left) image for the total 1000 frames. One can clearly identify speckles of different intensity, fluctuating on a higher or lower level. The intensity is scaled to the photon number between 0 and 3. The diagram in the lower right shows three horizontal line profiles from the first, the second, and the last frame, and the diagram in the middle the intensity difference with respect to the first frame. For a better visibility all profiles are restricted to a region of 44 pixels.

beating of the x-ray intensity with time and characteristic lines are visible in the temporal evolution of the line profiles (Fig. 5.7 upper right and lower left) . The line pattern is

produced by specific speckles that fluctuate on a higher or lower intensity level and the widths is determined by the speckle size. The intensity fluctuations correspond to what is expected of a dynamic speckle pattern in which speckles change their intensities due to a change in the interference of x-rays. A change in the domain pattern will change the interference conditions, varying from complete constructive to destructive interference and the speckle will light up or darken.

The diagram in Fig. 5.7 (lower right) shows a quantitative change of the photon intensity of a horizontal line profile of the first frame (red) in comparison to the second (blue) and the last frame (green). By eye one cannot find a closer relation between the first and the second frame than between the first and the last frame, which is confirmed by the profiles of the changes showing no systematic variation of the intensity with time (middle right). The diagrams are only exemplarily selected and represent the findings in the analysis of all the profiles. From this behavior one can already conclude that the time scale of the domain reorganization is either too slow and the system is still in an unstable dynamic situation or the time scale is too fast and the system has already approached a static situation. In this case the observed intensity fluctuations may arise from noise or instabilities, as discussed in the beginning.

To analyze the speckle intensity fluctuations, one first has to get an idea about the origin of these fluctuations. One possibility, which was already introduced, is a fluctuation due to domain reorganization. On the other site, the experiment consists of a complex CCD setup. This setup can introduce noise to the pattern. Therefore, it is important to compare the intensity variation with the noise level of the image. A detailed description of the different processes that contribute to the noise level of a CCD image can be found in App. A. As a subtraction of a dark image has already been done, readout noise and dark noise are accounted for, while only shot noise remains. Photon distributions are described by Poisson statistics for small events and approach a normal or Gaussian statistics for large numbers. In this limit the photon noise is given by the square root of the photon intensities in units of photon numbers. The information of the number of photons obtained in the previous section is therefore necessary to determine the noise level.

In Fig. 5.8 (a) a cut-out from the averaged image of the whole movie is shown, which displays the intensity in numbers of photons in the range from zero to one. In (b) the square root of the averaged image, which is equal to the photon noise in the high-photon limit, and in (c) the standard deviation of the whole movie are shown. The similarity between the standard deviation and the square root of the mean intensity gives a first quantitative indication that both are of the same order of magnitude.

For the case that the data show variations of the speckle intensity that are due to dynamics from the sample and which are superimposed by the photon noise one has to find a method to reduce the photon noise without reducing the intrinsic fluctuations. To reduce the photon noise, the data was summed in two different ways: first, a sequence of N frames was summed (frame-binning: F_N), and second, $n \times n$ pixels were summed (pixel-binning: $P_{n\times n}$). Therewith, the intensity per pixel increases and the relative (not absolute) photon noise can be reduced. In the limit of high counts the photon noise is equal to the square root of the intensity. Summation of $n \times n$ pixels and N frames will

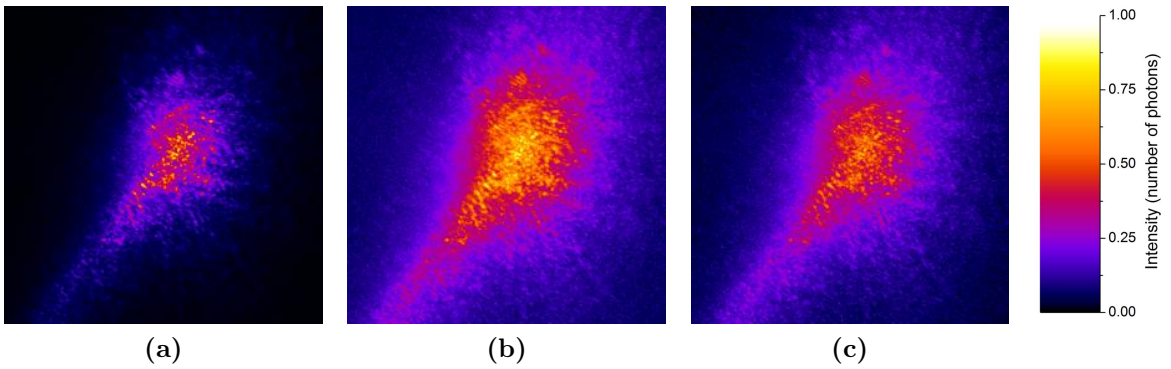

Fig. 5.8.: All three images show the same cut-out of the recorded data set. In (a) the mean intensity of all frames, in (b) the square root of the mean intensity and in (c) the activity is displayed

in average increase the intensity by a factor $I_{\text{bin}} = n \cdot n \cdot N$, whereas the noise is only increased by $\sqrt{n \cdot n \cdot N}$. The drawback is that the intensity fluctuations decrease. The influence of binning is best visible in a time series. In Fig. 5.9 a signal of a CCD-region is plotted versus time. The red curve shows the intensity of a single pixel, the blue and green curve of a binned pixel. Whereas binning can be used to increase the intensity per

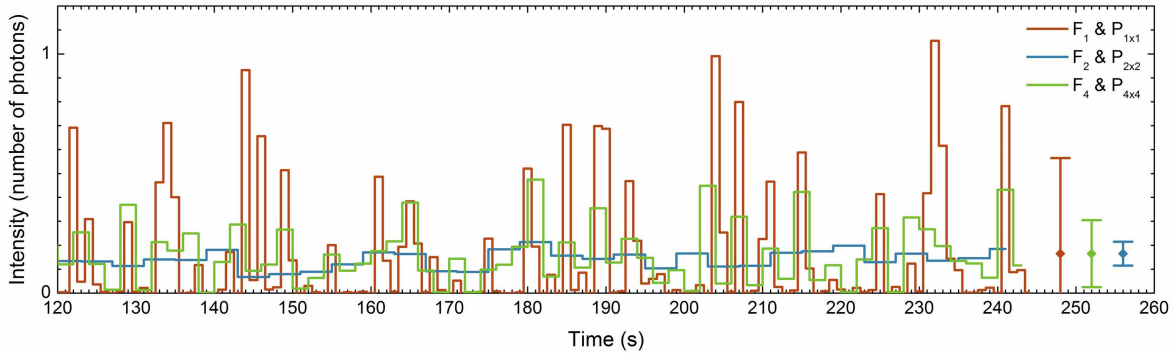

Fig. 5.9.: A time series of a single pixel or pixel cluster plotted for 120 s. The blue data are divided by 8 and the green data by 64. The binning of neighboring pixels ($P_{n\times n}$) and successive frames (F_N) increases the signal and reduces the noise. On the right side the mean value is shown by the colored circles and the square root of the mean value is used as error as valid in a Gaussian distribution.

pixel, the fluctuations are dramatically reduced. On the right side of the diagram the mean value and square root of the mean is displayed by the error bars. For the binned pixel the intensity, the mean value and the error are divided by I_{bin}.

Since we mainly record count numbers that belong to a single photon or even to a fraction of a photon (Fig. 5.4 and 5.7) the number of photons in our experiment is very low. For this reason, we use Poisson statistics to correctly analyze the fluctuations. The

Poisson distribution is given by:

$$P(x) = \frac{M^x \cdot e^{-M}}{x!},$$

in which $P(x)$ is the expected frequency for x and M is the mean or expectation value. A detailed analysis of the intensity fluctuations for different sets of binning and a comparison to the Poisson statistics is shown in Fig. 5.10. The analysis was carried out

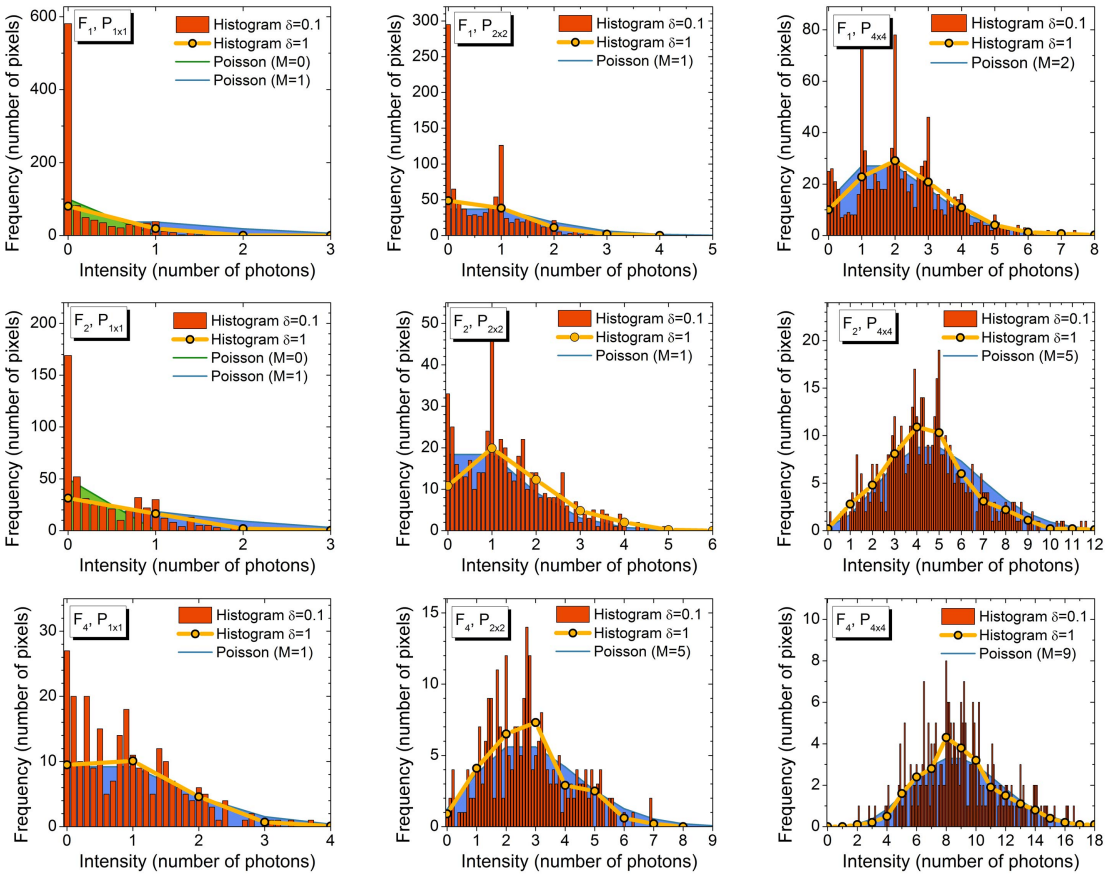

Fig. 5.10.: Histogram of a time-series of a single pixel or a pixel-cluster in comparison to Poisson statistics. The red bars show the histogram for a bin-size of 0.1 photons and the yellow symbols for a bin-size of 1 photon. In blue the Poisson distribution is plotted for the M value that is specified in each diagram. The pixel ($P_{n\times n}$) and frame-binnig (F_N) increases from upper left to lower right. The agreement between the Poisson distribution and the histogram is fairly well and indicates that the fluctuations arise from photon noise.

for different regions in the speckle pattern and is exemplarily depicted for a region in the center of the reflex. After binnig, the histogram of the resultant time series (red bar chart) was calculated. Since the Poisson distribution needs an integer mean value M as input (Eq. 5.4.1), the integer number that was closest to the mean value of the

times series was chosen. Especially for low counts the mean value was between 0 and 1. Therefore, the Poisson distribution (blue and green area) was calculated for both values. In all cases the Poisson distribution was scaled such that the integral was equal to the integral over the histogram. It is visible that the distribution describes the histogram fairly well, especially for higher binning. However, close to integer values, the discrepancy between the histogram and the Poisson distribution is large. If the bin-size of the histogram is increased (yellow circles) the agreement is much better, indicating that the discrepancy is due to the CCD detection mechanism, in which the charge carriers that are produced by a single photon impact are split between neighboring pixels.

To nevertheless follow the quantitative analysis, the intensity-intensity autocorrelation of different regions within the pattern was calculated. The g_2 autocorrelation function is defined as [173]:

$$g_2(\tau) = \frac{\langle I(t) \cdot I(t+\tau) \rangle_t}{\langle I(t) \rangle_t^2}, \tag{5.2}$$

where $I(t)$ is the intensity measured in a pixel or an area of the image at time t and $\langle\rangle_t$ denotes the time average. The g_2-function of a fluctuating time series has its maximum for $\tau = 0$, where every intensity is correlated with itself. For larger delays τ the g_2 typically approaches 1. After this period the intensity is completely uncorrelated. The autocorrelation-function of a static time series is always 1. In App. C some time series and their autocorrelation signals are presented. From there it is visible that a decay of the autocorrelation signal can be due to an oscillating and a de- or increasing signal. This justifies the intense pre-characterization that was done before.

To qualitatively determine the relaxation time τ_r and the contrast β a Kohlrausch-Williams-Watts (KWW) expression can be fitted to the autocorrelation [174]:

$$g_2(\tau) = 1 + \beta e^{-2(\tau/\tau_r)^\gamma}, \tag{5.3}$$

in which γ is an exponent that defines the shape of the decay. The KWW-function decays exponentially from $1 + \beta$ for $\tau = 0$ to 1. All parameters are positive.

The autocorrelation function was calculated from a $n \times n$ pixel spot in different regions of the sample. With increasing delay time the number of intensity pairs that is correlated decreases. Therefore, the g_2-function fluctuates much stronger at higher delay values. The g_2-functions that are shown in Fig. 5.11 are restricted to a delay time between 1 and 500 s. Beyond 500 s the noise was much stronger. The autocorrelation was recorded for different speckles in the reflex. In addition, the autocorrelation of a larger region in the center of the peak was calculated. The intensity autocorrelation of every pixel was calculated separately and averaged afterwards. From these results it is visible that the autocorrelation function drops down from its value at $\tau = 0$ and remains more or less static. To quantitatively check the decay of the g_2-function, a KWW-function (Eq. 5.3) was fitted to the autocorrelated data excluding the value for $\tau = 0$. Partly, a restriction of $\tau > 10$ was used if the $\tau > 0$ restriction gave a very small value that was only determined by the first data points. In all the data presented in Fig. 5.11 and in the data from other speckles in the pattern the KWW-fit was always constant. From

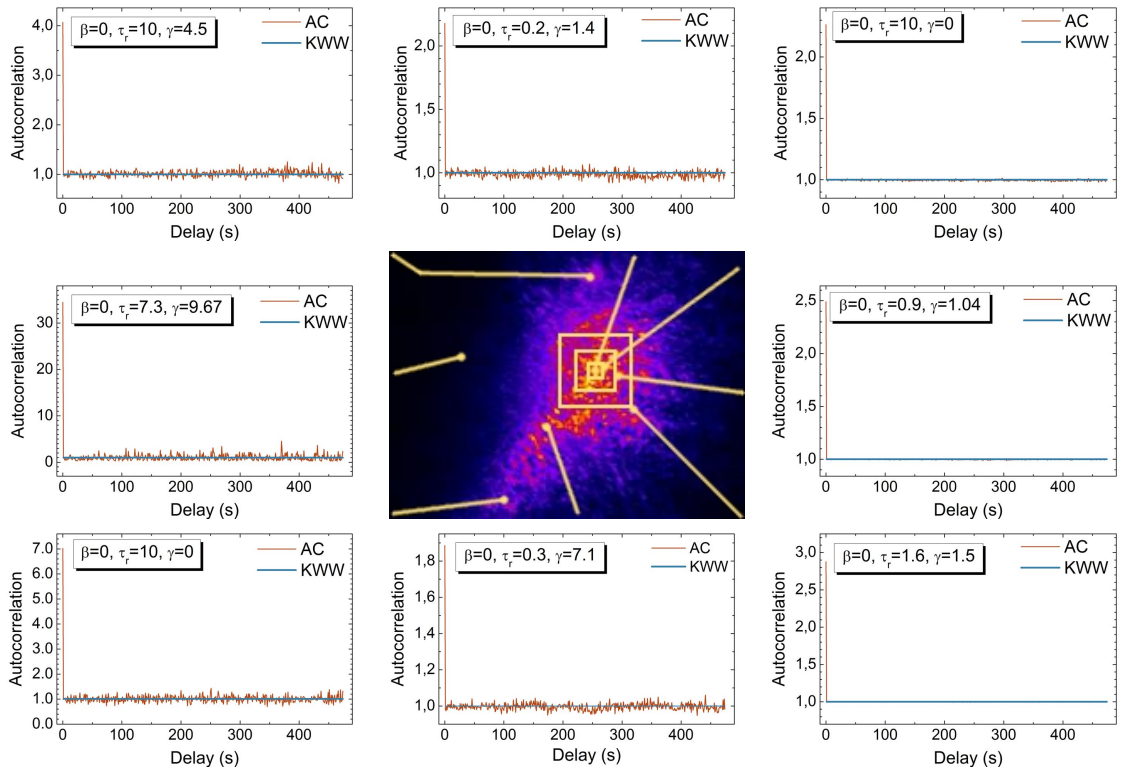

Fig. 5.11.: Autocorrelation and KWW-fit from different regions of the speckle pattern. The region that was correlated is indicated by the yellow lines in the speckle patter (middle). In the central region different sized areas were correlated (upper middle and right plots). The autocorrelation results oscillate around 1, which can only be understood if the intensity in the respective area is completely uncorrelated. The KWW-fit (Eq. 5.3) results are given in the boxes. In any case the contrast β vanished.

the autocorrelation we conclude that there is no ongoing dynamics with a characteristic time scale of seconds to minutes.

To exclude that there are long-term dynamics or fast dynamics that slowly vary in their magnitude, we further calculated the spatial contrast of each speckle pattern. The speckle contrast is given by [175]:

$$C = \frac{\sqrt{\langle I^2(x,y)\rangle_P - \langle I(x,y)\rangle_P^2}}{\langle I(x,y)\rangle_P}$$

in which $I(x,y)$ is the intensity at pixel (x,y) and $\langle\rangle_P$ denotes a pixel average. The speckle contrast was calculated for all frames of the movie and for all frame-binned speckle pattern with different F_N as visible from Fig. 5.12. The contrast is very stable over time and is reduced by frame-binning, as the superimposed contribution from the photon noise is reduced. The contrast for F_{50} is already close to the contrast of the

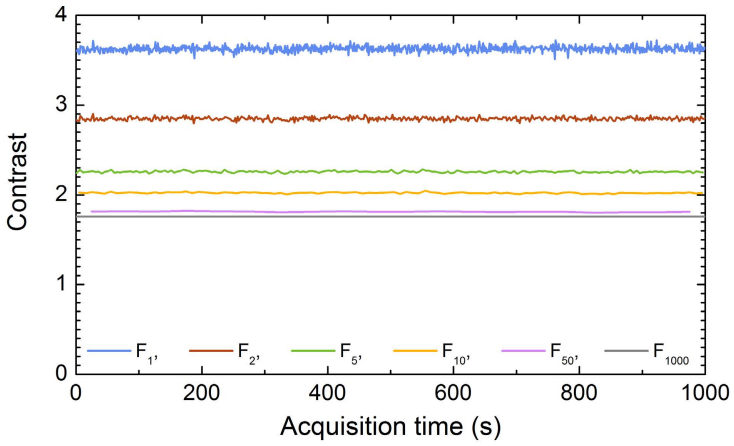

Fig. 5.12.: The spatial contrast of the speckle pattern is stable over time indicating that there are no long term dynamics within the acquisition time of several minutes. By binning N frames (F_N) the contrast is reduced. The grey curve (F_{1000}) is the lowest contrast determined from the sum over all frames.

averaged movie (F_{1000}). In both cases the contribution to the contrast arising from the photon noise is almost totally reduced. An averaged image will then show the static speckle pattern without any significant contribution from the photon noise.

Reciprocal space map of the reflex

Information about the exact orientation of the speckles on the pattern can be extracted by calculating the respective positions in reciprocal space. This is particularly important if dynamics are supposed to be addressed to the associated length scales. Although we did not find any dynamics, we will calculate the dimensions of the reflex in reciprocal space. For some basic information of how a CCD images cuts a reflex in reciprocal space see App. B. The coherently illuminated image of the reflex was used to calculate $(h\,k\,l)$ values for different positions on the CCD image (Fig. 5.13).

Evolution of the CCD pattern with temperature

Within the experiment at the ESRF some movies were taken during temperature changes. This was done with a fixed temperature gradient. The temperature range around the metal-insulator transition was scanned and the pattern was recorded. Figure 5.14 shows different patterns at temperatures between 80 and 190 K, which were recorded with a large and incoherent x-ray beam. Basically, every pattern consists of a round spot. For intermediate temperatures an elongated feature that runs diagonal across the detector evolves around 100 K and disappears above 170 K. Based on the reciprocal positions calculations in the previous section this elongated feature is roughly aligned along the body diagonal. The exact temperature values within this scan are not really reliable, as even after setting a temperature it took 30 minutes to one hour until the pattern did not change anymore.

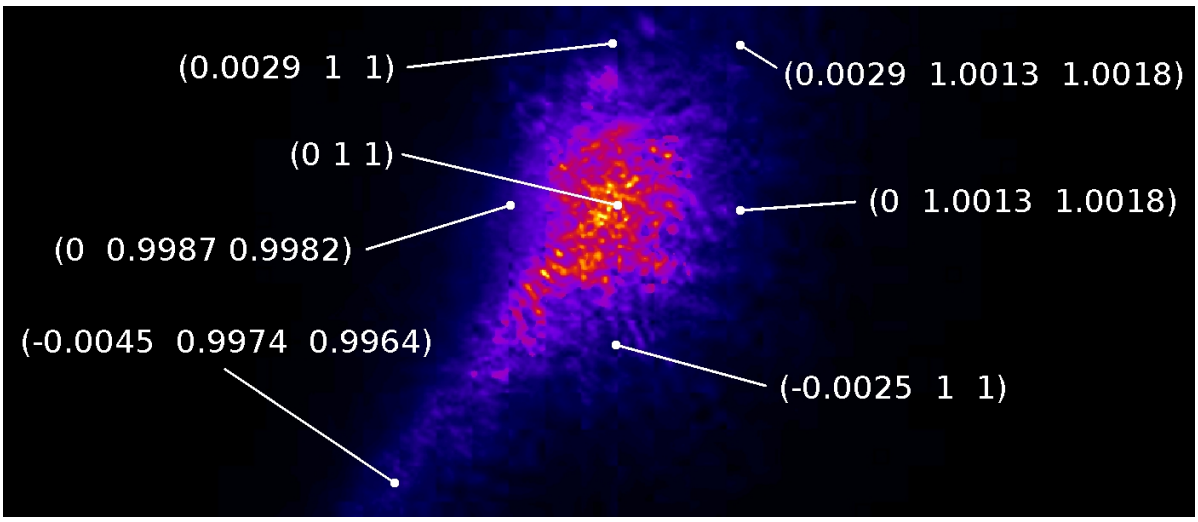

Fig. 5.13.: Respective (h k l) values that correspond to the positions marked on the CCD sensor and delimit the spatial extension of the reflex within the hard x-ray experiment.

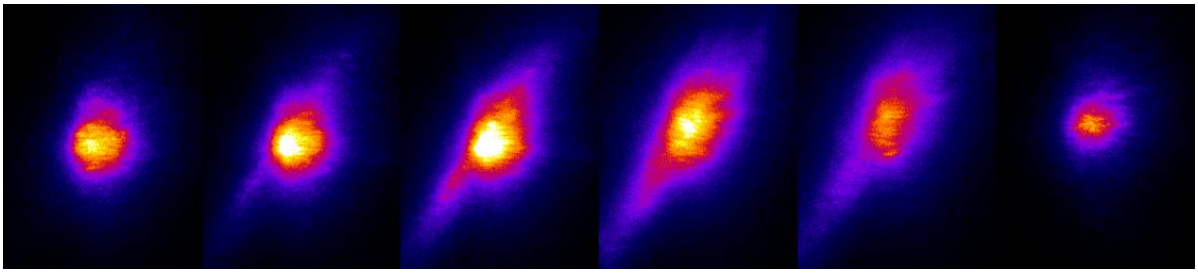

Fig. 5.14.: Temperature dependence taken during warm up. Temperature on the left is $\sim 80\,\mathrm{K}$ and on the right $\sim 190\,\mathrm{K}$. The vertical sample position was adjusted during the temperature sweep to compensate the expansion of the sample holder. The intensity variation between two pictures is therefore not always reliable. The shape of the pattern changes from a round spot to an ellipsoid at intermediate temperatures which is superimposed by an elongated feature and back to a round spot at higher temperatures.

5.4.2. High energy x-ray diffraction experiment at PETRA III

With the experience gained throughout the previous coherent x-ray diffraction experiments, including the development of an ultra-stable sample setup, another hard x-ray experiment was performed at PETRA III. Details on the ultra-bright synchrotron facility PETRA III can be found in Chap. 2. The experiments were performed at the P10 coherence applications beamline, which is well suited for coherent scattering experiments. A Princeton Instruments PI-LCX:1300 CCD camera was placed 1.4 m away from the sample, at a detector angle of roughly 20° in accordance with the 8.05 keV x-ray photons. The sensor consists of 1300×1340 pixels, each of them $20 \times 20\,\mu\mathrm{m}^2$ in size. The (0 1 1) oriented $Y_{0.64}Ca_{0.36}TiO_3$ sample, was mounted on a similar sample setup than the one which was used during the BESSY II experiments. The whole setup was installed

on a Huber 6-axis tower, which is placed on a two-circle diffractometer with horizontal scattering geometry. Cooling of the sample was done with a helium flow cryostat. First data of the (0 1 1) charge order reflex were taken during cooling. Below the MI transition a satellite reflection develops, which is weaker in intensity than the (0 1 1) main peak. To further analyze this satellite reflection, the main peak was blocked by a 1 mm thick wire, which was placed between the sample and the CCD. A few frames from a movie, taken during cooling from 140 to 85 K are shown in Fig. 5.15. Below 140 K the satellite

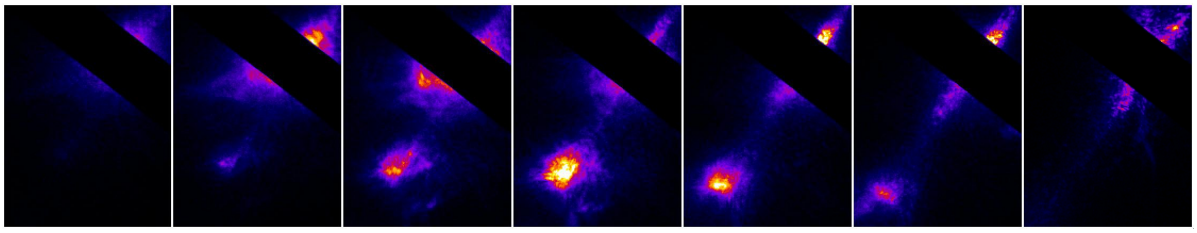

Fig. 5.15.: Evolution of the satellite during cooling from 140 to 85 K (from left to right). The satellite appears around 140 K and departs from the main peak, before he disappears below 85 K.

pops up and splits from the main peak. While the intensity of the satellite runs through a maximum at 120 K the intensity of the main peak decreases upon cooling. Around 100 K the satellite fades away and disappears around 85 K, whereas at the (0 1 1) peak position still some residual intensity remains. Further data were taken for fixed temperatures. As an example a movie that consists of 500 frames with an exposure time of 1 s was taken at a temperature of 117 K, which is approximately the temperature of the peak intensity maximum. An average image of the whole movie can be seen in Fig. 5.16 (a). From the histogram (b) the counts-to-photons conversion for the CCD camera at 8.05 keV is determined to be 850 counts per photon. With the conversion factor the number of photons that hit the detector per second within this movie is roughly 60000, from which approximately 20000 contribute to the satellite. Note that most of the photons are blocked by the wire. This enormous number of photons is attributed to the power of the new ultra-brilliant synchrotron facility PETRA III. In the following we will concentrate on the satellite. At 117 K the satellite appears at a position of (h k l)=(-0.0067 0.9966 0.9952) in reciprocal space. The temporal intensity profile of the satellite is plotted in the top diagram of Fig. 5.16 (c) and shows a lot of spikes that exceed the mean intensity by more than 20%. These sharp intensity maxima arise from the top-up mode of PETRA III. The horizontal and vertical center of mass (COM) positions of the satellite are stable within 1 pixel, although there might be some tendency of a slight drift in the vertical direction.

To determine the speckle size from the image a spatial correlation of a single frame was done. A cutout from the first frame that comprises the satellite peak is shown in Fig. 5.17 (a). The spatial autocorrelation from this single frame is shown in (b) and a horizontal line profile through the center of (b) is plotted as a red curve in (c). Interestingly, if N frames are binned and afterwards correlated, the sharp feature in the profile decreases for increasing N. This can be due to dynamic modulations of the

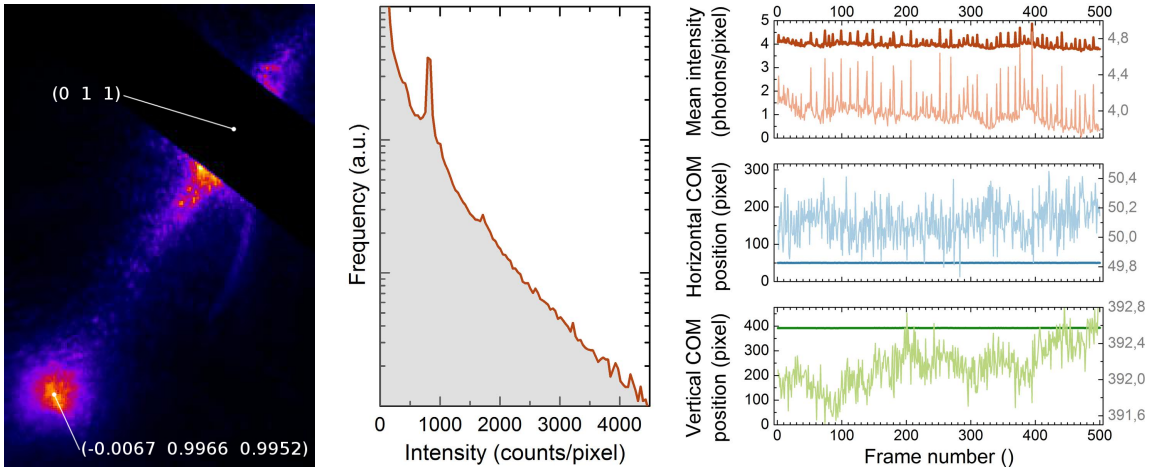

(a) (b) (c)

Fig. 5.16.: (a) Average image of the whole 117 K movie. The main peak is blocked by a wire. The satellite is located at (-0.0067 0.9966 0.9952) in the q-space. (b) Histogram of the movie. The peak at 850 counts indicates a single photon impact, the two photon impact peak at 1700 is hardly visible. (c) Mean intensity and center of mass position of the satellite plotted against the frame numbers within the whole movie.

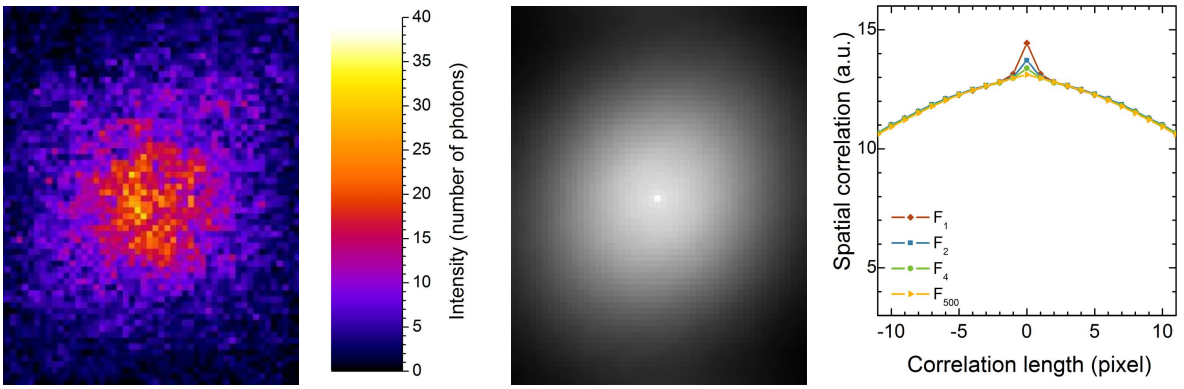

(a) (b) (c)

Fig. 5.17.: (a) Intensity of the satellite peak recorded during a single exposure of 1 s. The coherent flux of the P04 beamline yields a maximum of 40 photons/(pixel·s). (b) The spatial correlation of the single frame that is shown in (a). From the sharp maximum in the center of the image the speckle size can be extracted. (c) The speckle size is best visible in a single frame and gets less pronounced if calculated for an image which results by binning of N frames (F_N).

intensity, but can as well stem from the slight drift that is visible in the COM positions (Fig. 5.16) and comparably large to the extracted speckle size of 1 to 2 pixel. From Eq. 5.1 the speckle size on the detector is calculated to be 21 µm and matches 1 pixel (20 µm).

Unfortunately, even after hours the conditions were not stable to record data that can be analyzed in terms of an intensity-autocorrelation. In a second beamtime at PETRA III, at which I did not participate, static speckle pattern were found as well.

5.4.3. Soft x-ray diffraction experiments at BESSY II

Further XPCS experiments were performed at the UE46-PGM1 soft x-ray beamline of the Helmholtz-Zentrum Berlin at BESSY II. During a series of beamtimes within one and a half year the sample setup was improved to provide a stable sample environment. Besides $Er_{0.6}Ca_{0.4}TiO_3$ (ErCaTiO), $Y_{0.64}Ca_{0.36}TiO_3$ (YCaTiO) samples were used. All soft x-ray experiments were performed under UHV conditions. Within these beamtimes two different diffractometers were used, both designed at the FU Berlin [57, 58]. An Princeton Instruments PI-SX:2048 CCD camera, with a 2048×2048 pixel sensor, was placed in a distance of roughly 1 m from the center of the chamber to allow for a good resolution of the speckle pattern. An image of the setup can be seen in Fig. 2.4 (lower right). Each of the CCD pixels is $13 \times 13\,\mu m^2$ in size. Since the detector is placed in the extension of one of the diffractometer ports, the energy as well as the detector angle have to be chosen such that they match the diffractometer design. A larger detector angle requires lower energies, which give a higher photon flux in this energy regime. Therefore, a photon energy of 1400 eV ($\lambda = 8.8 \cdot 10^{-10}$ m) was chosen. At this energy the detector angle for the (0 1 1) charge order reflex is roughly 155°. A 10 µm pinhole was used to enhance the coherence of the incident soft x-rays. Further descriptions of the setup are given in Chap. 2 and of coherence in Chap. 1.

Comparison of coherent scattering with hard and soft x-rays

Although the output of the first beamtimes was limited by the instability of the sample setup, the recorded data can be used to demonstrate the differences in a soft x-ray experiment at BESSY II and a hard x-ray experiment at the ESRF and PETRA III.

Therefore, a movie taken from ErCaTiO at 150 K was analyzed. In Fig. 5.18 (a) an average of the movie is shown. This movie consists of 10 frames, each of them exposed to the scattered x-rays for 5 min. From the histogram of the whole movie the conversion factor from counts to photons is determined to be 255 counts/photon, meaning that 240 photons/s are detected on the CCD within this movie. This justifies the long exposure time. The coherent photon flux at BESSY II within this experiment is thus smaller by a factor of 30 if compared to the ESRF, and by, at least, another order of magnitude if compared to the coherent flux at PETRA III. In the latter case, the exact comparison is difficult, as part of the intensity was blocked during the PETRA III experiment and we have used different samples.

We continue with a comparison of the speckle size. The speckle size, given in Eq. 5.1, is proportional to the used wavelength. In the case of the BESSY experiment, the 10 µm pinhole defines a speckle size of 88 µm on the detector. This length corresponds to approximately 7 pixels on the detector. Similar to the hard x-ray data, the average image in Fig. 5.18 (a) can be spatially autocorrelated to experimentally obtain the speckle

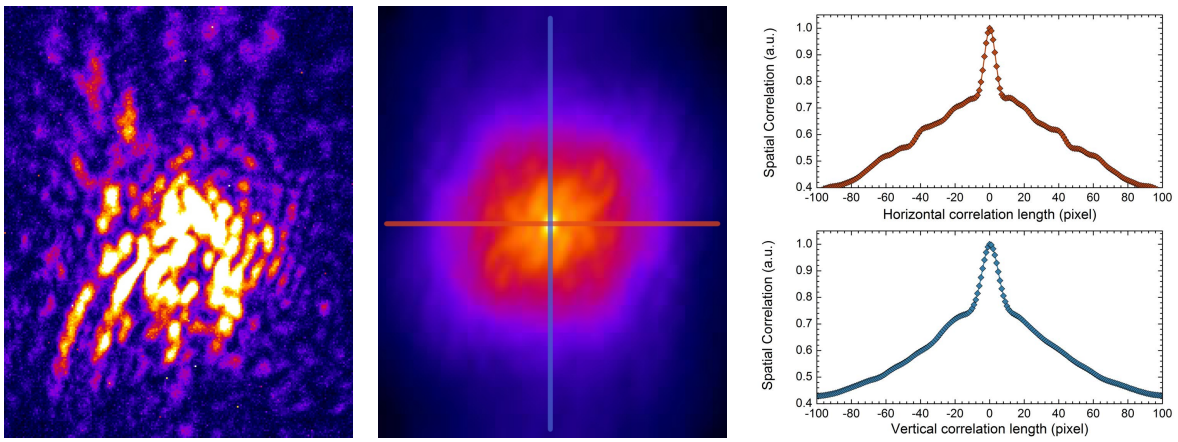

(a) **(b)** **(c)**

Fig. 5.18.: (a) Averaged image of the ErCaTiO charge order reflection at 150 K studied with coherent soft x-rays. (b) Spatial correlation of the averaged patter. Blue and red lines mark a vertical and horizontal line profile through the center which are shown in (c).

size. In (b) the autocorrelated image and in (c) the line profiles through the center are shown. The calculated speckle size of 7 pixels is, therefore, reproduced. This result nicely demonstrates that coherent x-ray experiments can be performed with soft x-rays even off resonance, and that, although the detector is closer as in both hard x-ray experiments, the speckle size is more than 3 times larger. This makes it possible to use an in-vacuum CCD camera in a soft x-ray experiment (Chap. 2).

The cut through reciprocal space that is performed in a soft x-ray experiment is different from the one in a hard x-ray experiment. For comparison the CCD pattern in Fig. 5.18 (a) was used to calculate the *hkl*-values that were probed within the soft x-ray experiment. These reciprocal space positions are compared to the *hkl*-dimensions obtained in the ESRF-experiment (Fig. 5.13). In Fig. 5.19 the *hkl*-values for different points on the CCD image are denoted. These positions can be used to construct a reciprocal-space map. The cut through a peak in reciprocal space within a CCD image depends on the wavelength that is used in the experiment. The q-profile of a detector scan within a soft (dark red circle) and a hard (light red circle) x-ray experiments is shown in Fig. 5.20 (a). As the experiment is tuned such that the (0 1 1) charge order reflex can be probed with both energies, both circles cross at this point in reciprocal space. During a CCD image a segment of the circle (or sphere in three dimensions) that depends on the dimensions and location of the CCD is recorded. If we neglect that the peak may have a different shape in both experiments we can mark the reciprocal space position from both experiments and fit the shape of the peak, assuming it is elliptical, to the four data points. A zoom of Fig. 5.20(a) is shown in (b), in which the spacing of the grid is 0.001 r.l.u. in both reciprocal directions. The green marker correspond to the positions that are delimited by the spatial dimensions of the peak on the CCD images for the hard and soft x-ray experiment (Fig. 5.13 and 5.19). The possible dimensions

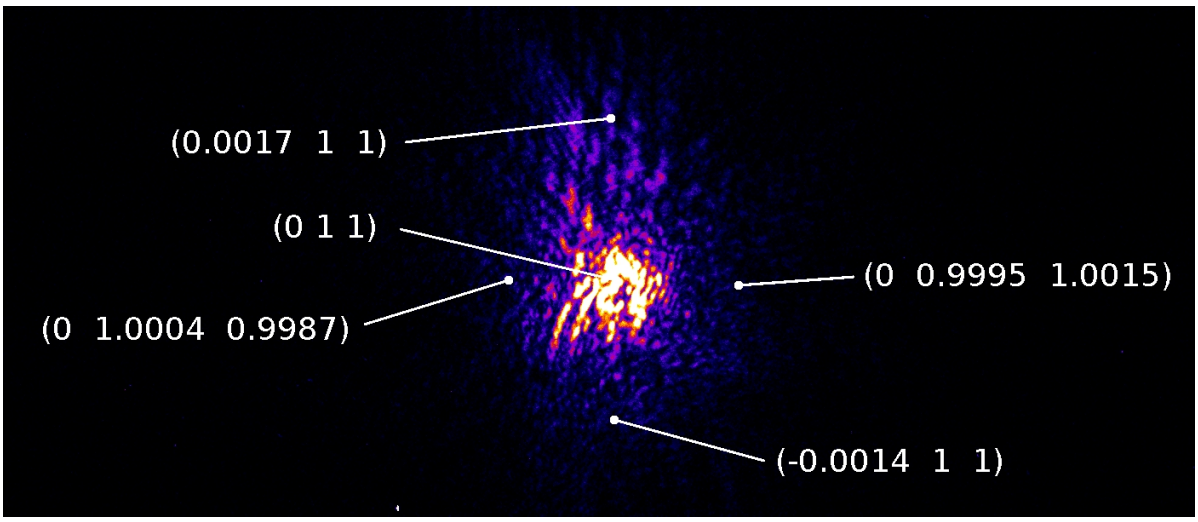

Fig. 5.19.: Respective (h k l) values that correspond to the positions marked on the CCD sensor and delimit the spatial extension of the reflex within the soft x-ray experiment.

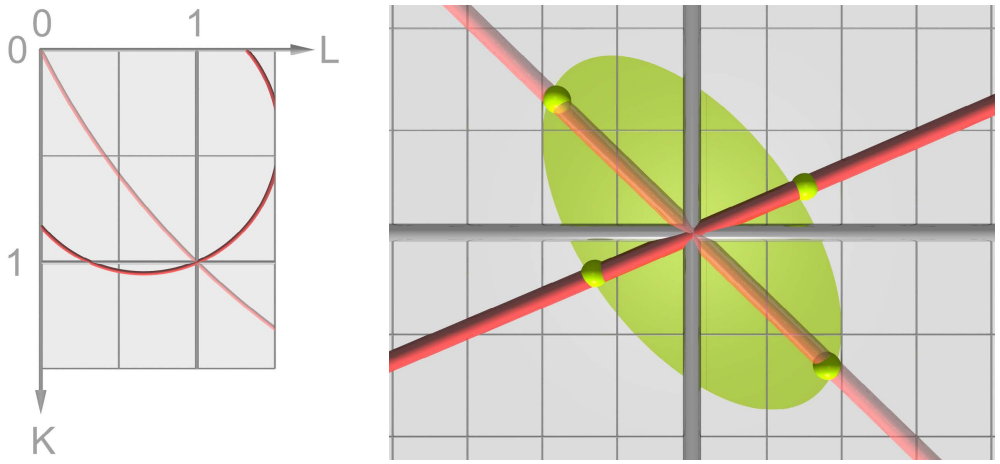

(a) **(b)**

Fig. 5.20.: (a) Detector scans with hard (light red) and soft (dark red) x-rays in reciprocal space. In two dimensions a detector scan is a circle, in three dimensions a spherical shell. (b) Zoom in to the charge order reflex position (0 1 1). The grid spacing is 0.001 r.l.u. (reciprocal lattice units). The positions of the green markers are taken from the CCD images and determine the dimensions of the peak.

of the reflex are delimited by the green elongated ellipse, which has an elongated axis along the diagonal and a shorter axis perpendicular to that.

5.5. Discussion

We have shown the feasibility of coherent soft and hard x-ray diffraction experiments. In all experiments the speckle patterns from the (0 1 1) charge super structure reflex

show a fine structure that can be attributed to the interference of metallic and charge-ordered insulating regions. The calculated speckle length was always retrieved from the experimental data. A comparison of soft and hard x-ray coherent diffraction has shown an increased speckle size. This is especially important for our new UHV diffractometer that was presented in Chap. 2, in which the in-vacuum CCD is mounted much closer to the sample.

One of the struggling difficulties is the stability of the experimental conditions. From the ESRF data only a small number of movies were found in which the peak did not significantly move across the detector. The analysis of the temporal intensity fluctuations in all these data revealed a static speckle pattern, which is superimposed by photon statistics. This was exemplarily shown in detail for one data set. In the soft x-ray experiments the sample setup was redesigned completely and a slightly modified version was used in the PETRA III experiments. However, we were not able to record any reliable data in the first PETRA III beamtime. In a second beamtime at PETRA III our findings from the ESRF, in which we could not find any dynamics on the time scales of minutes to hours, were confirmed.

From this we conclude that domain reorganizations and domain-wall movements in $Er_{0.6}Ca_{0.4}TiO_3$ and $Y_{0.64}Ca_{0.36}TiO_3$ take place on even shorter time scales than we were able to access in our experiments. The domain pattern changes with temperature and locks into a static configuration at each fixed temperature. Within all experiments is was experimentally difficult to distinguish fluctuations coming from the setup and those from dynamics within the sample. Experiments at new x-ray free electron facilities are promising to extend the search to even shorter time scales.

Summary and Perspective

Diffraction experiments offer an essential tool box to study condensed-matter systems with ordered phases. This dissertation deals with the application of resonant soft and coherent x-ray diffraction to study different ordered phases in transition-metal oxides.

To account for the requirements of resonant and coherent x-ray diffraction experiments a new UHV soft x-ray diffractometer was built up and commissioned. As the centerpiece of the experiment, the diffractometer has to allow for an independent movement of the sample and the detectors. The combination of a differentially pumped rotary feedthrough with a sufficiently large main chamber has shown its ability to carry complex detector installations, like an in-vacuum CCD. The power of such an area-resolved detector has been demonstrated on a simple example, in which a single scan of the sample rotation has been used to construct an reciprocal space map of the magnetic (001) reflex in $La_{2-2x}Sr_{1+2x}Mn_2O_7$ (LSMO) at the Mn-L_3 edge. From this reciprocal space map it is possible to directly extract all kind of scans that are typically performed with a point detector. First experiments with the new instrument have confirmed a successful interplay between all components. In combination with modern state-of-the-art detector installations and a stable CXD setup, the apparatus will allow to perform new kind of experiments and record more information during data acquisition.

The interplay between superconductivity and novel ordering phenomena like charge and spin stripe order is an ongoing matter of debate. For the first time we have found charge stripe order in the prototypical high-T_c superconductor $La_{1.88}Sr_{0.12}CuO_4$ (LSCO) by means of RSXD at the Cu-$L_{2,3}$ and O-K absorption edges. Remarkably, these findings differ from extensive search with complementary techniques. Clear evidence for the charge stripe ordering comes from comparison of diffraction spectra taken in LSCO and a $La_{1.48}Nd_{0.4}Sr_{0.12}CuO_4$ (LNSCO) reference sample, in which the existence of charge and spin stripes is well established. Further evidence for a charge modulation comes from the temperature dependence and peak positions in LSCO, which show exactly the behavior expected for charge stripe formation; however, we did not find any indications for charge stripe order in our bulk-sensitive high-energy x-ray experiments. Therefore,

we attribute the charge modulations to form in the near-surface area only. From the comparison of ex-situ polished and in-situ cleaved samples we can exclude an influence of the surface preparation method. The largest in-plane correlation length of about 5 nm, found in an a-oriented sample at the O-K edge, gives an estimation of the minimum thickness of the ordered near-surface layer, which can be much larger if an arrangement of 5 nm thick charge ordered regions is assumed. The charge ordered region comprises at least 14 unit cells and is thus not only stabilized in the first surface layers. The different findings in the hard and soft x-ray diffraction experiments emphasize that the bulk and near-surface region can have dramatically distinct properties. This has to be taken into account if results of surface or moderately surface-sensitive techniques, including RSXD, are interpreted in terms of bulk properties, and reconfirms that the study with complementary techniques, like neutron or high energy diffraction, is essential for a full understanding. Further investigations, especially of the octahedral tilting in the surface area, should answer the question whether charge stripe order can be found in a LTO phase as well or whether the formation of a LTT phase near the surface promotes charge stripe ordering in LSCO.

In our RSXD experiment in magnetite (Fe_4O_4) we have investigated the linear dichroic azimuthal dependence of the $(0\,0\,\frac{1}{2})$ charge-orbital order reflex and found a low-symmetry pattern. The pattern can only be accurately described by symmetry considerations if a monoclinic distortion is assumed. This is quite remarkable since, until the refinement within this year, structural investigations had only been possible using orthorhombic constraints. Our observation of a low-symmetry pattern, prior to the low-symmetry refinements of the structure, clearly shows the high sensitivity of RSXD experiments to the local electronic wave function symmetry. RSXD is thus an appropriate technique to search for systems in which the electronic symmetry deviates from the structural symmetry. With the new refinements of the crystal structure we find that the electronic symmetry fully matches the symmetry of the crystallographic lattice. Interestingly, a stabilization of a complex-coefficient orbital order with monoclinic symmetry was found in a three band Hubbard model calculation performed by A. Tanaka, assuming the orthorhombic lattice symmetry. Our experimental findings are correctly predicted by the complex-coefficient orbital ordering model and could not be described by the real coefficient orbital order models from Jeng et al. and Leonov et al. Further evidence for complex-coefficient orbital order in magnetite comes from the theoretical prediction of a circular dichroism in the diffraction signal, which we could verify experimentally. Thus, the question arises whether the stabilization of the low-symmetry complex-coefficient orbital order might be the cause or driving mechanism of the structural phase transition.

Coherent x-ray diffraction (CXD) experiments of phase-separated $Er_{0.6}Ca_{0.4}TiO_3$, showing a mixture of metallic and charge-ordered insulating regions, have shown to be feasible in the low and high energy x-ray regime. Studying the domain-wall dynamics of phase-separated systems is essential to connect macroscopic properties with the local electronic structure. This remains an open question in many materials, as for example in CMR-manganites, in which the CMR effect is believed to be caused by a reorganization of a small fraction of the sample. To provide a stable sample environment for CXD experiments, a new sample stage was developed in cooperation with the Uni-

versity of Amsterdam. In the analysis of the speckle pattern, which is the interference pattern of the (0 1 1) diffraction peak contributions from coherently illuminated charge ordered regions, we could not find any dynamics attributed to domain-wall motion on the time scales of minutes to hours. From this we conclude that domain-wall fluctuations take place on much shorter time scales and that the sample turns from one static to another static configuration during temperature changes. New x-ray free electron facilities, like LCSL or the upcoming European XFEL, offer a novel opportunity to study the domain-wall dynamics on much shorter time scales.

RSXD experiments have shown to be an essential tool to unravel the nature of complex electronic materials. With the advancing miniaturization and increasing interest in exploring the physics of interfaces they will be useful to detect ordering phenomena of even small layers. CXD in TMOs, which can as well be performed in resonance (RCXD), is a promising and fairly new tool. Extremely stable experimental conditions, suitable systems showing fluctuations on respective time scales, and modern x-ray sources are crucial to make use of the full potential of this technique.

APPENDIX A

CCD Noise

The CCD camera was invented in the late 1960s by George E. Smith and Williard Boyle [176], for which they were honored by the Nobel prize medal in 2009. To determine the statistical deviations within a CCD image, it is important to know the different mechanism that contribute to the noise. Therefore, we will give a short introduction into the basic operation mechanism of a charge-coupled device. Photons that hit the photoactive region of a CCD create an electric charge, which is proportional to the photon energy and number, at the surface of the semiconductor. In their original work [176] Boyle and Smith used a MOS capacitor that accumulates the charge. After the exposure process the readout takes place. During the readout time every capacitor moves its charge to its neighbor in a pre-defined direction. The last capacitor transfers the charges, one after another, to a charge amplifier, in which the amount of charge is amplified and read out. This complex process and the required design of a CCD introduce noise into every exposure, which is unwanted and can only partly be handled or reduced.

To start with, **dark noise** is generated in every pixel, even if not exposed to light. The amount of dark noise strongly depends on the temperature of the device and is effectively reduced by cooling the CCD chip A typical operating temperature is around -40°C. Furthermore, a dark image, which should be taken immediately before or after the image acquisition, can be subtracted from the exposed image to account for the residual dark intensity. A typical dark image can be seen in Fig. A.1. The distribution of darker and brigther pixels is random and as well strongly temperature dependent. Dark images should always be taken in the same settings as the image itself and, if possible, a small series should be taken, which is averaged afterwards.

Besides the dark noise, every pixel can have a different sensitivity to light (**pixel non-uniformity**). This can be compensated by recording a so-called flat-field image, where the CCD sensor is exposed to a homogeneous light source. The flat-field image can be used for normalization. This is especially important if intensities of different

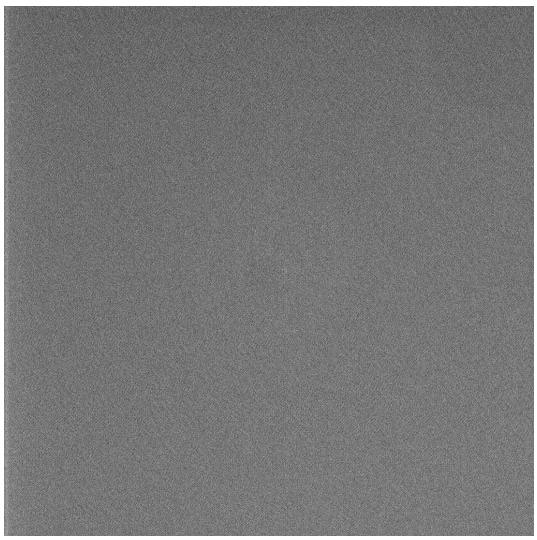

(a)

Fig. A.1.: Dark image taken with an ANDOR IkonM CCD camera during the ESRF photon-correlation beamtime.

pixels of the CCD should be compared. In a photon-correlation experiment, with its focus on the temporal intensity variation of an unchanged area, pixel non-uniformity can be neglected.

The readout process, which is based on conversion of the charge to a voltage and an analog to digital (A/D) conversion, introduces further noise, the so-called **readout noise**. The amount of readout noise is typically given in electrons RMS (root mean square) by the manufacturer, but can also be determined by recoding a bias image, which is an exposure with zero or almost zero length exposure time. However, readout noise is already accounted for by recording the dark image. Unlike dark noise, readout noise can be reduced by binning. As a bonus, the read out time is reduced by binning, as the most time consuming part of the read out is the digitization of the signal.

To be complete, as a CCD camera is a highly complex instrument, which contains of many electronical components that interact in a sophisticated manner, a cross-talk of all these components via **electronic interference** is always possible. To minimize these effects an elaborated design and setup of the camera is important, which makes a scientific CCD camera a costly part of the equipment, which has to be handled with care.

While all these noise sources are mainly inherent in the device itself, the **photon** or **shot noise** depends on the random arrival of the photons. The probability is described by a Poisson distribution and determines the noise level. In the high photon limit the photon statistics are described by a Gaussian or normal distribution and it follows that the photon noise is equal to the square root of the number of photons that hit the respective pixel.

The above mentioned information on noise generated in a CCD camera and even more detailed information on technical details of CCD cameras can be found online, on the

webpages of well-known CCD manufacturers, like Princeton Instruments or Hamamatsu [177, 178].

APPENDIX B

Scans in Reciprocal Space

The aim of this appendix is to discuss the exact cut through reciprocal space which is recorded by a detector in a specific diffraction geometry. This can be any kind of detector, although the focus is on an area detector like a CCD camera. The main difference is that the point detector gives back a single integrated value only, while the area detector resolves the recorded intensity pixelwise. The angular acceptance is usually chosen to

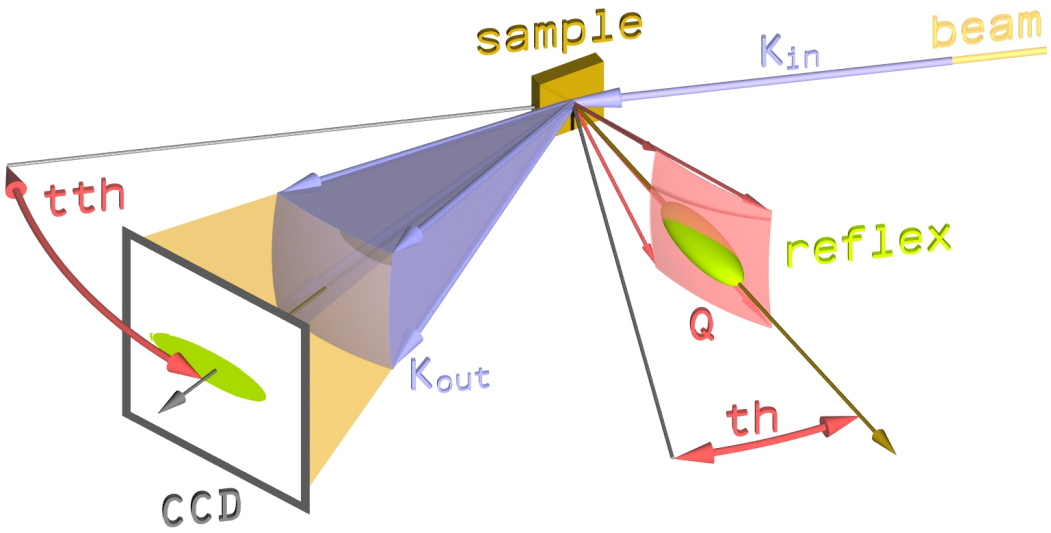

Fig. B.1.: Setup of a diffraction experiment with a CCD camera detector. Note that the schematic drawing is a mixture of real space and reciprocal space objects. For further information, please see text.

be much smaller for a point detector, like a photo diode, than for an area detector. To start with, the typical experimental setup, which is schematically shown in Fig. B.1 is described in the following. Afterwards the most common scans are described.

The incident x-ray beam hits the sample, is diffracted and recorded by the CCD detector. In this simplified scheme only two possible movements are discussed. These are the sample rotation (*th*) and the detector rotation (*tth*). *Th*= 0° is defined as the sample surface normal is perpendicular to the incident beam, while *th* is equal to 90° if the sample is facing the beam. The detector rotation *tth* is defined as zero for a sample to detector axis that is parallel to the incident beam, while the CCD sensor faces the x-ray source. The direction of rotation is defined to be positive for a counter-clockwise rotation if looking from the top. The incident x-ray photons are defined in direction and energy by the wavevector $\mathbf{k}_{\text{in}}$, the diffracted x-ray photons by the outgoing wavevector $\mathbf{k}_{\text{out}}$. As it is visible in Fig. B.1 an area detector collects various outgoing wavevectors. In the case of elastic scattering, where $|\mathbf{k}_{\text{out}}| = |\mathbf{k}_{\text{out}}| = k$, all of them end on the intersection of a sphere with radius k and the detector angular acceptance volume, which is indicated in Fig. B.1 by the transparent orange volume. The scaling of the reciprocal space to the real space is arbitrarily chosen for best visibility.

The q-space of the sample is directly connected to the sample and rotated in the same way as the sample is rotated. As an example the reflex, which is displayed in light green, is located in the direction of the surface normal at a specific point in q-space and extends to certain amount in all three reciprocal directions, most elongated along the surface normal direction. B.2. As an example the reflex is may be located at (0 0 1), as

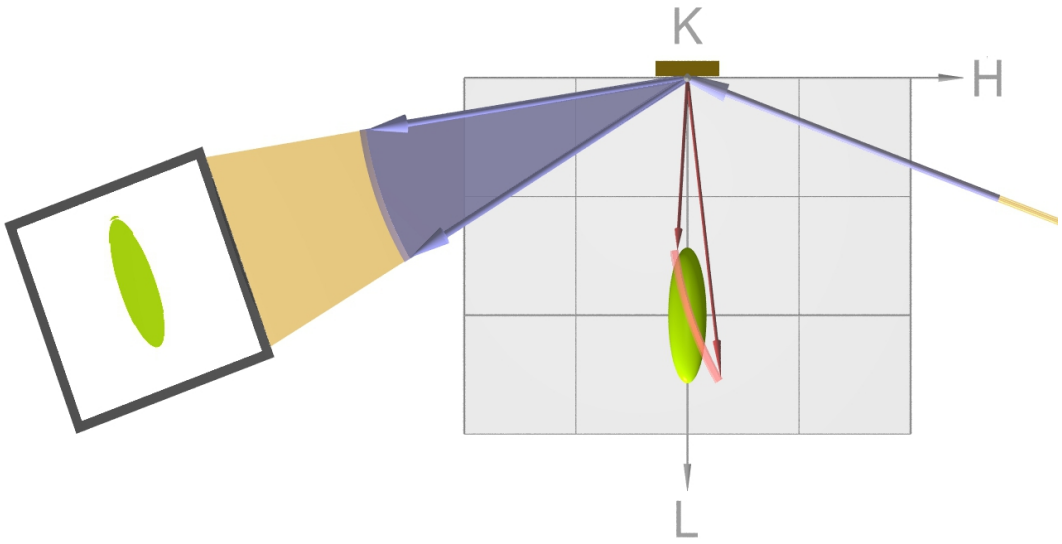

Fig. B.2.: Top view of the scattering geometry. Every pixel of the CCD camera collects photons with a different outgoing wave vector $\mathbf{k}_{\text{out}}$ (blue arrows pointing towards the CCD sensor. The point in reciprocal space that is probed by the pixel is given by $\mathbf{q} = \mathbf{k}_{\text{out}} - \mathbf{k}_{\text{in}}$ (dark red arrows). The whole CCD sensor probes a spherical cut through the reflex as indicated by the light red spherical segment.

visible in the top view of the setup (Fig. B.2). The cut through reciprocal space that is probed by the CCD camera is determined by $\mathbf{q} = \mathbf{k}_{\text{out}} - \mathbf{k}_{\text{in}}$, which is a translation by $-\mathbf{k}_{\text{in}}$ of the whole spherical segment of endpoints $\mathbf{k}_{\text{out}}$. This object is indicated by

the transparent red spherical shell segment that crosses the reflex. The thickness of this spherical shell segment is determined by the energy spread of the incident photons.

The CCD camera image is then the projection of the intensity within this volume on the CCD chip. By tuning the detector and sample angle, this probing volume can be used to map the reciprocal space in different ways. Here a closer look to a transversal, a detector and a radial scan is given. In the first one, the sample is rotated only, in the second the detector only and in the third both are rotated, leading to a sequence of different cuts of the reciprocal space.

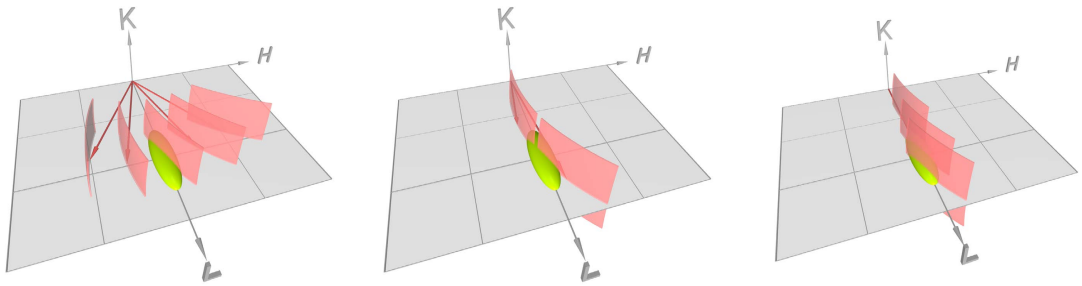

(a) **(b)** **(c)**

Fig. B.3.: Transversal (a), detector (b) and radial (c) scans. The volume that is probed by the CCD is displayed in light red and partly intersects the reflex in reciprocal space (light green). In (a) the sample only is rotated, in (b) the detector only and in (c) both are rotated, resulting in different series cuts through the reflex.

In the case of the transversal scan, the probing volume is rotated around the origin of reciprocal space, with its center thus defining a circle with radius $q = |\mathbf{q}|$. Depending on the size of the CCD sensor, the dimension of the reflex in reciprocal space and the sample angles, the reflex can be fully mapped by this kind of scan. In a detector scan, the probing volume which is a segment of a sphere is rotated around its own center. Thus a detector scan essential probes always the same cut through the reflex and is only useful if the reflex extents the detector angular acceptances. In a radial scan, the probing volume is shifted along a radial direction, while slightly rotated around its own. This leads to a more complex map of the reflex, but can be used if the dimension along a specific direction has to be determined.

Depending on the orientation of the probing volume and the dimensions of the reflex, the reflex can be mapped completely by using the above described scans. Furthermore the energy of the incident x-ray photons, the sample surface orientation and its azimuthal alignment can be tuned to extent the accessible reciprocal space and map a fraction of interest. The collected data can be used to rebuild the reciprocal object, taking into account that the recorded cuts are of spherical curvature and aligned under different angles with respect to each other. In this way it is possible to get back a three-dimensional image of reciprocal space objects.

APPENDIX C

Autocorrelation

The autocorrelation of a time series yields information about the characteristic time scales. Three examples of a constant, a sinusoidal and a linear intensity signal and their autocorrelations are shown in Fig. C.1. Interestingly, the autocorrelation of an oscillating and a linear signal are very similar. This should emphasize that (1) it is of crucial importantance to provide experimentally stable conditions since drift in the signal that are due to the setup will be visible in the autocorrelation, and (2) from the autocorrelation one cannot state whether the time series is oscillating or drifting.

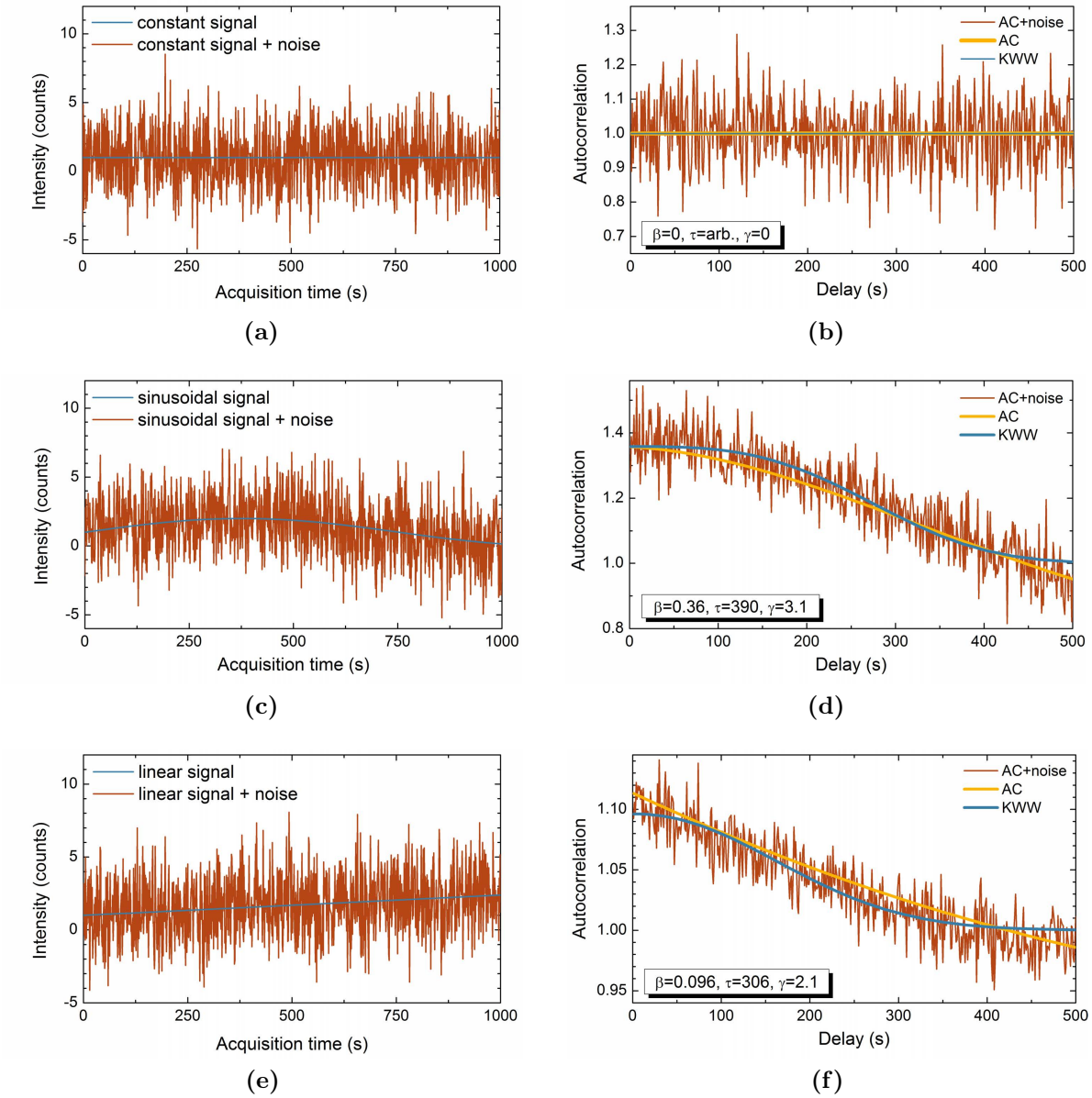

Fig. C.1.: Intensity autocorrelation (b,d,f) of three different signals (a,c,e): (a) constant signal, (c) a sinusoidal signal , and (e) a linear signal. The blue (red) lines are the signal and the autocorrelation without (with) noise. The yellow lines are the KWW-fit (EQ. 5.3). The fit results are listed in the boxes.

Bibliography

[1] J. G. Bednorz and K. A. Müller, Possible high-T_c superconductivity in the Ba-La-Cu-O system, Zeitschrift für Physik B Condensed Matter **64**, 189–193 (1986).

[2] C. Rao, Transition-metal oxides, Annual Review of Physical Chemistry **40**, 291–326 (1989).

[3] A. Haghiri-Gosnet and J. Renard, CMR manganites: physics, thin films and devices, Journal of Physics D: Applied Physics **36**(8), R127–R150 (2003).

[4] M. Imada, A. Fujimori, and Y. Tokura, Metal-insulator transitions, Rev. Mod. Phys. **70**, 1039–1263 (1998).

[5] E. Dagotto, Complexity in Strongly Correlated Electronic Systems, Science **309**(5732), 257–262 (2005).

[6] B. Raveau, M. Hervieu, A. Maignan, and C. Martin, The route to CMR manganites: what about charge ordering and phase separation?, Journal of Materials Chemistry **11**(1), 29–36 (2001).

[7] H. Y. Hwang, Y. Iwasa, M. Kawasaki, B. Keimer, N. Nagaosa, and Y. Tokura, Emergent phenomena at oxide interfaces, Nature Materials **11**(2), 103–113 (2012).

[8] A. V. Boris, Y. Matiks, E. Benckiser, A. Frano, P. Popovich, V. Hinkov, P. Wochner, M. Castro-Colin, E. Detemple, V. K. Malik, C. Bernhard, T. Prokscha, A. Suter, Z. Salman, E. Morenzoni, G. Cristiani, H. U. Habermeier, and B. Keimer, Dimensionality Control of Electronic Phase Transitions in Nickel-Oxide Superlattices, Science **332**(6032), 937–940 (2011).

[9] S.-W. Cheong, Transition metal oxides: The exciting world of orbitals, Nature Materials **6**(12), 927–928 (2007).

[10] J. Chakhalian, J. W. Freeland, H.-U. Habermeier, G. Cristiani, G. Khaliullin, M. van Veenendaal, and B. Keimer, Orbital reconstruction and covalent bonding at an oxide interface, Science **318**(5853), 1114–1117 (2007).

[11] E. Dagotto, Physics - When oxides meet face to face, Science **318**(5853), 1076–1077 (2007).

[12] N. Reyren, S. Thiel, A. D. Caviglia, L. F. Kourkoutis, G. Hammerl, C. Richter, C. W. Schneider, T. Kopp, A.-S. Ruetschi, D. Jaccard, M. Gabay, D. A. Muller, J.-M. Triscone, and J. Mannhart, Superconducting interfaces between insulating oxides, Science **317**(5842), 1196–1199 (2007).

[13] S. Wolf, D. Awschalom, R. Buhrman, J. Daughton, S. von Molnar, M. Roukes, A. Chtchelkanova, and D. Treger, Spintronics: A spin-based electronics vision for the future, Science **294**(5546), 1488–1495 (2001).

[14] W. Eerenstein, N. D. Mathur, and J. F. Scott, Multiferroic and magnetoelectric materials, Nature **442**(7104), 759–765 (2006).

[15] T. Kimura, T. Goto, H. Shintani, K. Ishizaka, T. Arima, and Y. Tokura, Magnetic control of ferroelectric polarization, Nature **426**(6962), 55–58 (2003).

[16] J. van den Brink and D. I. Khomskii, Multiferroicity due to charge ordering, Journal of Physics: Condensed Matter **20**(43), 434217 (2008).

[17] J. B. Goodenough, Theory of the Role of Covalence in the Perovskite-Type Manganites [La, M(II)]MnO_3, Phys. Rev. **100**, 564–573 (1955).

[18] D. Gibbs, D. R. Harshman, E. D. Isaacs, D. B. McWhan, D. Mills, and C. Vettier, Polarization and Resonance Properties of Magnetic X-Ray Scattering in Holmium, Phys. Rev. Lett. **61**, 1241–1244 (1988).

[19] J. P. Hannon, G. T. Trammell, M. Blume, and D. Gibbs, X-Ray Resonance Exchange Scattering, Phys. Rev. Lett. **61**(10), 1245–1248 (1988).

[20] C. Vettier, Neutrons and X-rays: two probes for magnetism, Physica B: Condensed Matter **192**(1-2), 1 – 13 (1993).

[21] C. Schüßler-Langeheine, E. Weschke, A. Yu, H. Grigoriev, H. Ott, R. Meier, D. Vyalikh, C. Mazumdar, C. Sutter, D. Abernathy, G. Grübel, and G. Kaindl, Resonant magnetic X-ray scattering from ultrathin Ho metal films down to a few atomic layers, Journal of Electron Spectroscopy and Related Phenomena **114 - 116**(0), 953 – 957 (2001).

[22] P. Abbamonte, L. Venema, A. Rusydi, G. Sawatzky, G. Logvenov, and I. Bozovic, A structural probe of the doped holes in cuprate superconductors, Science **297**(5581), 581–584 (2002).

[23] P. Abbamonte, G. Blumberg, A. Rusydi, A. Gozar, P. Evans, T. Siegrist, L. Venema, H. Eisaki, E. Isaacs, and G. Sawatzky, Crystallization of charge holes in the spin ladder of Sr14Cu24O41, Nature **431**(7012), 1078–1081 (2004).

[24] P. Abbamonte, A. Rusydi, S. Smadici, G. Gu, G. Sawatzky, and D. Feng, Spatially modulated 'Mottness' in La2-xBaxCuO4, Nature Physics **1**(3), 155–158 (2005).

[25] A. Rusydi, P. Abbamonte, H. Eisaki, Y. Fujimaki, G. Blumberg, S. Uchida, and G. A. Sawatzky, Quantum Melting of the Hole Crystal in the Spin Ladder of $Sr_{14-x}Ca_xCu_{24}O_{41}$, Phys. Rev. Lett. **97**, 016403 (2006).

[26] U. Staub, V. Scagnoli, A. M. Mulders, K. Katsumata, Z. Honda, H. Grimmer, M. Horisberger, and J. M. Tonnerre, Orbital and magnetic ordering in $La_{0.5}Sr_{1.5}MnO_4$ studied by soft x-ray resonant scattering, Phys. Rev. B **71**, 214421 (2005).

[27] S. B. Wilkins, N. Stojić, T. A. W. Beale, N. Binggeli, C. W. M. Castleton, P. Bencok, D. Prabhakaran, A. T. Boothroyd, P. D. Hatton, and M. Altarelli, Resonant soft x-ray scattering investigation of orbital and magnetic ordering in $La_{0.5}Sr_{1.5}MnO_4$, Phys. Rev. B **71**, 245102 (2005).

[28] C. Schüßler-Langeheine, J. Schlappa, A. Tanaka, Z. Hu, C. F. Chang, E. Schierle, M. Benomar, H. Ott, E. Weschke, G. Kaindl, O. Friedt, G. A. Sawatzky, H.-J. Lin, C. T. Chen, M. Braden, and L. H. Tjeng, Spectroscopy of Stripe Order in $La_{1.8}Sr_{0.2}NiO_4$ Using Resonant Soft X-Ray Diffraction, Phys. Rev. Lett. **95**, 156402 (2005).

[29] J. Schlappa, C. Schüßler-Langeheine, C. F. Chang, H. Ott, A. Tanaka, Z. Hu, M. W. Haverkort, E. Schierle, E. Weschke, G. Kaindl, and L. H. Tjeng, Direct Observation of t_{2g} Orbital Ordering in Magnetite, Phys. Rev. Lett. **100**, 026406 (2008).

[30] C. F. Chang, J. Schlappa, M. Buchholz, A. Tanaka, E. Schierle, D. Schmitz, H. Ott, R. Sutarto, T. Willers, P. Metcalf, L. H. Tjeng, and C. Schüßler-Langeheine, Intrinsic and extrinsic x-ray absorption effects in soft x-ray diffraction from the superstructure in magnetite, Phys. Rev. B **83**, 073105 (2011).

[31] A. Tanaka, C. F. Chang, M. Buchholz, C. Trabant, E. Schierle, J. Schlappa, D. Schmitz, H. Ott, P. Metcalf, L. H. Tjeng, and C. Schüßler-Langeheine, Symmetry of Orbital Order in Fe_3O_4 Studied by Fe $L_{2,3}$ Resonant X-Ray Diffraction, Phys. Rev. Lett. **108**, 227203 (2012).

[32] F. de Groot, X-ray absorption of transition metal oxides: An overview of the theoretical approaches, Journal of Electron Spectroscopy and Related Phenomena **62**(1 - 2), 111 – 130 (1993).

[33] C. T. Chen, L. H. Tjeng, J. Kwo, H. L. Kao, P. Rudolf, F. Sette, and R. M. Fleming, Out-of-plane orbital characters of intrinsic and doped holes in $La_{2-x}Sr_xCuO_4$, Phys. Rev. Lett. **68**, 2543–2546 (1992).

[34] B. T. Thole, G. van der Laan, and G. A. Sawatzky, Strong Magnetic Dichroism Predicted in the $M_{4,5}$ X-Ray Absorption Spectra of Magnetic Rare-Earth Materials, Phys. Rev. Lett. **55**, 2086–2088 (1985).

[35] G. Schütz, W. Wagner, W. Wilhelm, P. Kienle, R. Zeller, R. Frahm, and G. Materlik, Absorption of circularly polarized x rays in iron, Phys. Rev. Lett. **58**, 737–740 (1987).

[36] C. T. Chen, F. Sette, Y. Ma, and S. Modesti, Soft-x-ray magnetic circular dichroism at the $L_{2,3}$ edges of nickel, Phys. Rev. B **42**, 7262–7265 (1990).

[37] Y. Wu, J. Stöhr, B. D. Hermsmeier, M. G. Samant, and D. Weller, Enhanced orbital magnetic moment on Co atoms in Co/Pd multilayers: A magnetic circular x-ray dichroism study, Phys. Rev. Lett. **69**, 2307–2310 (1992).

[38] J. Stöhr, Exploring the microscopic origin of magnetic anisotropies with X-ray magnetic circular dichroism (XMCD) spectroscopy, Journal of Magnetism and Magnetic Materials **200**(1-3), 470–497 (1999).

[39] J. Chen, D. J. Huang, A. Tanaka, C. F. Chang, S. C. Chung, W. B. Wu, and C. T. Chen, Magnetic circular dichroism in Fe $2p$ resonant photoemission of magnetite, Phys. Rev. B **69**, 085107 (2004).

[40] M. M. Schwickert, G. Y. Guo, M. A. Tomaz, W. L. O'Brien, and G. R. Harp, X-ray magnetic linear dichroism in absorption at the L edge of metallic Co, Fe, Cr, and V, Phys. Rev. B **58**, R4289–R4292 (1998).

[41] J. Kuneš, P. Oppeneer, S. Valencia, D. Abramsohn, H.-C. Mertins, W. Gudat, M. Hecker, and C. Schneider, Understanding the XMLD and its magnetocrystalline anisotropy at the $L_{2,3}$-edges of $3d$ transition metals, Journal of Magnetism and Magnetic Materials **272**, 2146 – 2147 (2004).

[42] J. B. Kortright and S.-K. Kim, Resonant magneto-optical properties of Fe near its $2p$ levels: Measurement and applications, Phys. Rev. B **62**, 12216–12228 (2000).

[43] J. Fink, E. Schierle, E. Weschke, and J. Geck, Resonant elastic soft x-ray scattering, arXiv:1210.5387 , 1–110 (2012).

[44] D. H. Templeton and L. K. Templeton, Tetrahedral anisotropy of x-ray anomalous scattering, Phys. Rev. B **49**, 14850–14853 (1994).

[45] V. E. Dmitrienko, Forbidden reflections due to anisotropic X-ray susceptibility of crystals, Acta Crystallographica Section A **39**(1), 29–35 (Jan 1983).

[46] V. E. Dmitrienko, K. Ishida, A. Kirfel, and E. N. Ovchinnikova, Polarization anisotropy of X-ray atomic factors and 'forbidden' resonant reflections, Acta Crystallographica Section A **61**(5), 481–493 (2005).

[47] J. Hill and D. McMorrow, X-ray resonant exchange scattering: Polarization dependence and correlation functions, Acta. Cryst. A **52**(Part 2), 236–244 (1996).

[48] S. Di Matteo, Which orbital and charge ordering in transition metal oxides can resonant X-ray diffraction detect?, Journal of Physics: Conference Series **190**, 012008 (2009).

[49] M. W. Haverkort, *Spin and orbital degrees of freedom in transition metal oxides and oxide thin films studied by soft x-ray absorption spectroscopy*, PhD thesis, Universität zu Köln, 2005.

[50] K. D. Finkelstein, Q. Shen, and S. Shastri, Resonant x-ray diffraction near the iron K edge in hematite (α-Fe_2O_3), Phys. Rev. Lett. **69**, 1612–1615 (1992).

[51] S. Di Matteo, Y. Joly, and C. R. Natoli, Detection of electromagnetic multipoles by x-ray spectroscopies, Phys. Rev. B **72**, 144406 (2005).

[52] private communication with M. W. Haverkort.

[53] J. Als-Nielsen and D. McMorrow, *Elements of Modern X-Ray Physics*, John Wiley & Sons, 2001.

[54] K. Balewski, COMISSIONING OF PETRA III, Proceedings of IPAC 2010 (2010).

[55] K. Balewski, W. Brefeld, W. Decking, H. Franz, R. Roehlsberger, and E. Weckert, PETRA III: A Low Emittance Synchrotron Radiation Source - Technical Design Report, (2004).

[56] J. S. Lee, B. H. Seung, T. Y. Khim, H. Jang, K. T. Ko, B. G. Park, J. H. Park, K. B. Lee, and J. Y. Kim, Ultrahigh-vacuum-compatible diffractometer for soft X-ray scattering, Journal of the Korean Physical Society **52**(6), 1814–1817 (2008).

[57] E. Schierle, *Antiferromagnetism in thin films studied by resonant magnetic soft x-ray scattering*, PhD thesis, Freie Universität Berlin, 2006.

[58] V. Soltwisch, *Stripes and Cycloids - Komplexe Ordnungsphänomene in Übergangsmetalloxiden*, PhD thesis, Freie Universität Berlin, 2011.

[59] W. Jark and J. Stör, A high-vacuum triple-axis-diffractometer for soft X-ray scattering experiments, Nuclear Instruments and Methods in Physics Research Section A: Accelerators, Spectrometers, Detectors and Associated Equipment **266**(1-3), 654 – 658 (1988).

[60] D. G. Hawthorn, F. He, L. Venema, H. Davis, A. J. Achkar, J. Zhang, R. Sutarto, H. Wadati, A. Radi, T. Wilson, G. Wright, K. M. Shen, J. Geck, H. Zhang, V. Novák, and G. A. Sawatzky, An in-vacuum diffractometer for resonant elastic soft x-ray scattering, Review of Scientific Instruments **82**(7), 073104 (2011).

[61] T. Gau, Y. Jean, K. Liu, C. Chung, C. Chen, S. Lai, C. Shu, Y. Huang, C. Chao, Y. Lee, C. Chen, and S. Chang, Soft X-ray diffractometer for synchrotron radiation, Nuclear Instruments & Methods in Physics Research Section A: Accelerators Spectrometers Detectors and Associated Equipment **466**(3), 569–575 (2001).

[62] S. B. Wilkins, M. P. M. Dean, J. Fink, M. Hücker, J. Geck, V. Soltwisch, E. Schierle, E. Weschke, G. Gu, S. Uchida, N. Ichikawa, J. M. Tranquada, and J. P. Hill, Comparison of stripe modulations in $La_{1.875}Ba_{0.125}CuO_4$ and $La_{1.48}Nd_{0.4}Sr_{0.12}CuO_4$, Phys. Rev. B **84**, 195101 (2011).

[63] T. A. W. Beale, T. P. A. Hase, T. Iida, K. Endo, P. Steadman, A. R. Marshall, S. S. Dhesi, G. van der Laan, and P. D. Hatton, RASOR: An advanced instrument for soft x-ray reflectivity and diffraction, Review of Scientific Instruments **81**(7) (2010).

[64] T. Takeuchi, A. Chainani, Y. Takata, Y. Tanaka, M. Oura, M. Tsubota, Y. Senba, H. Ohashi, T. Mochiku, K. Hirata, and S. Shin, An ultrahigh-vacuum apparatus for resonant diffraction experiments using soft x rays (h nu=300-2000 eV), Review of Scientific Instruments **80**(2) (2009).

[65] S. Konings, *Pinning of magnetic domains studied with resonant x-rays*, PhD thesis, Universiteit van Amsterdam, 2007.

[66] J. D. Axe, A. H. Moudden, D. Hohlwein, D. E. Cox, K. M. Mohanty, A. R. Moodenbaugh, and Y. Xu, Structural phase transformations and superconductivity in $La_{2-x}Ba_xCuO_4$, Phys. Rev. Lett. **62**, 2751–2754 (1989).

[67] D. Vaknin, S. K. Sinha, D. E. Moncton, D. C. Johnston, J. M. Newsam, C. R. Safinya, and H. E. King, Antiferromagnetism in La_2CuO_{4-y}, Phys. Rev. Lett. **58**, 2802–2805 (1987).

[68] P. Bourges, L. Regnault, J. Henry, C. Vettier, Y. Sidis, and P. Burlet, Spin dynamics in the metallic state of the high-T_c superconducting system $YBa_2Cu_3O_{6+x}$, Physica B: Condensed Matter **215**(1), 30 – 40 (1995).

[69] M. Vojta, Lattice symmetry breaking in cuprate superconductors: stripes, nematics, and superconductivity, Advances in Physics **58**(6), 699–820 (2009).

[70] B. Keimer, A. Aharony, A. Auerbach, R. J. Birgeneau, A. Cassanho, Y. Endoh, R. W. Erwin, M. A. Kastner, and G. Shirane, Néel transition and sublattice magnetization of pure and doped La_2CuO_4, Phys. Rev. B **45**, 7430–7435 (1992).

[71] M. K. Crawford, R. L. Harlow, E. M. McCarron, W. E. Farneth, J. D. Axe, H. Chou, and Q. Huang, Lattice instabilities and the effect of copper-oxygen-sheet distortions on superconductivity in doped La_2CuO_4, Phys. Rev. B **44**, 7749–7752 (1991).

[72] P. Phillips, Fractionalize this, Nature Physics **6**(12), 931–933 (2010).

[73] S. Sachdev, Where is the quantum critical point in the cuprate superconductors?, arXiv:0907.0008v7 , 1–8 (2009).

[74] C. Castellani, C. Di Castro, and M. Grilli, Stripe formation: A quantum critical point for cuprate superconductors, Journal of Physics and Chemistry of Solids **59**(10-12), 1694–1698 (1998).

[75] C. Gough, M. Colclough, E. Forgan, R. Jordan, M. Keene, C. Muirhead, A. Rae, N. Thomas, J. Abell, and S. Sutton, Flux quantization in a high-T_c superconductor , Nature **326**(6116), 855 (1987).

[76] D. A. Wollman, D. J. Van Harlingen, W. C. Lee, D. M. Ginsberg, and A. J. Leggett, Experimental determination of the superconducting pairing state in YBCO from the phase coherence of YBCO-Pb dc SQUIDs, Phys. Rev. Lett. **71**, 2134–2137 (1993).

[77] C. C. Tsuei, J. R. Kirtley, C. C. Chi, L. S. Yu-Jahnes, A. Gupta, T. Shaw, J. Z. Sun, and M. B. Ketchen, Pairing Symmetry and Flux Quantization in a Tricrystal Superconducting Ring of $YBa_2Cu_3O_{7-\delta}$, Phys. Rev. Lett. **73**, 593–596 (1994).

[78] V. Emery and S. Kivelson, Importance of phase fluctuations in superconductors with small superfluid density, Nature **374**(6521), 434–437 (1995).

[79] P. W. Anderson, P. A. Lee, M. Randeria, T. M. Rice, N. Trivedi, and F. C. Zhang, The physics behind high-temperature superconducting cuprates: the 'plain vanilla' version of RVB, Journal of Physics: Condensed Matter **16**(24), R755 (2004).

[80] T. Senthil and M. P. A. Fisher, Fractionalization in the Cuprates: Detecting the Topological Order, Phys. Rev. Lett. **86**, 292–295 (2001).

[81] C. Varma, High-temperature superconductivity: Mind the pseudogap, Nature **468**(7321), 184–185 (2010).

[82] S. Julian, Pairing with Spin Fluctuations, Physics **5**, 17 (2012).

[83] J. Zaanen, A modern, but way too short history of the theory of superconductivity at a high temperature, arXiv:1012.5461v2 , 1–27 (2011).

[84] S. A. Kivelson, I. P. Bindloss, E. Fradkin, V. Oganesyan, J. M. Tranquada, A. Kapitulnik, and C. Howald, How to detect fluctuating stripes in the high-temperature superconductors, Rev. Mod. Phys. **75**, 1201–1241 (2003).

[85] J. Zaanen and O. Gunnarsson, Charged magnetic domain lines and the magnetism of high-T_c oxides, Phys. Rev. B **40**, 7391–7394 (1989).

[86] V. Emery, S. Kivelson, and J. Tranquada, Stripe phases in high-temperature superconductors, Proceedings of the National Academy of Sciences of the United States of America **96**(16), 8814–8817 (1999).

[87] J. Tranquada, B. Sternlieb, J. Axe, Y. Nakamura, and S. Uchida, Evidence for stripe correlations of spins and holes in copper oxide superconductors, Nature **375**(6532), 561–563 (1995).

[88] K. Yamada, C. H. Lee, K. Kurahashi, J. Wada, S. Wakimoto, S. Ueki, H. Kimura, Y. Endoh, S. Hosoya, G. Shirane, R. J. Birgeneau, M. Greven, M. A. Kastner, and Y. J. Kim, Doping dependence of the spatially modulated dynamical spin correlations and the superconducting-transition temperature in $La_{2-x}Sr_xCuO_4$, Phys. Rev. B **57**, 6165–6172 (1998).

[89] S.-W. Cheong, G. Aeppli, T. E. Mason, H. Mook, S. M. Hayden, P. C. Canfield, Z. Fisk, K. N. Clausen, and J. L. Martinez, Incommensurate magnetic fluctuations in $La_{2-x}Sr_xCuO_4$, Phys. Rev. Lett. **67**, 1791–1794 (1991).

[90] C. H. Chen, S.-W. Cheong, and A. S. Cooper, Charge modulations in $La_{2-x}Sr_xNiO_{4+y}$: Ordering of polarons, Phys. Rev. Lett. **71**, 2461–2464 (1993).

[91] J. M. Tranquada, D. J. Buttrey, and D. E. Rice, Phase separation, charge-density waves, and magnetism in $La_2NiO_{4+\delta}$ with δ=0.105, Phys. Rev. Lett. **70**, 445–448 (1993).

[92] M. Hücker, Electronic interlayer coupling in the low-temperature tetragonal phase of $La_{1.79}Eu_{0.2}Sr_{0.01}CuO_4$, Phys. Rev. B **79**, 104523 (2009).

[93] M. Huecker, G. D. Gu, J. M. Tranquada, M. von Zimmermann, H. H. Klauss, N. J. Curro, M. Braden, and B. Buechner, Coupling of stripes to lattice distortions in cuprates and nickelates, Physica C: Superconductivity and its Applications **460**(Part 1), 170–173 (2007).

[94] J. Tranquada, H. Woo, T. Perring, H. Goka, G. Gu, G. Xu, M. Fujita, and K. Yamada, Quantum magnetic excitations from stripes in copper oxide superconductors, Nature **429**(6991), 534–538 (2004).

[95] M. Von Zimmermann, A. Vigliante, T. Niemoller, N. Ichikawa, T. Frello, J. Madsen, P. Wochner, S. Uchida, N. Andersen, J. Tranquada, D. Gibbs, and J. Schneider, Hard-X-ray diffraction study of charge stripe order in $La_{1.48}Nd_{0.4}Sr_{0.12}CuO_4$, Europhysics Letters **41**(6), 629–634 (1998).

[96] J. Fink, E. Schierle, E. Weschke, J. Geck, D. Hawthorn, V. Soltwisch, H. Wadati, H.-H. Wu, H. A. Dürr, N. Wizent, B. Büchner, and G. A. Sawatzky, Charge

ordering in $La_{1.8-x}Eu_{0.2}Sr_xCuO_4$ studied by resonant soft x-ray diffraction, Phys. Rev. B **79**, 100502 (2009).

[97] J. C. Phillips and K. M. Rabe, Anomalous properties and microstructural model of superconductivity in $La_{2-x}(Ba,Sr)_xCuO_4$, Phys. Rev. B **44**, 2863–2866 (1991).

[98] A. R. Moodenbaugh, Y. Xu, M. Suenaga, T. J. Folkerts, and R. N. Shelton, Superconducting properties of $La_{2-x}Ba_xCuO_4$, Phys. Rev. B **38**, 4596–4600 (1988).

[99] M. Hücker, M. v. Zimmermann, G. D. Gu, Z. J. Xu, J. S. Wen, G. Xu, H. J. Kang, A. Zheludev, and J. M. Tranquada, Stripe order in superconducting $La_{2-x}Ba_xCuO_4$ ($0.095 \leqslant x \leqslant 0.155$), Phys. Rev. B **83**, 104506 (2011).

[100] J. M. Tranquada, J. D. Axe, N. Ichikawa, A. R. Moodenbaugh, Y. Nakamura, and S. Uchida, Coexistence of, and competition between, superconductivity and charge-stripe order in $La_{1.6-x}Nd_{0.4}Sr_xCuO_4$, Phys. Rev. Lett. **78**, 338–341 (1997).

[101] Q. Li, M. Hücker, G. D. Gu, A. M. Tsvelik, and J. M. Tranquada, Two-dimensional superconducting fluctuations in stripe-ordered $La_{1.875}Ba_{0.125}CuO_4$, Phys. Rev. Lett. **99**, 067001 (2007).

[102] J. M. Tranquada, Stripes and superconductivity in cuprates, Physica B: Condensed Matter **407**(11), 1771 – 1774 (2012).

[103] M. Fujita, H. Goka, K. Yamada, J. M. Tranquada, and L. P. Regnault, Stripe order, depinning, and fluctuations in $La_{1.875}Ba_{0.125}CuO_4$ and $La_{1.875}Ba_{0.075}Sr_{0.050}CuO_4$, Phys. Rev. B **70**, 104517 (2004).

[104] B. Büchner, M. Breuer, A. Freimuth, and A. P. Kampf, Critical buckling for the disappearance of superconductivity in rare-earth-doped $La_{2-x}Sr_xCuO_4$, Phys. Rev. Lett. **73**, 1841–1844 (1994).

[105] H. Kimura, Y. Noda, H. Goka, M. Fujita, K. Yamada, M. Mizumaki, N. Ikeda, and H. Ohsumi, Relationship between charge stripe order and structural phase transitions in $La_{1.875}Ba_{0.125-x}Sr_xCuO_4$, Phys. Rev. B **70**, 134512 (2004).

[106] M. Fujita, H. Goka, K. Yamada, and M. Matsuda, Competition between charge- and spin-density-wave order and superconductivity in $La_{1.875}Ba_{0.125-x}Sr_xCuO_4$, Phys. Rev. Lett. **88**, 167008 (2002).

[107] H.-H. Klauss, W. Wagener, M. Hillberg, W. Kopmann, H. Walf, F. J. Litterst, M. Hücker, and B. Büchner, From antiferromagnetic order to static magnetic stripes: the phase diagram of $(La,Eu)_{2-x}Sr_xCuO_4$, Phys. Rev. Lett. **85**, 4590–4593 (2000).

[108] M. Hücker, M. v. Zimmermann, M. Debessai, J. S. Schilling, J. M. Tranquada, and G. D. Gu, Spontaneous symmetry breaking by charge stripes in the high pressure phase of superconducting $La_{1.875}Ba_{0.125}CuO_4$, Phys. Rev. Lett. **104**, 057004 (2010).

[109] H. Kimura, K. Hirota, H. Matsushita, K. Yamada, Y. Endoh, S.-H. Lee, C. F. Majkrzak, R. Erwin, G. Shirane, M. Greven, Y. S. Lee, M. A. Kastner, and R. J. Birgeneau, Neutron-scattering study of static antiferromagnetic correlations in $La_{2-x}Sr_xCu_{1-y}Zn_yO_4$, Phys. Rev. B **59**, 6517–6523 (1999).

[110] L. Pintschovius and M. Braden, Anomalous dispersion of LO phonons in $La_{1.85}Sr_{0.15}CuO_4$, Phys. Rev. B **60**, R15039–R15042 (1999).

[111] G. Ghiringhelli, M. Le Tacon, M. Minola, S. Blanco-Canosa, C. Mazzoli, N. B. Brookes, G. M. De Luca, A. Frano, D. G. Hawthorn, F. He, T. Loew, M. M. Sala, D. C. Peets, M. Salluzzo, E. Schierle, R. Sutarto, G. A. Sawatzky, E. Weschke, B. Keimer, and L. Braicovich, Long-range incommensurate charge fluctuations in $(Y,Nd)Ba_2Cu_3O_{6+x}$, Science **337**(6096), 821–825 (2012).

[112] A. C. Komarek, *Complex ordering phenomena in transition metal oxides and oxyhalides*, PhD thesis, Universität zu Köln, 2009.

[113] O. Zachar, S. A. Kivelson, and V. J. Emery, Landau theory of stripe phases in cuprates and nickelates, Phys. Rev. B **57**, 1422–1426 (1998).

[114] Plinyt's Natural history. In thirty-seven books, `http://archive.org/details/plinysnaturalhis00plinrich`, n.d., Retrieved November 25, 2012.

[115] K. K. K. G. S. Parks, The heat capacities of some metallic oxides, J. Phys. Chem. **30**, 47 (1925).

[116] E. J. W. Verwey, Electronic conduction of magnetite (Fe_3O_4) and its transition point at low temperatures, Nature **144**, 327 (1939).

[117] E. Verwey and P. Haayman, Electronic conductivity and transition point of magnetite (Fe_3O_4), Physica **8**(9), 979 – 987 (1941).

[118] J. Garcia and G. Subias, The Verwey transition - a new perspective, Journal of Physics: Condensed Matter **16**(7), R145–R178 (2004).

[119] A. Goldman, *Modern Ferrite Technology*, Springer, 2006.

[120] E. Goering, Large hidden orbital moments in magnetite, Physica Status Solidi (B) - basic solid state physics **248**(10), 2345–2351 (2011).

[121] M. Iizumi and G. Shirane, Crystal symmetry of the low temperature phase of magnetite, Solid State Communications **17**(4), 433 – 436 (1975).

[122] J. Yoshida and S. Iida, X-ray study of the phase transition in magnetite, Journal of the Physical Society of Japan **47**(5), 1627–1633 (1979).

[123] M. Iizumi, T. Koetzle, G. Shirane, S. Chikazumi, M. Matsui, and S. TODO, Structure of magnetite (Fe_3O_4) below the Verwey transition temperature, Acta Crytallographica Section B: Structural Science **38**(AUG), 2121–2133 (1982).

[124] J. P. Wright, J. P. Attfield, and P. G. Radaelli, Long Range Charge Ordering in Magnetite Below the Verwey Transition, Phys. Rev. Lett. **87**, 266401 (2001).

[125] J. P. Wright, J. P. Attfield, and P. G. Radaelli, Charge ordered structure of magnetite Fe_3O_4 below the Verwey transition, Phys. Rev. B **66**, 214422 (2002).

[126] M. S. Senn, J. P. Wright, and J. P. Attfield, Charge order and three-site distortions in the Verwey structure of magnetite, Nature **481**(7380), 173–176 (2012).

[127] M. S. Senn, I. Loa, J. P. Wright, and J. P. Attfield, Electronic orders in the Verwey structure of magnetite, Phys. Rev. B **85**, 125119 (2012).

[128] I. Leonov, A. N. Yaresko, V. N. Antonov, M. A. Korotin, and V. I. Anisimov, Charge and Orbital Order in Fe_3O_4, Phys. Rev. Lett. **93**, 146404 (2004).

[129] H.-T. Jeng, G. Y. Guo, and D. J. Huang, Charge-Orbital Ordering and Verwey Transition in Magnetite, Phys. Rev. Lett. **93**, 156403 (2004).

[130] H.-T. Jeng, G. Y. Guo, and D. J. Huang, Charge-orbital ordering in low-temperature structures of magnetite: GGA + U investigations, Phys. Rev. B **74**, 195115 (2006).

[131] K. Yamauchi, T. Fukushima, and S. Picozzi, Ferroelectricity in multiferroic magnetite Fe_3O_4 driven by noncentrosymmetric Fe^{2+}/Fe^{3+} charge-ordering: First-principles study, Phys. Rev. B **79**, 212404 (2009).

[132] H. Uzu and A. Tanaka, Complex-Orbital Order in Fe_3O_4 and Mechanism of the Verwey Transition, Journal of the Physical Society of Japan **77**(7), 074711 (2008).

[133] J. van den Brink and D. Khomskii, Orbital ordering of complex orbitals in doped Mott insulators, Phys. Rev. B **63**, 140416 (2001).

[134] D. J. Huang, C. F. Chang, H.-T. Jeng, G. Y. Guo, H.-J. Lin, W. B. Wu, H. C. Ku, A. Fujimori, Y. Takahashi, and C. T. Chen, Spin and Orbital Magnetic Moments of Fe_3O_4, Phys. Rev. Lett. **93**, 077204 (2004).

[135] E. Goering, S. Gold, M. Lafkioti, and G. Schütz, Vanishing Fe 3d orbital moments in single-crystalline magnetite, EPL (Europhysics Letters) **73**(1), 97 (2006).

[136] J. C. Cezar, Z. Hu, J. Schlappa, Y. Y. Chin, A. Tanaka, Schüßler-Langeheine, N. B. Brookes, and L. H. Tjeng, The relation of orbital moment and t_{2g} orbital splitting in Fe_3O_4: x-ray absorption magnetic dichroism and resonant inelastic x-ray scattering studies., (**unpublished**) .

[137] G. Subías, J. García, J. Blasco, M. Grazia Proietti, H. Renevier, and M. Concepción Sánchez, Magnetite, a Model System for Mixed-Valence Oxides, Does Not Show Charge Ordering, Phys. Rev. Lett. **93**, 156408 (2004).

[138] D. J. Huang, H.-J. Lin, J. Okamoto, K. S. Chao, H.-T. Jeng, G. Y. Guo, C.-H. Hsu, C.-M. Huang, D. C. Ling, W. B. Wu, C. S. Yang, and C. T. Chen, Charge-Orbital Ordering and Verwey Transition in Magnetite Measured by Resonant Soft X-Ray Scattering, Phys. Rev. Lett. **96**, 096401 (2006).

[139] J. Schlappa, C. Schüßler-Langeheine, C. F. Chang, H. Ott, A. Tanaka, Z. Hu, M. W. Haverkort, E. Schierle, E. Weschke, G. Kaindl, and L. H. Tjeng, Direct Observation of t_{2g} Orbital Ordering in Magnetite, Phys. Rev. Lett. **100**, 026406 (2008).

[140] S. R. Bland, B. Detlefs, S. B. Wilkins, T. A. W. Beale, C. Mazzoli, Y. Joly, P. D. Hatton, J. E. Lorenzo, and V. A. M. Brabers, Full polarization analysis of resonant superlattice and forbidden x-ray reflections in magnetite, Journal of Physics: Condensed Matter **21**(48), 485601 (2009).

[141] S. B. Wilkins, S. Di Matteo, T. A. W. Beale, Y. Joly, C. Mazzoli, P. D. Hatton, P. Bencok, F. Yakhou, and V. A. M. Brabers, Critical reexamination of resonant soft x-ray Bragg forbidden reflections in magnetite, Phys. Rev. B **79**, 201102 (2009).

[142] T. Kasama, N. S. Church, J. M. Feinberg, R. E. Dunin-Borkowski, and R. J. Harrison, Direct observation of ferrimagnetic/ferroelastic domain interactions in magnetite below the Verwey transition, Earth and Planetary Science Letters **297**(1-2), 10 – 17 (2010).

[143] W. C. Hamilton, Neutron Diffraction Investigation of the 119° K Transition in Magnetite, Phys. Rev. **110**, 1050–1057 (1958).

[144] L. R. Bickford, The Low Temperature Transformation in Ferrites, Rev. Mod. Phys. **25**, 75–79 (1953).

[145] C. F. Chang, *Study of Charge, Spin, and orbital States in Strongly Correlated Transition-Metal Oxides*, PhD thesis, Universität zu Köln, 2009.

[146] A. Tanaka, C. F. Chang, M. Buchholz, C. Trabant, E. Schierle, J. Schlappa, D. Schmitz, H. Ott, P. Metcalf, L. H. Tjeng, and C. Schüßler-Langeheine, Analysis of Charge and Orbital Order in Fe_3O_4 by Fe $L_{2,3}$ Resonant X-Ray Diffraction, (**unpublished**) .

[147] H. Ott, C. Schüßler-Langeheine, E. Schierle, A. Y. Grigoriev, V. Leiner, H. Zabel, G. Kaindl, and E. Weschke, Magnetic x-ray scattering at the M_5 absorption edge of Ho, Phys. Rev. B **74**, 094412 (2006).

[148] E. Schierle, V. Soltwisch, D. Schmitz, R. Feyerherm, A. Maljuk, F. Yokaichiya, D. N. Argyriou, and E. Weschke, Cycloidal Order of $4f$ Moments as a Probe of Chiral Domains in $DyMnO_3$, Phys. Rev. Lett. **105**, 167207 (2010).

[149] H. A. Dürr, E. Dudzik, S. S. Dhesi, J. B. Goedkoop, G. van der Laan, M. Belakhovsky, C. Mocuta, A. Marty, and Y. Samson, Chiral Magnetic Domain Structures in Ultrathin FePd Films, Science **284**(5423), 2166–2168 (1999).

[150] G. van der Laan, E. Dudzik, S. Collins, S. Dhesi, H. Durr, M. Belakhovsky, K. Chesnel, A. Marty, Y. Samson, and B. Gilles, Soft X-ray magnetic scattering from striped magnetic domain structures, Physica B **283**(1-3), 171–174 (2000).

[151] M. Uehara, S. Mori, C. Chen, and S. Cheong, Percolative phase separation underlies colossal magnetoresistance in mixed-valent manganites, Nature **399**(6736), 560–563 (1999).

[152] F. M. Woodward, J. W. Lynn, M. B. Stone, R. Mahendiran, P. Schiffer, J. F. Mitchell, D. N. Argyriou, and L. C. Chapon, Field-induced avalanche to the ferromagnetic state in the phase-separated ground state of manganites, Phys. Rev. B **70**, 174433 (2004).

[153] F. Giesen, B. Damaschke, V. Moshnyaga, K. Samwer, and G. A. Müller, Suppression of interface-induced electronic phase separation in all-manganite multilayers by preservation of the Mn-O chain network, Phys. Rev. B **69**, 014421 (2004).

[154] A. Kleine, Y. Luo, and K. Samwer, Electronic phase separation in LaMnO 3 + d -layers: Usable as a tunneling barrier?, EPL (Europhysics Letters) **76**(1), 135 (2006).

[155] M. C. Dekker, A. D. Rata, K. Boldyreva, S. Oswald, L. Schultz, and K. Dörr, Colossal elastoresistance and strain-dependent magnetization of phase-separated $(Pr_{1-y}La_y)_{0.7}Ca_{0.3}MnO_3$ thin films, Phys. Rev. B **80**, 144402 (2009).

[156] D. Senff, O. Schumann, M. Benomar, M. Kriener, T. Lorenz, Y. Sidis, K. Habicht, P. Link, and M. Braden, Melting of magnetic correlations in charge-orbital ordered $La_{1/2}Sr_{3/2}MnO_4$: Competition of ferromagnetic and antiferromagnetic states, Phys. Rev. B **77**, 184413 (2008).

[157] W. Bao, C. Chen, S. Carter, and S.-W. Cheong, Electronic phase separation and charge ordering in $(Sr,La)_2MnO_4$: Indication of triplet bipolarons, Solid State Communications **98**(1), 55 – 59 (1996).

[158] A. Komarek, M. Reuther, T. Lorentz, A. Cousson, P. Link, W. Morgenroth, D. Trots, C. Baehtz, and M. Braden, Evidence for charge and orbital order in the doped titanates $RE_{(1-x)}Ca_xTiO_3$ (RE=Y, Er, Lu), arXiv:1109.0234 , 1–4 (2011).

[159] H. Matsuhata, F. Iga, M. Tsubota, T. Nakano, T. Takabatake, and K. Kato, Phase separation in $Y_{1-x}Ca_xTiO_3$ associated with the insulator-to-metal transition: Observation by transmission electron microscopy, Phys. Rev. B **70**, 134109 (2004).

[160] T. Becker, C. Streng, Y. Luo, V. Moshnyaga, B. Damaschke, N. Shannon, and K. Samwer, Intrinsic Inhomogeneities in Manganite Thin Films Investigated with Scanning Tunneling Spectroscopy, Phys. Rev. Lett. **89**, 237203 (2002).

[161] T. Hanaguri, C. Lupien, Y. Kohsaka, D. Lee, M. Azuma, M. Takano, H. Takagi, and J. Davis, A 'checkerboard' electronic crystal state in lightly hole-doped $Ca_{2-x}Na_xCuO_2Cl_2$, Nature **430**(7003), 1001–1005 (2004).

[162] D. Polli, M. Rini, S. Wall, R. W. Schoenlein, Y. Tomioka, Y. Tokura, G. Cerullo, and A. Cavalleri, Coherent orbital waves in the photo-induced insulator-metal dynamics of a magnetoresistive manganite, Nature Materials **6**(9), 643–647 (S 2007).

[163] D. Abernathy, G. Grubel, S. Brauer, I. McNulty, G. Stephenson, S. Mochrie, A. Sandy, N. Mulders, and M. Sutton, Small-angle X-ray scattering using coherent undulator radiation at the ESRF, Journal of Synchrotron Radiation **5**(Part 1), 37–47 (1998).

[164] Y. Taguchi, Y. Tokura, T. Arima, and F. Inaba, Change of electronic structures with carrier doping in the highly correlated electron system $Y_{1-x}Ca_xTiO_3$, Phys. Rev. B **48**, 511–518 (1993).

[165] Y. Tokura, Fillingness dependence of electronic structures in strongly correlated electron systems: Titanates and vanadates, Journal of Physics and Chemistry of Solids **53**(12), 1619 – 1625 (1992).

[166] Y. Tokura, Y. Taguchi, Y. Okada, Y. Fujishima, T. Arima, K. Kumagai, and Y. Iye, Filling dependence of electronic properties on the verge of metal–Mott-insulator transition in $Sr_{1-x}La_xTiO_3$, Phys. Rev. Lett. **70**, 2126–2129 (1993).

[167] K. Kumagai, T. Suzuki, Y. Taguchi, Y. Okada, Y. Fujishima, and Y. Tokura, Metal-insulator transition in $La_{1-x}Sr_xTiO_3$ and $Y_{1-x}Ca_xTiO_3$ investigated by specific-heat measurements, Phys. Rev. B **48**, 7636–7642 (1993).

[168] Y. Tokura, Y. Taguchi, Y. Moritomo, K. Kumagai, T. Suzuki, and Y. Iye, Barely metallic states with enhanced carrier mass in $Y_{1-x}Ca_xTiO_3$, Phys. Rev. B **48**, 14063–14066 (1993).

[169] K. Kato, E. Nishibori, M. Takata, M. Sakata, T. Nakano, K. Uchihira, M. Tsubota, F. Iga, and T. Takabatake, The metal–insulator transition in $Y_{1-x}Ca_xTiO_3$ caused by phase separation, Journal of the Physical Society of Japan **71**(9), 2082–2085 (2002).

[170] H. Nakao, S. Kodama, K. Kiyoto, D. Bizen, Y. Murakami, M. Tsubota, F. Iga, and T. Takabatake, Metal-insulator transition in $Y_{1-x}Ca_xTiO_3$ studied by x-ray scattering, Journal of Magnetism and Magnetic Materials **310**(2, Part 1), 895 – 897 (2007).

[171] Andor, High energy detection - solutions beyond the visible, `http://www.andor.com/pdfs/literature/Andor_High_Energy_Detection_Brochure.pdf`, n.d., Retrieved November 25, 2012.

[172] F. Westermeier, T. Autenrieth, C. Gutt, O. Leupold, A. Duri, A. Menzel, I. Johnson, C. Broennimann, and G. Grübel, Fast two-dimensional detection for X-ray photon correlation spectroscopy using the PILATUS detector, Journal of Synchrotron Radiation **16**(5), 687–689 (2009).

[173] G. Gruebel, X-Ray Photon Correlation Spectroscopy at the European X-Ray Free-Electron Laser (XFEL) facility, Comptes Rendus Physique **9**(5 - 6), 668 – 680 (2008).

[174] Y. Chushkin, C. Caronna, and A. Madsen, A novel event correlation scheme for x-ray photon correlation spectroscopy, Journal of Applied Crystallography **45**(4), 807–813 (2012).

[175] Y. Piederrière, J. Cariou, Y. Guern, B. L. Jeune, G. L. Brun, and J. Lortrian, Scattering through fluids: speckle size measurement and Monte Carlo simulations close to and into the multiple scattering, Opt. Express **12**(1), 176–188 (2004).

[176] W. Boyle and G. Smith, Charge coupled semiconductor device, Bell System Technical Journal **49**(4), 587 (1970).

[177] Princeton Instruments, `http://www.princetoninstruments.com/`, n.d., Retrieved November 25, 2012.

[178] Hamamatsu, `http://www.hamamatsu.com/`, n.d., Retrieved November 25, 2012.

Abstract

Transition-metal oxides (TMOs) show rich phase diagrams with various magnetic and electronic phases that arise from the complex interplay between spin, charge, orbital, and lattice degrees of freedom. The most prominent class of materials, which has attracted a lot of attention in the last decades, are probably high-temperature superconductors (HTS), in which the resitivity drops to zero below a critical temperature. Further examples are different kind of complex ordering phenomena, for example a modulation of the charge, spin or orbital density. In some systems a coexistence of energetically close phases is found.

X-ray diffraction experiments are sensitive to a periodic arrangement of an electron-density modulation. If tuned to an absorption edge of one of the contained elements, a virtual transition from the core states to the valence states probes the occupation of the intermediate state and makes the process spectroscopically sensitive to the scattering center. Many of the interesting x-ray absorption edges of TMOs are in the energy interval between 400 and 3000 eV, in which also the absorption in air is strong.

In Chap. 2 we report about commissioning and building up a novel ultar-high vacuum (UHV) diffractometer for soft x-ray diffraction experiments, which is meant as an user endstation at P04 beamline of the new synchrotron facility PETRA III. The instrument is based on a sufficiently large vacuum chamber with two differentially pumped rotary feedthroughs for an independent sample and detector rotation. The large detector circle allows to use complex detector setups, like an in-vacuum CCD and polarization analyzer. Therefore, the diffractometer is well suited for new techniques of gaining importance, like coherent x-ray diffraction (CXD), in which the finestructure of a diffraction reflex reveals information about the domain-wall dynamics, and like resonant soft x-ray diffraction (RSXD), which shows its full power when combined with a polarization analysis of the diffracted photons. In first experiments at DESY, BESSY II, and FLASH, the new machine has been successfully operated and helped to obtain data in unprecedented precision. Data recorded from multilayer reflectors, which will be used for the setup of the new polarization analyzer, and data that were recorded with the new CCD detector are presented in this chapter as well. Further data, from a RSXD experiment on magnetite

are presented in Chap. 4.

In Chap. 3 we report about a moderately surface-sensitive RSXD experiment in which for the first time charge stripe order in the proto-typical HTS $La_{1.88}Sr_{0.12}CuO_4$ (LSCO) was found. The strong similarity of the resonant diffraction spectra from the charge order reflex in LSCO to those from an $La_{1.6-x}Nd_{0.4}Sr_xCuO_4$ (LNSCO) reference sample, in which the existence of charge stripe order is well established, clearly shows the similar electronic origin. While charge stripe peaks were found in all LSCO samples that were studied, including in-situ cleaved and ex-situ polished ones, we could not find a reflex with bulk-sensitive hard x-ray diffraction experiments. From this we conclude that LSCO is close to the formation of a charge stripe order that already the reduced dimensionality in the near-surface region is sufficient to stabilize them in a layer of at least 5 nm thickness.

In Chap. 4 we present a RSXD experiment from the $(0\,0\,\frac{1}{2})$ charge-orbital order reflex in Fe_3O_4. The azimuthal dependence of the linear dichroism shows a low-symmetry pattern, which reflects a strong monoclinic symmetry of the electronic $3d$ wave function. We found this monoclinic deviation prior to the refinements from the pseudo-orthorhombic to the monoclinic crystal structure, which was published this year. From the orbital ordering models that were proposed so far only a calculation, which is based on a complex-coefficient orbital ordering, could predict our experiment correctly. This theory further predicts a circular dichroism in the diffraction signal, which we indeed found in our experiment.

In Chap. 5 we report about our results of CXD experiments on doped titanates, in which a coexistence of charge-ordered insulating an metallic regions was found. Charge ordered regions are characterized by superstructure reflections. Coherent illumination of these regions allows to produce an interference pattern that reflects information on the spatial arrangement of the insulating regions. The temporal evolution of this pattern provides insight into the dynamics due to domain reorganizations and domain-wall movements. First experiments at the ESRF and BESSY II were seriously limited due to the lacking stability of the sample setup. CXD experiments at BESSY II and PETRA III with a new sample setup, which was developed in cooperation with the University of Amsterdam, have shown that domain-wall dynamics take place on even shorter time scales than accessible.

RSXD and CXD are powerful tools to study various properties of TMOs, ranging from the local electronic d wave symmetry in magnetite to the reorganization of mesoscopic domains. The new UHV diffractometer will allow to perform these kind of experiments with high precision and modern detector setups.

Kurzzusammenfassung

Übergangsmetalloxide zeigen eine Vielzahl von Phänomenen, die durch starke elektronische Korrelationen und Kopplungen unterschiedlicher Freiheitsgrade zustande kommen. Eines der bekanntesten Beispiele ist Hochtemperatursupraleitung in Kupraten. In vielen dieser Systeme finden sich komplexe räumliche Modulationen der elektronischen Freiheitsgrade, wie dem Spin, der Ladung und der orbitalen Besetzung. In den letzen Jahren wurden zudem Systeme gefunden, in denen unterschiedliche Phasen koexistieren können, da sie energetisch sehr eng beieinander liegen.

In Röntgenbeugungsexperimenten, bei denen das Photon an der Elektronenhülle der Atome gestreut wird, kann man Modulationen der elektronischen Dichte untersuchen. In der Nähe einer Absorptionskante von einem der beteiligten Elemente findet der Streuprozess in Zusammenhang mit einer virtuellen Anregung in einen unbesetzten Zwischenzustand statt, über dessen Besetzung und Energiezustände man durch den Prozess Aufschluss erhält. Die interessantesten Anregungen finden im weichen Röntgenbereich statt. Gegenstand dieser Arbeit ist der Aufbau und Test einens neuen Instruments zur resonanten Beugung im weichen Röntgenbereich sowie die Untersuchung von Ordnungsphänomenen in den prototypischen Übergangsmetalloxiden $La_{1.88}Sr_{0.12}CuO_4$ (LSCO) und Fe_3O_4 (Magnetit). Der Effekt der Phasenkoexistenz wurde für dotierte Titanate mittels Beugung kohärenter Röntgenstrahlung untersucht.

In Kapitel 2 wird über den Aufbau und die Inbetriebnahme der neuen Ultrahochvakuum-Streukammer berichtet, die als Nutzerinstrument am Weichröntgen-Strahlrohr der neuen Synchrotronstrahlungsquelle PETRA III vorgesehen ist. Erste Experimente mit der neuen Kammer am Hasylab, bei BESSY II und bei FLASH haben die Funktionalität des neuen Instruments gezeigt, die es ermöglicht, Daten mit noch nie dagewesener Genauigkeit zu messen.

In Kapitel 3 wird die erste experimentelle Beobachtung von Ladungsstreifenordnung in dem prototypischen Hochtemperatursupraleiter LSCO präsentiert. In einem resonanten Beugungsexperiment mit weicher Röntgenstrahlung fand sich ein Reflex an der gleichen Stelle, an der im Referenzsystem $La_{1.6-x}Nd_{0.4}Sr_xCuO_4$ (LNSCO) Ladungsstreifen gefunden wurden. Die Bestätigung einer vergleichbaren elektronischen Ordnung ergibt

sich aus der Ähnlichkeit der Streuspektren in LSCO und LNSCO an den Sauerstoff-K- und Kupfer-$L_{2,3}$ Kanten. Obgleich sich Ladungsstreifen in mehreren sowohl polierten als auch gespaltenen LSCO-Proben im Weichröntgenexperiment fanden, ließ sich keine Streifenordnung in volumenempfindlichen harten Röntgenbeugungsexperimenten finden. Aus unseren Beobachtungen folgt, dass LSCO an der Grenze zur Stabilisierung von Ladungsordnung ist und dass kleine Veränderungen, wie eine reduzierte Dimensionalität an der Oberfläche, die Stabilisierung der Streifenordnung begünstigen.

Kapitel 4 beschreibt ein resonantes Beugungsexperiment am $(0\,0\,\frac{1}{2})$ Ordnungsreflex von Fe_3O_4. Die Azimuthabhängigkeit des Lineardichroismus lässt Rückschlüsse auf die lokale Symmetrie der $3d$ Wellenfunktion zu. Wir konnten eine ausgeprägte monokline Symmetrie identifizieren. Von allen Modellen der orbitalen Ordnung, die bisher für Magnetit vorgeschlagen wurden, kann nur ein komplexzahliges orbitales Ordnungsmodel diese Experimente richtig beschreiben. Das Modell sagt einen sehr ungewöhnlichen Grundzustand für das Material voraus, in dem sich spontan ein orbitales Moment bildet. Rechnungen, die auf diesem Modell basieren, haben eine Azimuthabhängigkeit des Zirkulardichroismus vorausgesagt, die experimentell bestätigt werden konnte.

Kapitel 5 stellt erste Ergebnisse kohärenter Beugungsexperimente vor. Das verwendeten Modellsystem sind dotierte Titanate, in denen es zur Koexistenz von metallischen und isolierenden Regionen kommt, wobei letztere durch Überstrukturreflexe charakterisiert ist. Die kohärente Bestrahlung mehrerer Domänen führt zu einer Interferenz im Beugungssignal, die Auskunft über die Anordnung der Regionen in der Probe gibt. Durch die zeitliche Entwicklung des Beugungsbildes kann man für das System charakteristische Zeitkonstanten finden. Erste Experimente in Kooperation mit der Uni Amsterdam haben gezeigt, dass die Domänendynamik auf Zeitskalen deutlich unterhalb einiger Minuten stattfindet.

Resonante und kohärente Röntgenbeugung sind mächtige Techniken, um Eigenschaften von Übergangsmetalloxiden auf unterschiedlichen Längenskalen zu testen. Diese reichen von der Symmetrie der lokalen elektronischen Wellenfunktion bis hin zu der Umgruppierung unterschiedlicher Domänen. Mit dem neu in Betrieb genommenen Röntgendiffraktometer sind ideale Bedingungen für hochpräzise Experimente mit modernen Detektoraufbauten gegeben.

Acknowledgement

At this point I want to thank all those people that are involved in this thesis by some means or other.

First of all, I want to thank three people: Dr. Christian Schüßler-Langeheine, Prof. Dr. Liu Hao Tjeng, and Prof. Dr. Markus Braden. Thank you, for giving me the possibility to work in your groups.

Christian, I greatly thank you for all those discussion we had. These discussions really helped me to understand resonant scattering and the physics of correlated oxides. Thanks for exploring coherent scattering together and discussing how to improve our experimental conditions. Besides that, I enjoyed the trips and delicious places you showed us.

Hao, many thanks for the support during the last years and keeping in touch with me, although there is obviously so much you have to take care of. I am still deeply amazed about your knowledge. Thanks for everything.

Prof. Braden, I deeply thank you for not only formally adopting me into your group, instead I really felt welcome in your group.

Secondly, I want to thank Prof. Dr. Ladislav Bohatý for taking over the chair of the examination board.

Christoph Trabant, I deeply thank you for your support and the nice collaboration during so many beamtimes.

Christian Schüßler-Langeheine, Chun-Fu Chang, Christoph Trabant, Pascal Vogt, Marita Döhler, Jeroen Goedkoop, Bo Shi, Hsueh-Hung Wu, Holger Ott, Christian Gutt, Matthias Cwik, Stephen Price, Tobias Burnus, Vasco Tenner, Franziskus Heigl, Hans Ellermeijer, thanks for all the joint work during a plenty of beamtimes, and thanks for all the social events and time we shared.

Chun-Fu, Justina Schlappa, Holger Ott, and all co-workers, I thank you for the nice pre-work on magnetite, which was really crucial for our experimental success. Arata Tanaka, Maurits W. Haverkort, Zhiwei Hu thanks for theory, data and discussions. Patricia Metcalf, Chun-Fu, and Marita thanks for providing magnetite samples.

Thanks to Alexander Komarek, and Martin v. Zimmermann for the high-energy x-ray experiments on LSCO. Thanks to Susanne Heijligen for the susceptibility measurements of LSCO. Special thanks to Enrico Schierle, Detlef Schmitz, Eugen Weschke, Victor Soltwisch, for the help and discussions at the UE46-PGM1 beamline at BESSY II and providing there UHV diffractometers. Thanks to Fumihiko Nakamura for the samples.

The coherent scattering experiments benefited from the knowledge of the people from the University of Amsterdam, especially Jeroen Goedkoop, Bo Shi, Hans Ellermeijer, Vasco Tenner, and the people from DESY, especially Michael Sprung, Christian Gutt, Sergej Bondarenko, Alexey Zozulya, Fabian Westermeier, Maria Teresa Nunez Pardo de Vera, and Gerhard Grübel. Thanks to the discussions and support. I thank Federico Zontone and Anders Madsen for their help at the ID10a beamline of the ESRF. Alexander Komarek, thank you for providing excellent samples.

Thanks to the finacial support by the German Ministry for Science and Education (BMBF) through contracts 05KS7PK1 and 05K10PK2BMBF.

Thanks to Lucie Hamdan, Werner Külzer, Andreas Freimut, Peter Hansmann, Rainer Bauer, Timur Zent, Gerhard Menz, Harald Lüttgen, Klaus Lehmann and all the other people from the mechanical and electrical workshops of the institute, for supporting our projects with your technical skills.

Thanks to the formerly group of Prof. Tjeng and the group of Prof. Braden, and all the other people from the institute for the collaboration and scientific help.

Thanks for the IT-support from Jonas Weinen, Oliver Breunig, Sigurd Skoda and Christoph Grams.

A heartfelt thanks goes Fabio Strigari, Jonas Weinen, Thomas Finger and Thomas Koethe for their support in the last weeks.

I deeply thank all those people and colleagues I met during my time at the University of Cologne: Jonas Weinen, Tim Haupricht, Rainald Gierth, Matthias Heidemann, Andreas Hendriks, Thomas Willers, Simone Altendorf, Thomas Koethe, Andrea Severing, Fabio Strigari, Jan Gegner, Nils Hollmann, Michael Zell, Timm Gerber, Johanna Brand, Thomas Finger, Thomas Bardenheuer. Thanks to all of you for sharing time, a room, a joke, a coffee, a meal, a drink, a cookie, sweets, thanks for celebrating birthdays, organizing events, thanks for listening to my words or at least making me believe you did, thanks for all the discussions and hours of silence, thanks for humming, singing, being crazy, making me smile, making me lough.

I thank all those people that I forgot to mention and apologize for the inattention.

Finally, with all my heart, I thank Steffi, my parents Petra and Willi, my brothers and sisters Tim and Tanja, my family and all my friends. I am grateful for your love and support in my life. Thank you for being considerate for the lack of time, especially in the last year.

Erklärung

Ich versichere, dass ich die von mir vorgelegte Dissertation selbständig angefertigt, die benutzten Quellen und Hilfsmittel vollständig angegeben und die Stellen der Arbeit - einschließlich Tabellen, Karten und Abbildungen -, die anderen Werken im Wortlaut oder dem Sinn nach entnommen sind, in jedem Einzelfall als Entlehnung kenntlich gemacht habe; dass diese Dissertation noch keiner anderen Fakultät oder Universität zur Prüfung vorgelegen hat; dass sie - abgesehen von unten angegebenen Teilpublikationen - noch nicht veröffentlicht worden ist sowie, dass ich eine solche Veröffentlichung vor Abschluss des Promotionsverfahrens nicht vornehmen werde. Die Bestimmungen der Promotionsordnung sind mir bekannt. Die von mir vorgelegte Dissertation ist von Prof. Dr. Markus Braden, Prof. Dr. Liu Hao Tjeng und Dr. Christian Schüßler-Langeheine betreut worden.

Köln, den 14. März 2013